

**TWO-DIMENSIONAL ELECTRON TRANSPORT IN GALLIUM NITRIDE AND  
GALLIUM ARSENIDE-BASED HETEROSTRUCTURES**

**by**

**Hailing Cheng**

A dissertation submitted in partial fulfillment  
of the requirements for the degree of  
Doctor of Philosophy  
(Physics)  
in the University of Michigan  
2011

Doctoral Committee:

Associate Professor Çagliyan Kurdak, Chair  
Professor Roy Clarke  
Professor Luming Duan  
Professor Rachel S. Goldman  
Professor Ctirad Uher

© Hailing Cheng 2011  
All Rights Reserved

## **ACKNOWLEDGEMENTS**

When I came to the University of Michigan, I never thought I would graduate as an experimentalist. My first deep thanks go to my advisor, Çagliyan Kurdak, who coached me and hammered me into a qualified experimentalist. I remember few years ago a cold leak happened in our He3 Dewar and we needed to ship it for fixing. While I worried about the container to box it, Çagliyan showed me what an experimentalist could do. He took me to a local Home-Depot and bought wooden pieces and a lot of carpenter tools. In an afternoon, we worked as carpenters and made a beautiful container. At that moment, I had a strong feeling about what an experimentalist meant.

Those days really fly and I miss my time in U of M so much, not to mention the Michigan football games and March meetings. Those are my golden days and it would never come back again. In this limited space here, I would say my thanks to all the people I need to thank, though this list would never be complete. Many thanks go to my committees: Prof. Roy Clarke, Luming Duan, Rachel S. Goldman and Ctirad Uher, for their always support. Special goes to Roy for allowing me to stay in his lab to learn MBE, to Ctirad for allowing me to steal his liquid helium, to Rachel for beautiful GaAs samples, and to Prof. Morkoc for high quality GaN samples. I also need to thank Nadine for hosting my farewell party, Yu Jin for the collaborations, Vladimir for his talking in the midnight, Yan and Nan for their always-be-there-for-me. Again I need to thank Elizabeth, Richard and Steven for dissertation proofreading and lab supports, and finally I need to thank my family for reasons no need to mention.

## TABLE OF CONTENTS

<b>ACKNOWLEDGEMENTS .....</b>	<b>ii</b>
<b>LIST OF FIGURES .....</b>	<b>vi</b>
<b>LIST OF APPENDICES .....</b>	<b>xii</b>
<b>ABSTRACT.....</b>	<b>xiii</b>
<b>CHAPTER</b>	
<b>1. INTRODUCTION.....</b>	<b>1</b>
1.1 Overview.....	1
1.2 Heterostructures with a Two-Dimensional Electron Gas .....	2
1.3 Changing the 2DEG carrier density .....	7
1.4 Magnetotransport measurement on Hall bar samples.....	8
1.5 Van der Pauw method.....	10
1.6 AlGaN/AlN/GaN heterostructures.....	12
1.7 InAlN/GaN heterostructures .....	13
1.8 Dissertation Objectives .....	15
1.9 Dissertation outline .....	16
<b>2. MAGNETOTRANSPORT MEASUREMENTS IN AlGaN/AlN/GaN HETEROSTRUCTURES .....</b>	<b>19</b>
2.1 Landau Level .....	19
2.2 Magneto transport measurements and Shubnikov-de Hass Effect.....	22
2.3 AlGaN/InN/GaN sample growth .....	23
2.4 Sample Characterization .....	25
<b>3. TWO SUBBANDS CONDUCTION IN A GATED HIGH DENSITY InAlN/AlN/GaN HETEROSTRUCTURE .....</b>	<b>29</b>
3.1 InAlN/GaN sample growth.....	29

3.2 Magnetotransport measurements .....	31
3.3 Two conduction subbands with high mobility .....	34
3.4 Charge distribution in two conductive subbands .....	36
3.5 Summary and future directions.....	42
<b>4. MAGNETOTRANSPORT MEASUREMENTS IN AlGaN/AlN/GaN 2DEGs WITH PARASITIC CHANNEL.....</b>	<b>44</b>
4.1 Al <sub>x</sub> Ga <sub>1-x</sub> N/AlN/GaN heterostructures grown on epitaxial lateral overgrown GaN templates.....	44
4.2 Magnetotransport measurements in AlGaN/AlN/GaN control samples ...	51
4.3 Magnetotransport measurements in SiN-GaN samples .....	55
4.4 Modeling of contact resistances in Hall bar samples.....	61
4.5 Magnetotransport measurements in ELO-GaN samples.....	67
4.6 Summary.....	70
<b>5. SPIN-ORBIT INTERACTION IN GaN HETEROSTRUCTURES 72</b>	
5.1 Spin-Orbit Interaction in Semiconductors .....	72
5.2 Spin-Orbit Coupling in AlGaN/GaN heterostructures.....	73
5.3 Weak Antilocalization measurements in AlGaN/GaN heterostructures...	75
5.4 Spin-splitting energy in AlGaN/GaN heterostructures .....	78
5.5 Phase Coherence in AlGaN/GaN heterostructures .....	81
5.6 Spin-Orbit Coupling in InAlN/GaN heterostructures .....	83
5.7 InAlN/GaN heterostructures samples .....	85
5.8 WAL measurements for InAlN/GaN heterostructures samples.....	89
5.9 SO field and Spin-Splitting energy in InAlN/GaN heterostructures.....	91
5.10 SO parameters from SdH oscillations.....	95
5.11 Conclusion .....	98
<b>6. ENERGY RELAXATION MEASURED BY WEAK ANTILOCALIZATION IN AlGaN/GaN HETEROSTRUCTRES ... 100</b>	
6.1 Electron-Phonon Interaction in AlGaN/GaN Heterostructures.....	100
6.2 AlGaN/GaN Heterostructures samples .....	101
6.3 Characterization of AlGaN/GaN Heterostructures Samples.....	101
6.4 Weak antilocalization measurements.....	105
6.5 Power dissipation in AlGaN/GaN Heterostructures .....	109
6.6 Clean limit versus dirty limit .....	110

6.7 Conclusion .....	115
<b>7. OPERATION OF A SINGLE ELECTRON TRANSISTOR PLACED ON STACKED INTEGER QUANTUM HALL LAYERS AS A MAGNETOMETER.....</b>	<b>116</b>
7.1 AlGaAs/GaAs heterostructures and the quantum Hall effect .....	116
7.2 Charge imbalance and long lived bulk currents.....	117
7.3 Screening of additional magnetic field at high filling fractions.....	122
7.4 Stacked quantum hall layers and single electron transistor sample .....	124
7.5 Charge/ magnetic field ratio measured by the DC pulse and AC techniques .....	131
7.6 The IQHL and SET composite device performs as a magnetometer.....	134
7.7 Conclusion .....	137
<b>8. CHARGE MOTIONS DETECTED BY SINGLE ELECTRON TRANSISTORS IN QUANTUM HALL LIQUID.....</b>	<b>138</b>
8.1 Topological quantum computation and quantum Hall liquids.....	138
8.2 The single electron transistors .....	140
8.3 Charge motion detected by a single electron transistor in multiple QHL .....	141
8.4 Charge dynamics in normal and antidot QHL samples .....	150
8.5 Characterization of the FQHL sample and the SETs.....	154
8.6 Responses of QHL to the backgate voltage .....	157
8.7 Responses of QHL to the magnetic pulse and the backgate voltage together .....	162
8.8 Conclusions and future directions.....	172
<b>9. SUMMARY AND SUGGESTIONS FOR FUTURE WORK.....</b>	<b>174</b>
9.1 Summary of present work.....	174
9.2 Suggestions for future work.....	180
<b>APPENDICES .....</b>	<b>184</b>
<b>BIBLIOGRAPHY .....</b>	<b>214</b>

## LIST OF FIGURES

### Figure

- Fig.1.1: Potential energy versus distance in the growth direction in heterostructure. 2DEG wave function is confined at the triangle potential on the interface of the heterostructure. ....5
- Fig.1.2: Schematic diagram of a Hall bar structure. Lead 1-5 are labeled in the diagram. The aspect ratio is  $L/W$ . The metal gate covers the active area of the Hall bar. ....9
- Fig.1.3: Schematic diagram of different four terminal resistance measurements on Van der Pauw sample. The arrows are the directions in which currents flow. ....11
- Fig.1.4: Bandgap energy versus lattice constants for some III-V semiconductors. This diagram is adapted from reference [29]. ....14
- Fig.2.1: Density of states in 2DEG as a function of energy in different magnetic fields (low magnetic field and high magnetic field). ....21
- Fig.2.2: SdH and Hall measurements of a Gated  $\text{Al}_{0.25}\text{Ga}_{0.75}\text{N}/\text{AlN}/\text{GaN}$  sample. The gate voltages were varied from -0.5V to 0.4V. ....26
- Fig.2.3: Mobility vs. Carrier densities. The red dots are the fit for low carrier densities data with function  $\mu \sim n^{1.6}$  and purple dashes are the fit for high carrier densities data with function  $\mu \sim n^{-1.1}$ . ....27
- Fig.3.1: TEM image and EDXS measurement of the InAlN/GaN sample...30
- Fig.3.2: Longitudinal magneto transportation measurements at gate voltages from 0 V to -1.8V (from top to bottom in 0.2V steps). ....32
- Fig.3.3: FFT for first and second subbands SdH components at  $V_{\text{gate}} = -0.8\text{V}$ . The data was fitted into Dingle formula and quantum lifetime  $\tau_q$  and carrier density has been extracted. ....33
- Fig.3.4:  $\ln[R^* \text{sing}(X)/X]$  vs  $1/B$  at  $V_{\text{gate}} = -0.8\text{V}$ . The data was fitted into linear line and the slope was used to calculate the quantum lifetime  $\tau_q$ ....34

Fig.3.5:	Carrier densities vs gate voltage. The solid dots are the carrier densities for the first and second subbands, where data for the second subband is shown according to the right scale.....	35
Fig.3.6:	Quantum lifetime vs gate voltage. The second subband quantum lifetime is greater than first subband quantum lifetime in all gate voltages.....	36
Fig.3.7:	Energy of subband versus distance in growth direction in heterostructure. This is obtained by ATLAS simulations for 2DEG band calculations.....	39
Fig.3.8:	Subband energy vs gate voltage. Solid points are calculation results from ATLAS simulation and hollow points are experimental data.	40
Fig.3.9:	Mobility vs Carrier Density. Hollow points are experimental data from AlGaN/AlN/GaN samples and solid points are InAlN/AlN/GaN data.....	42
Fig.4.1:	Growth on lattice-mismatched sapphire substrates, attempting to filter the threading dislocations by utilizing defect-blocking mask layers, which is referred as the epitaxial lateral overgrowth (ELO).	46
Fig.4.2:	Sample structures used in this chapter. From left to right: AlGaN/AlN/GaN control samples, SiN-GaN samples and ELO-GaN samples. This diagram is from the courtesy of Prof. Morkoc's group .....	47
Fig.4.3:	(a) 10x10 $\mu\text{m}^2$ AFM image of the SiN-GaN template surface showing smooth surface and clear atomic steps.....	48
Fig.4.4:	(a) SdH and Hall resistivity versus magnetic field measured at 1.6 K for the $\text{Al}_{0.30}\text{Ga}_{0.70}\text{N}/\text{AlN}/\text{GaN}$ control sample. (b) 2DEG mobility versus carrier density for $\text{Al}_{0.30}\text{Ga}_{0.70}\text{N}/\text{AlN}/\text{GaN}$ sample.....	52
Fig.4.5:	Images of the active region of Hall bar structures prepared by scratching the top surface of the heterostructure by a diamond tip.	54
Fig.4.6:	SdH and Hall resistivity versus magnetic field measured at 1.6 K for $\text{Al}_{0.20}\text{Ga}_{0.80}\text{N}/\text{AlN}/\text{GaN}$ sample grown on SiN-GaN template before the sample etch.	56
Fig.4.7:	SdH and Hall resistivity versus magnetic field measured at 1.6 K for SiN-GaN samples before and after etching.....	58

Fig.4.8:	(a) Conductivity versus magnetic field before and after etching. (b) Conductivity subtracted using before and after etching data versus magnetic field.....	59
Fig.4.9:	Schematic diagram of a heterostructure with a parasitic conduction channel .....	60
Fig.4.10:	Diagram for contact resistances model in a symmetric Hall bar samples.....	63
Fig.4.11:	Simulation results of $\rho_{xx}$ and $\rho_{xy}$ versus magnetic field in Hall bar. (a): Contact resistance $R=0 \Omega$ . (b): Contact resistance $R=100 \Omega$ .(c): Contact resistance $R=10000 \Omega$ .....	64
Fig.4.12:	Resistivity and conductivity versus magnetic field for two 2DEG channels with contact resistance $R=100 \Omega$ .....	65
Fig.4.13:	Top: SdH and Hall resistivity versus magnetic field measured at 1.6 K for the parallel Hall-bar sample fabricated on $\text{Al}_{0.20}\text{Ga}_{0.80}\text{N}/\text{AlN}/\text{GaN}$ grown on ELO-GaN template before and after recess etch.....	68
Fig.4.14:	Top: Measured SdH and Hall resistivity versus magnetic field at 1.6 K for the perpendicular Hall bar sample fabricated on $\text{Al}_{0.20}\text{Ga}_{0.80}\text{N}/\text{AlN}/\text{GaN}$ grown on ELO-GaN template before and after recess etch.....	69
Fig.4.15:	Experimental electron mobility versus carrier density data extracted from $\text{Al}_x\text{Ga}_{1-x}\text{N}/\text{AlN}/\text{GaN}$ 2DEG samples grown on conventional u-GaN (reference), SiN-GaN, and ELO-GaN templates. All samples were measured at 1.6 K.....	71
Fig.5.1:	Longitudinal resistivity versus magnetic field traces for five samples with different carrier densities at 1.6 K.....	76
Fig.5.2:	(a) and (b) Conductivity after the subtraction of the zero field background of two samples versus magnetic field at $T=1.6 \text{ K}$ . The solid lines are theoretical fits to the data. (c) $B_{so}$ extracted from WAL fits versus carrier density for six samples.....	77
Fig.5.3:	The spin splitting energy extracted from WAL measurements versus Fermi wavevector .....	79
Fig.5.4:	Raw data of resistance versus magnetic field for sample B at temperature from 1.8 K to 3.5 K.....	81

Fig.5.5:	(Upper panels) Magnetoconductivity after the subtraction of the zero field background for samples B, D, and E at different temperatures.....	82
Fig.5.6:	Well pronounced SdH oscillations were shown in InAlN Sample B's longitudinal measurements for various gate voltages.. .....	87
Fig.5.7:	Upper diagram is the Hall measurements for InAlN sample B. ....	88
Fig.5.8:	$\Delta\sigma = \sigma(B) - \sigma(0)$ .Conductivity after the subtraction of the zero field background of two samples versus magnetic field at 0.3 K. .	89
Fig.5.9:	Spin-orbit field versus carrier density. The solid dots are the AlGaN/GaN data from our previous experiment [91].....	92
Fig.5.10:	The spin splitting energy versus Fermi wavevector. The solid dots are the AlGaN/GaN data from our previous experiments [91].....	95
Fig.5.11:	Spin-orbit energy versus carrier density extracted from beating pattern of SdH oscillations. The data of SdH1 [82] , SdH2 [94], SdH3 [95], SdH4 [96], SdH5 [97] and SdH6 [98] are from literatures.....	96
Fig.5.12:	Longitudinal resistance of a Van der Pauw Al <sub>x</sub> Ga <sub>1-x</sub> N/AlN/GaN sample versus magnetic field at 0.3 K.....	97
Fig.6.1:	(a) Sample A: Longitudinal resistance measurements at gate voltages from -4 V to 4 V at 0.28 K, with clear SdH oscillations shown.....	102
Fig.6.2:	Upper diagram: Carrier density versus gate voltage for GaN sample A.....	104
Fig.6.3:	Experimental magnetoconductivity $\Delta\sigma=\sigma(B)-\sigma(0)$ of sample A with $V_g=0$ V.....	105
Fig.6.4:	Experimental magnetoconductivity $\Delta\sigma=\sigma(B)-\sigma(0)$ of sample B. 107	
Fig.6.5:	WAL amplitude can be used as a thermometer for electron temperature.....	108
Fig.6.6:	Power dissipated per electron versus electron temperature for Samples A and B.....	109
Fig.7.1:	A schematic sketch of a 2DEG in a perpendicular magnetic field is shown above.....	119

Fig.7.2:	The radial electric field at different distance above a uniformly charged disk of radius $R$ and charge density $\sigma$ .....	120
Fig.7.3:	The axial magnetic field generated by the persistent bulk currents at different distance above a uniformly charged disk of radius $R$ at a filling fraction $v=1$ .....	121
Fig.7.4:	The ratio of the magnetic field generated by the bulk currents at the center of the disk $B_z(0)$ and the additional external magnetic field $B_I$ versus filling fraction .....	123
Fig.7.5:	Multiple layers sample structure with 25 identical AlGaAs/GaAs layers.....	125
Fig.7.6:	Longitudinal and Hall resistance versus magnetic field for multiple layers 2DEG sample.....	126
Fig.7.7:	(a) The double shadow evaporation of Al film. Between the two evaporation, an oxidation step was performed to form the tunnel junctions. (b) The SEM image of the SET. (c) The SEM image of the tunnel junction.....	127
Fig.7.8:	(a) Illustrative sketch of a SET coupled to a 2DEG sample. ....	129
Fig.7.9:	(a) A sketch of driven-in current induced by changing a small amount of magnetic field $dB$ .....	130
Fig.7.10:	Differential conductance of the SET versus time with an AC magnetic field modulated at frequency 4.137 Hz with magnitude 170 nT.....	132
Fig.7.11:	Charge/magnetic field conversion ratio versus inverse magnetic field.....	134
Fig.7.12:	Noise level versus frequency at 7.09 Tesla (filling fraction $n=2$ )..	136
Fig.8.1:	The quantum interferometer. The orange area is the fractional quantum Hall liquid.....	140
Fig.8.2:	Upper: The SET current versus the SET voltage at different gate voltages. ....	142
Fig.8.3:	Upper: The SET conductance versus time when an 11mT magnetic pulse applied at time 0 at $n=6$ quantum plateau (2.67 Tesla). ....	146

Fig.8.4:	Upper: The SET conductance versus time when an 11mT magnetic pulse applied at time 0 at $n=4$ quantum plateau (4.42 Tesla). ....	147
Fig.8.5:	Upper: The SET conductance versus time when an 11mT magnetic pulse applied at time 0 at $n=3$ quantum plateau (6.04 Tesla). ....	148
Fig.8.6:	Upper: The SET conductance versus time when an 11mT magnetic pulse applied at time 0 at $n=2$ quantum plateau (7.34 Tesla). ....	149
Fig.8.7:	Loading of the quasi-particles to the normal QHL sample without antidot pattern and the antidot sample by the backgate and by the magnetic field, respectively.. ....	152
Fig.8.8:	SEM images of four SET samples at different magnifications....	154
Fig.8.9:	Hall measurement of the FQHL sample at base temperature 20 mK. We observed the quantum plateau $n=1/3, 1, 2, 3, 4$ , and 6 in this sample and the carrier density of 2DEG can be extracted from this measurement. ....	155
Fig.8.10:	Characterization of SET A, B, C and D.....	156
Fig.8.11:	SET conductance to backgate voltage 0.15 V versus time in different positions of quantum plateau $n=1$ , the range of which was labeled by grey shade in (a). ....	158
Fig.8.12:	Number of oscillations in SET conductance seen over time in different positions of quantum plateau $n=1$ , for backgate voltage pulse 0.15V and -0.15V. ....	161
Fig.8.13:	SET conductance monitored after a magnetic field pulse ramping from 2.702T to 2.710T and a backgate voltages 0V were applied at time 0.. ....	163
Fig.8.14:	Responses of SET conductance to the magnetic field pulse ramping from 2.702T to 2.710T applied at time 0 and different backgate voltage pulses in quantum plateau $n=1$ .....	165
Fig.8.15:	Reponses of SET conductance to magnetic field pulse ramping from 2.710T to 2.702T applied at time 0 and different backgate voltage pulses in quantum plateau $n=1$ .....	166
Fig.8.16:	Cross section of the charge profile around the SET antidot. ....	169
Fig.8.17:	Oscillations observed in the SET conductance measurements before the turning point versus backgate voltages for SET A. ....	170

## **LIST OF APPENDICES**

### Appendix

A	DILUTION REFRIGERATOR OPERATION.....	184
B	EVAPORATION PROCEDURE.....	193
C	GaAs 2DEG HALL BAR FABRICATION.....	198
D	NPGS AND PHILIPS XL30 EBEAM LITHOGRAPHY INSTRUCTIONS .....	201
E	TIPS FOR SINGLE ELECTRON TRANSISTOR FABRICATION.	209

## **ABSTRACT**

### **TWO-DIMENSIONAL ELECTRON TRANSPORT IN GALLIUM NITRIDE AND GALLIUM ARSENIDE-BASED HETEROSTRUCTURES**

**by**

**Hailing Cheng**

**Chair: Çagliyan Kurdak**

The emergence of III-V semiconductor heterostructures has enabled the study of a broad range of two-dimensional phenomena. These heterostructures are the building blocks of high frequency field-effect transistors (FETs).

GaN-based heterostructures will have great impact in FET applications as they have the highest carrier densities achievable. In this thesis we studied electron transport in AlGaN/GaN samples covering a broad range of carrier density, from  $0.5 \times 10^{12} \text{ cm}^{-2}$  to  $1.0 \times 10^{13} \text{ cm}^{-2}$ . We found at carrier densities below  $5.0 \times 10^{12} \text{ cm}^{-2}$ , electron scattering from threading dislocations were the dominant scattering mechanism. The electron mobilities can be greatly enhanced by reducing the density of threading dislocations based on novel patterned growth techniques. We extended our studies to even higher carrier densities using lattice matched  $\text{In}_{0.16}\text{Al}_{0.84}\text{N}/\text{GaN}$  heterostructures. In particular, we investigated the magnetotransport regime in the

presence of two subbands by using gated Hall bar samples.

In addition to scattering processes, we also studied the spin-orbit interaction and phase coherence in GaN 2DEG samples by performing weak antilocalization (WAL) measurements. The spin-splitting energies extracted from WAL were found to be much smaller than the previous reports based on Shubnikov-de Haas measurements. By studying the spin splitting energies as a function of Fermi wave-vector we obtained the linear and cubic spin-orbit parameters for GaN 2DEG system. Furthermore, we used the WAL feature as a thermometer for the electron system, which allowed us to study energy relaxation processes in GaN.

In contrast to GaN heterostructures, we used GaAs/AlGaAs heterostructures to study two-dimensional electron transport at very low carrier densities. We focused on the deep insulation regime of integer quantum Hall liquids (IQHLs), a transport regime not accessible by ordinary transport measurements. We explored the charge dynamics in this regime by using single electron transistors (SET) in both unpatterned and antidot structures. SETs allowed us to monitor slow motion of charges in and out of the IQHLs. We found that, near zero temperature, IQHLs can be viewed as magnetic flux-to-charge transformers and confirmed our ideas by making a SET based magnetometer with an SET placed on an AlGaAs/GaAs heterostructure with 25 identical quantum wells.

# **CHAPTER 1**

## **INTRODUCTION**

### **1.1 Overview**

It is remarkable that an earlier prediction by Gordon E Moore[1], that the number of transistors placed on integrated circuits would double approximately every two years has continued to be correct for about 40 years. Of course this trend will end once the size of semiconductor devices reaches a limit of a few atoms, i.e. the nanoscale. Therefore, the research on nanoscale and low dimensional systems is crucial for the semiconductor industry. In the nanoscale and in low-dimensional systems, the quantum effects cannot be ignored. The first difference comes from the density of states. In a three-dimensional semiconductor crystal, the density of states is a smooth parabola while it changes to a staircase in a two-dimensional system. This feature actually has been used to enhance the optical properties in many optoelectronics devices[2].

There has been tremendous effort to enhance the materials properties of two-dimensional semiconductor systems. Modulation doping technique had been introduced to separate the carrier channel from the doping impurity in many semiconductor systems[2] which enabled us to realize two-dimensional electron systems with superior transport properties. For example, the mean free path of electrons in the highest quality GaAs/AlGaAs heterostructures has reached 0.1 mm at low temperatures. These high quality two-dimensional systems also exhibit unusual physics, such as integer[3-4] and

fractional quantum hall effects [5-8] when placed in high magnetic fields at low temperatures. More surprisingly, in graphene even the room temperature Hall Effect has been observed [9], which indicates that there is still a lot of unknown area to explore in two-dimensional physics.

## 1.2 Heterostructures with a Two-Dimensional Electron Gas

A heterojunction is an interface between two different semiconductor materials [10]. Heterostructure devices typically contain multiple heterojunctions. Thanks to the availability of many different bandgap semiconductor materials and their alloys, it is possible to design the energy landscape seen by the electrons leading to the field of the “band engineering”. Today, by varying composition, thickness and growth condition, a huge variety of new devices are fabricated based on semiconductor heterostructures. With the improvement of growth techniques[11] like molecular-beam epitaxy (MBE) and metal-organic chemical vapor deposition (MOCVD), heterostructures with atomic precision can be grown.

In the design of heterostructures it is critical to deal with the lattice mismatch between different semiconductors. Defect free heterostructures with thick layers cannot be grown when there is significant lattice mismatch between the semiconductors. The lattice mismatch between GaAs and AlAs is less than 0.15%; therefore it is possible to have multi-layers sample of GaAs/AlGaAs without much strain and without a significant level of dislocations associated with lattice mismatch. This is exactly the reason why GaAs/AlGaAs has been the material of choice for realizing high quality 2DEG systems.

In recent years, GaN based heterostructures have also attracted intense attention due to the spontaneous polarization of wurzite GaN structure and wide band gap. The spontaneous polarization of GaN means that it is possible to grow 2DEG without doping, therefore reducing the scattering from alloy components and doping impurities, and in principle, resulting in a better quality sample if the problem of lattice mismatch could be overcome.

In my thesis work I have used two-dimensional electron systems based on both the GaAs and GaN heterostructures. Before focusing on these realistic systems, it is instructive to discuss the ideal free electron systems. The density of states,  $dN(E)/dE$ . of an electron system depend on its dimension: in the 1-d case, the density of state is

$$n_{1D}(E) = \frac{1}{\pi\hbar} \sqrt{\frac{2m}{E}} ; \text{ in the 2-d case, it is a constant } n_{2D}(E) = \frac{m}{\pi\hbar^2} ; \text{ and in the 3-d case}$$

$$n_{3D}(E) = \frac{m\sqrt{2mE}}{\pi^2\hbar^3}. \text{ If we take into account the occupation of states at finite temperature}$$

$T$ , the total density  $N$  will be an integration of the density of states with the Fermi-Dirac distribution function, which is usually not in an analytical form. But, there is an interesting result for 2-d, which can be integrated analytically:

$$N_{2D}(E) = \frac{mk_B T}{\pi\hbar^2} \ln(1 + \exp(E_F/k_B T)). \quad (1.2)$$

However, all the equations above are based on the free electron model. The validation of this model definitely fails when we consider the case in semiconductors, which is actually a many-body system, and strictly speaking, should be treated by a many body theory. Luckily, due to the success of Landau Fermi-liquid [12] and band theories, the interacting many particles in dimensions greater than 2 can be described

by a single particle theory with some modifications, for example, replacing the bare electron mass by the effective mass and treating external or impurity potentials as perturbations. In the effective mass approximation, the wave function contains two parts, the kernel part which is the Bloch function and the envelop function part. What appears in the final equations are the envelop functions and the effect of Bloch function has been reduced to an effective mass. Due to this powerful approximation, most of semiconductor physics can be described in the language of a single particle picture. But of course, there are exceptions like what we see in the fractional quantum Hall effect. Despite that, the effective mass approximation grasps the essence in most cases and provides us with a straightforward intuitional understanding of the physics in such condensed matter systems.

In most parts of this thesis, we will discuss the physics by using the effective mass language. For different material structures, the effective mass of electrons is different. For example, the effective mass for the GaAs conduction band is around  $0.067 m_e$  and  $0.20 m_e$  for GaN conduction band, where  $m_e$  is the bare electron mass in vacuum. In some situations, the non-parabolic band structure gives a different value for the effective mass, as we will discuss in later chapters, there can be a deviations from this simplified effective mass picture in real systems.

Based on the effective mass approximation, we are able to treat the 2DEG forming on the interface of a typical heterostructures (see Fig 1.1) in a much simplified framework. Usually due to the band gap offset on the interface, the charge carrier will diffuse from one side to the other side until equilibrium is fulfilled. The diffusion of

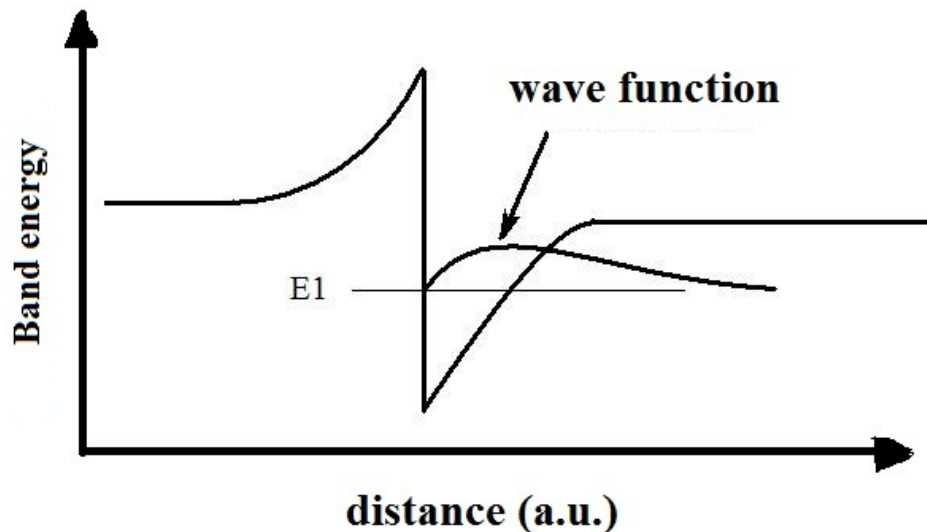


**Fig.1.1:** Potential energy versus distance in the growth direction in heterostructure. 2DEG wave function is confined at the triangle potential on the interface of the heterostructure.

carrier density will induce the buildup of internal electrical field and hence the bending of the energy band. A triangle-like potential will form on the interface of the heterostructure (Fig 1.1). This triangular potential well will confine electrons in the growth direction inside this potential. In the direction parallel to heterostructure plane, an electron is “free” to move as a single particle with its own effective mass decided by the band structure. Due to the confinement in the growth direction and freedom in the other two directions, a two dimensional electron gas (2DEG) is formed. Usually there is no analytical solution for the triangular potential with finite height in the growth direction confinement; however, the analytical solution for an infinite triangular potential well is available and can be used as a good approximation.

. As a useful approximation, we can solve the Schrodinger equation for a triangle

potential well with infinite height in one direction, which is exactly the potential well created by a constant electrical field and also very close to the actual shape of the potential well in the heterostructure. In the other two directions the electron is moving as a free particle, so the solution is very trivial and will not be repeated here. In other words, we will only focus on the growth direction and treat it as a 1-d problem. Assuming the growth direction is in the z-direction, for  $z < 0$ , there is an infinite high barrier, and for  $z > 0$  the potential is a linear function as  $V(z) = A|z|$ , where  $A$  is the slope of the potential well. The Schrodinger equation is

$$\left(-\frac{\hbar^2}{2m^*} \frac{d^2}{dz^2} + Az\right)\psi(z) = E\psi(z) \quad (1.3)$$

where  $m^*$  is the electron effective mass. The solution to this equation is called the Airy integral function[13] which has two independent solutions  $A_i(z)$  and  $B_i(z)$ . Usually  $A_i(z)$  is chosen to make  $A_i(z)$  approach 0 when  $z$  approaches infinity while  $B_i(z)$  diverges for large  $z$ . Therefore, the function that is physically meaningful would be the function  $A_i(z)$ . To solve for (1.3), it is usually convenient to define

$$z_0 = \left(\frac{\hbar^2}{2m^* A}\right)^{1/3}, \varepsilon = Az_0 \quad (1.4)$$

as the scales for distance and energy.

The final solution is

$$\psi_n(z) = A_i\left(\frac{Az - E_n}{\varepsilon}\right), n=1, 2, 3\dots \quad (1.5)$$

where  $A_i()$  is the airy function, with eigenenergy  $E$  valued as

$$E_n = a_n \left[\frac{(A\hbar)^2}{2m}\right]^{1/3}, n=1, 2, 3\dots \quad (1.6)$$

Those  $a_n$  are constants and can only be solved numerically. The lowest few values are

$$a_1 = 2.338, a_2 = 4.088, a_3 = 5.521, a_4 = 6.787.$$

We notice that the eigenenergy is proportional to  $A^{2/3}$ , where  $A$  is the slope of the triangular potential well. This form will have an important implication in this thesis work when we describe two-dimensional systems with multiple subbands. In such systems if we can change the slope of the triangular potential well in the heterostructure, we expect to observe the eigenenergy shift, for example the energy difference between the first and second subbands of the 2DEG inside the heterostructure.

### 1.3 Changing the 2DEG carrier density

It is important to be able to change the carrier density of 2DEG for experimental and application purposes. One method to change the carrier density is achieved by shining light using the persistent photoconductivity (PPC) effect. At cryogenic temperatures the increase of carrier density by the illumination of light in the materials lasts for a long time after the illumination. The PPC effect has been reported in materials such as AlGaAs, InP, GaAsP, and carbon nanotubes. Different mechanisms have been proposed to explain the PPC effect. In a random-potential-fluctuation model, the PPC is attributed to the separation of photo-excited charge carriers by the local-potential fluctuations [14-16]. Another mechanism attributes the PPC effect to the photo-excitation of electrons from deep trap centers (DX-centers) undergoing a large lattice relaxation (LLR)[17-18], which was used to interpret the observations in AlGaAs [19-20]. In our 2DEG samples, the PPC effect is successfully employed to increase the carrier density in the 2DEG, and at low temperature (from 0.02 K to 20 K),

the PPC effect lasts long enough to be viewed as a permanent change.

Another method to change the 2DEG carrier density is using a metal gate deposited on top or below the 2DEG by lithography method. In reality, a 2DEG can be viewed as a metal gas in two dimensions due to those free electrons in the heterostructure plane. Therefore by depositing another plate of metal, the 2DEG and metal gate will form a capacitor, and the capacitance is described by the formula for a normal capacitor as  $C = \frac{S \cdot \epsilon}{d}$ , where  $S$  is the surface area and  $d$  is the distance between two planes. The carrier density change can be expressed as

$$\Delta n_e = \frac{\Delta V \cdot \epsilon}{d} \quad (1.7)$$

In the case of a top gate, a positive gate voltage will increase the electron density in 2DEG while a negative voltage will do the opposite.

#### 1.4 Magnetotransport measurement on Hall bar samples

To characterize the 2DEG sample and extract parameters such as carrier density and mobility, etc., we need to perform the magnetotransport measurements. In magnetotransport measurements, the transverse and longitudinal resistances are recorded as a function of magnetic field. Usually the samples are fabricated into Hall bar structures (see Fig 1.2). First, the shape of Hall bar is defined by photolithography and the unwanted 2DEG area is etched away. The Ohmic contacts are made by metal diffusion using a high temperature alloying process. Then a metal gate is deposited on

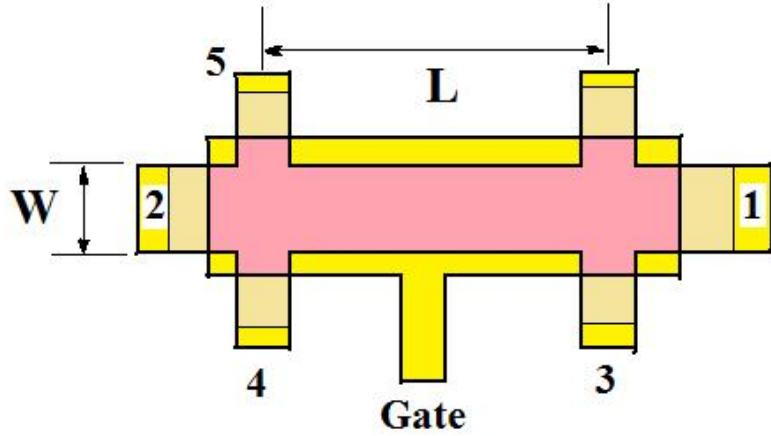


**Fig.1.2:** Schematic diagram of a Hall bar structure. Leads 1 to 5 are labeled in the diagram. The aspect ratio is  $L/W$ . The metal gate covers the active area of the Hall bar.

top of the Hall bar. The function of the gate is to change the carrier density of 2DEG by applying the gate voltage. In a typical measurement, the magnetic field was applied perpendicular to the 2DEG plane and an AC current,  $I_{1,2}$ , was passed from lead 1 to lead 2. The voltage drop was measured between 3 and 4,  $V_{3,4}$ , (translational measurement) and between 4 and 5  $V_{4,5}$ , (Hall measurement) using a lock-in amplifier. The four-terminal resistances are determined by  $R_{3,4;1,2} = V_{3,4}/I_{1,2}$  and  $R_{4,5;1,2} = V_{4,5}/I_{1,2}$ . The aspect ratio of the Hall Bar in Fig. 1.2 is  $L/W$  and the longitudinal and transverse resistivities of the 2DEG are determined from the measured four terminal resistances using the following equations:  $\rho_{xx} = R_{1,2;3,4}W/L$  and  $\rho_{xy} = R_{1,2;4,5}$ .

Usually in 2DEG in a magnetic field, the resistivity and conductivity are 2x2 tensors.

$$\rho = \begin{pmatrix} \rho_{xx} & \rho_{xy} \\ \rho_{yx} & \rho_{xx} \end{pmatrix} = \begin{pmatrix} \rho_0 & B/ne \\ -B/ne & \rho_0 \end{pmatrix}, \quad (1.8)$$

$$\sigma = \begin{pmatrix} \sigma_{xx} & \sigma_{xy} \\ \sigma_{yx} & \sigma_{xx} \end{pmatrix} = \rho^{-1}. \quad (1.9)$$

One unique property of a two-dimensional system, when  $\rho_{xy} \gg \rho_{xx}$ ,  $\sigma_{xx}$  is proportional to  $\rho_{xx}/(\rho_{xy}^2 + \rho_{xx}^2)$  due to matrix inversion.

In a magnetic field, the transverse (usually called Hall) resistivity,  $\rho_{xy}=B/(en)$ , which is due to the Lorentz force, can be used to extract carrier density

$$n_{Hall} = \frac{B}{e\rho_{xy}}. \quad (1.10)$$

After we determine carrier density  $n$ , we can extract mobility  $\sigma$  from equation  $\rho_{xx}=1/ne\sigma$  and hence mobility  $\mu=\sigma/ne$ .

## 1.5 Van der Pauw method

Magnetotransport measurements can also be performed using van der Pauw geometry. Unlike Hall bar samples, the van der Pauw samples can be prepared without lithography. In van der Pauw measurements [21], the 2DEG samples are usually cut into square pieces, and ohmic contacts are made at four corners. In Fig 1.3 we showed the diagram for van der Pauw measurements. The current passes between two leads and the voltage is measured across the other two leads. According to Fig 1.3, we labeled four leads as  $1, 2, 3, 4$  and the resistance extracted from the different van der Pauw geometry as  $R_1, R_2, R_3$  and  $R_4$ , where  $R_i=V_i/I_i$ ,  $i=1,2,3,4$  etc. Among them, usually  $R_1$  and  $R_2$  correspond to longitudinal measurements and  $R_3$  and  $R_4$  correspond to Hall measurements in the Hall bar, respectively. However, due to imperfections in the sample geometry (i.e. not perfect square) and other factors such

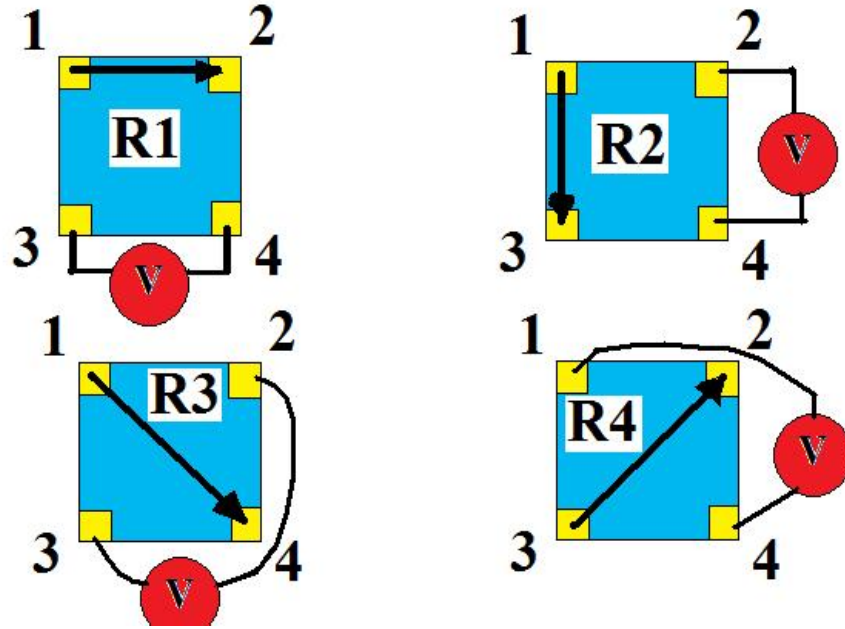


**Fig.1.3:** Schematic diagram of different four terminal resistance measurements on a Van der Pauw sample. The arrows are the directions in which currents flow.  $R_1$  is the resistance extracted by passing the current from 1 to 2 and measuring the voltage between 3 and 4.  $R_2$  is the resistance extracted by passing the current from 1 to 3 and measuring the voltage between 2 and 4.  $R_3$  is the resistance extracted by passing the current from 1 to 4 and measuring the voltage between 2 and 3.  $R_4$  is the resistance extracted by passing the current from 3 to 2 and measuring the voltage between 1 and 4.

as the finite size of the Ohmic contacts, the  $R_1$  and  $R_2$  might carry partial Hall signal and  $R_3$  and  $R_4$  might carry partial longitudinal signal. To overcome this problem, we will need to use the magnetotransport data from negative to positive magnetic field. Because the longitudinal resistivity is symmetric in magnetic field and Hall resistivity is anti-symmetric in magnetic field, we can filter out the longitudinal signal by using  $R_i = (R_i(+B) + R_i(-B))/2$ ,  $i=1,2$  and Hall signal by using  $R_i = (R_i(+B) - R_i(-B))/2$ ,  $i=3,4$ .

After we successfully extract the  $R_1$ ,  $R_2$ ,  $R_3$  and  $R_4$ , we use the equation developed by van der Pauw [21] to extract the longitudinal and Hall resistivity as

$$\rho_{xx} = \frac{\pi}{\ln 2} \frac{(R_1 + R_2)}{2} f \quad (1.11)$$

$$\rho_{xy} = \frac{R_3 + R_4}{2} \quad (1.12)$$

where  $f$  is a function of  $R_1/R_2$ . Let us assume  $R_1 > R_2$ , then  $f$  satisfies

$$\frac{R_1 - R_2}{R_1 + R_2} = f \cdot \arccos h \left\{ \frac{\exp(\ln 2/f)}{2} \right\} \quad (1.13).$$

If  $R_1$  is close to  $R_2$ , then  $f$  is usually very close to 1. After we extract the longitudinal and Hall resistivity, we can extract the carrier density and mobility of the 2DEG sample (see chapter 2) in the same way as in Hall bar measurements.

## 1.6 AlGaN/AlN/GaN heterostructures

GaN is a wide bandgap semiconductor material with a bandgap of 3.39eV at the room temperature. Due to the wide bandgap, the  $\text{Al}_x\text{Ga}_{1-x}\text{N}/\text{AlN}/\text{GaN}$  material system has been widely used in high frequency, high temperature microwave applications, optoelectronics and high efficiency lighting applications [22-23]. Compared to traditional GaAs heterostructures, AlGaN/AlN/GaN heterostructures have several unique physical properties which make them promising for realizing low-dimensional electron systems. First of all, the spontaneous polarization and the piezoelectric effect between AlGaN/AlN/GaN interfaces due to reduced crystal symmetry will induce a two dimensional gases (2DEG) in the heterostructures, which makes modulation doping unnecessary and furthermore removes a major scattering mechanism. Second, the relatively high effective mass ( $\sim 0.23 m_e$ ) and low dielectric constant make electron-

electron interactions more significant compared to GaAs.

The transport properties of such structures are important for understanding the device physics and applications in the real world. Because of their technological promises, much attention has been paid to improving the GaN sample quality as well as transport properties. Unfortunately GaN wafers are currently not available, thus GaN based heterostructures are either grown on SiC or sapphire substrates. To achieve better samples, better quality templates and optimized growth conditions are needed [24-28].

For further progress in improving the sample quality, it is important to understand and minimize the scattering mechanisms and crystal defects. For studying the scattering mechanisms in AlGaN/AlN/GaN heterostructures we have performed magnetotransport measurements on wide range of 2DEGs with different carrier densities.

## 1.7 InAlN/GaN heterostructures

Despite those efforts to improve the AlGaN/GaN sample quality, there is an internal obstacle for achieving the ultra high quality AlGaN/GaN heterostructures: the lattice mismatch between the GaN and the AlGaN layers. This mismatch induces surface strain and dislocations, and therefore limits the sample quality. As a result, in the race for high quality GaN samples, other possible solutions should also be considered.

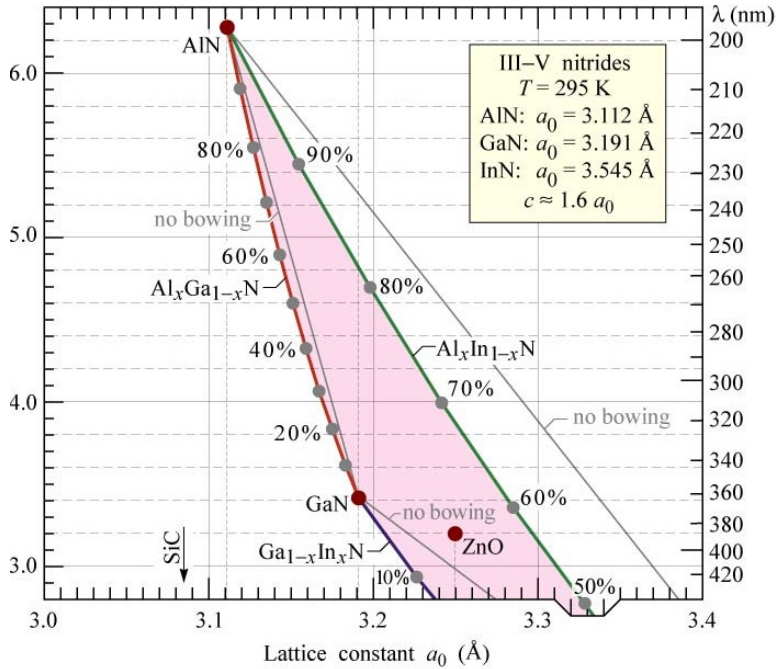


**Fig.1.4:** Bandgap energy versus lattice constants for some III-V semiconductors. This diagram is adapted from reference [29].

One advantage of InAlN/GaN heterostructures [30-32] over the traditional AlGaN/GaN heterostructures is the lattice match between the  $\text{In}_{0.17}\text{Al}_{0.83}\text{N}$  barrier and the GaN channel layer (see Fig 1.4), which is beneficial to reduce the strain in heterostructures to achieve high quality devices. We should note here that the lattice matching molar fraction of InN in the barrier depends on the strain state of the GaN channel layer [33]. Furthermore, the spontaneous polarization difference between GaN and  $\text{In}_{0.17}\text{Al}_{0.86}\text{N}$  is larger than that in the typically-used AlGaN/GaN heterostructures, which could result in a higher density two-dimensional electron gas (2DEG). The practical motivation is then with InAlN/GaN heterostructures we expect to achieve higher current densities and powers, which is important in the device applications.

In this dissertation, we have also studied the magnetotransport measurement in

InAlN/GaN samples and explored a high carrier density regime which is not accessible with the AlGaN/AlN/GaN heterostructures.

## 1.8 Dissertation Objectives

This thesis is focused on the fundamental studies of electron transport in different 2DEG materials systems, specifically on GaN and GaAs systems. The first objective is to study the transport properties of GaN 2DEG systems which are particularly important for high power field effect applications. We have studied electron transport in wide range of samples including in a high carrier density regime where a second conductive subband channel was occupied. We have identified leading scattering mechanisms at different carrier densities and discussed possible strategies for improving electron mobility which can be viewed as a figure-of-merit for sample quality.

With GaN's potential to be a material for spintronics application, we were also interested in the study of spin-orbit interaction in the GaN systems. In the second part of this dissertation, we characterized the spin-orbit interaction in the GaN heterostructures by using the weak antilocalization measurements. We were able to extract the spin-orbit parameters for this material system which happened to be very different from the previous reports based on Shubnikov-de Haas measurements. Also during the study, we found that the weak antilocalization measurements could also be used to extract the electrons' temperatures. Thus, we were able to study the energy relaxation processes in the GaN systems, which are crucially important to understand the power dissipation in the GaN based devices.

In the third part, we studied the quantum Hall effect (QHE), this time by using AlGaAs/GaAs samples, which have a higher mobility than GaN. We were able to study the quantum Hall liquids in their deep insulating regime by using single electron transistors, which is not accessible by ordinary transport measurements. There has been recent interest in this material system as some of these quantum Hall liquids have been proposed as a promising candidate to perform the topological quantum computation. To date, there have been limited progresses on the experimental side. The objective of the third part was to understand the charge motions in the quantum Hall liquid in an antidot structure, a particularly important structure for possible device applications. We have also shown that the response associated with the motion of electrons in the bulk of the integer quantum Hall layer could be enhanced by using multiple layers. This finding led us to a magnetometer application which was demonstrated by using a heterostructure with 25 identical multiple quantum wells.

## 1.9 Dissertation outline

This dissertation is organized as follows:

Chapter 2 is devoted to the introduction of fundamental theoretical frames such as Landau levels in the 2DEG and the magneto-transport measurements of the AlGaN/GaN samples covering from low to relative high carrier density range. From the mobility versus carrier density data, possible scattering mechanisms limiting the mobility are discussed.

Chapter 3 investigates the magnetotransport properties of a high carrier density  $\text{In}_{0.16}\text{Al}_{0.84}\text{N}/\text{AlN}/\text{GaN}$  gated Hall bar sample at different gate voltages. A two-

subbands occupation is observed. Carrier densities and quantum lifetimes in the two subbands have been extracted. This sample is particularly interesting for two reasons. First, there is a lattice match between the  $\text{In}_{0.16}\text{Al}_{0.84}\text{N}$  and the GaN layers. Second, a very high carrier density of  $2.32 \times 10^{13} \text{ cm}^{-2}$  has been achieved. Also in that sample, the mechanism for different rates of change of the electron density vs. the gate bias,  $dn/dV_g$ , in two subbands is discussed.

Chapter 4 focuses on the transport measurement of several AlGaN/GaN samples grown by different techniques, aiming for reducing the density of threading dislocations. In samples grown by these techniques, a parasitic conductive channel was discovered and its possible impact on the magnetotransport was discussed. Despite the presence of a parasitic channel, we were able to extract lower bounds for electron mobility and determined that associated with the reduction in the density of threading dislocations there was significant enhancement of electron mobility.

Chapter 5 is dedicated to the study of the spin-orbit interaction and phase coherence in the GaN 2DEG samples. A wide range GaN 2DEG samples are used to cover a broad range in the carrier density. For the first time we were able to extract linear and cubic spin-orbit parameters for this material systems using weak antilocalization measurements.

In chapter 6, we use the weak antilocalization measurements as a method to explore the phonon-electron interactions in the GaN systems. The electron temperature,  $T_e$ , is measured as a function of the bias current in the GaN heterostructures with polarization induced 2DEG in the Bloch-Gruneisen regime. We calculate the power dissipated per electron,  $P_e$ , as a function of  $T_e$  for different screening models of

piezoelectric electron-phonon coupling, and corresponding formulas are derived respectively.

In chapter 7, we explore the charge dynamics in the integer quantum Hall liquid (IQHL). We fabricate a hybrid device with a single electron transistor (SET) placed on top of an AlGaAs/GaAs heterostructure with 25 identical quantum wells. We calculate the response of an IQHL to a small magnetic field and it is shown that when the effective filling fraction  $\nu > 1/\alpha = 137$ , the IQHL behaves like a perfect diamagnet. We perform experiments to verify this effect and also find that this device can be used as a magnetometer.

Chapter 8 is devoted to the study of the charge dynamics in a multiple quantum wells sample as well as in a single layer quantum liquid antidot sample. The charge movements are detected by the single electron transistors. The charge equilibration process has been studied by applying small magnetic or electrical pulses and monitoring the relaxation of charged carriers by a SET. In the antidot sample, we report an interesting charge moving-in and moving-out motion and proposed a possible mechanism for loading edge states of an antidot.

Chapter 9 is the conclusions and suggestions for future work.

## CHAPTER 2

### MAGNETOTRANSPORT MEASUREMENTS IN AlGaN/AlN/GaN HETEROSTRUCTURES

#### 2.1 Landau Levels

Before I present our magnetotransport measurements, I would like to introduce the theoretical framework needed to describe two-dimensional electrons in magnetic field. It is well known that the electric and magnetic fields can be expressed as

$$\vec{E} = -\nabla\varphi - \frac{d\vec{A}}{dt}, \vec{B} = \nabla \times \vec{A}. \quad (2.1)$$

where there is a gauge freedom for potential  $\varphi$  and vector potential  $\mathbf{A}$ . For example, if we choose

$$\vec{A} \rightarrow \vec{A} + \nabla\chi, \varphi \rightarrow \varphi - \frac{d\chi}{dt}, \quad (2.2)$$

the electric and magnetic field will be the same. However, in quantum mechanics the solution to Schrödinger equation

$$\left\{ \frac{1}{2m} [\hat{p} - e\vec{A}]^2 + e\varphi \right\} \Psi(\vec{R}, t) = i\hbar \frac{d}{dt} \Psi(\vec{R}, t). \quad (2.3)$$

would take a different form.

Consider an electron confined in a quantum well potential, in which the electron mass is replaced by the effective mass to account for the effect of periodic crystal

potential, and under constant magnetic field in the z-direction, there is usually a convenient choice for gauge to make the solution to the Schrödinger equation more favorable. One of the most usable gauges is the Landau gauge[13]. In the Landau gauge, we take  $\mathbf{A}=(0, Bx, 0)$ . Then the Schrödinger equation will be

$$\left\{ \frac{-\hbar^2}{2m} \nabla^2 - \frac{ie\hbar Bx}{m} \frac{\partial}{\partial y} + \frac{(eBx)^2}{2m} + V(z) \right\} \Psi(\vec{R}, t) = E\Psi(\vec{R}, t). \quad (2.4)$$

where  $V(z)$  is the confining potential in z-direction.

In this equation, we can separate x, y and z components by using a wave function in the following form:

$$\Psi(\vec{R}, t) = u(x) \exp(iky) v(z). \quad (2.5)$$

Note that the y-component of the wave function,  $\exp(iky)$ , is simply a plane wave, whereas the z-component,  $v(z)$ , is the solution to the confining potential in the z-direction. Following separation of variables, we obtain the following one-dimensional equation:

$$\left\{ \frac{-\hbar^2}{2m} \frac{d^2}{dx^2} + \frac{1}{2} m \omega_c^2 \left( x + \frac{\hbar k}{eB} \right)^2 \right\} u(x) = \varepsilon u(x) \quad (2.6)$$

where  $\omega_c = \frac{eB}{m}$  is the classical cyclotron frequency. The solution to this is the harmonic

oscillator centered at  $x_k = -\hbar k / eB$ , with

$$\varepsilon_{nk} = (n - 1/2) \hbar \omega_c \quad (2.7)$$

$$\phi_{nk}(x, y) \propto H_{n-1}\left(\frac{x - x_k}{l_B}\right) \exp\left[-\frac{1}{2} \left(\frac{x - x_k}{l_B}\right)^2\right] \exp(iky), \quad (2.8)$$

where  $l_B = \sqrt{\frac{\hbar}{eB}}$ ,  $H_{n-1}(x)$  is an integer Hermite function.

It is interesting to note that the energy of the electron depends only on  $n$  but not on  $k$ , which means for the energy level  $n$  we get degenerate states with different  $k$ . The density of states for 2DEG convert to series  $\delta$ -functions called Landau levels. In reality, the  $\delta$ -functions will be broadened due to disorder in real systems. The number of states in each landau level is  $n_B = eB/h$ .

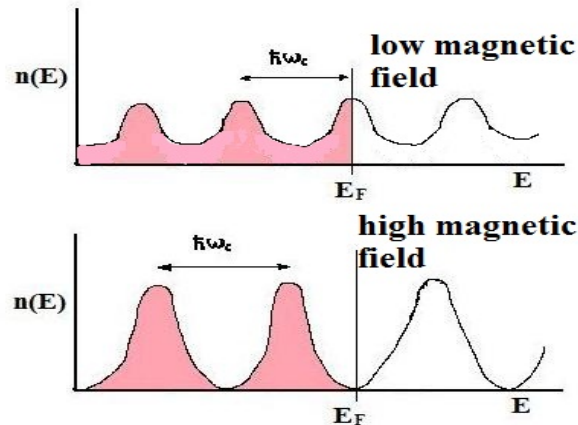


**Fig.2.1:** Density of states in 2DEG as a function of energy in different magnetic fields (low magnetic field and high magnetic field). As magnetic field increases, the number of states in each Landau level increases, as well as adjacent Landau levels splitting energy. The Fermi energy  $E_F$  changes accordingly to make the total occupied number of states a constant.

The density of states of a 2DEG with broadened Landau levels at two different magnetic fields is shown in Fig 2.1. At high magnetic field (lower figure), the separation and degeneracy of the Landau levels are higher. It is important to note that the position of the Fermi energy must be determined from the carrier density, and for a given carrier density the Fermi energy would change periodically as a function of  $1/B$ . The density of states at the Fermi energy and the transport properties (i.e. diagonal resistivity) are also expected to vary periodically as a function of  $1/B$ . We will be characterizing the two-dimensional electron layers using the oscillations in

magnetoresistance, also known as Shubnikov-de Haas (SdH) oscillations.

The above description does not include the spin degree of freedom for electrons. In real systems, there can be splitting in the Landau levels due to the Zeeman splitting of electrons. Typically, the Zeeman splitting energy is smaller than the cyclotron energy, and at low magnetic fields where the Zeeman splitting energy is less than the thermal energy  $kT$ , the two spin levels can be viewed as degenerate. Then we would keep the same picture and modify the number of states in each Landau level by a factor of 2.

## 2.2 Magnetotransport measurements and Shubnikov-de Hass Effect

Since the density of states at the Fermi level varies with changing magnetic field, the transport properties of a 2DEG are expected to vary with magnetic field as well. Therefore, by measuring the transportation of 2DEG in the magnetic field, we can extract some important quantities such as carrier density, scattering rates, and mobility. In low magnetic field, the longitudinal resistivity of 2DEG does not have a significant feature. When the magnetic field increases, the Fermi surface will be a periodical function of  $1/B$ ; therefore, the conductivity and resistivity will change in the same manner. When the Fermi level is between the two landau levels, we get  $B_n = \frac{hn_{2D}}{en}$  and the Fermi surface will have a minimum value. Consequently the conductivity and resistivity will both have a minimal value. This phenomenon is known as Shubnikov-de Hass (SdH) oscillations. In a high mobility sample the minimum of resistivity can be very close to zero, and the transverse resistance (the Hall resistance) will show a

quantum plateau at that magnetic field, known as quantum Hall effect. From the relationship of these resistivity minima and corresponding magnetic field,

$$B_n = \frac{hn_{SdH}}{en}, \quad (2.9)$$

we can extract carrier density. Usually this carrier density will agree with Hall density

$$n_{Hall} = \frac{B}{e\rho_{xy}}. \quad (2.10)$$

But in the case of parallel conduction channels in 2DEG, the Hall measurement will be close to the total carrier density and SdH oscillation will disclose the carrier density in each individual channel.

The SdH oscillations (see Fig. 2.2) usually can be described by the Dingle formula [34]

$$\rho_{xx}(B) = A + C \exp\left(\frac{-\pi}{\omega\tau_q}\right) \frac{\xi}{\sinh(\xi)} \cos\left(\frac{2\pi\Delta E}{\hbar\omega} + \varphi\right), \quad (2.11)$$

where  $A$ ,  $C$ , and  $\varphi$  are fitting constants. In this formula  $B$  is the magnetic field,  $\omega = \frac{eB}{m^*}$  is the cyclotron frequency ( $m^*$  is the effective mass),  $\tau_q$  is the quantum lifetime,  $\xi = \frac{2\pi^2 k_B T}{\hbar\omega}$ ,  $\Delta E = \frac{\pi\hbar^2 n}{m^*}$  is the energy difference between the Fermi level and the subband energy level, and  $n$  is the carrier density.

### 2.3 Growth of AlGaN/AlN/GaN heterostructures

In this chapter, we will focus on AlGaN/AlN/GaN heterostructures and try to understand the major scattering mechanisms which limit their electron mobility.

The  $\text{Al}_x\text{Ga}_{1-x}\text{N}/\text{AlN}/\text{GaN}$  heterostructures used in this chapter were grown by a customer designed rotating-disk low-pressure metal-organic vapor-phase epitaxy (LP-MOVPE) system in Prof. Morkoç's group at Virginia Commonwealth University. Nitrogen, gallium, and aluminum sources have been introduced by using ammonia ( $\text{NH}_3$ ), trimethylgallium (TMGa), and trimethylaluminum (TMAI) as precursors, respectively. Hydrogen was the carrier gas and growth was accomplished under high-speed rotation (~500 rpm). The samples were grown on c-plane (0001) sapphire substrates. A 25-nm thick low-temperature (~550 °C) GaN nucleation layer initiated the growth, followed by a 3 μm thick undoped GaN epilayer grown at 1000 °C under 200 mTorr using a V/III ratio of 4000. The average growth rate was measured at ~1.6 μm/hr. This u-GaN template served as a basis-template for all samples. Atomic force microscopy scans and etch-pit studies showed that the threading dislocation density of the basis template was in the low  $10^9 \text{ cm}^{-2}$  range.

$\text{Al}_x\text{Ga}_{1-x}\text{N}$  layers were grown on top of the u-GaN templates to form the 2DEG systems. An additional ~1 μm GaN layer, ~1 nm thick AlN interfacial layer, ~25 nm  $\text{Al}_x\text{Ga}_{1-x}\text{N}$  layer, and ~3 nm GaN cap layer, all nominally undoped, were grown on top of u-GaN templates. The 2DEG channel was formed between the GaN/AlN interface. The AlN interfacial spacer layer was used to improve the sample quality and reduce the alloy disorder scattering by minimizing the wavefunction penetration from the 2DEG channel into the  $\text{Al}_x\text{Ga}_{1-x}\text{N}$  layer [35-36]. The heterostructure layers were grown at 1060 °C under 30 mTorr using a V/III ratio of ~600. The Al concentration ranged from 10% to 30% and Ohmic contacts were formed using Ti/Al/Ti/Au (30 nm/100 nm/30 nm/50 nm) alloyed at 900 °C for 1 min.

## 2.4 Sample Characterization

The AlGaN/GaN samples were characterized by magnetotransport measurements in a cryogenic variable temperature cryostat equipped with an 8 T superconducting magnet. In Fig. 2.2, we plot the low temperature magneto resistance traces for a typical  $\text{Al}_{0.25}\text{Ga}_{0.75}\text{N}/\text{AlN}/\text{GaN}$  sample with gate voltage from -0.5 V to 0.4 V. In the longitudinal measurements, this sample exhibited obvious SdH oscillations at 1.6 K, which is a clear indication of single subband occupation in the 2DEG channel. Using equation (2.11), we have extracted carrier densities from the SdH oscillations. Carrier densities are also extracted from Hall measurements using equation (2.10), which are found to be in agreement the SdH results suggesting that there is a single subband occupation in these heterostructures. If the carrier densities from Hall results are larger than those from SdH results, it indicates there are other conductor channels or subbands in the heterostructure as well.

In this chapter, we measured four AlGaN/AlN/GaN heterostructures with Al composition as 10%, 15%, 25% and 30%, respectively. The growth conditions for those samples were aforementioned with Al composition varied accordingly. Carrier densities and mobilities were extracted from magnetotransport measurements. Some typical magnetotransport data for a gated  $\text{Al}_{0.25}\text{Ga}_{0.75}\text{N}/\text{AlN}/\text{GaN}$  sample are shown in Fig.2.2. The carrier density was varied by a top metal gate. In Fig.2.2, we observed well pronounced single frequency SdH oscillations and the carrier densities extracted from SdH oscillations agreed with those extracted from Hall data, which was an indication of a high quality single conducting channel sample.

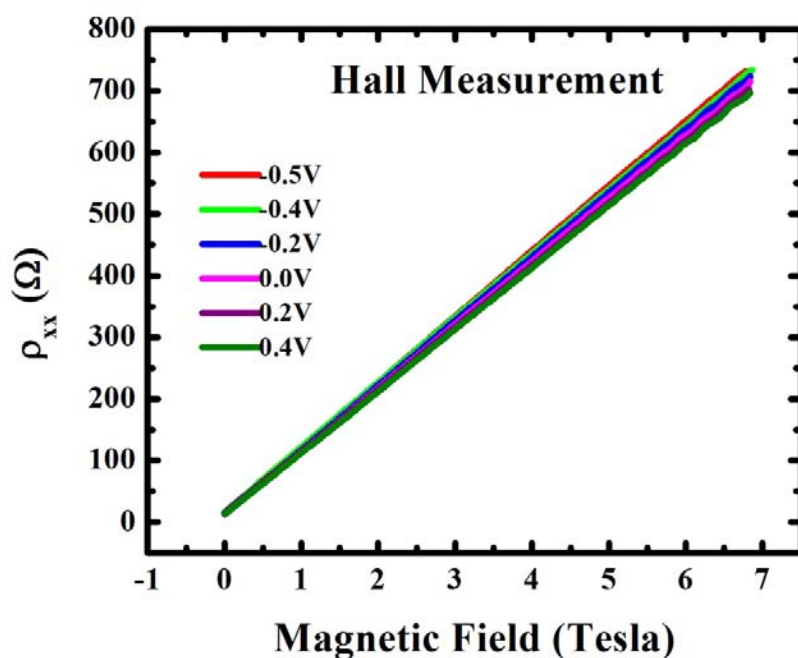
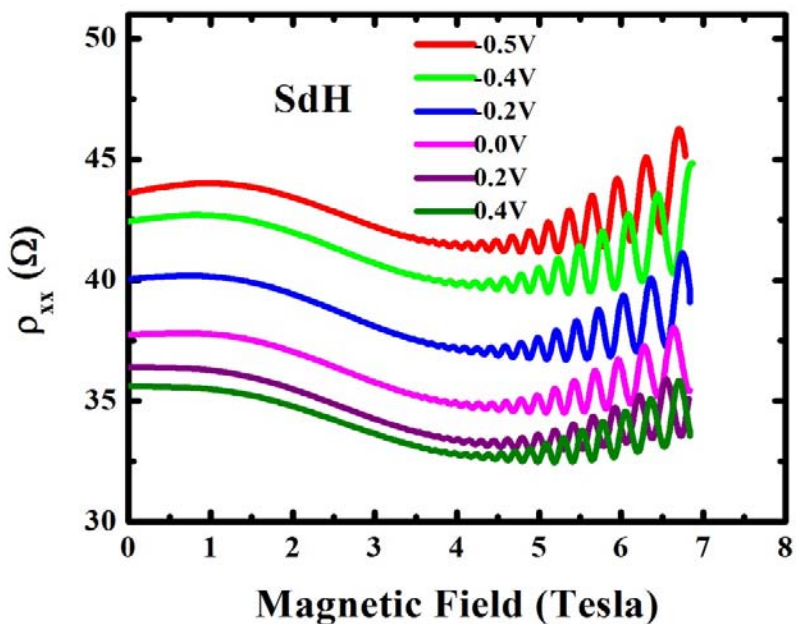


**Fig.2.2:** SdH and Hall measurements of a Gated  $\text{Al}_{0.25}\text{Ga}_{0.75}\text{N}/\text{AlN}/\text{GaN}$  sample. The gate voltages were varied from -0.5V to 0.4V. SdH oscillations have been observed in the longitudinal measurements, from which the carrier densities and mobilities can be extracted.

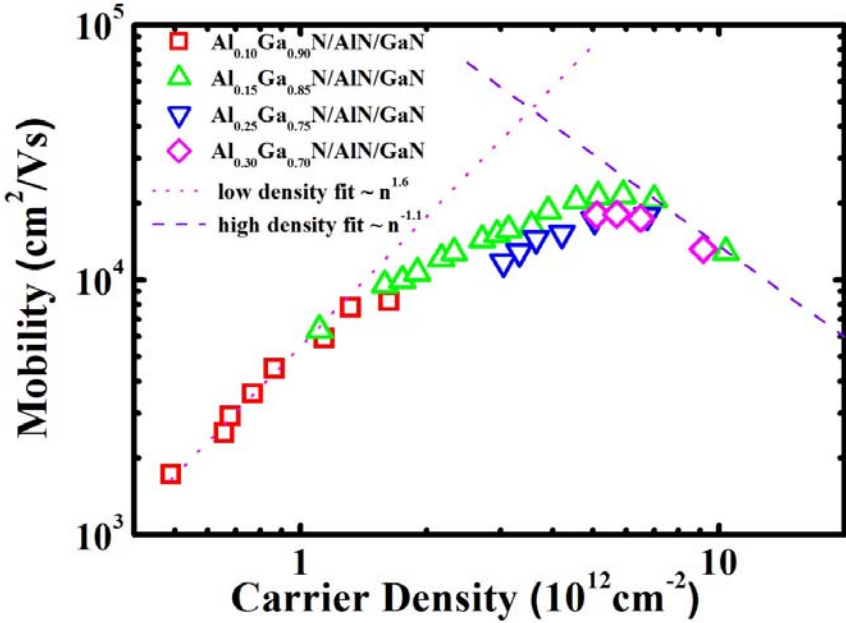


**Fig.2.3:** Mobility vs. Carrier densities. The red dots are the fit for low carrier densities data with function  $\mu \sim n^{1.6}$  and purple dashes are the fit for high carrier densities data with function  $\mu \sim n^{-1.1}$ .

In Fig.2.3, we plotted the mobility versus carrier density data for all samples. A key feature of this plot is that the mobility increases as carrier density increases in the low carrier density regime and decreases as a function of carrier density in the high carrier density regime. The peak in mobility occurs at carrier densities close to  $5 \times 10^{12} \text{ cm}^{-2}$ . We used two fitted lines to capture this trend in the figure. In the low carrier density regime, the fitting function is  $\mu \sim n^{1.6}$  while at high carrier density the fitting function is  $\mu \sim n^{-1.1}$ . When the carrier density is low, the mobility is mostly limited by long-range Coulomb scattering mechanisms[24,37-39] such as charged threading dislocations[27,40], remote donors[41], charged surface states, residual background impurities, and other charged dislocations[41-42]. In the high carrier density regime, the increasing electron screening would decrease the effects caused by long-range Coulomb scattering. As carrier density increases more, the wave-function penetration

into interface and alloy also increases, and the mobility is limited by the alloy and interface roughness scattering [24,38-39] in the high carrier density regime.

In summary, we have investigated magnetotransport properties of four AlGaN/AlN/GaN gated Hall bar samples at different gate voltages. Well pronounced single frequency SdH oscillations have been observed at 1.6 K, which indicated high sample quality. We found that the mobility increases with increasing carrier density in the low carrier density regime, and decreases as a function of increasing carrier density in the high carrier density regime. The peak mobility occurs at carrier density close to  $5 \times 10^{12} \text{ cm}^{-2}$ . When the carrier density is low, the mobility is mostly limited by long-range Coulomb scattering processes arising from charged threading dislocations, remote donors, charged surface states, residual background impurities and other charged dislocations. As carrier density increases more, the mobility is limited by the alloy and interface roughness scattering in the high carrier density regime.

Based on our experiments performed on GaN/AlGaN 2DEG heterostructures, we have rather good understanding of electron transport and scattering process in GaN systems. The factors limiting the maximum electron mobility in GaN heterostructures are mostly from lattice mismatch of the substrate to the GaN layers and the threading dislocations induced henceforth. As a historic trend, with advances in growth methods there have been significant improvements in the threading dislocations in GAN heterostructures. As a result of these improvements, the maximum mobilities in the GaN based heterostructures has been increasing and are expected to continue to increase in the future.

## CHAPTER 3

### TWO SUBBANDS CONDUCTION IN A GATED HIGH DENSITY InAlN/AlN/GaN HETEROSTRUCTURE

#### 3.1 InAlN/GaN sample growth

As introduced in chapter 1, InAlN/GaN heterostructures have the advantage of lattice matching between the  $\text{In}_{0.17}\text{Al}_{0.83}\text{N}$  barrier and the GaN channel layer, which could potentially lead to a high quality heterostructures [33]. In AlGaN/GaN heterostructures, the high carrier density regime has been studied previously and occupation of multiple subbands was observed in magnetotransport measurements at low temperatures [43-45]. A carrier density as high as  $1.4 \times 10^{13} \text{ cm}^{-2}$  was achieved in non-gated samples, which in one case was observed using the persistent photoconductivity (PPC) effect[45]. When the PPC effect is used, the change of sample carrier density cannot be reversed at low temperatures and the non-uniformity of carrier density could be a potential issue as it can affect the SdH measurements.

In this chapter, we report two-subbands conduction in a high carrier density gated  $\text{In}_{0.16}\text{Al}_{0.84}\text{N}/\text{AlN}/\text{GaN}$  Hall bar sample. We changed the carrier density of the 2DEG in the sample by using a metallic gate and the highest carrier density in this sample was  $2.3 \times 10^{13} \text{ cm}^{-2}$ . We monitored the occupation of the two subbands using SdH oscillations. The density of electrons in both sublevels increased linearly with increasing gate voltage, but with different slopes, which is explained by an increase of the energy level separation between two subbands induced by the increasing gate

voltage.

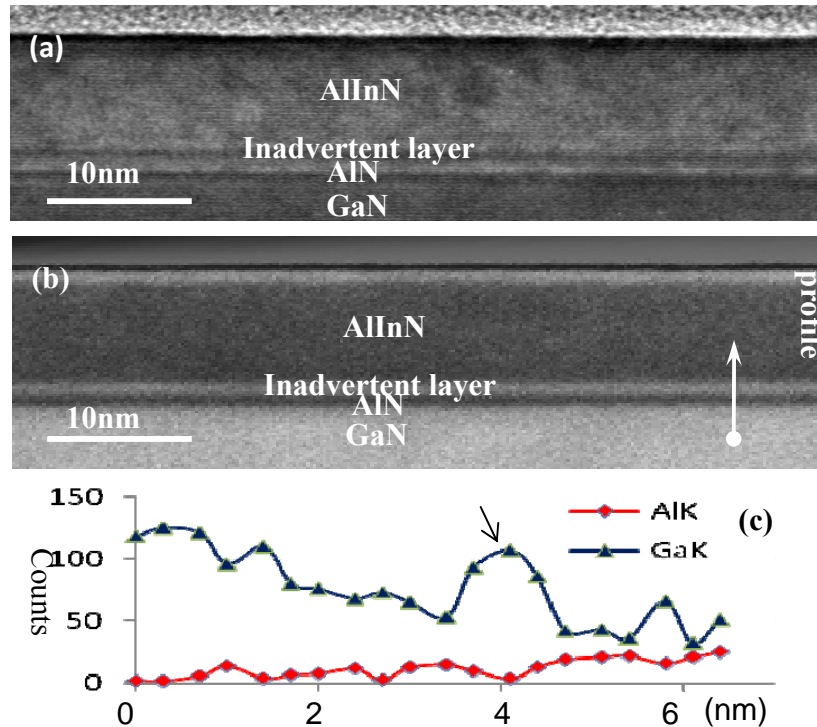


**Fig.3.1:** TEM image and EDXS measurement of the InAlN/GaN sample. (a) Bright-field TEM image; (b) High-angle annular-dark-field (HAADF) scanning transmission electron microscopy (STEM) image; and (c) corresponding EDXS line profile of the InAlN/AlN/GaN region illustrating inclusion of the inadvertent Ga interlayer. The EDXS EELS line profile demonstrates that the inadvertent layer contains considerable Ga. This diagram is from Prof. Morkoc's group.

The InAlN/AlN/GaN [46-47] heterostructures (see Fig. 3.1) were grown by Prof. Morkoc's group at Virginia Commonwealth University with a custom-designed low-pressure organometallic-vapor-phase epitaxy (OMVPE) system on a sapphire substrate by using trimethylgallium (TMGa), trimethylaluminum (TMAI), trimethylindium (TMIIn), and ammonia as the Ga, Al, In, and N sources. A 250 nm initiation layer of AlN was grown at a pressure of 30 torr and temperature of  $\sim 1030$  °C, followed by a 3.0  $\mu\text{m}$  of undoped GaN at 200 torr and temperature of  $\sim 1000$  °C. Due to

unintentional GaN contamination deposited on the sample holder [47], the sample growth was interrupted a short time prior to the heterointerface and the sample holder was replaced with a clean one. Subsequently the growth was continued with a 100 nm GaN layer, followed by an optimized 1 nm AlN spacer layer at 1000 °C, a 15 nm of  $\text{In}_{0.16}\text{Al}_{0.84}\text{N}$  at 740 °C and finally a 2 nm GaN cap layer. The gated Hall bar ( $600 \mu\text{m} \times 100 \mu\text{m}$ ) was fabricated using the following three steps: (1) a Ti/Al/Ni/Au contact metal stack was deposited and then alloyed at 900 °C to form ohmic contacts, (2) the Hall bar pattern was defined using photolithography followed by a mesa isolation etched in a SAMCO inductively coupled plasma (ICP) etch tool using a Cl-based chemistry, and (3) Pt/Au (30/50nm) was deposited as the gate.

### 3.2 Magnetotransport measurements

The sample was characterized by magnetotransport measurements in a low-temperature Helium-3 cryostat with a base temperature of 0.28 K at different gate voltages. In Fig.3.2, we plot the low temperature magnetoresistance traces for the sample from -1.8 V to 0 V gate bias in 0.2 V steps. The sample exhibited clear SdH oscillations at 0.28 K, and starting from -1.6 V we observed well-pronounced two frequency SdH oscillations up to 0.4 V, which is a clear indication of two-subband occupation in the 2DEG channel (see the inset of Fig.3.2). To separate the two frequency oscillation components from the SdH oscillation data, we first plotted the data as a function of inverse magnetic field ( $1/B$ ), then we used a Fast Fourier Transform (FFT) to filter out the high and low frequency components, and then

converted the filtered data back to the B scale. Then those two frequency components were fitted to a typical Dingle form[34] in Fig 3.3.

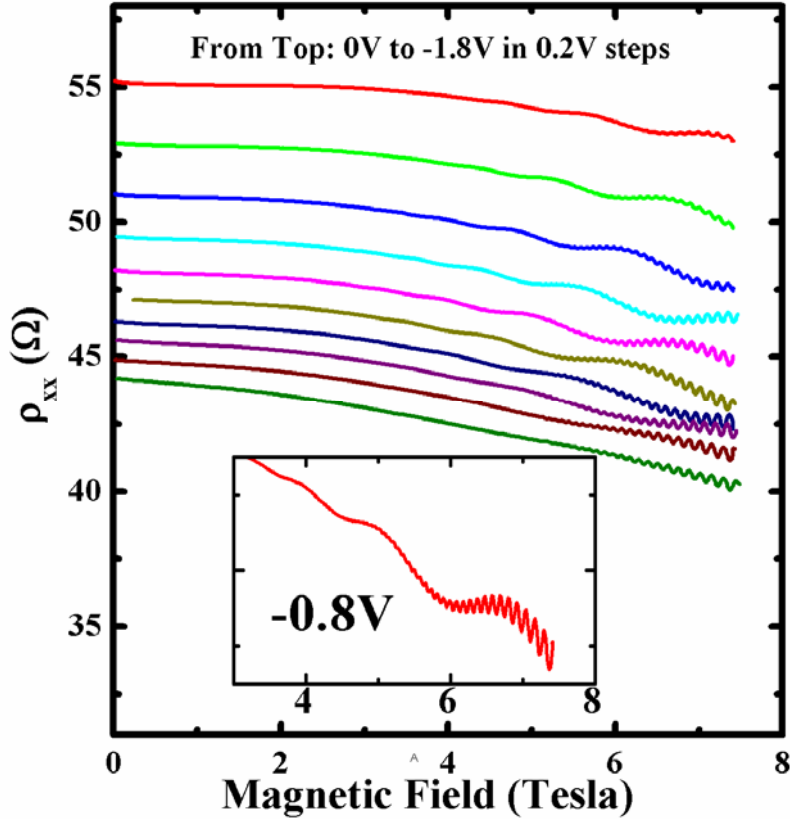


**Fig.3.2:** Longitudinal magnetotransport measurements at gate voltages from 0 V to -1.8V (from top to bottom in 0.2V steps). The insert is a typical data at  $V_{\text{gate}} = -0.8 \text{ V}$  with well pronounced two frequency SdH oscillations shown.

The SdH oscillation usually can be described by Dingle formula [34]

$$\rho_{xx}(B) = A + C \exp\left(\frac{-\pi}{\omega\tau_q}\right) \frac{\xi}{\sinh(\xi)} \cos\left(\frac{2\pi\Delta E}{\hbar\omega} + \varphi\right), \quad (3.1)$$

where  $A$ ,  $C$ , and  $\varphi$  are fitting constants. In this formula  $B$  is the magnetic field,  $\omega = eB/m^*$  is the cyclotron frequency,  $m^*$  is the effective mass,  $\tau_q$  is the quantum

lifetime,  $\xi = 2\pi^2 k_B T / (\hbar \omega)$ ,  $\Delta E = \pi \hbar^2 n / m^*$  is the energy difference between Fermi level and the subband energy level, and  $n$  is the carrier density.

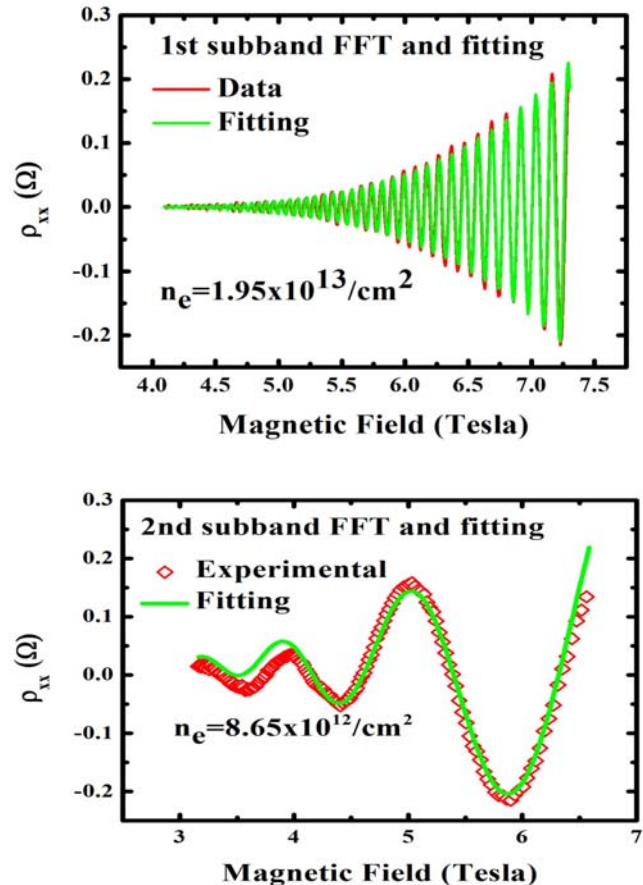


**Fig.3.3:** FFT for first and second subbands SdH components at  $V_{\text{gate}} = -0.8\text{V}$ . The data was fitted into Dingle formula and quantum lifetime  $\tau_q$  and carrier density has been extracted.

Also, the quantum lifetime can be found by plotting  $\ln(R \sinh(\chi)/\chi)$  vs  $1/B$  and calculating the scattering time from the linear fitting slope (see Fig 3.4). The result was found to agree with Dingle fitting.

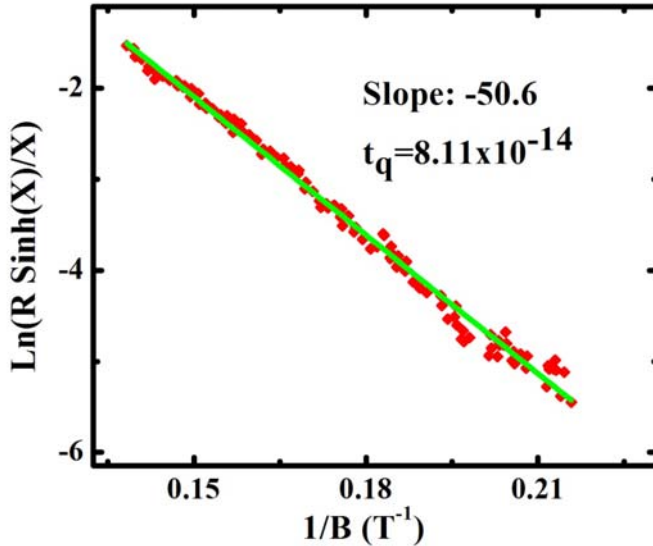


**Fig.3.4:**  $\ln[R \cdot \sinh(X)/X]$  vs  $1/B$  at  $V_{\text{gate}} = -0.8V$ . The data was fitted into linear line and the slope was used to calculate the quantum lifetime  $\tau_q$ .

### 3.3 Two conduction subbands with high mobility

For gate voltages from -1.4 V to 0.4 V, we extracted  $\tau_q$ ,  $n$ , and  $\Delta E$  for both first and second subbands. Beyond this range, the second subband frequency signal was too weak to fit with confidence. However, the first subband signal was strong enough to allow for fitting in the range from -2.4 V to 0.6 V. In Fig. 3.5, we plot the carrier densities at different gate voltages. In this figure, the solid data points represent the carrier densities for the first and second subbands extracted from the SdH oscillations. Also, the sum of the two subbands and the carrier density extracted from Hall measurements (not shown) are plotted together for comparison. We see a small but noticeable deviation from the Hall data and the sum of two subbands, which is due to the mobility difference in the two subbands [48].

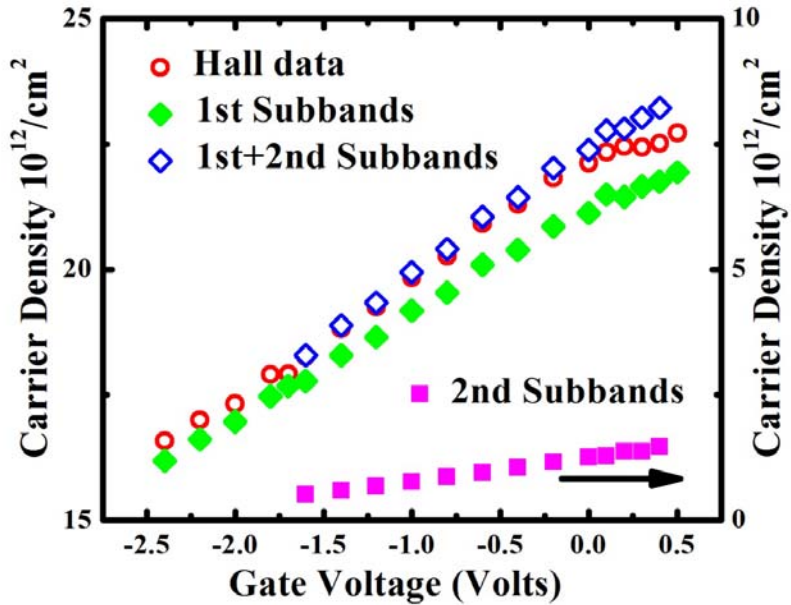


**Fig.3.5:** Carrier densities vs gate voltage. The solid dots are the carrier densities for the first and second subbands, where data for the second subband is shown according to the right scale. The hollow circle is the carrier density extracted from Hall slope and the hollow diamond is the sum of the first and second subband carrier densities.

We also plotted quantum lifetime vs. gate voltage in Fig.3.6. The second subband exhibits quantum lifetimes  $\tau_{2q}$  ranging from  $1.2 \times 10^{-13}$  to  $2.1 \times 10^{-13}$  s and the first subband exhibits quantum lifetimes  $\tau_{1q}$  ranging from  $0.55 \times 10^{-13}$  to  $0.95 \times 10^{-13}$  s. It is important to emphasize that the quantum lifetime extracted from SdH oscillations is different from the momentum relaxation time extracted from mobility measurements in that the momentum relaxation time is sensitive only to large angle scattering. Both the quantum lifetime and the momentum relaxation time can be used as a figure-of-merit for the quality of 2DEG. In our case, since the second subband shows almost double the quantum lifetime of the first subband, we expect that the second subband has a higher mobility than the first subband.

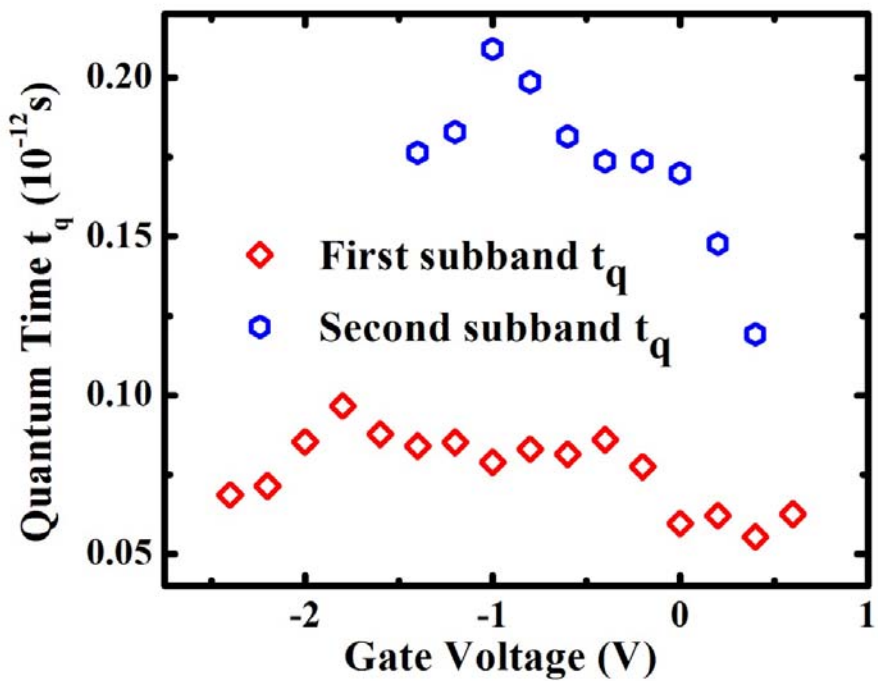


**Fig.3.6:** Quantum lifetime vs gate voltage. The second subband quantum lifetime is greater than first subband quantum lifetime in all gate voltages.

### 3.4 Charge distribution in two conductive subbands

The total carrier density in the 2DEG channel should be the sum of first and second subband carrier densities, which is found to vary with gate voltage linearly, consistent with a simple capacitance model. For gate voltages from -1.6 V to 0.4 V, the total carrier densities are remarkably high, changing from  $1.83 \times 10^{13} \text{ cm}^{-2}$  to  $2.32 \times 10^{13} \text{ cm}^{-2}$ . The second subband carrier density is much smaller and ranged from  $0.51 \times 10^{12}$  to  $1.46 \times 10^{12} \text{ cm}^{-2}$ . When we extrapolate the data to lower gate voltages, we would expect to enter a single subband conduction regime at a carrier density of  $1.6 \times 10^{13} \text{ cm}^{-2}$ .

In a two-dimensional system with multiple occupied subbands, the electron density in each sublevel is given by  $n_i = \frac{m^*(E_F - E_i)}{\pi\hbar^2}$  where  $m^*$  is the effective mass,  $E_F$  is the Fermi energy, and  $E_i$  is the energy level in the  $i^{th}$  subband. In this picture, the Fermi energy is expected to increase with the addition of new electrons, and these additional electrons would be shared equally between all occupied sublevels. We note, however, that the electrons added into the two-dimensional channel by increasing the gate voltage did not share equally between the two subbands. The change in the carrier densities of the first and second subbands with respect to the gate voltage  $\frac{dn_i}{dV_g}$  were  $2.01 \times 10^{12} \text{ cm}^{-2}/\text{V}$  and  $0.47 \times 10^{12} \text{ cm}^{-2}/\text{V}$ , respectively. In a recent work, researchers used the PPC effect to study two-subband conduction in an AlGaN/GaN heterostructure by varying the total carrier concentration[44]. Interestingly, most of the additional electrons provided by the PPC effect were observed to split between the first and second subbands with a 4-to-1 ratio, which is very close to the split ratio observed in our gated structure.

The uneven splitting of additional electrons between the two subbands can arise from either the different effective mass of electrons in two subbands, or from the variations in the confinement associated with gating. In low bandgap semiconductors, such as in AlAsSb/InGaAs heterostructures [49], the uneven splitting of additional electrons provided by a gate voltage between the two subbands has been attributed to different effective masses in the two subbands due to nonparabolicity of the conduction band.

Due to the large bandgap of GaN, the nonparabolicity of the conduction band is not expected to be significant. Therefore, we must consider the possible shifts in the subband energy levels to be the cause. In particular, an increase in the energy level separation between the two subbands,  $E_{2l}=E_2-E_1$ , with increasing gate voltage is needed to explain our data. We note that similar energy shifts in energy levels associated with gating have been previously studied in AlGasAs/GaAs heterostructures [50-51].

If we consider the confining potential for 2DEG as a triangular potential and use the approximation of infinite triangular potential, the eigenenergy is

$$E_n = a_n \left[ \frac{(A\hbar)^2}{2m} \right]^{1/3},$$

where A is the slope of triangular potential [13]. Therefore,  $E_{21}$  is expected to scale as  $A^{2/3}$ . When we increase the electron density either by gating or by the PPC effect, the confinement potential changes in a way to increase the value of  $E_{21}$ . To support our premise, we performed ATLAS simulations of the conduction band diagram for different gate voltages. The parameters[52] used for spontaneous polarizations: GaN  $2.12 \times 10^{13}$ , AlN  $5.62 \times 10^{13}$ ,  $\text{Al}_{0.85}\text{In}_{0.15}\text{N}$   $4.61 \times 10^{13}$ --this includes a bowing parameter of -0.07 C/m<sup>2</sup>; piezoelectric polarization of  $2.9 \times 10^{13}$  for AlN (same direction as spontaneous polarization for Ga-face AlN on GaN). The dielectric constants for GaN, AlN, and InAlN are of 8.9, 7.8, 8, respectively. All layers were assumed to have doping levels of  $2 \times 10^{16}/\text{m}^3$ . The top GaN was "doped" to  $4 \times 10^{20}/\text{m}^3$  to account for surface donors (without this the channel density is too low). In reality we believe there are many amphoteric traps on the surface which provide an infinite electron supply to the channel--using only donors can change the surface potential but

for the band diagram this should be all right. The Pt gate was assumed to have a work function of 5.6eV.

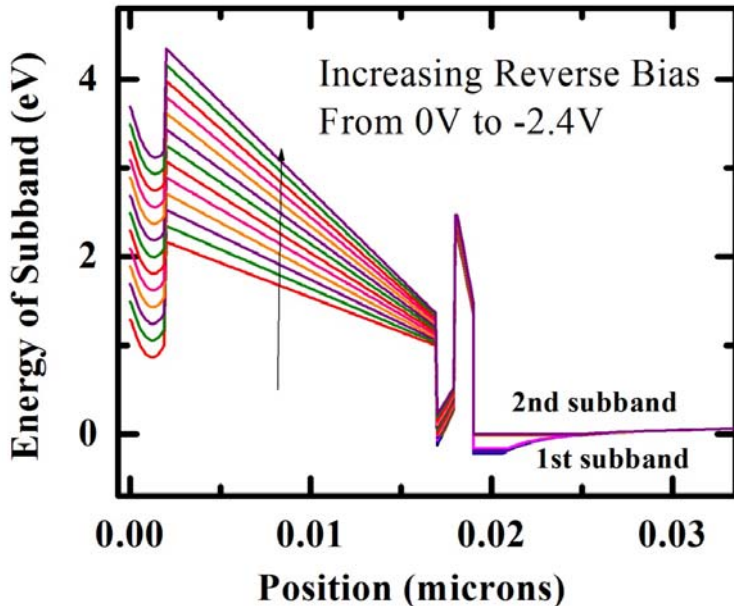


**Fig.3.7:** Energy of subband versus distance in growth direction in heterostructure. This is obtained by ATLAS simulations for 2DEG band calculations. The positions of the first and second subband energies and changing potential slopes at different gate voltages are clearly shown.

Fig. 3.7 shows a plot of calculated subband energies as well as the subband energies extracted from SdH measurements *vs.* gate voltage. The calculated energy levels from ATLAS simulation agree with our experimental result both qualitatively and quantitatively. From the calculation, we conclude that  $E_{21}$  increases with increasing gate voltage and that it is the major contribution to the uneven splitting of added electrons into the two subbands.

The calculation results for two subband energy levels, as well as our experimental data for comparison with  $m^*_1 = m^*_2 = 0.23m_e$ , is shown in Fig.3.8. Here the

calculated data from ATLAS simulation agrees with our experimental result not only qualitatively, but also quantitatively.

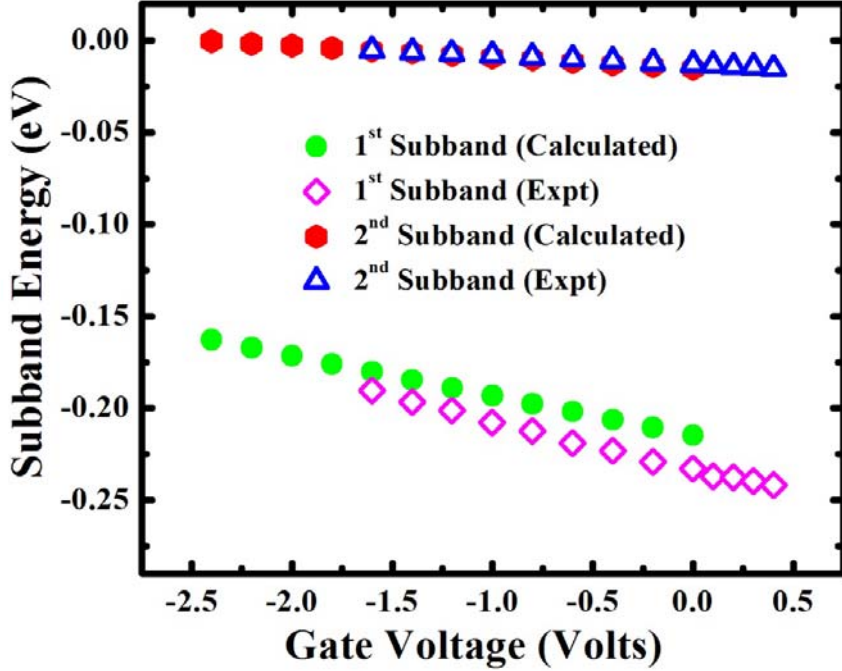


**Fig.3.8:** Subband energy vs gate voltage. Solid points are calculation results from ATLAS simulation and hollow points are experimental data.

The mobilities of electrons in the first and second subbands are not expected to be the same[48]. Since the concentration of carriers in the first subband is much higher than that of the second subband, the transport is mainly dominated by the electrons in the first subband. Thus, we can only extract the mobility of the electrons in the first subband reliably. Considering that the approximate ratio of the quantum lifetimes extracted from SdH oscillations was  $\tau_{1q}/\tau_{2q} \sim 1/2$ , we assumed that the ratio of momentum relaxation times was also  $\tau_{1m}/\tau_{2m} \sim 1/2$ , where  $\tau_{1m}$  and  $\tau_{2m}$  are the momentum relaxation time for first and second subbands respectively. Following this assumption,

we extracted the mobilities for the first subband; these ranged from 7400 to 4290 cm<sup>2</sup>/Vs as the carrier density increased from  $18.3 \times 10^{12}$  cm<sup>-2</sup> to  $23.2 \times 10^{12}$  cm<sup>-2</sup>. The mobilities extracted were weakly dependent on the exact value of  $\tau_{1m}/\tau_{2m}$ ; when we assumed  $\tau_{1m}/\tau_{2m}=1$ , we extracted mobilities for the first subband which ranged from 7610 to 4560 cm<sup>2</sup>/Vs. In this high carrier density regime, the surface roughness and alloy scattering are expected to be the dominant scattering mechanisms which would lead to a decrease in electron mobility with increasing carrier concentration, consistent with our measurements. Finally, the momentum relaxation times extracted from the mobility measurements are found to be about an order of magnitude larger than the quantum lifetimes extracted from the SdH oscillations. This is a typical result, since the quantum relaxation is sensitive to small angle scattering processes while the momentum relaxation is not [34,51,53-54].

We should point out that in Fig 3.8 the small deviation of calculation and experimental data for first subband might be due to small deviation of effective mass induced by band hybridization or nonparabolic band structure. Furthermore, in Fig 3.9 the InAlN/GaN samples appear to have a better mobility than the AlGaN/GaN sample. This shows that InAlN/GaN has a better quality which is most likely due to the lattice matching. It also has higher carrier density due to stronger spontaneous polarization and larger bandgap offset between InAlN and GaN.

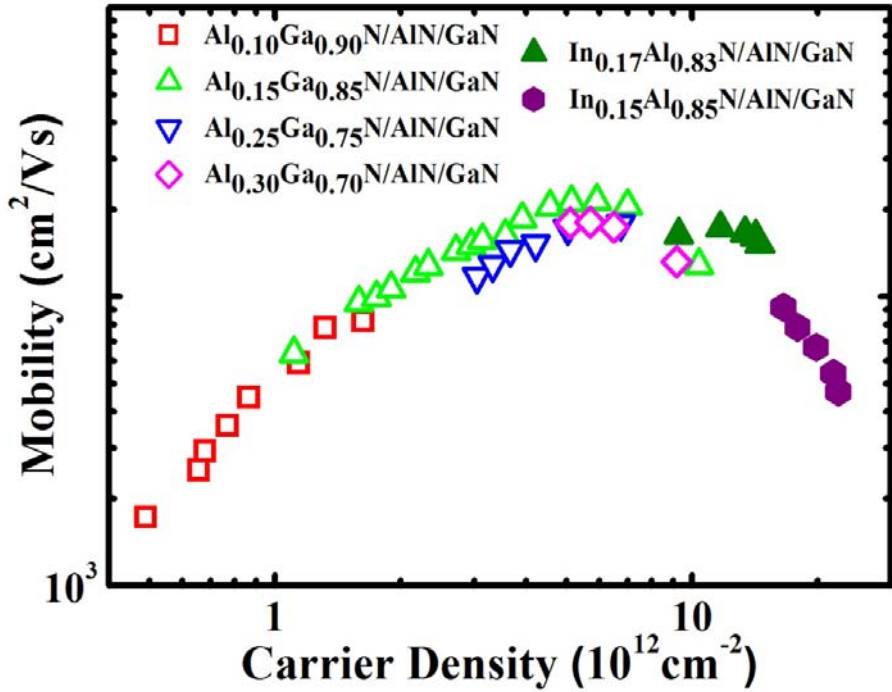


**Fig.3.9:** Mobility vs Carrier Density. Hollow points are experimental data from AlGaN/AlN/GaN samples and solid points are InAlN/AlN/GaN data. If we extend the mobility trend line of AlGaN/AlN/GaN to high carrier density, then InAlN/AlN/GaN has a higher mobility.

### 3.5 Summary and future directions

In summary, we have investigated magnetotransport properties of an  $\text{In}_{0.16}\text{Al}_{0.84}\text{N}/\text{AlN}/\text{GaN}$  gated Hall bar sample at different gate voltages. Well-pronounced two frequency SdH oscillations have been observed at 0.28 K, which was due to the occupation of two subbands. Carrier densities and quantum lifetimes in those two subbands have been extracted from SdH oscillations and the highest total carrier density reaches  $2.32 \times 10^{13} \text{ cm}^{-2}$ . We also observed different rate of change of the electron density *vs.* gate bias,  $dn/dV_g$ , in two subbands, which is explained by the increase in energy level separation between the first and second subbands induced by

increasing gate voltage. The InAlN/AlN/GaN samples appear to have a better quality than the AlGaN/AlN/GaN samples, which is most likely due to the lattice matching, and they also have higher carrier densities due to stronger spontaneous polarization and larger bandgap offset.

In the future, we need to measure more high quality InAlN/GaN samples and the carrier density range from  $1\times10^{12}$  cm $^{-2}$  to  $10\times10^{12}$  cm $^{-2}$  should be measured to compare with the results of AlGaN/GaN samples. In our measurements, we found that the gate current leakage was a problem beyond the gate voltage range from -1.6 V to 0.4 V. Therefore, a different gate fabrication recipe should be used to reduce the gate current leakage. If necessary, an insulator layer between the gate and the 2DEG sample should be deposited before the gate fabrication.

## CHAPTER 4

### MAGNETOTRANSPORT MEASUREMENTS IN AlGaN/AlN/GaN 2DEGs WITH PARASITIC CHANNEL

#### 4.1 Al<sub>x</sub>Ga<sub>1-x</sub>N/AlN/GaN heterostructures grown on epitaxial lateral overgrown GaN templates

In chapter 3, we discussed experiments performed on GaN 2DEG samples with two high mobility conductive channels, in which case the carrier density is too high to be contained in a single subband channel. In collaboration with Prof. Morkoç's group we have been exploring better growth strategies, which can lead to higher quality heterostructures. However, in some of the 2DEG samples, even if the carrier density is not high enough, we observed deviations from single channel conduction due to the existence of a low mobility parasitic channel. In most cases because of the low mobility of the parasitic channel, we were able to extract useful information about the 2DEGs from the detailed analysis of the conduction features. We demonstrated that there were significant enhancements in device quality. The presence of a parasitic channel is not significant in vertical devices such as light emitting diodes; however, they need to be fully avoided in lateral devices such as in field effect transistors.

As we discussed in chapter 1, the bottleneck for GaN device performances eventually comes from the difficulty of improving transport properties, which requires better quality templates and optimized growth conditions [24-26,28,40,55]. Reducing and characterizing crystal defects is both essential and challenging for further progress.

AlGaN/GaN 2DEG mobility extracted from low-temperature magneto-transport measurements can be used as a figure of merit to characterize the defect properties in the GaN system. The electron mobility in the GaN heterostructures can indicate the density level of crystal defects; an example of this is the threading dislocations generated at the lattice-mismatched GaN/Al<sub>2</sub>O<sub>3</sub> interface. The fewer threading dislocations there are, the higher the corresponding electron mobilities are due to reduced associated scattering which is effective in the low-density regime [41-42]. Our collaborating group at the Virginia Commonwealth University uses the overgrown method to grow the GaN heterostructure samples. This method relies on filtering the threading dislocations by utilizing defect-blocking mask layers during the growth on lattice-mismatched sapphire substrates, which is employed by epitaxial lateral overgrowth (ELO) from the nearly defect-free GaN facets[56]. Those laterally overgrown GaN samples will have lower dislocation densities compared to normal growth samples. However, the weakness of this method is that the threading dislocations will extend along the unmasked (window) areas where GaN grows vertically and new defects will be produced at the coalescence boundaries. Different masking techniques for ELO have been tested successfully, including porous SiN<sub>x</sub> [57-61] or TiN [62] layers and the more conventional *ex situ* deposited SiN<sub>x</sub> or SiO<sub>2</sub> striped mask templates [36,63-66]. Among them, the porous SiN<sub>x</sub> mask layer has the advantage of being grown *in situ*, avoiding the trouble induced by any processing/growth outside the growth chamber, such as contamination and oxidation on the surface. A sketch of ELO methods is shown in Fig.4.1.

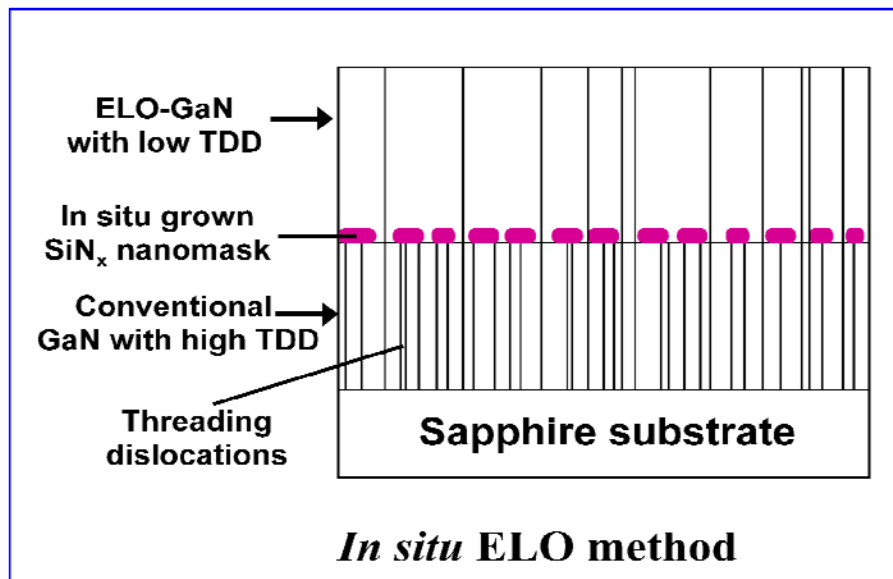
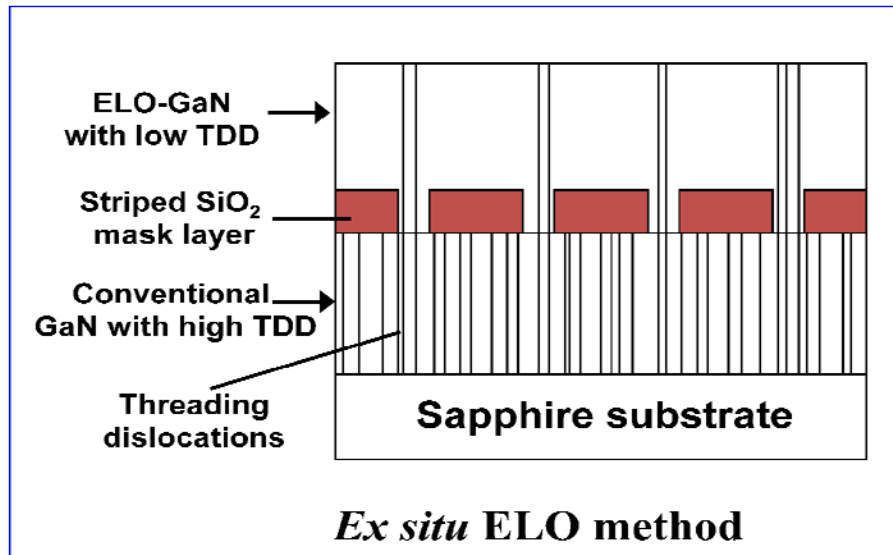


**Fig.4.1:** Growth on lattice-mismatched sapphire substrates, attempting to filter the threading dislocations by utilizing defect-blocking mask layers, which is referred as the epitaxial lateral overgrowth (ELO). Upper diagram: the *Ex situ* ELO:  $\text{SiO}_2$  mask layer is grown and stripe-patterned outside the growth reactor. Lower diagram: the *In situ* ELO:  $\text{SiN}_x$  nanomask layer is grown within growth chamber. This diagram is from Prof. Morkoc's group.

The growth methods for  $\text{Al}_x\text{Ga}_{1-x}\text{N}/\text{AlN}/\text{GaN}$  heterostructures on ELO-GaN templates and SiN-GaN templates are shown on Fig. 4.1 and the sample structures in Fig. 4.2.

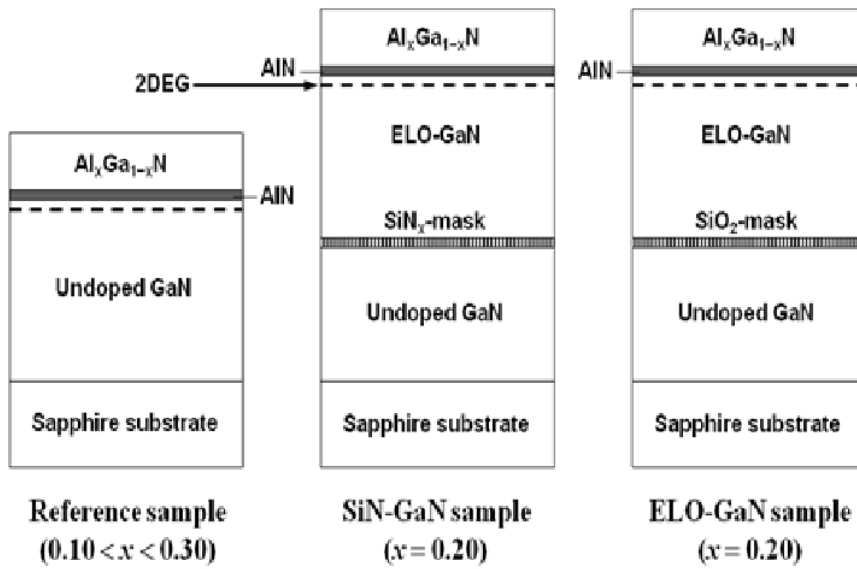


**Fig.4.2:** Sample structures used in this chapter. From left to right: AlGaN/AlN/GaN control samples, SiN-GaN samples and ELO-GaN samples. This diagram is from the courtesy of Prof. Morkoc's group.

The  $\text{Al}_x\text{Ga}_{1-x}\text{N}/\text{AlN}/\text{GaN}$  heterostructures were grown [67] by a custom rotating-disk low-pressure metal-organic vapor-phase epitaxy (LP-MOVPE) system. The samples were grown on c-plane (0001) sapphire substrates. The growth was initiated with a 25-nm thick low-temperature ( $\sim 550$  °C) GaN nucleation layer. A 3  $\mu\text{m}$  thick undoped GaN epilayer was then grown at 1000 °C under 200 mTorr, using a V/III ratio of 4000. This u-GaN template served as a basis-template for all samples. Atomic force microscopy scans and etch-pit studies showed that the threading dislocation density of the basis template was in the low- $10^9 \text{ cm}^{-2}$  range.

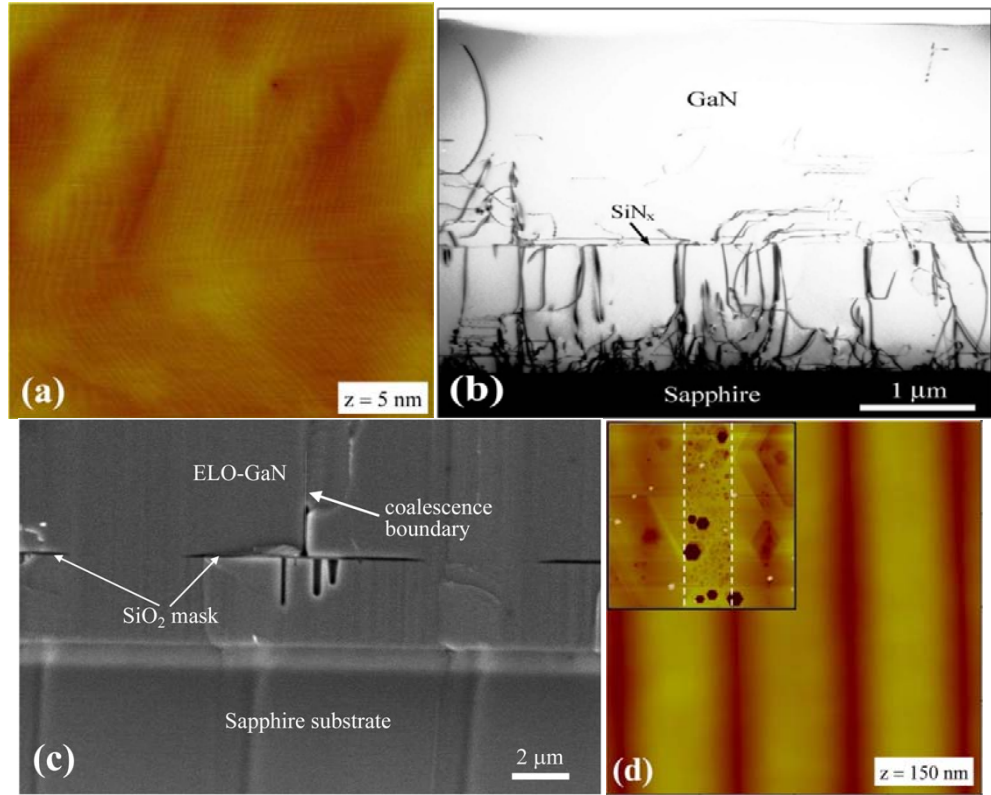


**Fig.4.3:** (a)  $10 \times 10 \mu\text{m}^2$  AFM image of the  $\text{SiN}-\text{GaN}$  template surface showing smooth surface and clear atomic steps. (b)  $\text{SiN}-\text{GaN}$  template's cross-sectional TEM picture showing blocking of threading dislocations by  $\text{SiN}$  nanomask layer. (c) Cross-sectional SEM picture of ELO-GaN template in which  $\text{SiO}_2$  mask and coalescence boundary of ELO-GaN is shown. (d)  $40 \times 40 \mu\text{m}^2$  AFM scan of the ELO-GaN template, where the dark lines correspond to the coalescence boundaries of ELO-GaN. The inset shows  $20 \times 20 \mu\text{m}^2$  scan of the same template after 2 min KOH-etch for the etch-pit study. The window area is marked within the dashed lines.

The  $\text{SiN}-\text{GaN}$  template was grown by the *in situ* ELO technique. On top of the u-GaN epilayer, a porous  $\text{SiN}_x$  layer was grown at  $1020^\circ\text{C}$ . The nominal thickness of this porous  $\text{SiN}_x$  layer was about 2 nm. Subsequently, lateral overgrowth started from the GaN openings in the pores of the  $\text{SiN}_x$  nanomask layer. ELO was performed at  $1040^\circ\text{C}$  under a reduced reactor pressure (76 mTorr) and V/III ratio (2000) to increase the lateral overgrowth rate. After 3 hours of overgrowth, complete coalescence was

achieved. Figure 4.3 (a) shows a  $10 \times 10 \mu\text{m}^2$  AFM scan of the SiN-GaN template surface where clear atomic steps are observed. The top-view and cross-sectional transmission electron microscopy (TEM) pictures demonstrated the reduced threading dislocation density by the  $\text{SiN}_x$  nanomask layer. In Figure 4.3 (b), a cross-sectional TEM picture is shown, where the  $\text{SiN}_x$  nanomask layer efficiently blocks the threading dislocations from penetrating into the upper ELO-GaN layer. The average threading dislocation density in the SiN-GaN template is  $\sim 6 \times 10^7 \text{ cm}^{-2}$ . A similar density of threading dislocations was found using an etch-pit study where a piece of SiN-GaN template was etched in molten KOH solution for couple of minutes and the resulting hexagonal etch-pits were counted with AFM.

For the *ex situ* ELO-GaN template, the sample was coated with a  $\sim 150 \text{ nm}$   $\text{SiO}_2$  layer in an ultrahigh-vacuum chemical vapor deposition (UHV-CVD) system. By lithography and etching, parallel  $10 \mu\text{m}$ -wide  $\text{SiO}_2$  mask stripes separated by  $4 \mu\text{m}$  wide window areas were formed in the  $\text{SiO}_2$  mask layer. The stripe pattern was aligned along the  $<1\bar{1}00>$  direction for the lateral growth to take place along the  $<11\bar{2}0>$  direction, which will maximize the lateral growth rate of ELO-GaN. The sample was then reloaded into the MOVPE reactor. ELO commenced from the  $4 \mu\text{m}$  wide GaN window areas without any nucleation on the dielectric mask. The lateral-to-vertical growth rate was optimized at a ratio of 3:1 such that within 2 hours of overgrowth the overgrown GaN wings met at the coalescence boundary. The additional growth following coalescence served to smooth the sample surface, which is critical for the growth of high-mobility 2DEG heterostructures. A cross-sectional scanning electron microscopy (SEM) image of the completed ELO-GaN template is shown in Fig. 4.3(c).

The surface morphology of the ELO-GaN template is shown by a 40x40  $\mu\text{m}^2$  AFM picture in Fig. 4.3(d). The dark regions correspond to the coalescence boundary where a ~50-70 nm dip is observed. The window region, where GaN is vertically overgrown, is at the center of the brighter areas. An etch-pit study was performed to estimate the density of threading dislocations of ELO-GaN template. The inset in Fig. 4.3(d) shows a 20x20  $\mu\text{m}^2$  AFM image scanned after 2 min KOH etch. The highly-defective window area (marked with dashed lines) can be easily differentiated from the low-dislocation wing area. Along the window stripes, the vertically overgrown GaN allows most of the threading dislocations to propagate from the substrate to the upper surface. Counting the pits resulted in an average dislocation density of  $\sim 6 \times 10^8 \text{ cm}^{-2}$  in the window area. The number of dislocations in the wing area was significantly reduced with most of the dislocations located at the coalescence boundary where the two overgrowing GaN wings meet. The ~4  $\mu\text{m}$  stripe area between the window and coalescence boundary is the area with very few dislocations. The average density of dislocations in the wing region was estimated as  $\sim 1 \times 10^7 \text{ cm}^{-2}$ . The overall average threading dislocation density of the ELO-GaN template was  $\sim 2 \times 10^8 \text{ cm}^{-2}$ .

$\text{Al}_x\text{Ga}_{1-x}\text{N}$  layers were grown on top of the aforementioned templates to form the 2DEG systems. The heterostructure consisted of an additional ~1  $\mu\text{m}$  GaN layer, a ~1 nm thick AlN interfacial layer, a ~25 nm  $\text{Al}_x\text{Ga}_{1-x}\text{N}$  layer, and a ~3 nm GaN cap layer, all nominally undoped. The 2DEG channel was formed at the GaN/AlN heterointerface. The AlN interfacial layer was used to reduce the alloy disorder scattering by minimizing the wavefunction penetration from the 2DEG channel into the  $\text{Al}_x\text{Ga}_{1-x}\text{N}$  layer. The heterostructure layers were grown at 1060 °C. The Al concentration was

changed from 10% to 30% for the reference samples whereas 20% was used for the SiN-GaN and ELO-GaN samples. Six-contact Hall-bar samples were prepared in some samples. Ohmic contacts were formed using Ti/Al/Ti/Au (30 nm/100 nm/30 nm/50 nm) alloyed at 900 °C for 1 min.

#### 4.2 Magnetotransport measurements in AlGaN/AlN/GaN control samples

Magnetotransport measurements were carried out at 1.6 K in a variable temperature liquid helium cryostat with magnetic field ability up to 8 T. Low-noise AC lock-in technique was used to record the sample voltages. To avoid sample heating, low excitation current of 1  $\mu$ A was used. The experimental data were converted to resistivity and used to determine the carrier density and mobility of the 2DEG samples.

$\text{Al}_x\text{Ga}_{1-x}\text{N}/\text{AlN}/\text{GaN}$  grown on conventional u-GaN templates with  $x=0.10, 0.15, 0.25$ , and  $0.30$  were measured as control samples to compare with the 2DEG samples grown on SiN-GaN and ELO-GaN templates. Magneto-transport measurements showed clear single-period Shubnikov-de Haas (SdH) oscillations in all samples, confirming the existence of a high mobility 2DEG at the AlN/GaN interface.

Figure 4.4 shows the SdH and Hall measurement results for the  $\text{Al}_{0.30}\text{Ga}_{0.70}\text{N}/\text{AlN}/\text{GaN}$  sample, recorded at 1.6 K. The  $\rho_{xx}$  curve (referred as longitudinal resistivity) displays strong SdH oscillations commencing around 3 T, whereas the  $\rho_{xy}$  curve (Hall resistivity) increases linearly with magnetic field, as expected. The corresponding 2DEG carrier density values were calculated using two methods.

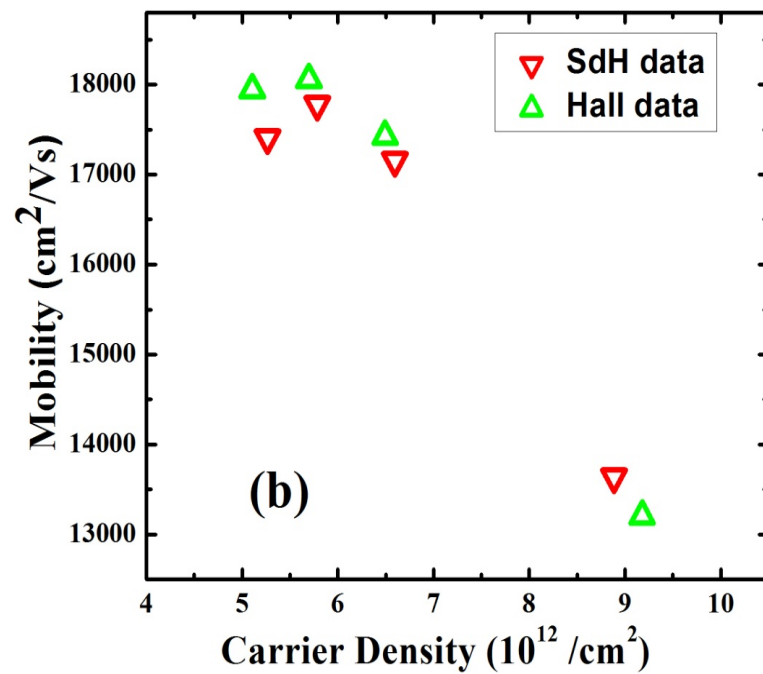
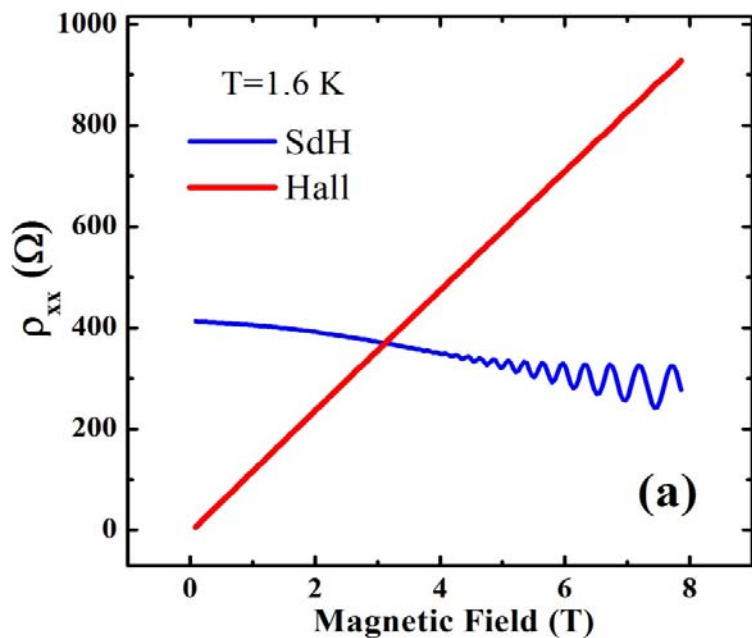


**Fig.4.4:** (a) SdH and Hall resistivity versus magnetic field measured at 1.6 K for the  $\text{Al}_{0.30}\text{Ga}_{0.70}\text{N}/\text{AlN}/\text{GaN}$  control sample. (b) 2DEG mobility versus carrier density for the  $\text{Al}_{0.30}\text{Ga}_{0.70}\text{N}/\text{AlN}/\text{GaN}$  sample.

In the conventional method, Hall data was used to extract carrier density. Alternatively, one can also use the SdH oscillation data to extract the 2DEG carrier density (see Chapter 2). In an ideal 2DEG system, the carrier density values evaluated by these methods should be consistent with each other.

Figure 4.4(b) shows the carrier density and mobility of the same  $\text{Al}_{0.30}\text{Ga}_{0.70}\text{N}/\text{AlN}/\text{GaN}$  sample determined by these two methods. The carrier density of the sample was altered (increased) by persistent photoconductivity (PPC) using optical illumination [68]. As the sample was illuminated, the carrier density increased from  $5.2 \times 10^{12} \text{ cm}^{-2}$  to  $9.0 \times 10^{12} \text{ cm}^{-2}$ . The corresponding electron mobility slightly increased when  $n$  is up to  $6 \times 10^{12} \text{ cm}^{-2}$  and decreasing thereafter. The maximum mobility recorded was  $\mu = 17,900 \text{ cm}^2/\text{Vs}$  at a carrier density of  $5.7 \times 10^{12} \text{ cm}^{-2}$ . The carrier density and mobility values calculated using Hall and SdH data are fairly close to each other, meaning that the 2DEG is of good quality and that there is no other conducting (parallel) channel present in the sample structure. Similar results were obtained with the other reference 2DEG samples with different Al compositions. By increasing the Al content in the barrier layer from 10% to 30% and by using the PPC effect, we were able to change the carrier density from  $5 \times 10^{11} \text{ cm}^{-2}$  to  $1 \times 10^{13} \text{ cm}^{-2}$ . The mobility increased with the carrier density, saturated at approximately  $6 \times 10^{12} \text{ cm}^{-2}$  and decreased for  $n > 7 \times 10^{12} \text{ cm}^{-2}$ . Peak mobilities just above  $20,000 \text{ cm}^2/\text{Vs}$  were recorded with the illuminated  $\text{Al}_{0.15}\text{Ga}_{0.85}\text{N}/\text{AlN}/\text{GaN}$  sample.

Field-dependent longitudinal resistance ( $\rho_{xx}$ ) and transverse (Hall) resistance ( $\rho_{xy}$ ) measurements were conducted at  $T = 1.6 \text{ K}$  in a variable temperature liquid-He cryostat equipped with an 8 T superconducting magnet. Low-noise ac lock-in

technique along with a low-noise current pre-amplifier was used to record the sample voltages. To avoid sample heating, low excitation current of  $1 \mu\text{A}$  was used. The experimental data were converted to resistivity and used to determine the carrier density and mobility of the 2DEG samples.

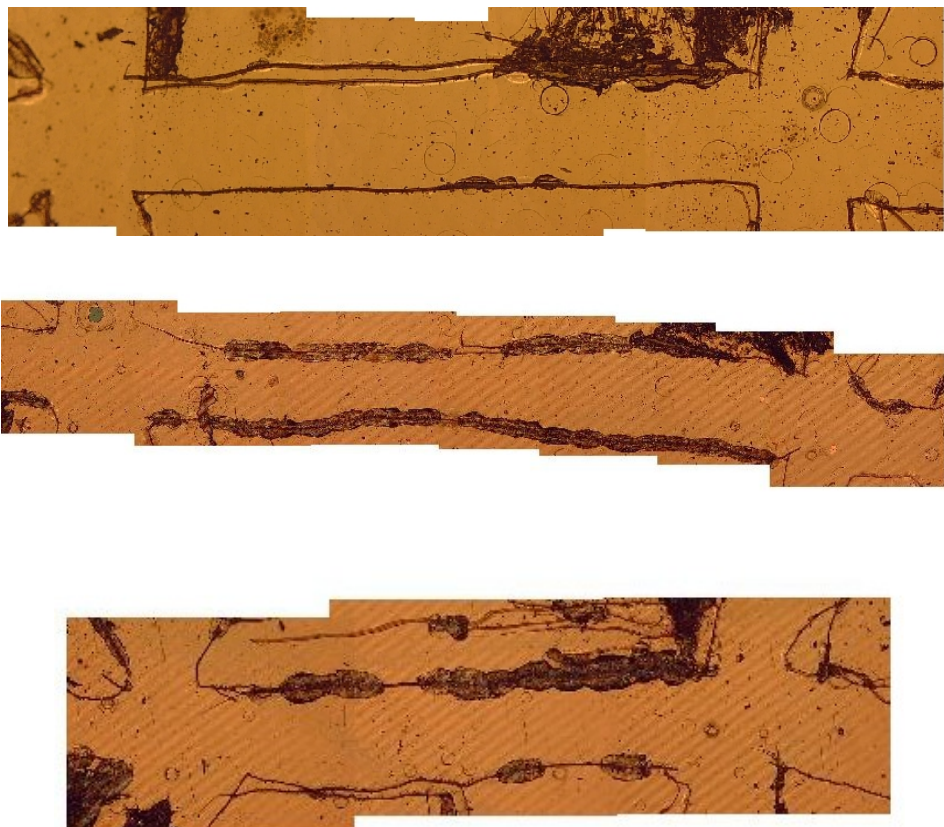


**Fig.4.5:** Images of the active region of Hall bar structures prepared by scratching the top surface of the heterostructure by a diamond tip. From top to bottom: scratched SiN-GaN sample, parallel ELO-GaN and perpendicular ELO-GaN sample.

Sometime when we cannot fabricate lithographically defined Hall bar structures due to etching problems, we can scratch the samples to make them into a Hall bar configuration. Images of some of the Hall bar samples prepared using the scratching

technique are shown in Fig. 4.5. It might not look nice, but the data extracted from the measurements could still be trusted, especially for Hall measurements. For the longitudinal resistivity measurements, one needs to analyze the aspect ratio of each scratched sample individually. Following such an analysis the error in electron mobility is expected to be within 10 percent.

### 4.3 Magnetotransport measurements in SiN-GaN samples

The  $\text{Al}_{0.20}\text{Ga}_{0.80}\text{N}/\text{AlN}/\text{GaN}$  sample grown on SiN-GaN template showed different magnetotransport characteristics from the 2DEG samples grown on conventional templates. Longitudinal resistivity and raw Hall data measured at 1.6 K are plotted in Fig. 4.6. The Hall data deviated from linear behavior at the high magnetic field, pointing towards the existence of another conducting channel in the structure. Besides a high-mobility carrier, which is due to 2DEG electrons, a lower-mobility parasitic electron channel also appears which corresponds to the bulk electrons in the parallel channel. Therefore, the single 2DEG channel formula for  $\rho_{xx}$  and  $\rho_{xy}$  do not apply in this case. The obvious evidence is the deviation of  $\rho_{xy}$  from linear behavior at the high magnetic field. In the coexistence of parasitic channel with 2DEG, electrical field is the same for both channels. Therefore, it is more convenient to use the 2-dimensional conductivity matrix to describe the transport in these heterostructures with parasitic conduction channels.

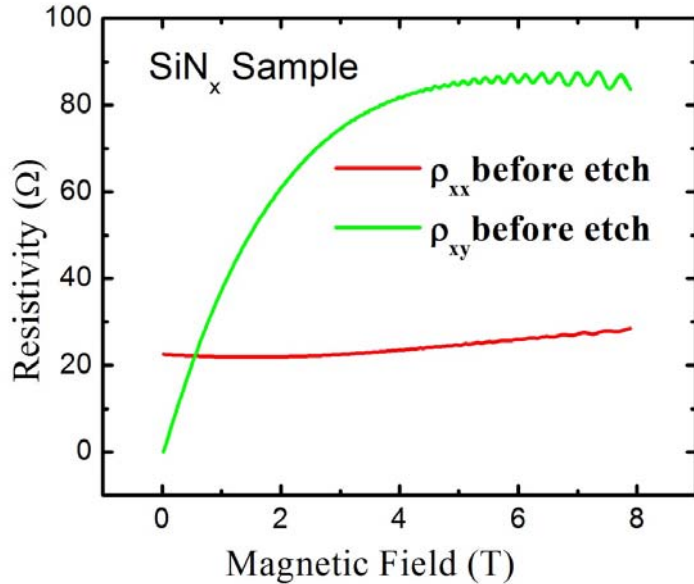


**Fig.4.6:** SdH and Hall resistivity versus magnetic field measured at 1.6 K for  $\text{Al}_{0.20}\text{Ga}_{0.80}\text{N}/\text{AlN}/\text{GaN}$  sample grown on  $\text{SiN}_x$ -GaN template before the sample etch.

To address the parasitic channel problem we designed the following experiment: by etching the top  $\text{Al}_{0.20}\text{Ga}_{0.80}\text{N}/\text{AlN}$  layers we first removed the 2DEG and then repeated the magneto-transport measurements on the etched samples which contained the parallel channel only. Having two sets of longitudinal and Hall resistance data, we converted the resistivity data into the conductivity tensor elements  $\sigma_{xx}$  and  $\sigma_{xy}$  data using the following equations:

$$\sigma_{xx} = \frac{\rho_{xx}}{\rho_{xx}^2 + \rho_{xy}^2} \quad (4.1)$$

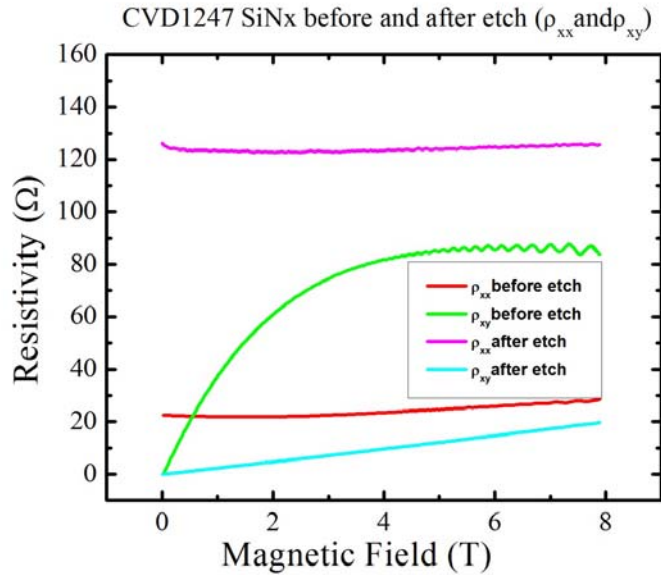
$$\sigma_{xy} = \frac{\rho_{xy}}{\rho_{xx}^2 + \rho_{xy}^2} \quad (4.2)$$

If the contact resistance to both 2DEG and parallel channel is negligible, the 2DEG conductivity can be extracted by subtracting the parallel channel conductivity from the total conductivity:

$$\sigma_{xx}^{2DEG}(B) = \sigma_{xx}^{Total}(B) - \sigma_{xx}^{Bulk}(B) \quad (4.3)$$

Using the zero-field conductivity value, the mobility of the 2DEG can be determined if the carrier density is known. On the other hand, the raw Hall data cannot be used for carrier density calculations since the Hall curve is not linear due to the multiple conduction channels. Fortunately SdH oscillations were observed in this sample, making it possible to calculate the 2DEG carrier density using the SdH method.

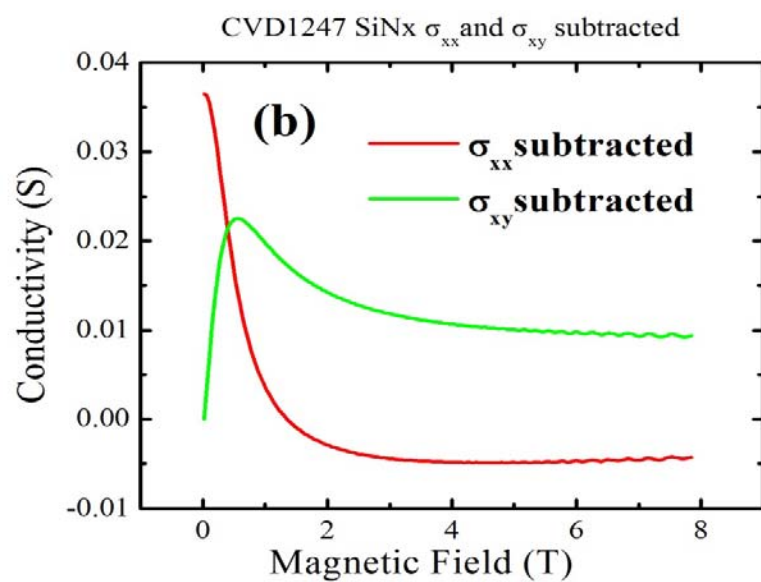
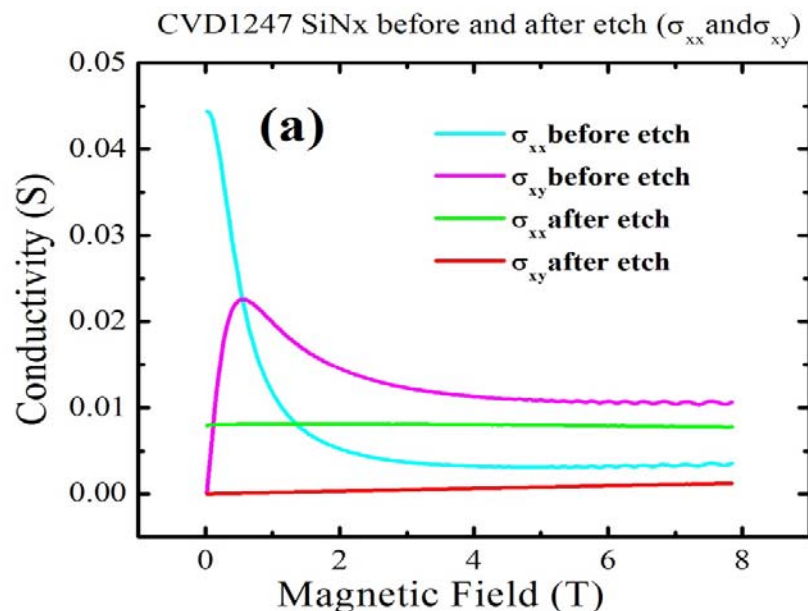
Prior to etching, the SdH oscillations can clearly be seen in Fig. 4.6. The carrier density derived from SdH data was  $7.0 \times 10^{12} \text{ cm}^{-2}$ . After etching the  $\sim 100 \text{ nm}$  top layer using  $\text{BCl}_3$ -plasma reactive ion etching, the SdH oscillations did not exist anymore, indicating that the 2DEG channel has been etched away. We then measured the low temperature SdH and Hall resistance again. Fig. 4.7 shows the measured resistivity data. Several differences were observed: SdH oscillations disappeared as expected and the Hall resistance became linear, confirming the complete removal of the 2DEG conduction. From Hall data we found the parallel channel carrier density to be  $2.5 \times 10^{14} \text{ cm}^{-2}$ . The mobility of this bulk conduction was calculated to be  $200 \text{ cm}^2/\text{Vs}$ .



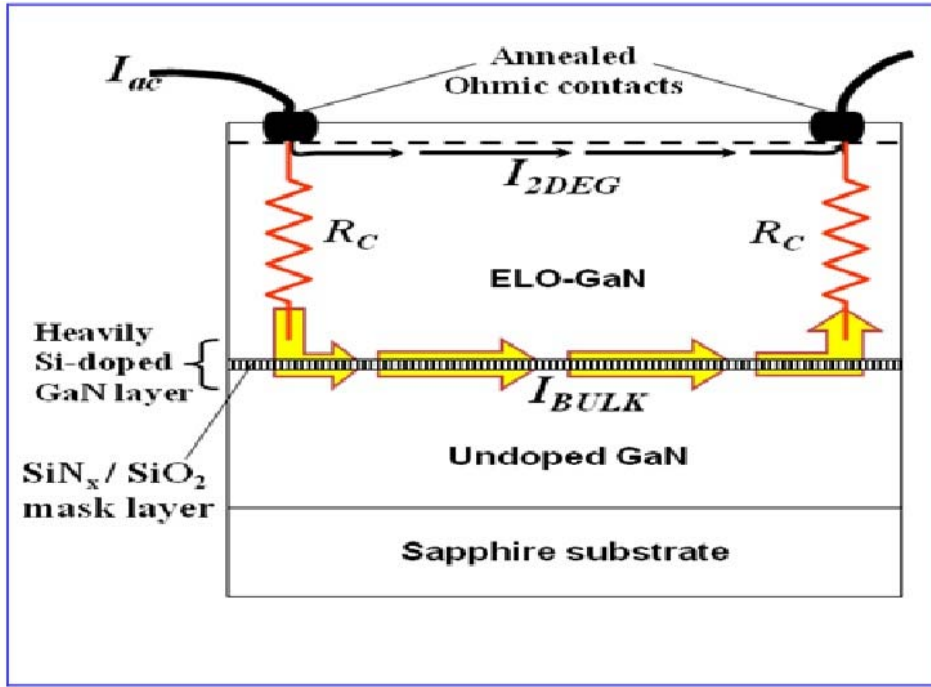
**Fig.4.7:** SdH and Hall resistivity versus magnetic field measured at 1.6 K for SiN-GaN samples before and after etching.

Fig. 4.8 shows how the 2DEG conductivity was extracted from the measured data sets before and after the recess-etch. If the contact resistance between 2DEG and bulk parasitic channel could be negligible, this subtracted conductivity would be the 2DEG's conductivity. However, we note that the subtracted  $\sigma_{xx}$  is negative at large magnetic field, which does not have a physical meaning if it represents the 2DEG's conductivity. Therefore, this unphysical negative conductivity indicates that the contact resistance cannot be negligible (see Fig.4.9).

Because of the contact resistance problem, the 2DEG conductivity extracted in this manner should only be viewed as a lower bound for the conductivity of the actual 2DEG. The contact resistance problem is most pronounced at higher magnetic fields ( $B>1.3$  T) where the 2DEG conductivity is negative.



**Fig.4.8:** Conductivity versus magnetic field before and after etching. (b) Conductivity subtracted using before and after etching data versus magnetic field.



**Fig.4.9:** Schematic diagram of a heterostructure with a parasitic conduction channel. The contact resistance,  $R_C$ , must be included in the modeling of such a structure.

On the other hand, an upper bound for the 2DEG conductivity can be estimated by considering the extreme case where the 2DEG conductivity is equal to the total conductivity (no parallel conduction case). The true conductivity curve of the 2DEG is between these two boundaries: from the conductivity data at zero field we determined the lower and upper bounds for 2DEG mobility as  $32,400 \text{ cm}^2/\text{Vs}$  and  $39,400 \text{ cm}^2/\text{Vs}$ , respectively. The true 2DEG mobility is between these limits, most probably closer to the lower bound.

The derived carrier density and mobility values for the 2DEG are  $1.4 \times 10^{13} \text{ cm}^{-2}$  and  $\sim 18,000 \text{ cm}^2/\text{Vs}$ , respectively. The bulk electron carrier density of the parallel channel was calculated as  $3.1 \times 10^{14} \text{ cm}^{-2}$  with a mobility of  $1100 \text{ cm}^2/\text{Vs}$ . We note that

the carrier density of the 2DEG is significantly larger than that of the control samples as the parallel channel is far below ( $\sim 5 \mu\text{m}$ ) the 2DEG channel. The annealed Ohmic metal contacts are expected to extend only to the vicinity of the 2DEG layer, causing the contact resistance to the parallel channel to be relatively large (about  $10^2$ - $10^3 \Omega$  for the parallel channel). As a result, in our measurements the contribution of the parallel channel is suppressed in the Hall bar structures containing both the 2DEG and the parallel conducting channel.

#### 4.4 Modeling of contact resistances in Hall bar samples

In Fig. 4.10, to model the real Hall bar samples, we assume the contact resistances,  $R$ , exist only between ohmic contacts of two conducting channels and are the same for all six leads in Hall bar. The resistance of the ohmic contacts can be negligible in this model. The sizes of the Hall bar are labeled as  $W_1$ ,  $W_2$ ,  $W_3$ ,  $L_1$ , and  $L_2$  in the figure, and the current densities are  $J_{1x}$ ,  $J_{1y}$ ,  $J_{2x}$ ,  $J_{2y}$ ,  $J_{3x}$ ,  $J_{3y}$ ,  $J_{4x}$  and  $J_{4y}$ . The electrical fields of the two channels are  $E_{1x}$ ,  $E_{1y}$ ,  $E_{2x}$ , and  $E_{2y}$ , and the resistivities in the two channels are  $\rho_{1xx}$ ,  $\rho_{1xy}$ ,  $\rho_{2xx}$  and  $\rho_{2xy}$ . The equations for this model are as follows:

$$\begin{aligned}
 & (J_{1y} + J_{2y}) \left\{ \left( W_3 + \frac{W_1}{2} \right) (\rho_{1xx} + \rho_{2xx}) + W_2 R \right\} + \rho_{1xy} \left[ 2J_{1x} + (J_{1y} - J_{2y}) \frac{W_2}{W_1} \right] \frac{W_1}{2} \\
 &= \rho_{2xy} \left[ 2J_{2x} + (J_{2y} - J_{1y}) \frac{W_2}{W_1} \right] \frac{W_1}{2} \\
 \rho_{1xx} J_{1x} (L_2 + \frac{W_2}{2}) &= J_{2x} W_1 R + \rho_{2xx} J_{2x} (L_2 + \frac{W_2}{2}) + J_{1y} W_2 R - (2J_{2x} + (J_{2y} - J_{1y}) \frac{W_2}{W_1}) \rho_{2xy} W_1 / 4 \\
 &+ (2J_{1x} + (J_{1y} - J_{2y}) \frac{W_2}{W_1}) \rho_{1xy} W_1 / 4 + \left( \frac{W_1}{2} + W_2 \right) J_{1y} (\rho_{2xx} + \rho_{1xx}) + \frac{W_2}{4} (J_{1y} + J_{2y}) (\rho_{1xy} - \rho_{2xy})
 \end{aligned}$$

$$\begin{aligned}
& \rho_{1xx} J_{1x} \left( L_2 + \frac{W_2}{2} \right) + \left( J_{1x} + (J_{1y} - J_{2y}) \frac{W_2}{W_1} \right) (W_2 + L_1) \rho_{1xx} - \left( J_{1y} + J_{2y} \right) \rho_{1xy} \frac{W_2}{2} = \\
& J_{2x} \left( W_2 R + \rho_{2xx} (W_2 + L_2) \right) + \left( J_{2x} + (J_{2y} - J_{1y}) \frac{W_2}{W_1} \right) (W_2 / 2 + L_1) \rho_{2xx} + \left( J_{1y} + J_{2y} \right) \rho_{2xy} \frac{W_2}{2} \\
& + \left( \frac{W_1}{2} + W_3 \right) J_{3y} (\rho_{2xx} + \rho_{1xx}) + J_{3y} W_2 R + \left( 2J_{1x} + (2J_{1y} - 2J_{2y} + J_{3y} - J_{4y}) \frac{W_2}{W_1} \right) \rho_{1xy} W_1 / 4 \\
& - \left( 2J_{2x} + (2J_{2y} - 2J_{1y} + J_{4y} - J_{3y}) \frac{W_2}{W_1} \right) \rho_{2xy} W_1 / 4 \\
& (2J_{1x} + (2J_{1y} - 2J_{2y} + J_{3y} - J_{4y}) \frac{W_2}{W_1}) \rho_{1xy} W_1 / 2 + \left( J_{4y} + J_{3y} \right) \left( \rho_{2xx} + \rho_{1xx} \right) \left( \frac{W_1}{2} + W_3 \right) + W_2 R \\
& = (2J_{2x} + (2J_{2y} - 2J_{1y} + J_{4y} - J_{3y}) \frac{W_2}{W_1}) \rho_{2xy} W_1 / 2 \\
& (J_{1x} + (J_{1y} - J_{2y} + J_{3y} - J_{4y}) \frac{W_2}{W_1}) \rho_{1xx} \left( L_2 + \frac{W_2}{2} \right) - \left( J_{3y} + J_{4y} \right) \rho_{1xy} \frac{W_2}{4} \\
& = (2J_{1x} + (2J_{1y} - 2J_{2y} + J_{3y} - J_{4y}) \frac{W_2}{W_1}) \rho_{1xy} W_1 / 4 + J_{4y} (W_2 R + (\rho_{2xx} + \rho_{1xx})(W_3 + W_1 / 2)) \\
& - (2J_{2x} + (2J_{2y} - 2J_{1y} + J_{4y} - J_{3y}) \frac{W_2}{W_1}) \rho_{2xy} W_1 / 4 \\
& + (J_{2x} - (J_{1y} - J_{2y} + J_{3y} - J_{4y}) \frac{W_2}{W_1}) \left( \rho_{2xx} \left( L_2 + \frac{W_2}{2} \right) + W_1 R \right) - \left( J_{3y} + J_{4y} \right) \rho_{2xy} \frac{W_2}{4}
\end{aligned} \tag{4.4}$$

The analytical solution for those equations are extremely complicated, hence we extracted the solution by solving the equations numerically in Mathematica. In the simulation, we took  $W_1=W_2=100$   $\mu\text{m}$ ,  $W_3=L_3=300$   $\mu\text{m}$ , and  $L_1=700$   $\mu\text{m}$ . For the first 2DEG channel we took  $\rho_{1xx}=50$   $\Omega$ ,  $\rho_{1xy}=100 \times B$   $\Omega$ , and for the second 2DEG channel  $\rho_{2xx}=50$   $\Omega$  and  $\rho_{2xy}=5 \times B$   $\Omega$ , where  $B$  is the magnetic field in the unit of Tesla (see Fig. 4.10).

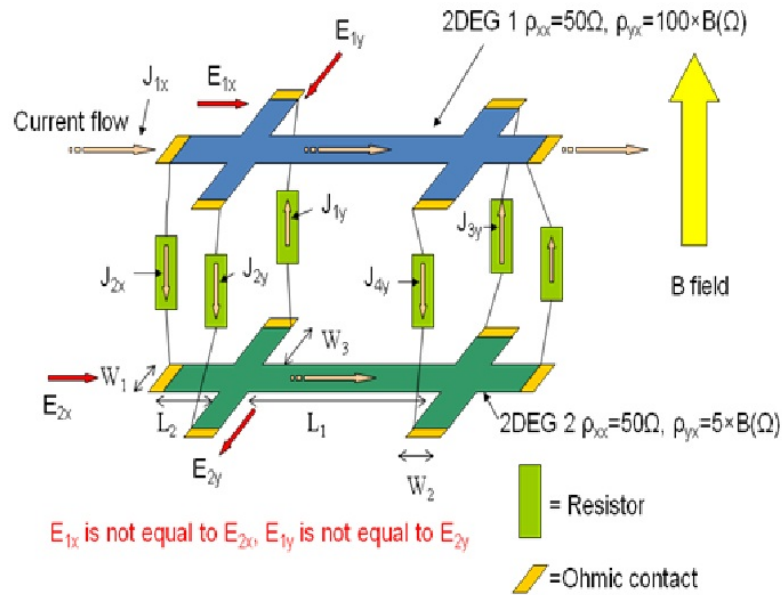


**Fig.4.10:** Diagram for contact resistances model in a symmetric Hall bar samples. For simplicity, we assume the contact resistances,  $R$ , exist only between the Ohmic contacts of two conducting channels and are same for all six leads in the Hall bar. The sizes of the Hall bar are labeled as  $W_1$ ,  $W_2$ ,  $W_3$ ,  $L_1$ , and  $L_2$  in the figure. The current densities are  $J_{1x}$ ,  $J_{1y}$ ,  $J_{2x}$ ,  $J_{2y}$ ,  $J_{3x}$ ,  $J_{3y}$ ,  $J_{4x}$  and  $J_{4y}$ . The electrical fields of in two channels are  $E_{1x}$ ,  $E_{1y}$ ,  $E_{2x}$ , and  $E_{2y}$ . Finally, the longitudinal and Hall resistivities in two channels are  $\rho_{1xx}$ ,  $\rho_{1xy}$ ,  $\rho_{2xx}$  and  $\rho_{2xy}$ .

The results for contact resistance  $R=0\ \Omega$ ,  $R=100\ \Omega$ , and  $R=10000\ \Omega$  were plotted in the Fig 4.11 (a) (b) and (c), respectively. In the figure, the  $\rho_{xy}$  deviated from linear behavior at high magnetic field for the  $R=0\ \Omega$  and  $R=100\ \Omega$  cases, which is similar to what we observed in experiment. For  $R=10\ 000\ \Omega$ , the contact resistance is much larger than 2DEG's resistance, thus the second 2DEG can be considered as insulated from the first 2DEG. Therefore, the simulated  $\rho_{xx}$  and  $\rho_{xy}$  are just the resistivity of the first 2DEG.

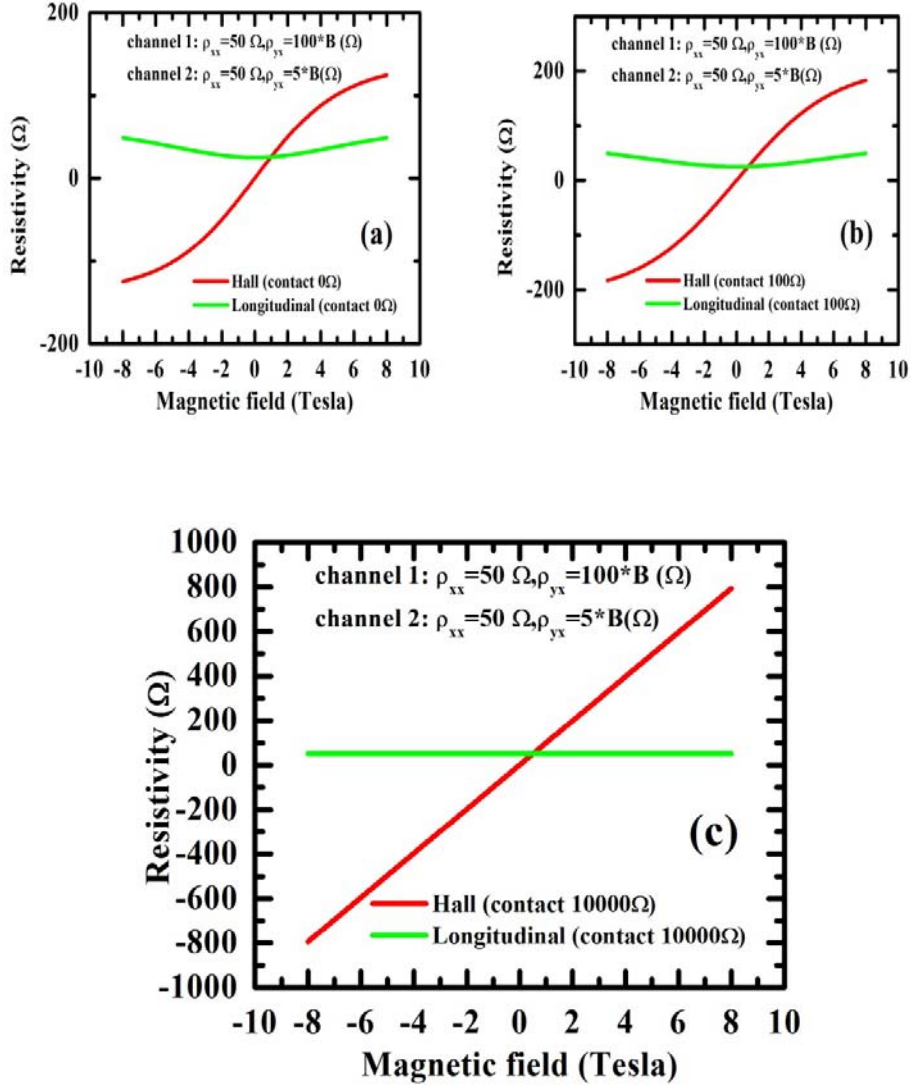


**Fig.4.11:** Simulation results of  $\rho_{xx}$  and  $\rho_{xy}$  versus magnetic field in Hall bar. (a): Contact resistance  $R=0 \Omega$ . (b): Contact resistance  $R=100 \Omega$ . (c): Contact resistance  $R=10000 \Omega$ .

The  $\rho_{xy}$  curves for low contact resistance ( $<1000 \Omega$ ) is much similar to our observed data for the SiN-GaN sample. To further demonstrate this similarity, we chose the simulated data for  $R=100 \Omega$  and did the same conductivity analysis that we did for the SiN-GaN data. The results are plotted in Fig. 4.12.

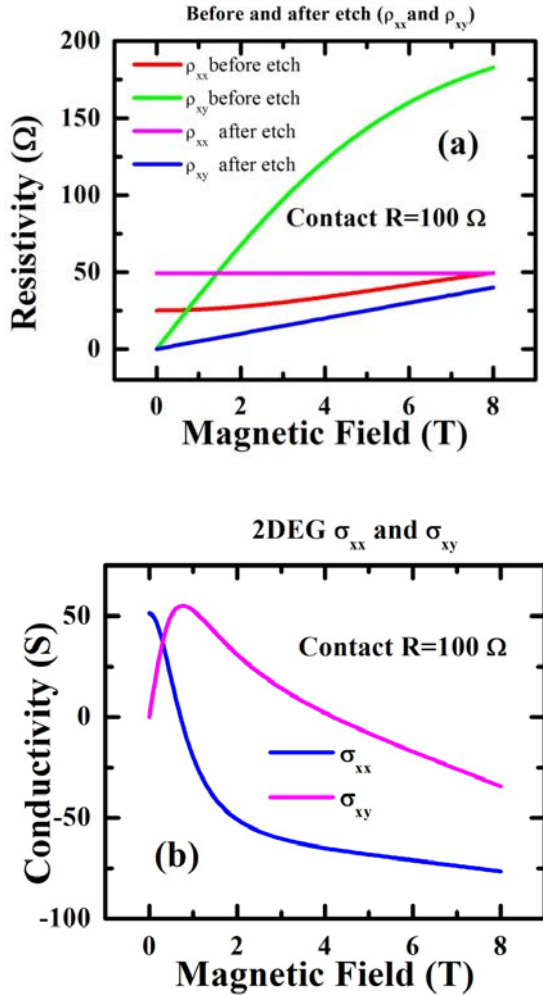


**Fig.4.12:** Resistivity and conductivity versus magnetic field for two 2DEG channels with contact resistance  $R=100 \Omega$ . (a) Simulated  $\rho_{xx}$  and  $\rho_{xy}$  data versus magnetic field before and after the first 2DEG etched. (b) The resulting conductivity versus magnetic field obtained by subtracting the second 2DEG's conductivity from the first 2DEG's conductivity. The  $\sigma_{xx}$  curve is negative beyond 1 Tesla.

In Fig. 4.12 (a), the simulated  $\rho_{xx}$  and  $\rho_{xy}$  data before and after the first 2DEG etched are shown. We converted this data into conductivity and subtracted the data after the etching from the data before the etching. The resulting conductivity  $\sigma_{xx}$  and  $\sigma_{xy}$  are shown in Fig.4.12 (b). We notice that the  $\sigma_{xx}$  curve is negative beyond 1 Tesla, which is similar to the data we observed in the SiN-GaN sample. The simulation confirmed that

we had the contact resistances between 2DEG and parasitic channel, and that it is the reason we saw a negative  $\sigma_{xx}$  curve for the subtracted  $\sigma_{xx}$  data in the SiN-GaN sample.

We modeled our structure as a two-layer channel with a finite contact resistance in between. Using the experimental resistivity and carrier density values, we arrived at similar negative conductivity for  $B>1$  T, which is compatible with our experimental findings. Due to the contact resistances, the 2DEG mobility value we calculated actually represents a lower bound on mobility. If the contact resistance were zero, the extracted 2DEG conductivity would be larger, leading to a higher mobility. At this point we can safely state that the 2DEG on the SiN-GaN template exhibits an electron mobility of at least 32,400 cm<sup>2</sup>/Vs. This value represents an enhancement of more than 60% over the mobility for the reference 2DEG sample with similar carrier density.

When we compare the results for the parallel conduction, the mobility and carrier density are in reasonable agreement. From the reference sample results, we know that bulk electrons freeze out in u-GaN at low temperatures. The high electron density at 1.6 K suggests that the parallel conduction occurs in the heavily-doped SiN<sub>x</sub> layer. We suggest that the porous SiN<sub>x</sub> layer supplies a sufficient density of Si atoms to the bottom face of the overgrown GaN epilayer, resulting in the formation of a degenerate impurity band. Such a degenerately doped layer would not exhibit carrier freeze-out, which is the case for our sample. Thus, we believe that parallel conduction at 1.6 K is due to a highly degenerate impurity band in the heavily Si-doped GaN region at the GaN/SiN<sub>x</sub> interface.

#### 4.5 Magnetotransport measurements in ELO-GaN samples

Two different Hall bars were fabricated on the  $\text{Al}_{0.20}\text{Ga}_{0.80}\text{N}/\text{AlN}/\text{GaN}$  sample grown on ELO-GaN template. One Hall bar was aligned to be parallel to the  $\text{SiO}_2$  stripes (parallel sample), whereas in the other Hall bar the  $\text{SiO}_2$  stripes were perpendicularly aligned (perpendicular sample). Our aim was to investigate the orientation dependence of electron transport in a 2DEG on ELO-GaN template. As in the case of the SiN-GaN sample, measurements were carried out at 1.6 K, before and after the recess-etch.

Figure 4.13 shows the longitudinal and Hall resistivity curves measured for the parallel Hall bar before and after the recess etch. The resistivity increased after the 2DEG was removed, which is the result of decreased conductivity. As with the SiN-GaN sample, to estimate the electron mobility we had to repeat the longitudinal and Hall resistance measurements after the removal of the 2DEG. The Hall resistance obtained after etching gives the bulk electron density of ELO-GaN template to be  $7.1 \times 10^{13} \text{ cm}^{-2}$ . The Hall mobility of this parallel channel was determined to be 1550  $\text{cm}^2/\text{Vs}$ . Although not as high as in the SiN-GaN sample, a high carrier density parallel channel exists in the ELO-GaN sample as well. The source for the parallel conduction in ELO-GaN samples can be attributed to the  $\text{SiO}_2$  mask layers due to the formation of a degenerately doped layer by diffusion of Si atoms into the ELO-GaN, which did not show carrier freeze-out at low temperature. The 2DEG conductivity was extracted by subtracting the bulk conductivity from the total conductivity. The corresponding conductivity curves are plotted in Figure 4.13. Similar to the SiN-GaN sample, the

2DEG conductivity became negative for  $B > 1$  T, which may be attributed to the unknown contact resistances of the parallel channel.

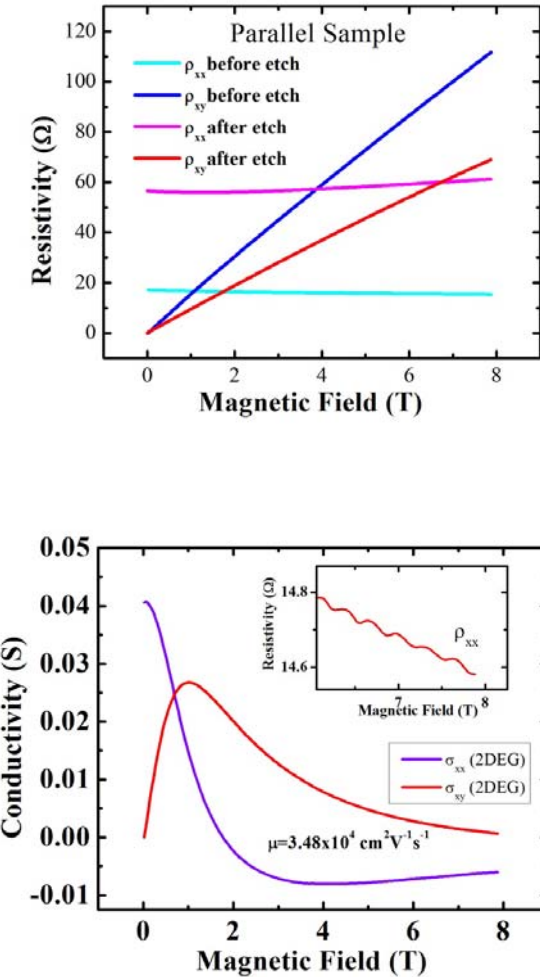


**Fig.4.13:** Top: SdH and Hall resistivity versus magnetic field measured at 1.6 K for the parallel Hall-bar sample fabricated on  $\text{Al}_{0.20}\text{Ga}_{0.80}\text{N}/\text{AlN}/\text{GaN}$  grown on ELO-GaN template before and after recess etch. Bottom: extracted 2DEG conductivity versus magnetic field with SdH oscillations shown in the insert.

The magnetoresistance data for the perpendicular ELO-GaN sample before and after the recess etch measured at 1.6 K is shown in Fig. 4.14. Clear single-period SdH oscillations were observed before etching which disappeared after removal of 2DEG.

The longitudinal resistance increased after etching. To find the 2DEG conductivity, we subtracted the parallel channel (etched sample) conductivity from the total (pre-etch sample) conductivity. Figure 4.14 shows the extracted 2DEG conductivity curves.

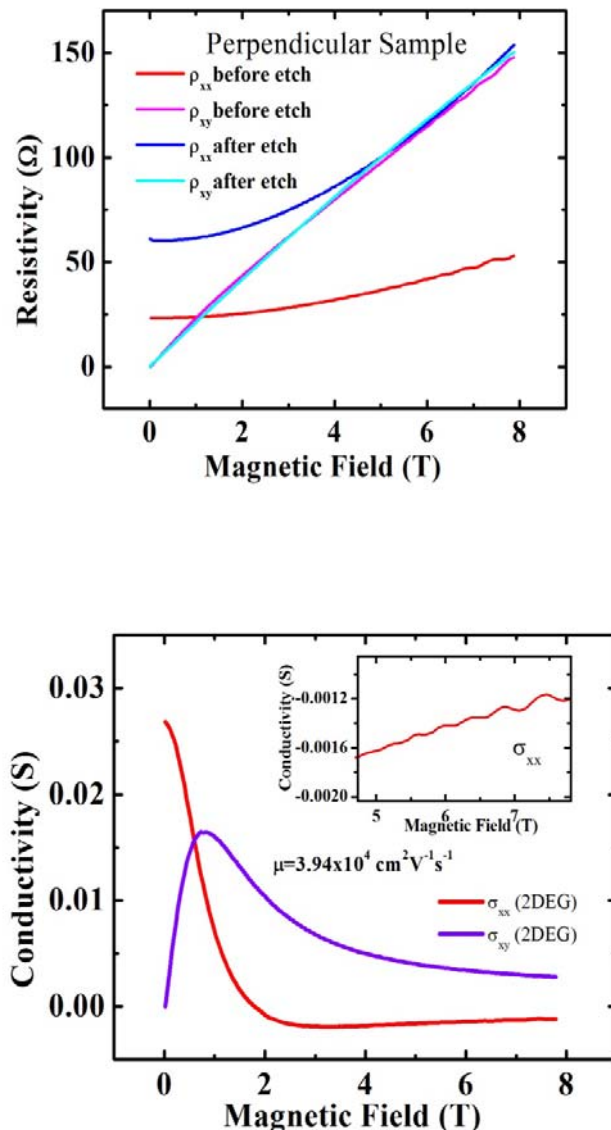


**Fig.4.14:** Top: Measured SdH and Hall resistivity versus magnetic field at 1.6 K for the perpendicular Hall bar sample fabricated on  $\text{Al}_{0.20}\text{Ga}_{0.80}\text{N}/\text{AlN}/\text{GaN}$  grown on ELO-GaN template before and after recess etch. Bottom: 2DEG Conductivity versus magnetic field with SdH oscillations shown in the insert.

The extracted conductivity data for 2DEG lead to a lower-bound mobility of  $39,400 \text{ cm}^2/\text{Vs}$ . The estimated lower-bound for the 2DEG electron mobility represents a more than two-fold enhancement with respect to the reference 2DEG samples. When we calculate the upper limit of the 2DEG mobility using the pre-etch conductivity data, we obtain  $63,500 \text{ cm}^2/\text{Vs}$ . The parallel channel exhibited a carrier density of  $3.3 \times 10^{13} \text{ cm}^{-2}$  along with a bulk electron mobility of  $3120 \text{ cm}^2/\text{Vs}$ . When compared with the bulk conduction of the parallel ELO-GaN sample, we note that the parallel bulk conduction also shows orientation dependence. For this sample, the bulk carrier density is smaller and shows higher electron mobility.

#### 4.6 Summary

The results of the mobility and carrier density values achieved with the AlGaN/GaN control sample, SiN-GaN, and ELO-GaN samples are summarized in Figure 4.15.

Lower-bound mobilities of  $40,700 \text{ cm}^2/\text{Vs}$  and  $32,400 \text{ cm}^2/\text{Vs}$  were extracted for 2DEG samples grown on ELO-GaN and SiN-GaN templates, respectively. The improvement in the electron mobility in 2DEG structures grown on lateral overgrown templates is obvious. Both SiN-GaN and ELO-GaN templates with reduced threading dislocation densities helped to increase the low-temperature electron mobility in the overgrown 2DEG structures. The results show that both *in situ* grown SiN<sub>x</sub> and *ex situ* grown SiO<sub>2</sub> masking layers effectively block the threading dislocations. We can safely state that the mobility enhancement factor is around 2 or higher; however, we currently

do not know the exact mobility values of these samples due to the unknown contact resistances to the parallel channel.

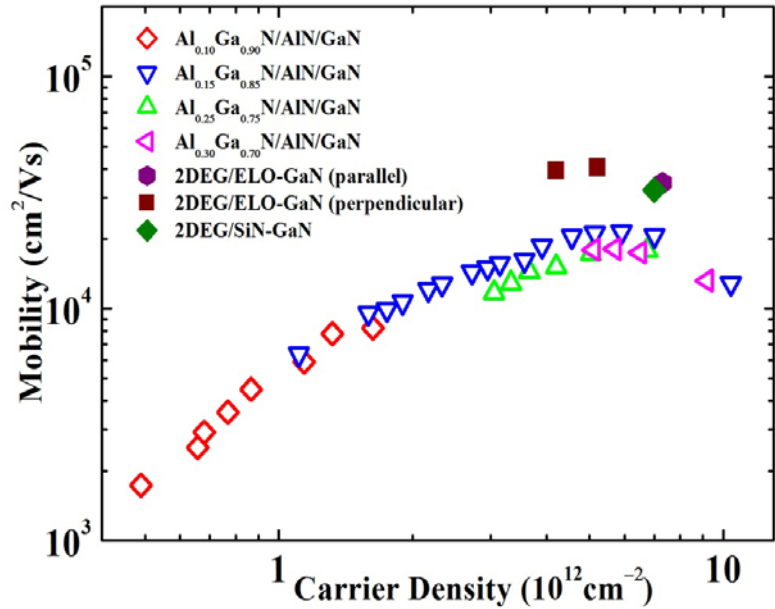


**Fig.4.15:** Experimental electron mobility versus carrier density data extracted from  $\text{Al}_x\text{Ga}_{1-x}\text{N}/\text{AlN}/\text{GaN}$  2DEG samples grown on conventional u-GaN (reference), SiN-GaN, and ELO-GaN templates. All samples were measured at 1.6 K.

The 2DEG samples grown on conventional u-GaN templates demonstrated electron mobilities up to  $20,000 \text{ cm}^2/\text{Vs}$ . The peak occurs around  $6 \times 10^{12} \text{ cm}^{-2}$  in the mobility curve for the reference samples and the mobility decreases for higher carrier densities due to alloy scattering caused by increased Al mole fraction and interface roughness scattering. The laterally overgrown GaN 2DEG samples show lower-bound mobility values higher than  $40,000 \text{ cm}^2/\text{Vs}$ . Finally, the trend shows that the mobility curve will increase toward lower carrier density regime and peaks in the low  $10^{12} \text{ cm}^{-2}$ s due to the reduced charged-dislocation scattering in these samples.

## CHAPTER 5

### SPIN-ORBIT INTERACTION IN GaN HETEROSTRUCTURES

#### 5.1 Spin-Orbit Interaction in Semiconductors

Spin-Orbit (SO) interaction in atomic physics has a Pauli SO term as

$$H_{SO} = -\frac{\hbar}{4m_0^2 c^2} \vec{\sigma} \cdot \vec{p} \times (\nabla V_0), \quad (5.1)$$

where  $\hbar$  is the Planck's constant,  $m_0$  is the mass of an electron,  $c$  is the light speed,  $\vec{p}$  is the momentum operator,  $V_0$  is the potential term and  $\vec{\sigma}$  is the Pauli spin matrices. In semiconductors, SO coupling[69] can have a profound effect on energy structure due to the momentum operator,  $\vec{p}$ . A famous example is the splitting of the topmost valence band in GaAs. In a semiconductor, without considering SO effect, usually the elementary model for band structure of a direct semiconductor will have results as

$$H_{c/v}(\vec{k}) = \pm \left( \frac{E_g}{2} + \frac{\hbar^2 k^2}{2m^*} \right) \quad (5.2)$$

where  $\vec{k}$  is the wave vector,  $E_g$  is the band gap, and  $m^*$  is the effective mass of conduction or valence band. When more information about band structure is needed, usually  $\mathbf{k}\cdot\mathbf{p}$  method[10] is used as the theoretical tool to explore the band structure of semiconductors. In  $\mathbf{k}\cdot\mathbf{p}$  frame, the Schrodinger equation will be expanded for Bloch functions  $e^{ikr} u_{vk}(r)$  as

$$\left[ \frac{p^2}{2m_0} + V_0(r) + \frac{\hbar^2 k^2}{2m_0} + \frac{\hbar}{m_0} \vec{k} \cdot \vec{p} \right] u_{vk}(r) = E_v(k) u_{vk}(r) \quad (5.3)$$

Including the SO coupling, this equation will become

$$\left[ \frac{p^2}{2m_0} + V_0(r) + \frac{\hbar^2 k^2}{2m_0} + \frac{\hbar}{m_0} \vec{k} \cdot (\vec{p} + \frac{\hbar}{4m_0 c^2} \vec{\sigma} \times \nabla V_0) + \frac{\hbar}{4m_0^2 c^2} \vec{p} \cdot \vec{\sigma} \times (\nabla V_0) \right] u_{vk}(r) = E_v(k) u_{vk}(r) \quad (5.4)$$

From above equations, we can see that SO coupling is important to understand some fundamental processes in semiconductors, such as spin coherence and band structure splitting.

## 5.2 Spin-Orbit Coupling in AlGaN/GaN heterostructures

The successful implementation of spintronics [70] devices relies heavily on the availability of right materials systems. GaN based devices attracted research attention due to its excellent performance in high frequency, high RF and high temperature applications[22], the maturity of growth and fabrication technique and the prediction of above room temperature ferromagnetism in GaN based dilute magnetic semiconductors[71]. In this context, the study of spin processes in GaN is crucial for GaN based spintronics device performance in a controllable manner. Spin-orbit interactions[72] induces the spin relaxation in low dimensional semiconductor systems and can be potentially controlled to manipulate the spin process in spintronic devices[73]. These are challenging tasks, since spin is not a conserved quantity in semiconductor heterostructures; therefore, it is essential to understand the spin-orbit coupling and the associated zero-field electron spin-splitting in GaN based 2 dimensional (2D) electron systems.

It is well known that the spin-splitting for a 2D electron system originates from both the structural inversion asymmetry (SIA), i.e. Rashba term, of the quantum well

(QW) [74] as well as the bulk inversion asymmetry (BIA) of the crystal [75-76]. The spin-splitting arising from the SIA, known as the Rashba effect, scales linearly with the Fermi wavevector,  $k_F$ , whereas there are two terms associated with BIA effect for a wurtzite structure: one scales as  $k_F$  and the other scales as  $k_F^3$  and is anisotropic in the plane of QW[77-78]. The Rashba coupling is of particular interest for gate controlled spin transistor applications[73] and the  $k_F$  linear BIA spin-orbit term is only specific to a wurzite (W) bulk crystal and does not exist in zinc-blende (ZB) structure. However, in a c-axis-oriented W-structure 2D system, both SIA effect and BIA effect have similar terms in effective spin-orbit coupling Hamiltonians[74]. The contributions of these terms have not been measured independently for the GaN/AlGaN heterostructures; therefore, it remains a challenging task to differentiate the contribution from SIA and BIA effect in W-structure materials. Recently, zero-field spin-orbit splitting parameter has been calculated theoretically in wurtzite GaN/AlGaN heterostructures and a large spin orbit coupling is predicted due to strong polarization field at the interface and polarization-induced doping [78-80]. However, in Ref.[80], the BIA coupling coefficients in III-nitrides were estimated from parameters of other semiconductor materials and only an effective linear coupling coefficient was obtained. BIA terms were expected to be larger than SIA term in III-nitride QW [80]; which means effective cubic BIA term scaling with  $k_F^3$  is not negligible in W-GaN QW systems especially when carrier density is high. Furthermore, there have been conflicting reports on the size of spin-splitting energies based on beat patterns of the Shubnikov-de Haas (SdH) oscillations [81].

### 5.3 Weak Antilocalization measurements in AlGaN/GaN heterostructures

To extract the SO coupling parameters, we use the weak antilocalization (WAL) measurements instead [77-78,82]. WAL measurements, which are reliable for studying the spin-orbit coupling, have been consistent with each other and revealed that the spin splitting energies scale linearly with  $k_F$  at low carrier densities. One of our goals is to extend the WAL measurements to higher carrier densities and report the contribution of the cubic  $k_F^3$  term from BIA effect in  $\text{Al}_x\text{Ga}_{1-x}\text{N}/\text{AlN}/\text{GaN}$  heterostructures.

We use  $\text{Al}_x\text{Ga}_{1-x}\text{N}/\text{AlN}/\text{GaN}$  heterostructures with a wide range of carrier densities in this experiment. The heterostructures were all grown by metalorganic vapor phase epitaxy [68] on c-plane sapphire substrates and consist of the following layers: a 3  $\mu\text{m}$  GaN buffer layer, a 1 nm AlN interfacial layer, a 25 nm  $\text{Al}_x\text{Ga}_{1-x}\text{N}$  layer and a 3 nm GaN cap layer where the Al composition  $x$  ranged from 0.1 to 0.35. All layers were undoped and the 2DEG is induced by spontaneous and piezoelectric polarization effects just below the AlN interfacial layer, which was used to suppress alloy scattering. To study the magnetotransport properties, 600  $\mu\text{m}$  long 100  $\mu\text{m}$  Hall bar structures were fabricated by photolithography followed by dry etching. Ti/Al/Ti/Au contacts annealed at 900 °C were then used to form Ohmic contacts to the 2DEG. The Hall bar samples A, B, C, D, and E were fabricated using heterostructures with Al composition  $x=0.1, 0.15, 0.25, 0.3$  and 0.35, respectively. We also fabricated a gated Hall bar structure, sample F, which is identical to sample E except a metal gate was deposited on the heterostructure to vary the carrier density of 2D electrons.

The samples are characterized by magnetoresistance and Hall measurements in a variable temperature cryostat with a base temperature of 1.6 K. Carrier density

extracted from Hall and Shubnikov-de Hass (SdH) oscillations (see Fig 5.1) were in agreement with each other.

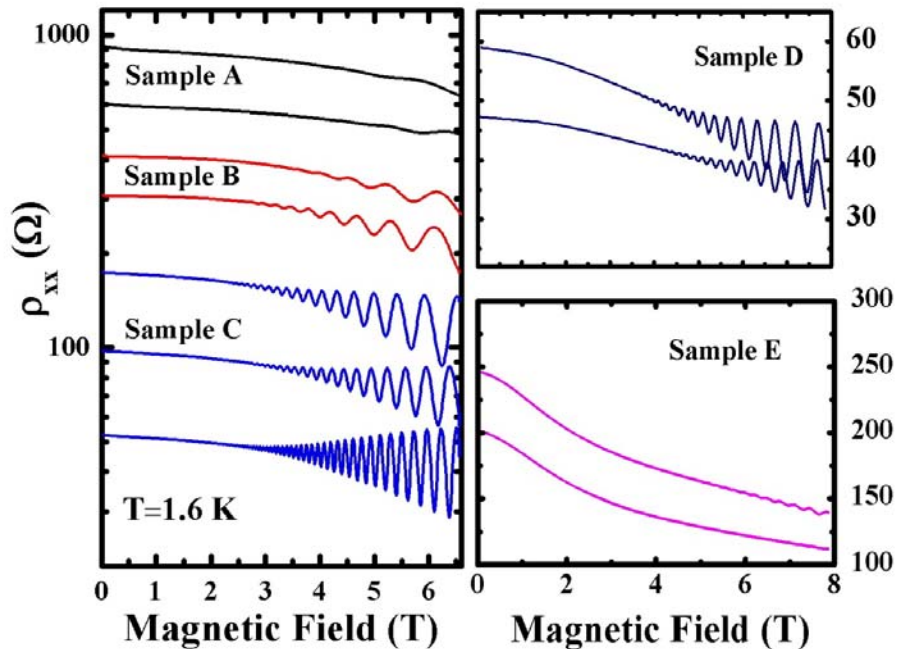


**Fig.5.1:** Longitudinal resistivity versus magnetic field traces for five samples with different carrier densities at 1.6 K. The carrier density of each sample is changed by the use of persistent photoconductivity effect.

By employing the persistent photoconductivity effect in sample A to E [68], we were able to vary the carrier density of the samples in a controllable manner over the ranges of  $0.8-1.3 \times 10^{12} \text{ cm}^{-2}$ ,  $1.7-4.9 \times 10^{12} \text{ cm}^{-2}$ ,  $3.1-6.7 \times 10^{12} \text{ cm}^{-2}$ ,  $5.3-8.9 \times 10^{12} \text{ cm}^{-2}$ , and  $8.1-10.6 \times 10^{12} \text{ cm}^{-2}$  for the five heterostructures, respectively [78] at 1.8 K. In sample F, by applying a gate voltage from -1900 mV to 300 mV, we were able to cover a carrier density range of  $9.3-10.6 \times 10^{12} \text{ cm}^{-2}$ . As expected, the sample with highest Al concentration,  $x=0.35$ , had the highest carrier density. In terms of mobility, Sample B,

with the Al concentration of  $x=0.15$ , had the highest electron mobility of  $\mu=20,300 \text{ cm}^2/\text{V}\cdot\text{s}$  at a carrier concentration of  $n = 4.9 \times 10^{12} \text{ cm}^{-2}$  at 4.2 K [78].

To extract the spin-orbit coupling and the associated spin-splitting energies, we measured quantum corrections to conductance at low magnetic fields. Typical traces of magnetoconductivity after the subtraction of the zero field background,  $\Delta\sigma = \sigma(B) - \sigma(0)$ , obtained from two samples are shown in Fig. 5.2 (a-b).

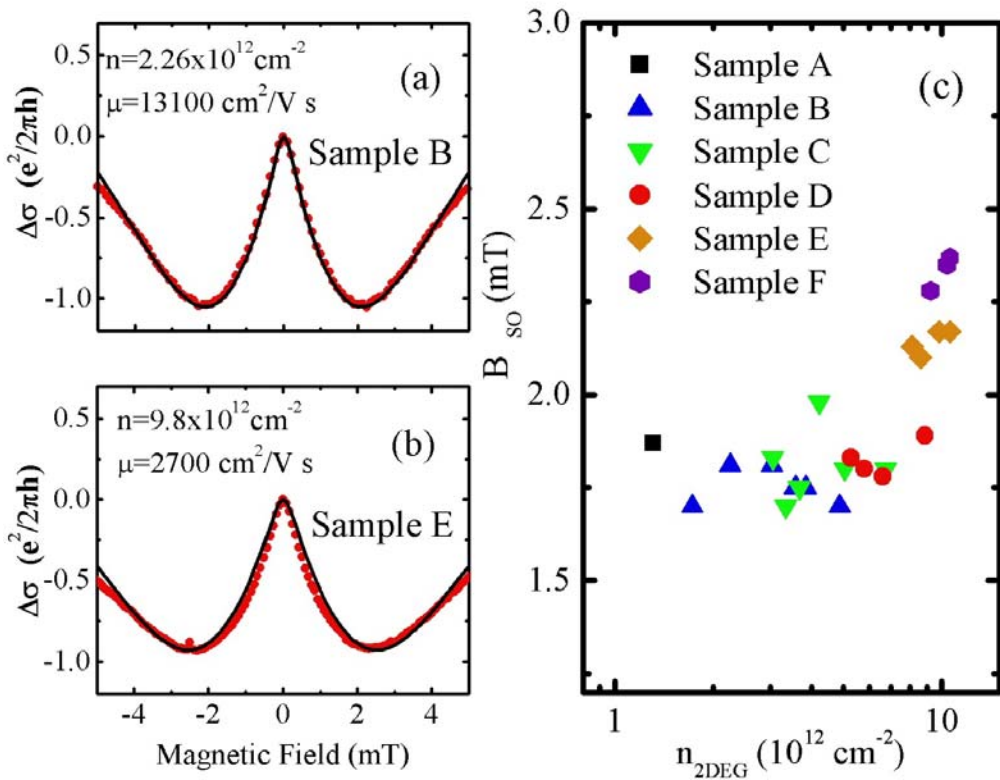


**Fig.5.2:** (a) and (b) Conductivity after the subtraction of the zero field background of two samples versus magnetic field at  $T=1.6$  K. The solid lines are theoretical fits to the data. (c)  $B_{so}$  extracted from WAL fits versus carrier density for six samples.

There is a clear WAL behavior at magnetic fields below 2 mT at 1.8 K. This feature arises from the quantum interference of spin-dephased paths and can be used to quantify spin-orbit coupling in semiconductors. The size of WAL feature is strongly

temperature dependent and decreases with increasing temperature, whereas the width of the peak does not vary with temperature.

#### 5.4 Spin-splitting energy in AlGaN/GaN heterostructures

We analyzed the WAL by using the Iordanskii, Lyanda-Geller, and Pikus (ILP) equations [83]. For each sample, we determine the elastic scattering time  $\tau_{tr}$ , the diffusion constant  $D = v_F^2 \tau_{tr} / 2$ , and the characteristic transport field  $B_{tr} = \hbar / 4eD\tau_{tr}$  using the measured values of carrier density and mobility. A typical transport field,  $B_{tr}$ , is around 7 mT in our experiment. We fit the data with two adjustable parameters, the spin-orbit field  $B_{SO} = \hbar / 4eD\tau_{SO}$  and the phase coherence field  $B_\phi = \hbar / 4eD\tau_\phi$ , where  $\tau_{SO}$  and  $\tau_\phi$  are the spin-orbit and phase coherence times, respectively. For the traces shown in Fig. 5.2 (a-b), best fits are obtained using  $B_{SO} = 1.81$  and  $2.17$  mT and  $B_\phi = 0.095$  and  $0.133$  mT, for samples B and E, respectively.

In Fig. 5.2 (c) we show  $B_{SO}$  versus carrier density and a striking feature appears: As carrier density varies from  $1.7$  to  $10.6 \times 10^{12}$  cm<sup>-2</sup>,  $B_{SO}$  varies from  $1.7$  mT to  $2.37$  mT. Since  $B_{SO}$  is proportional to spin-orbit coupling parameter, roughly speaking, this observation indicates spin-orbit energy is no longer a linear function of  $k_F$  at high carrier density.

The spin-splitting energy,  $E_{ss} = 2\hbar\Omega$ , can be calculated from the spin-orbit field using the equation  $B_{SO} = (\hbar / 4eD)2\Omega^2\tau$ , where  $\Omega$  is the spin-orbit frequency. We plot the spin splitting energies extracted from all the samples, as a function of

Fermi wavevector  $k_F$ , in Fig. 5.3. At low carrier densities, the spin-splitting energy is expected to scale linearly with  $k_F$ . At higher carrier densities there should be a crossover to the cubic region. A deviation from the linear behavior is evident in the data shown in Fig. 5.3.

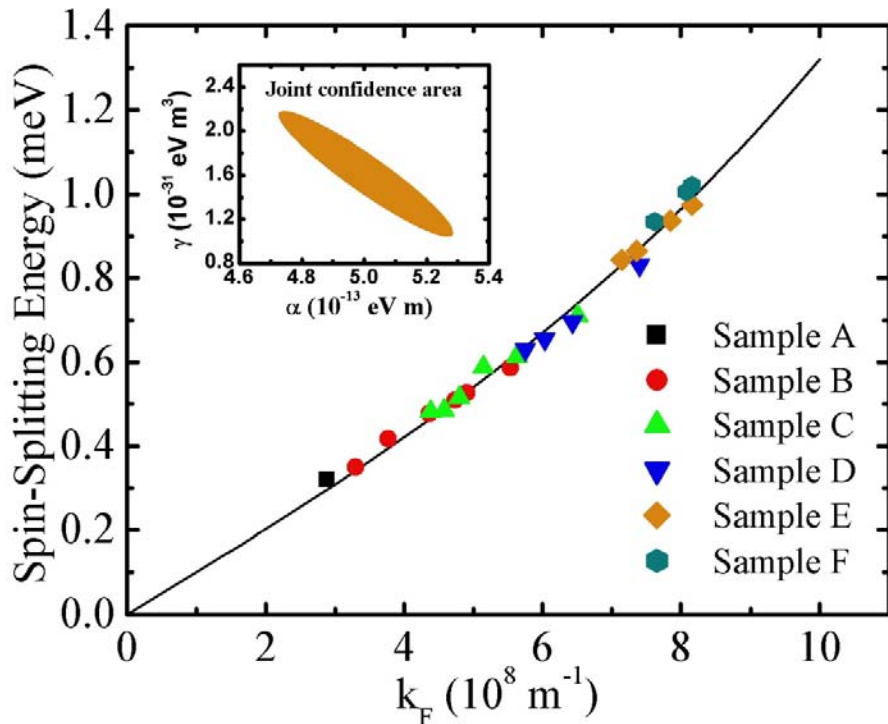


**Fig.5.3:** The spin splitting energy extracted from WAL measurements versus Fermi wavevector. The solid line is a fit to the data which includes both the linear and cubic terms for spin orbit interaction. The inset shows the 95% joint confidence area in the  $\alpha$ - $\gamma$  parameter space.

We should note that the Fermi wavevector is determined from the measured carrier density using  $k_F = \sqrt{2\pi n}$ , which assumes that the 2D electrons only occupy the lowest sublevel of the confinement potential. This assumption may no longer be valid

at high carrier densities ( $10^{13} \text{ cm}^{-2}$ ) where the second subband would start to be occupied. Thus, the actual  $k_F$  would be a bit smaller than that given by the equation, in which case the deviation from the linear behavior observed in Fig. 5.3 would get even more enhanced.

By fitting the data to a form  $E_{ss} = 2(\alpha k_F + \gamma k_F^3)$ , we extracted linear and cubic spin-orbit parameters of  $\alpha = 5.0 \pm 0.3 \times 10^{-13} \text{ eV} \cdot \text{m}$  and  $\gamma = 1.6 \pm 0.6 \times 10^{-31} \text{ eV} \cdot \text{m}^3$  respectively. This is the first measurement of the cubic spin-orbit parameter for the GaN/AlGaN system. We also show in the inset of Fig. 5.3 a 95% joint confidence area for the linear and cubic spin-orbit parameters based on statistical error analysis of our data. The joint confidence area is a tilted ellipsoid in the  $\alpha$ - $\gamma$  parameter space; for the 95% confidence region it covers a range of  $4.7\text{--}5.3 \times 10^{-13} \text{ eV} \cdot \text{m}$  in  $\alpha$  and  $0.9\text{--}2.2 \times 10^{-31} \text{ eV} \cdot \text{m}^3$  in  $\gamma$ .

For a W-Al<sub>x</sub>Ga<sub>1-x</sub>N/AlN/GaN heterostructure, both the SIA of the quantum well (Rashba term) and the BIA of the crystal contribute to the linear term. We note that we did not observe any significant difference in spin-splitting energies for sample E and F where the carrier density was varied by the persistent photoconductivity effect and by gating, respectively. This suggests that the spin-orbit coupling cannot be varied easily by gating in this material system. Further theoretical and experimental work is needed to quantify the individual contribution of BIA and SIA to the linear term. In contrast, the cubic spin-orbit parameter purely arises from the BIA of the crystal. We note that the cubic parameter of GaN extracted from our measurement is two orders of magnitude smaller than that of GaAs [84].

## 5.5 Phase Coherence in AlGaN/GaN heterostructures

In addition to spin-orbit parameters, we could also extract the information of the electron decoherence processes from the WAL measurements. The coherence of electrons is typically characterized by the use of phase coherence time,  $\tau_\phi$ , which determines the time scale over which the electron retains its quantum mechanical phase information. There has been renewed interest in understanding physical mechanisms for decoherence, especially within the context of quantum information processes. The phase coherence processes have not been studied in detail for the GaN system.

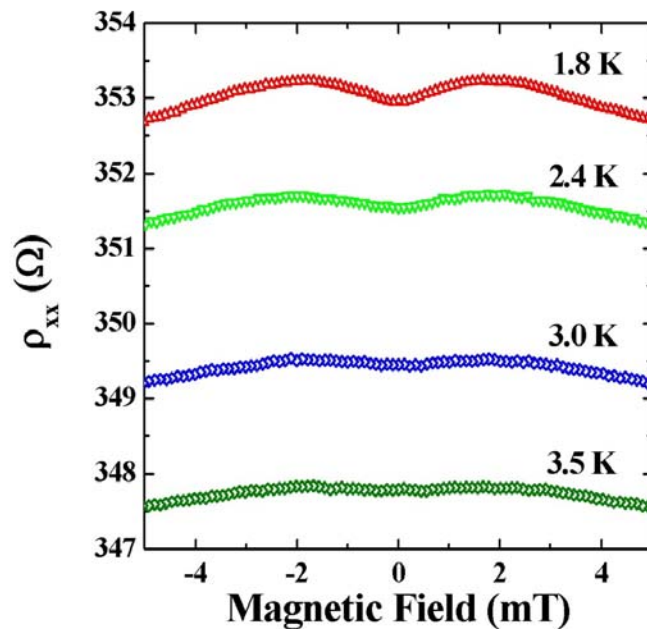


**Fig.5.4:** Raw data of resistance versus magnetic field for sample B at temperature from 1.8 K to 3.5 K. Notice in these measurements, the current passed through sample was 1  $\mu$ A to avoid sample heating.

The phase coherence process has a strong temperature dependence, which is shown in Fig. 5.4. As temperature increases, the phase coherence time,  $\tau_\phi$ , decrease rapidly due mostly to the increasing electron-electron interactions.

In Fig. 5.5 we display the WAL feature for three samples. Unlike the spin-orbit time, the phase coherence time is strongly temperature dependent. This is clearly evident in our data where the size of the WAL feature decreases with increasing temperature.

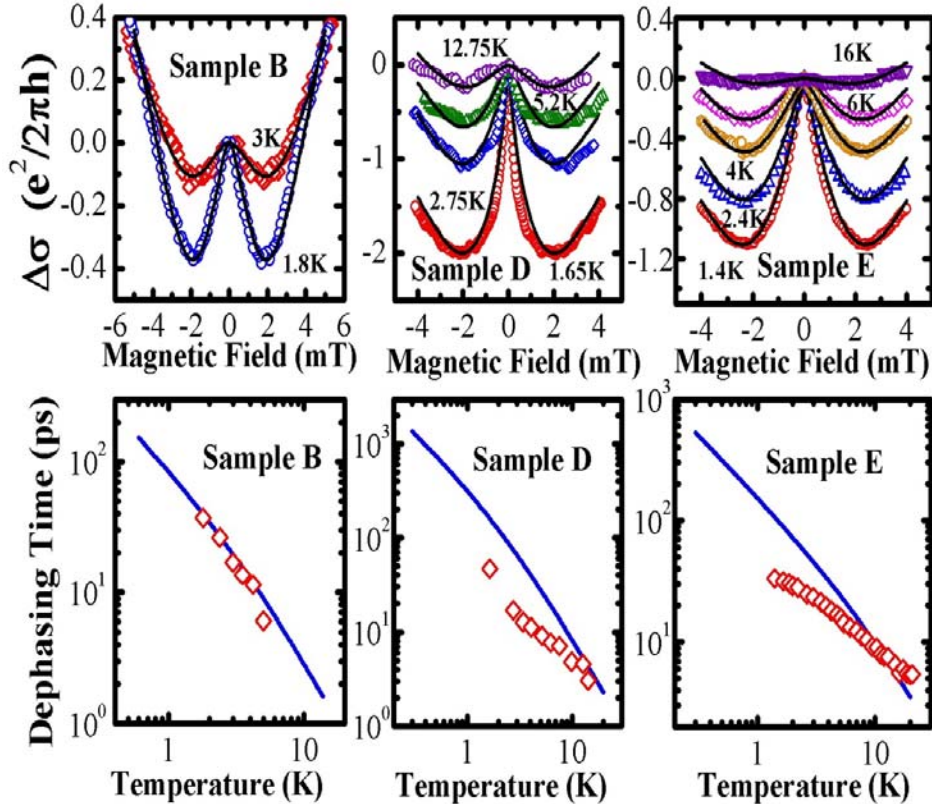


**Fig.5.5:** (Upper panels) Magnetoconductivity after the subtraction of the zero field background for samples B, D, and E at different temperatures. The solid lines are theoretical fits using ILP equations. (Lower panels) The phase coherence time extracted from the ILP fits versus temperature for the three samples. The solid lines are the theoretical values of the phase coherence time calculated using equation 5.5.

Phase coherence times obtained by fitting the WAL traces are shown in the lower panels of this figure. Similar to other 2D electron systems, electron-electron interactions are expected to be the dominant source for decoherence for the GaN system at cryogenic temperatures. The theories of electron coherence have been improved in

the last two decades. We will use the following equations provided by Narozhny *et al.*, which include both the singlet and triplet channels as well as the Fermi liquid normalization of the triplet channel[85]:

$$\frac{1}{\tau_\phi} = \left( 1 + \frac{3(F_0^\sigma)^2}{(1+F_0^\sigma)(2+F_0^\sigma)} \right) \frac{T}{g} \ln[g(1+F_0^\sigma)] + \frac{\pi}{4} \left( 1 + \frac{3(F_0^\sigma)^2}{(1+F_0^\sigma)^2} \right) \frac{T^2}{E_F} \ln(E_F \tau) \quad (5.5)$$

where  $F_0^\sigma$  is the interaction constant in the triplet channel,  $E_F$  is the Fermi energy, and  $g = \sigma/(e^2/h)$  is the dimensionless conductance of the 2D electron system.  $F_0^\sigma$  is a function of the interaction strength and is calculated from the carrier density[85]. We note that there are no adjustable parameters in the theory. For comparison, we plotted the theoretical values of  $\tau_\phi$  calculated using the above equation in Fig. 5.5. There is very good agreement between the theory and our measurements for sample B. For samples D and E, the temperature dependence of the phase coherence time is a bit weaker than that of the theory.

## 5.6 Spin-Orbit Coupling in InAlN/GaN heterostructures

Previous sections focus mainly on the SO interaction in AlGaN/AlN/GaN heterostructures. In this section, we studied the spin-orbit interaction on two InAlN/AlN/GaN heterostructures [30-32] samples, whose advantage over traditional AlGaN/GaN heterostructures (see chapter 1) is the beneficial lattice match between the  $\text{In}_{0.17}\text{Al}_{0.83}\text{N}$  barrier and the GaN layer. Also there is a larger spontaneous polarization difference between GaN and  $\text{In}_{0.17}\text{Al}_{0.86}\text{N}$ , which could be used to achieve a higher carrier density, therefore to cover a broader carrier density parameter space.

In 2DEG system, the zero field spin-splitting usually originates from two effects: the structural inversion asymmetry (SIA) of the quantum well (QW)[74] , known as Rashba effect, and the bulk inversion asymmetry (BIA) of the crystal [75-76]. In the two-band  $\mathbf{k}\cdot\mathbf{p}$  model [86] of the wurtzite GaN samples, the Rashba term scales linearly with the wavevector  $k$  ,

$$H_R(k) = \alpha_R (\sigma_x k_y - k_x \sigma_y), \quad (5.6)$$

and there are two terms associated with BIA effect

$$H_{BIA}(k) = (\alpha_{BIA} - \gamma k_{\parallel}^2) (\sigma_x k_y - k_x \sigma_y), \quad (5.7)$$

where  $\alpha_R$  is the Rashba coefficient;  $\sigma$  is the Pauli matrix;  $k_{\parallel}^2 = k_x^2 + k_y^2$ ; and  $\alpha_{BIA}$  and  $\gamma$  are coefficient associated with BIA[86]. For simplicity, we can define an effective SO coefficient  $\alpha_{SO}(k) = \alpha_R + \alpha_{BIA} - \gamma k_{\parallel}^2$  and the total SO interaction can be simplified as

$$H_{SO}(k) = \alpha_{SO} (\sigma_x k_y - k_x \sigma_y). \quad (5.8)$$

The effective spin-splitting energy at Fermi surface is  $\delta E(k_F) = 2\alpha_{SO}(k_F)k_F$ , where  $k_F$  is the Fermi wavevector. The Rashba coefficient,  $\alpha_R$  , and BIA coefficient,  $\alpha_{BIA}$  , usually only depend on the sample structure and electrical field inside the heterostructure and not the Fermi wavevector explicitly. However, the carrier density as well as Fermi wavevector is a function of gate voltage.  $\alpha_R$  and  $\alpha_{BIA}$  are explicit functions of gate voltage and implicit functions of Fermi wavevector,  $k_F$ . Therefore, the effective SO coefficient  $\alpha_{SO}(k_F)$  is not necessary a quadratic function of  $k_F$  , but would have a more complicated expression as a function of  $k_F$ . It is usually hard to

differentiate the contribution of  $\alpha_R$  and  $\alpha_{BIA}$  separately for the total spin splitting energy from experiment.

The idea of gate controlled spin transistor [73] depends mostly on Rashba effect. The c-axis-oriented wurtzite structure 2D system is very unique in that both Rashba effect and BIA effect have the similar terms in effective spin-orbit coupling Hamiltonians, which is not the case in zinc-blende (ZB) structure such as GaAs [75]. In literature, theoretical calculation of zero-field spin-orbit splitting parameters have been reported in wurtzite GaN heterostructures [79-80] and Rashba coefficient was estimated based on experimental observation and theoretical assumptions. Experimentally, it is hard to distinguish SIA parameter from linear BIA linear parameter[87] and usually only linear and cubic parameters were estimated from the experimental results. In the previous chapters we presented results from six AlGaN/GaN samples with carrier density ranging from 0.8 to  $10.6 \times 10^{12} \text{ cm}^{-2}$ . Using the InAlN/GaN heterostructures discussed in chapter 4, we are able to extend our measurements beyond  $10.6 \times 10^{12} \text{ cm}^{-2}$ . This carrier density regime is particularly significant where the deviations from the linear  $k_F$  behavior can be more pronounced.

## 5.7 InAlN/GaN heterostructures samples

Two InAlN/AlN/GaN [46-47] samples were grown by a low-pressure organometallic-vapor-phase epitaxy (OMVPE) system on a sapphire substrate. In both samples, a 250 nm initiation layer of AlN was grown first, followed by a 3.0  $\mu\text{m}$  of undoped GaN. In InAlN sample A, to avoid unintentional GaN contamination deposited on the sample holder [47], the sample growth was interrupted after the growth of

undoped GaN and the sample holder was replaced with a clean one. In InAlN sample B, the growth was continued without growth interruption. The growth then was continued with a 100 nm GaN layer, followed by an optimized 1 nm AlN spacer layer at 1000 °C. In sample A, a 15 nm of  $\text{In}_{0.16}\text{Al}_{0.84}\text{N}$  and finally a 2 nm GaN cap layer were grown. In sample B, the growth was finalized by a 15nm of  $\text{In}_{0.15}\text{Al}_{0.85}\text{N}$  and a 2nm GaN cap layer. The gated Hall bar ( $600 \mu\text{m} \times 100 \mu\text{m}$ ) samples were fabricated by using Ohmic contact Ti/Al/Ni/Au deposited and alloyed at 900 °C. The Hall bar pattern was formed by photolithography followed by a mesa isolation etch in a SAMCO inductively coupled plasma (ICP) etch tool using a Cl-based chemistry. Finally, a Pt/Au (30/50nm) was deposited as the gate.

The samples were characterized by magneto-transport measurements in a low-temperature He3 cryostat with a base temperature of 0.28 K at different gate voltages [47,88]. We applied DC voltage on the metal gate to change the carrier densities in both samples. The carrier densities and mobilities were extracted from longitudinal and Hall resistance measurements. Both samples exhibited SdH oscillations at 0.28 K. We observed well-pronounced two frequency SdH oscillations in sample A (see chapter 3), indicating two-subband occupation in the 2DEG channel [88]. We performed Fast Fourier Transform (FFT) to separate the two frequency components, and corresponding carrier densities in each subband of sample A were extracted. In sample A, for gate voltages from -0.7 V to 0.2 V, the carrier densities in the first and second subband changed from  $19.9 \times 10^{12} \text{ cm}^{-2}$  to  $21.5 \times 10^{12} \text{ cm}^{-2}$  and from  $0.91 \times 10^{12} \text{ cm}^{-2}$  to  $1.36 \times 10^{12} \text{ cm}^{-2}$ , respectively; and the total mobilities varied from  $6.34 \times 10^3 \text{ cm}^2/\text{V}\cdot\text{s}$  to  $5.05 \times 10^3 \text{ cm}^2/\text{V}\cdot\text{s}$ . In single subband sample B (see fig. 5.6 and fig. 5.7), for gate voltages

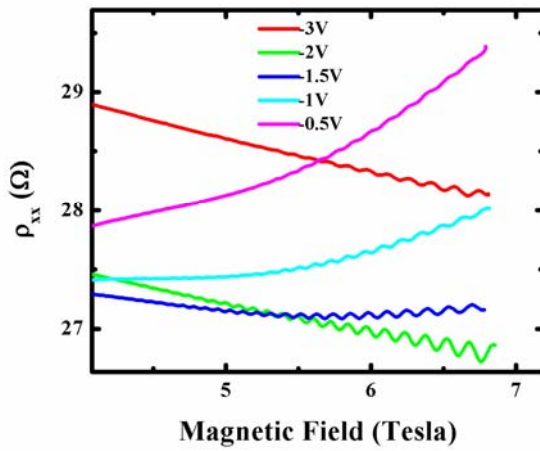
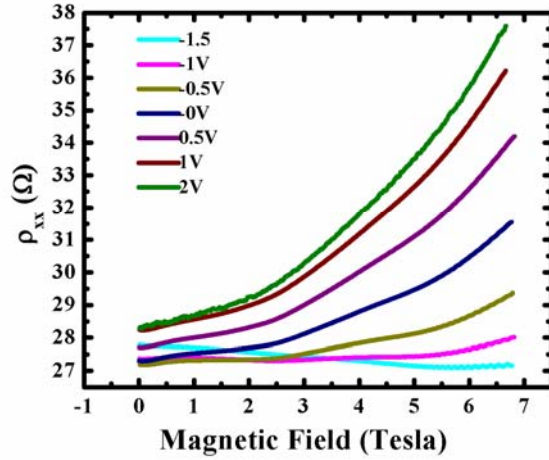


**Fig.5.6:** Well pronounced SdH oscillations were shown in InAlN Sample B's longitudinal measurements for various gate voltages. There is a transition occurring at  $V_{\text{gate}} = -2\text{V}$ , which is due to the electron occupation of a parasitic channel.

from  $-3.0\text{ V}$  to  $-0.5\text{ V}$ , the total carrier densities changed from  $12.2 \times 10^{12}\text{ cm}^{-2}$  to  $14.1 \times 10^{12}\text{ cm}^{-2}$ , with mobilities varying from  $1.72 \times 10^4\text{ cm}^2/\text{V}\cdot\text{s}$  to  $1.63 \times 10^4\text{ cm}^2/\text{V}\cdot\text{s}$ , respectively. Notice in InAlN sample B, the electrons starts to occupy a parasitic channel starting from gate voltage  $-2\text{V}$ [47].

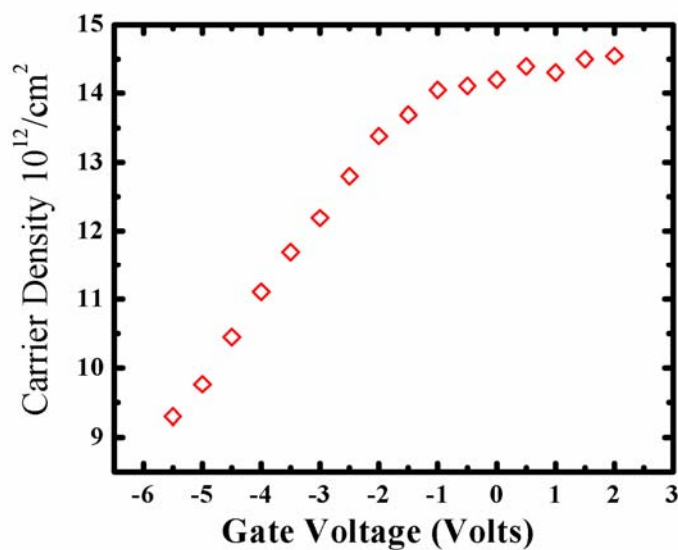
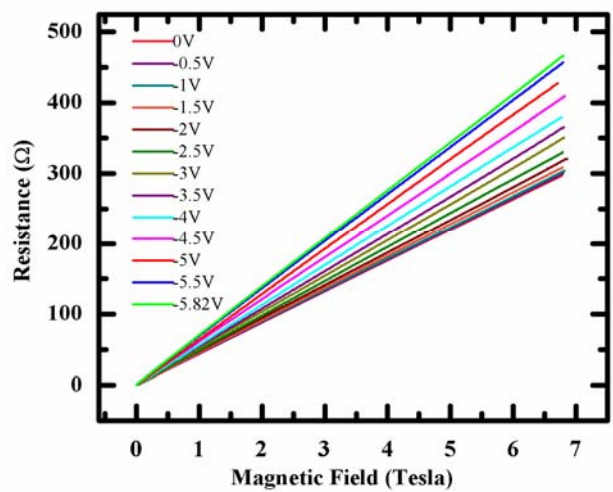


**Fig.5.7:** Upper diagram is the Hall measurements for InAlN sample B. In the lower diagram, the carrier density versus gate voltage clearly indicates a parasitic channel occupation starting at  $V_{\text{gate}} = -2\text{V}$ .

## 5.8 WAL measurements for InAlN/GaN heterostructures samples

As in AlGaN/GaN samples, we used WAL measurement to measure the quantum corrections to conductance at low magnetic fields for high carrier density InAlN samples A and B. In Fig. 5.8, two typical traces of magneto-conductivity for InAlN sample A and B after the subtraction of the zero field background,  $\Delta\sigma = \sigma(B) - \sigma(0)$ , are shown.

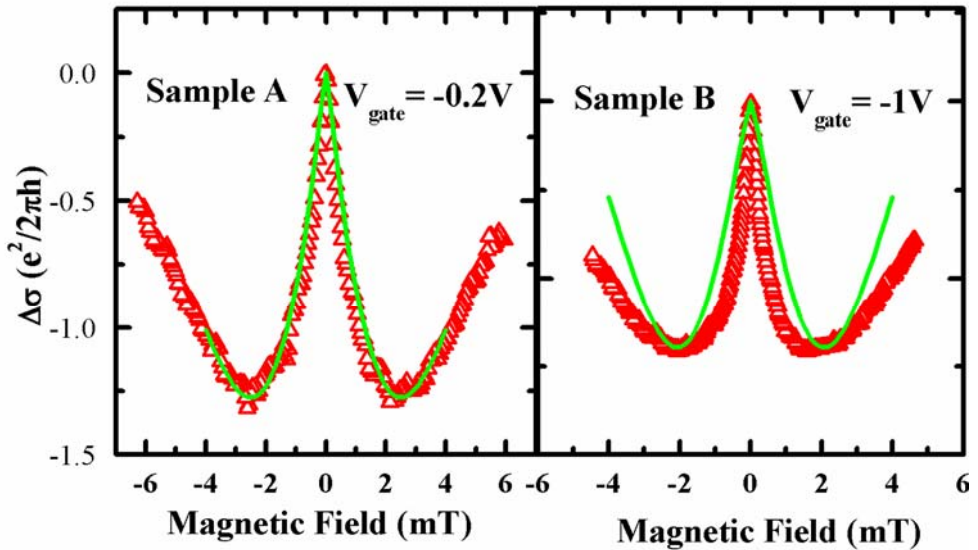


**Fig.5.8:**  $\Delta\sigma = \sigma(B) - \sigma(0)$ . Conductivity after the subtraction of the zero field background of two samples versus magnetic field at  $T=0.3$  K. Left: InAlN Sample A at gate voltage -0.2V. The solid lines are theoretical fits to the data. Right: InAlN Sample B at gate voltage -1V. The solid lines are theoretical fits to the data.

There is a clear WAL behavior in magnetic fields ranging from -6 mT to 6 mT at 0.3 K. For InAlN sample A at gate voltage -0.2V and InAlN sample B at gate voltage -1V, the carrier density is  $20.9 \times 10^{12}$  cm<sup>-2</sup> and  $13.4 \times 10^{12}$  cm<sup>-2</sup>, and the mobility is  $5.66 \times 10^3$  cm<sup>2</sup>/V·s and  $1.66 \times 10^4$  cm<sup>2</sup>/V·s, respectively. The WAL features arise from

the quantum interference of spin-dephasing paths and can be used to quantify the spin dephasing mechanism [84] and spin-orbit coupling in semiconductors. The size of WAL feature depends on the dephasing time which usually is strongly temperature dependent; whereas the width of the peak is related with spin-orbit time and usually does not vary with temperature.

The WAL feature in semiconductors can be caused by two different spin-dephasing mechanisms. The Elliot mechanism originates from the spin-orbit scattering from the electric field of impurities, and its feature is that the spin-orbit field will be proportional to the transport field [89]. The D'yakanov and Perel' (DP) mechanism[90] originates from the spin-orbit coupling of the underlying band structure and does not have a strong mobility dependence. In our samples, we did not observe strong mobility dependence of WAL features, and we therefore concluded that the DP scattering was the dominant spin-dephasing mechanism.

We analyzed the WAL by using the Iordanskii, Lyanda-Geller, and Pikus (ILP) equations [83] developed based on the DP mechanism. In the ILP model fitting, we extracted the elastic scattering time,  $\tau_{tr}$  ; the diffusion constant,  $D = v_F^2 \tau_{tr} / 2$  ; and the transport field,  $B_{tr} = \hbar / 4eD\tau_{tr}$  , from the measured values of carrier density and mobility. Note that in InAlN sample A, we had two subband occupations and we used the carrier density and mobility data of the first subband occupation for the WAL calculation. This is based on the assumption that the second subband occupation is too small ( $\sim 5\%$ ) and the WAL feature comes mostly from the first subband transport. We used two adjustable parameters, the spin-orbit field,  $B_{SO} = \hbar / 4eD\tau_{SO}$ , and the phase coherence field,  $B_\phi = \hbar / 4eD\tau_\phi$  , to fit the data, where  $\tau_{SO}$  and  $\tau_\phi$  are the spin-orbit and

phase coherence times, respectively. For example, in the WAL trace of InAlN sample A, shown in Fig. 5.8, the best fit was obtained by using  $B_{SO} = 2.14$  mT and  $B_\phi = 0.089$  mT. Error bars of both parameters were estimated from the model fitting and it was determined that the error bars for  $B_{SO}$  and  $B_\phi$  are  $\pm 0.1$  mT and  $\pm 0.06$  mT, respectively. For InAlN sample B, the ILP model does not fit the data satisfactorily (see Fig. 5.8). However, we can still estimate  $B_{SO}$  from the data considering the fact that  $B_{SO}$  is usually very close to  $B_{min}$ , the magnetic field at which the magneto-conductivity minimum occurs [77]. Based on that, in InAlN sample B we used  $B_{min}$  to represent  $B_{SO}$  and the error bars for  $B_{SO}$  were estimated from the experimental data directly.

## 5.9 SO field and Spin-Splitting energy in InAlN/GaN heterostructures

In Fig. 5.9, we show  $B_{SO}$  versus carrier density for the InAlN samples A and B as well as our previous data of AlGaN/GaN samples [91]. From our previous work on AlGaN/GaN samples, we covered a carrier density range from  $1.7$  to  $10.6 \times 10^{12}$  cm $^{-2}$  and saw the increase of spin-orbit field  $B_{SO}$ , which indicates the existence of a cubic  $k_F$  term in spin-orbit splitting energy[91] coming from the BIA effect. Starting at carrier density from  $12.2 \times 10^{12}$  cm $^{-2}$  to  $14.1 \times 10^{12}$  cm $^{-2}$  in sample B,  $B_{SO}$  starts to decrease. Then  $B_{SO}$  increases again when the carrier density increases from  $19.9 \times 10^{12}$  cm $^{-2}$  to  $21.5 \times 10^{12}$  cm $^{-2}$  in sample A. The  $\sqrt{B_{SO}}$  is proportional to the effective SO

coefficient  $\alpha_{SO}(k_F)$ . This observation indicates that  $\alpha_{SO}(k_F)$  is neither a constant nor a quadratic function of  $k_F$ , but rather in a complicated form.

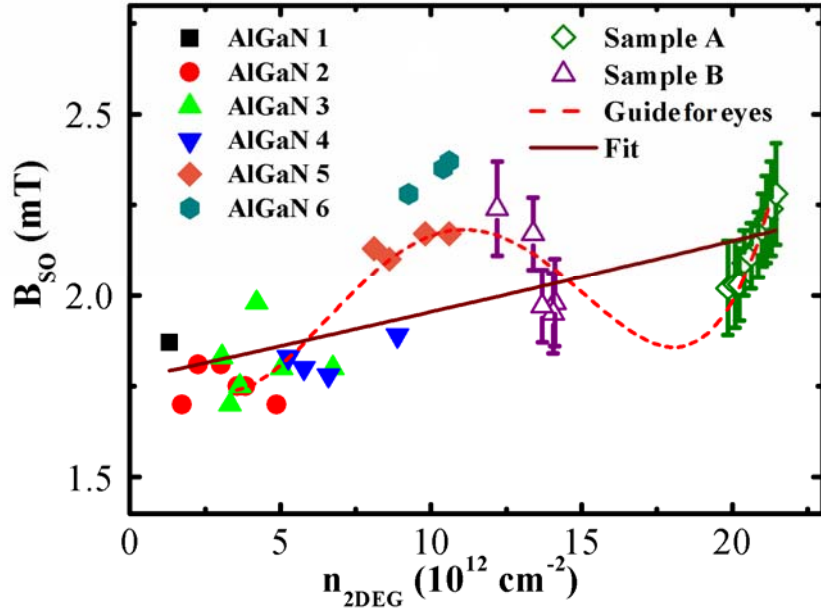


**Fig.5.9:** Spin-orbit field versus carrier density. The solid dots are the AlGaN/GaN data from our previous experiment [91]. The hollow dots are the data extracted from our InAlN/GaN sample A and B with error bars labeled. The fit is based on a model with linear and cubic parameters. The dashed line is a guide for the eyes.

First, it is possible that the SIA (Rashba) term dominates the spin-splitting processes and the true  $B_{SO}(k_F)$  (therefore  $\alpha_{SO}(k_F)$ ) could be nearly a constant by noticing that the error bars are relatively large ( $\sim 5\%$ ) in our data. The data presented in Fig.5.9 could be just a random distribution of  $B_{SO}(k_F)$  around an average value of 2.1 mT. If we assume that a spin-splitting energy of  $E_{SS}=2(\alpha k_F + \gamma k_F^3)$ , we can extract the linear and cubic spin-orbit parameters [91] of  $\alpha=5.4\times 10^{-13}$  eV m and  $\gamma=4.4\times 10^{-32}$  eV m<sup>3</sup> from the data (see Fig.5.9 Fit). Notice that the cubic parameter is much smaller than value we extracted previously on AlGaN/GaN samples (see previous sections).

However, due to the different heterostructure interface of AlGaN/GaN and InAlN/GaN, we would expect that the Rashba coefficients, which are sensitive to the interface structures, in AlGaN/GaN and InAlN/GaN samples to be totally different.

The second interpretation would interpret the data by the different Rashba coefficients for AlGaN/GaN samples, sample A and sample B, respectively. In this case, both SIA and BIA effects would contribute to the final spin-splitting energies. The only difference is that the SIA and BIA coefficients,  $\alpha_R$  and  $\alpha_{BIA}$ , is different in these three groups. Note that  $\alpha_{BIA}$  has an implicit dependence on the heterostructure interface due to a  $\langle k_z^2 \rangle$  term[80], though the name of BIA might misleadingly imply that it is only GaN bulk related. Our previous interpretation for AlGaN/GaN samples might still hold true in this interpretation [91]. The decreasing dependence of  $B_{SO}(k_F)$  on carrier density from  $12.2 \times 10^{12} \text{ cm}^{-2}$  to  $14.1 \times 10^{12} \text{ cm}^{-2}$  for sample B might be just a random distribution due to the relatively large error bars. And the increase of  $B_{SO}(k_F)$  with increasing carrier density from  $19.9 \times 10^{12} \text{ cm}^{-2}$  to  $21.5 \times 10^{12} \text{ cm}^{-2}$  for sample A might be attributed to the existence of a cubic BIA spin-splitting energy term,  $\gamma k_{\parallel}^2(\sigma_x k_y - k_x \sigma_y)$ , same as in AlGaN/GaN samples [91].

Finally, we might be able to interpret the data in a more coherent perspective. Note that different heterostructures, whether AlGaN/GaN or InAlN/GaN, only provide different confinement potential profiles for the 2DEG, and the different confinement potential profiles are highly correlated to the carrier densities. Therefore, we might be able to interpret the  $B_{SO}(k_F)$  data purely from carrier density perspective no matter whether the change of carrier density is due to a gate or different heterostructures. In

the Fig.3 of Litvinov's paper [80], the spin splitting energy versus gate voltage was calculated and showed an increasing then decreasing feature, similar to our data from carrier densities  $1.7$  to  $14.1 \times 10^{12} \text{ cm}^{-2}$  (including the data from AlGaN/GaN and sample B). Notice that Litvinov's calculation assumes a constant carrier density, therefore his spin-splitting energy is proportional to our  $\sqrt{B_{SO}(k_F)}$  and his gate voltage corresponds to our carrier density. In this way, our data from carrier densities  $1.7$  to  $14.1 \times 10^{12} \text{ cm}^{-2}$  can be qualitatively explained by Litvinov's calculation. We should point out that the decrease of  $\alpha_{SO}(k_F)$  (therefore  $B_{SO}(k_F)$ ) with respect to increasing carrier density has also been observed experimentally [92] in AlGaN/GaN structures in the carrier density range from  $8.85$  to  $9.06 \times 10^{12} \text{ cm}^{-2}$ , which is close to our data quantitatively if we convert  $\alpha_{SO}(k_F)$  to  $B_{SO}(k_F)$ . Finally, the increase of  $B_{SO}(k_F)$  on the carrier density from  $19.9 \times 10^{12} \text{ cm}^{-2}$  to  $21.5 \times 10^{12} \text{ cm}^{-2}$  in sample A, could still be interpreted in terms of BIA cubic term  $\gamma k_{\parallel}^2 (\sigma_x k_y - k_x \sigma_y)$ , or the interband scattering due to the population of the second subband[93].

The spin-splitting energy  $E_{ss} = 2\hbar\Omega$ , where  $\Omega$  is the spin-orbit frequency and can be calculated from the spin-orbit field as  $B_{SO} = (\hbar/4eD)2\Omega^2\tau$ . In Fig. 5.10, we plot the spin splitting energies versus Fermi wavevector  $k_F$  for all the samples. As seen from the Fig. 5.10, it is clear that the spin-splitting energy scales linearly with  $k_F$  at low carrier densities.

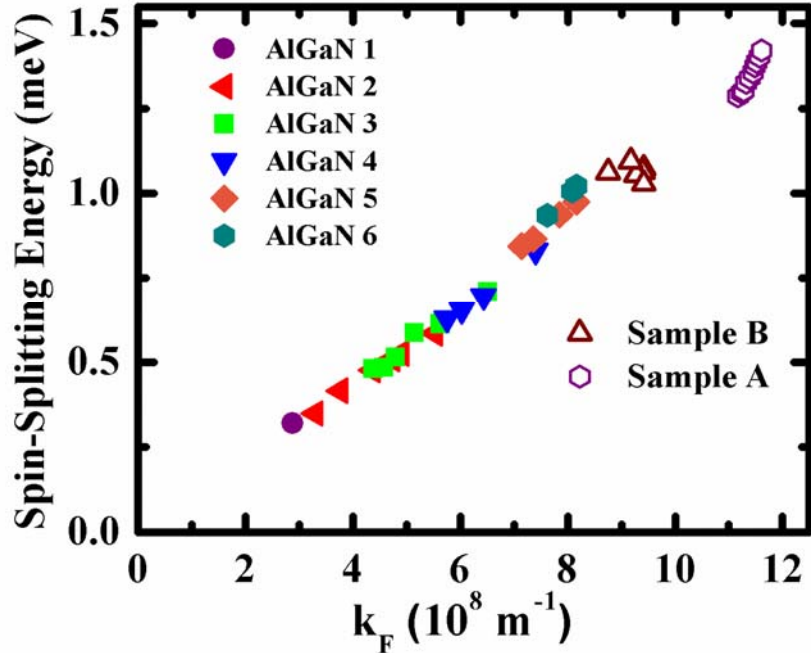


**Fig.5.10:** The spin splitting energy versus Fermi wavevector. The solid dots are the AlGaN/GaN data from our previous experiments [91]. The hollow dots are the data extracted from our InAlN/GaN sample A and B.

At higher carrier densities there is a deviation from linear behavior corresponding to the feature of  $B_{SO}(k_F)$  at high carrier densities. The highest spin-splitting energy is 1.42 meV which occurs at carrier density  $21.5 \times 10^{12} \text{ cm}^{-2}$  in InAlN/GaN sample A.

### 5.10 Spin-Orbit parameters from SdH oscillations

We should point out that the spin-orbit coupling parameters have also been extracted by using the SdH oscillations beating patterns by different groups [82,94-98], which are not in agreement with that of our WAL results. It is important to note that in SdH oscillations measurements, the beating patterns claimed to be due to spin-splitting actually could also come from other factors like nonuniformities in the carrier densities

[82]. We plot the results from literature [82,94-98] in Fig.5.11, and the spin-orbit energies extracted from these papers actually are not consistent with each other. Therefore, simply observing the beating patterns in SdH oscillations cannot be served as an indisputable evidence for the spin-orbit interaction.

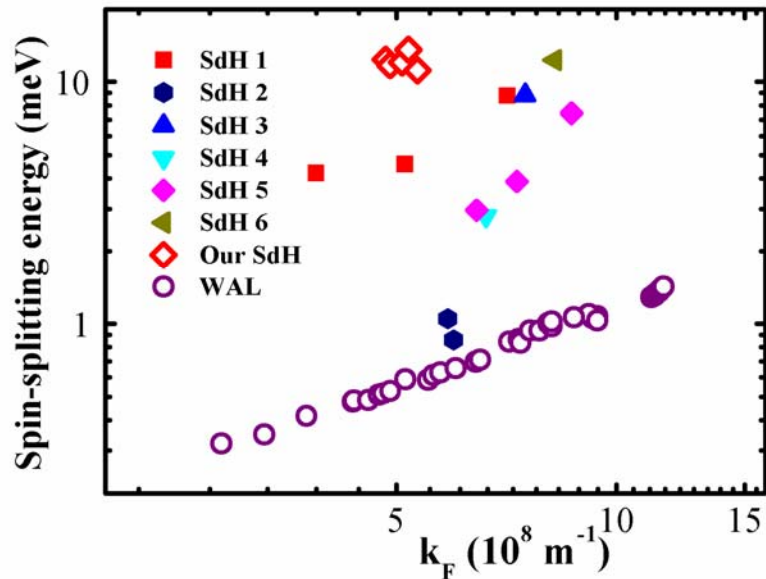


**Fig.5.11:** Spin-orbit energy versus carrier density extracted from beating pattern of SdH oscillations. The data of SdH1 [82] , SdH2 [94], SdH3 [95], SdH4 [96], SdH5 [97] and SdH6 [98] are from literatures, compared to our results extracted from WAL and SdH measurements.

In a few cases we have also observed beating pattern in SdH oscillations. In Fig.5.12, the SdH oscillations measurements of an  $\text{Al}_x\text{Ga}_{1-x}\text{N}/\text{AlN}/\text{GaN}$  2DEG sample are shown.

This sample was cut into the Van der Pauw geometry and the longitudinal and Hall measurements have been performed. When the sample is in the dark, a clear beating pattern is observed. We used persistent photoconductivity (PPC) effect to change the carrier densities in the sample.

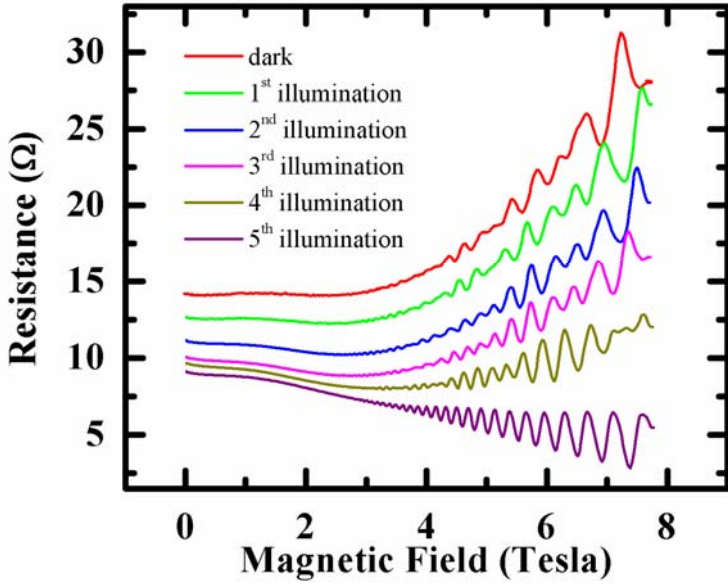


**Fig.5.12:** Longitudinal resistance of an Van der Pauw  $\text{Al}_x\text{Ga}_{1-x}\text{N}/\text{AlN}/\text{GaN}$  sample versus magnetic field at 0.3 K. In the data, SdH beating pattern is observed. We changed the carrier density in the sample by illuminating the sample using a LED, known as the PPC effect. The data for the sample in the dark and after 5 illuminations is shown. After the 5<sup>th</sup> illumination, the beating pattern disappears.

We illuminate the sample by turning on a white light LED close to the sample. After illuminating the sample for couple minutes, we turn off the LED and perform the magneto-transport measurement, and obvious change has been observed in the magneto-transport measurements. We repeat this process for several times. After several illuminations circles performed, the beating pattern disappeared completely (see Fig. 5.12). If the beating pattern is due to the SO interactions, the beating pattern would be more pronounced because the SO coupling would be enhanced in higher carrier densities regime. In our sample, we saw the opposite. We concluded that the beating pattern in the SdH oscillations in our sample was due to the nonuniformity of the carrier density. When we change the sample by using the PPC effect, the sample's carrier

density became more uniform, therefore the beating pattern disappeared. Because of our observation, we believe that the beating patterns in SdH oscillations cannot be used as conclusive evidences of spin-orbit interaction.

Also we need to point out that the Van der Pauw samples are particularly vulnerable to the nonuniformities in carrier density. In this material system, even at the room temperature, we can still observe some PPC effect, which means we would observe a difference if we load the sample in the dark or with light on into the cryogenic dewar. From our experience, every time we cool down the sample from room temperature to a few Kelvin, there will be a slight difference in the magnetotransport measurements. Therefore, special caution is needed to avoid the non-uniformity in GaN samples, which might come from the variations due to large sample size or from the PPC effect.

## 5.11 Conclusion

In summary, we have studied spin-orbit coupling and electron phase coherence in wurtzite  $\text{Al}_x\text{Ga}_{1-x}\text{N}/\text{AlN}/\text{GaN}$  2D electron systems by WAL measurements. The heterostructures had different Al concentrations ranging from  $x=0.1$  to  $0.35$ . By employing the persistent photoconductivity effect and gating, we changed the carrier density of the electrons. Densities up to  $10.6 \times 10^{12} \text{ cm}^{-2}$  have been explored in AlGaN/GaN 2DEGs. It was found that the electron spin splitting energy does not scale linearly with  $k_F$  at high carrier densities. We were able to extract the linear and cubic spin-orbit parameters,  $\alpha=5.01 \times 10^{-13} \text{ eV}\cdot\text{m}$  and  $\gamma=1.6 \times 10^{-31} \text{ eV}\cdot\text{m}^3$ , respectively, for this material system. The linear spin-orbit coupling parameter is consistent with previous

reports based on WAL measurements and should be viewed as an effective coupling constant which is a sum of the Rashba parameter and the linear spin-orbit coupling parameter associated with the BIA of the crystal. The cubic parameter, however, has not been measured previously and arises purely from the BIA of the crystal. Meanwhile, we found that the SO parameters extracted from SdH oscillations from literature didn't agree with WAL measurement.

Furthermore, we were not able to change the spin orbit coupling significantly by the use of gating effect. This suggests employing the Rashba effect in spin-transistors would be particularly challenging in the GaN system.

We also measured the phase coherence times for AlGaN/GaN system. Similar to other 2D electron systems, phase coherence was strongly temperature dependent and was in agreement with theories based on electron-electron interactions.

We expanded the measurements to an even higher carrier density regime by using two InAlN/AlN/GaN 2DEG samples to investigate the spin-orbit coupling in InAlN/GaN systems. The carrier density reaches as high as  $21.5 \times 10^{12} \text{ cm}^{-2}$ . We find that the spin-orbit field is not a constant at high carrier densities and the electron spin splitting energies shows a deviation from linear behavior with  $k_F$ . Possible mechanisms have been proposed to explain the experimental data. Our observations in this experiment may evoke further experimental and theoretical research on the SO coupling in GaN system.

# CHAPTER 6

## ENERGY RELAXATION MEASURED BY WEAK ANTILOCALIZATION IN AlGaN/GaN HETEROSTRUCTURES

### 6.1 Electron-Phonon Interaction in AlGaN/GaN Heterostructures

In the previous chapter, we talked about the spin-orbit interaction in the GaN systems. In this chapter, we will focus on the electron-phonon interaction in AlGaN/GaN heterostructures. Many of the semiconductor devices are operated at high bias voltages such that the electrons would equilibrate with each other at a much higher temperature than the lattice temperature. The temperature of these hot electrons is determined by the emission rate of phonons by the hot electrons. The study of electron-phonon (e-p) interaction processes is particularly important in this context.

Recent experiments have used noise measurement, Shubnikov-de Hass (SdH) effect, or sample resistivity as thermometers in GaN two-dimensional electron gas (2DEG) systems to probe the e-p interactions [99-103]. However, those thermometers have their own limitations. As a complementary method, in this experiment we utilized the weak antilocalization (WAL) effect as a thermometer at very low temperatures to study e-p interactions in GaN heterostructures.

It is well known that the WAL arises from quantum interference of spin-dephased electrons and that the spin dephasing process is temperature sensitive. In our previous work, we have used WAL measurements to extract the spin-orbit splitting parameter in the GaN systems [78,91]. From that experiment, we found the size of the

WAL feature showed strong temperature dependence and could be utilized as a thermometer to study the dynamic processes of the 2DEG system.

## 6.2 AlGaN/GaN Heterostructures samples

To understand the fundamental energy relaxation processes in GaN, we studied two GaN heterostructures with different barriers [104]. Both heterostructures were grown by metalorganic vapor phase epitaxy on c-plane sapphire substrates. GaN sample A has a 25 nm  $\text{Al}_{0.15}\text{Ga}_{0.85}\text{N}$  barrier layer and GaN sample B has a 20nm  $\text{Al}_{0.83}\text{In}_{0.17}\text{N}$  barrier. Both were grown with a  $\sim 3\text{-}4 \mu\text{m}$  GaN buffer layer and capped with  $\sim 2\text{nm}$  GaN. To enhance the electron mobility at low temperature, a thin AlN spacer layer ( $\sim 1 \text{ nm}$ ) was included between GaN channel and the barrier in both samples. In both heterostructures, all layers were undoped and each 2DEG was formed just below the AlN spacer by spontaneous and piezoelectric polarization effects. To study the magnetotransport properties,  $600 \mu\text{m} \times 100 \mu\text{m}$  Hall bar structures were fabricated by photolithography followed by dry etching. Ti/Al/Ti/Au contacts annealed at  $900^\circ\text{C}$  were then used to form ohmic contacts to the 2DEG. In addition, a Ni/Au gate was deposited on top of sample A to modulate the electron density of the 2DEG.

## 6.3 Characterization of AlGaN/GaN Heterostructures Samples

The samples were characterized by longitudinal magnetoresistance and Hall measurements in two low-temperature cryostats with base temperatures of 0.28 K and 1.5 K, respectively. In Fig.6.1 (a), we plot low temperature magnetoresistance traces for

Sample A at gate voltages -4 V, 0 V and 4 V. This sample exhibited clear SdH oscillations at 0.28 K.

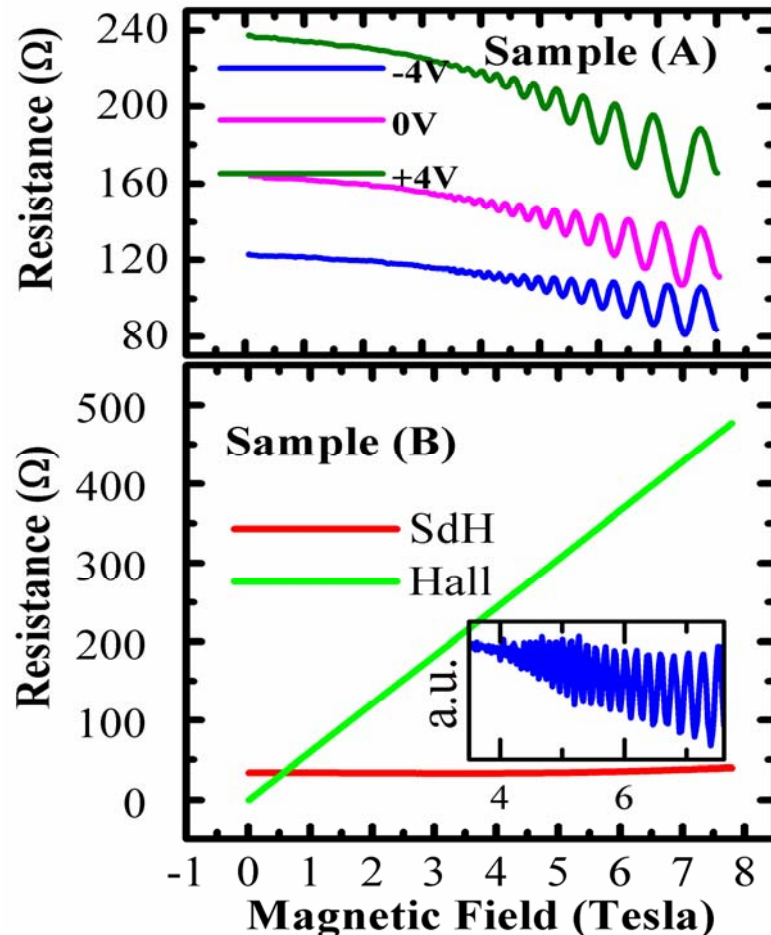


**Fig.6.1:** (a) Sample A: Longitudinal resistance measurements at gate voltages from -4 V to 4 V at 0.28 K, with clear SdH oscillations shown. (b) Sample B: Longitudinal and Hall measurements at 1.5 K. The insert is the differential resistance  $dR/dB$  with clear SdH oscillations shown.

The carrier density extracted from the SdH oscillations, as well as Hall slopes (not shown), is found to vary with gate voltages, which is consistent with a simple capacitance model. For gate voltage of -4V and 4V, the carrier densities were  $3.41 \times 10^{12} \text{ cm}^{-2}$  and  $4.92 \times 10^{12} \text{ cm}^{-2}$  and the corresponding mobilities were  $8.5 \times 10^3 \text{ cm}^2/\text{V}\cdot\text{s}$  and

$10.7 \times 10^3$  cm $^2$ /V·s, respectively. Magnetoresistance and Hall traces for Sample B are shown in Fig. 6.1 (b). Unlike Sample A, the SdH oscillations were not well pronounced for Sample B. However, we were able to resolve the SdH oscillations in dR/dB as shown in the insert of Fig. 6.1 (b). These relatively small SdH oscillations were most likely due to the small spread of non-uniformity of carrier density in Sample B. The onset of SdH oscillations for samples A and B were 3 Tesla and 3.5 Tesla, respectively. For sample B, the carrier density was  $10.26 \times 10^{12}$  cm $^{-2}$  with mobility  $17.8 \times 10^3$  cm $^2$ /V·s at 1.5 K.

We showed the carrier density versus gate voltage as well as mobility versus carrier density for sample A in Fig. 6.2. Sample A's carrier density has a linear dependence on gate voltage, which agrees with a simple capacitance model which indicates that there was no a parasitic conduction channel. The mobility is found to increase with increasing carrier density which is consistent with our expectations in this carrier density range.

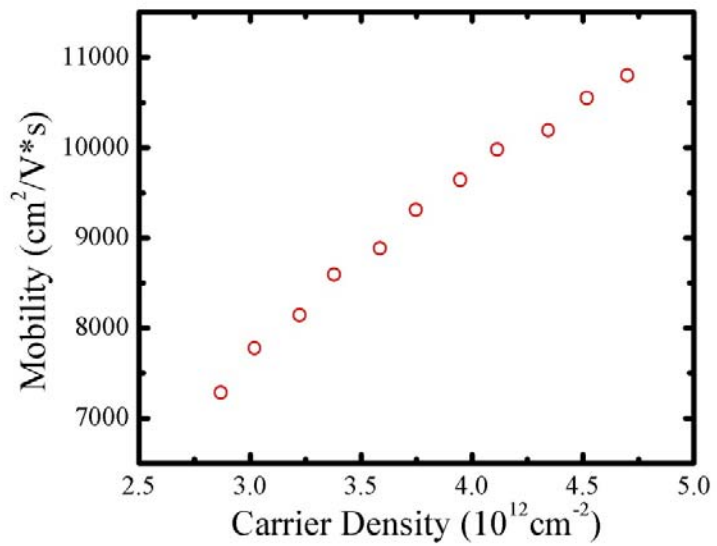
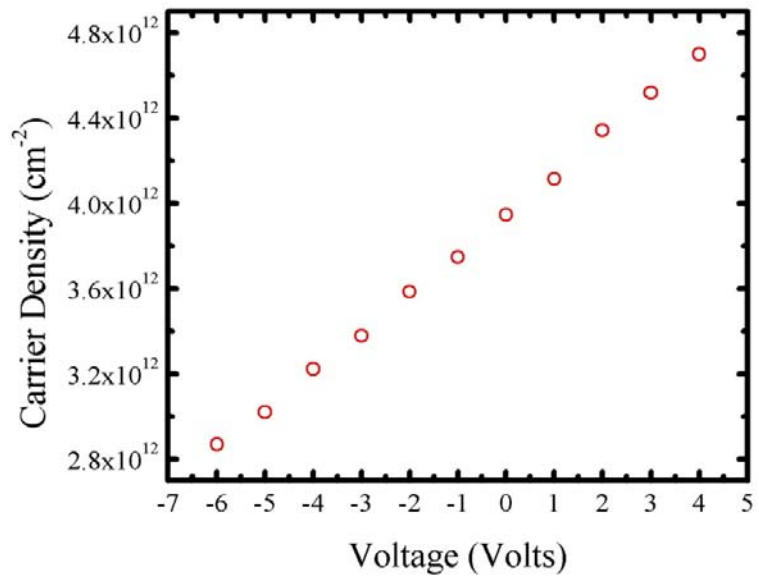


**Fig.6.2:** Upper diagram: Carrier density versus gate voltage for GaN sample A.  
 Lower diagram: Mobility versus carrier density for GaN sample A.

## 6.4 Weak antilocalization measurements

We measured the temperature dependence of the quantum corrections to conductance at low magnetic fields using standard four-terminal ac-lock-in techniques. Representative traces of magneto-conductivity after subtraction of the zero field background,  $\Delta\sigma = \sigma(B) - \sigma(0)$ , obtained from sample A with gate voltage  $V_g = 0$  V at different temperatures are shown in Fig. 6.3 (a).

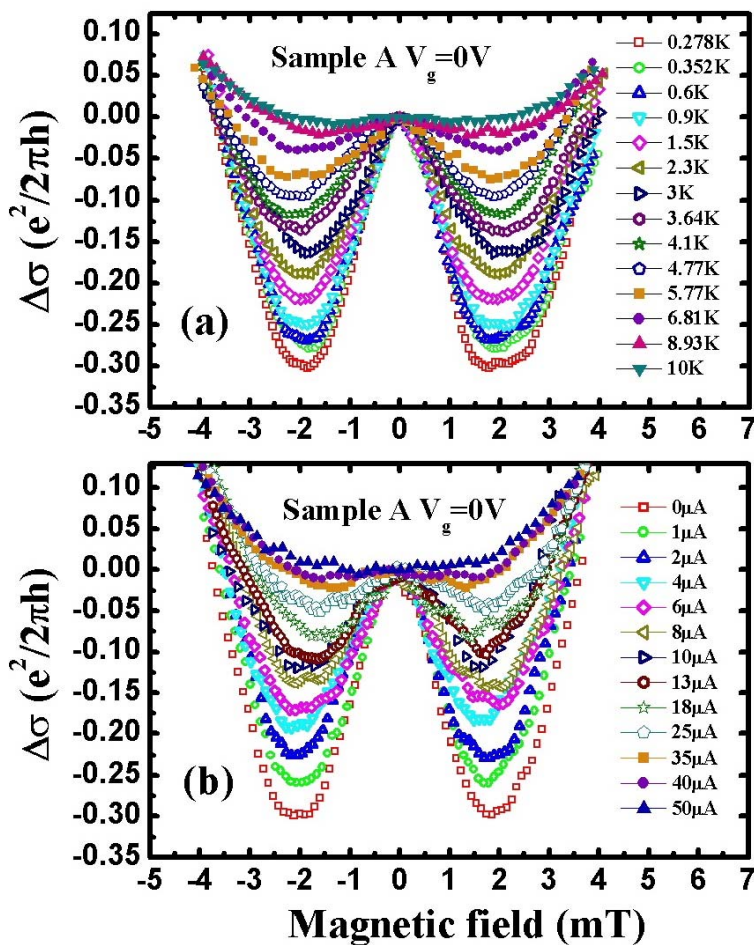


**Fig.6.3:** Experimental magnetoconductivity  $\Delta\sigma = \sigma(B) - \sigma(0)$  of sample A with  $V_g = 0$  V  
(a) At different temperatures (b) At different bias dc currents at 0.28 K.

There was a clear WAL behavior at magnetic fields below 2 mT from 0.28 K up to 10 K. This feature arises from the quantum interference of spin-dephased paths and can be used to quantify spin-orbit coupling in semiconductors. It is obvious in our data that the size of the WAL feature is strongly temperature dependent and decreases with increasing temperature whereas the width of the peak does not vary with temperature [78].

For AC excitation currents in the range of 10-100 nA, there was no noticeable change in the size of WAL feature. This means that when such small excitation currents are used, there is no significant Joule heating in the electron gas; the electron temperature,  $T_e$ , is close to the lattice temperature,  $T_l$ . However, if we pass larger DC bias currents, the electron system would be hotter and the WAL feature would be suppressed. In order to study this heating effect, we kept the sample at the base temperature of the cryostat and passed a DC bias current and a small AC modulation current through the Hall bar structures. The magnetoresistance traces were again measured using the AC lock-in technique. In Fig. 6.3 (b), we plot typical magnetoconductance traces for the sample A at different dc bias currents. We find that the WAL feature decreases with increasing DC bias current. The same happens to sample B (see Fig. 6.4).

There is a striking similarity between the traces obtained at higher temperatures and those obtained with higher DC bias currents (Fig. 6.3 and Fig. 6.4). By comparing such sets of WAL traces, we were able to extract the electron temperature,  $T_e$ , for different bias currents. Instead of plotting electron temperature as a function of bias current, we calculated the power dissipated per electron,  $P_e$ , in the active region of the

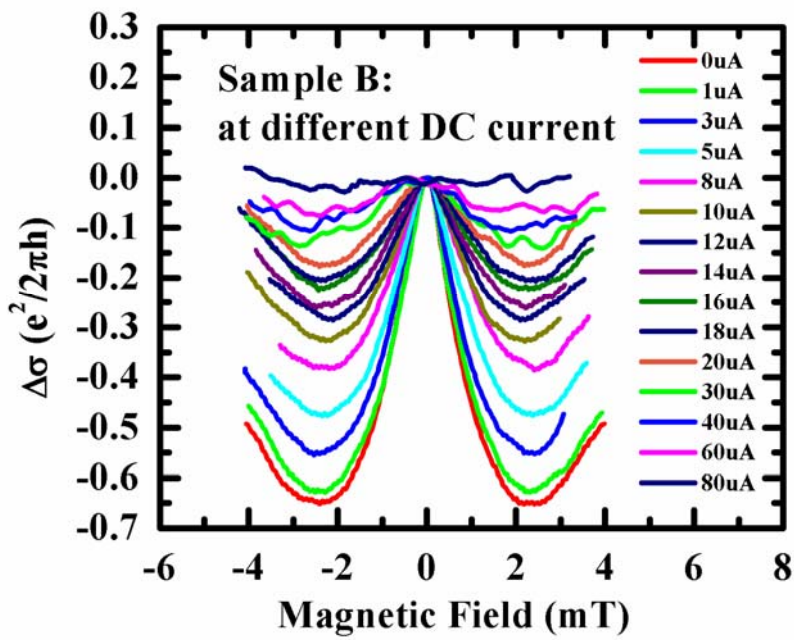
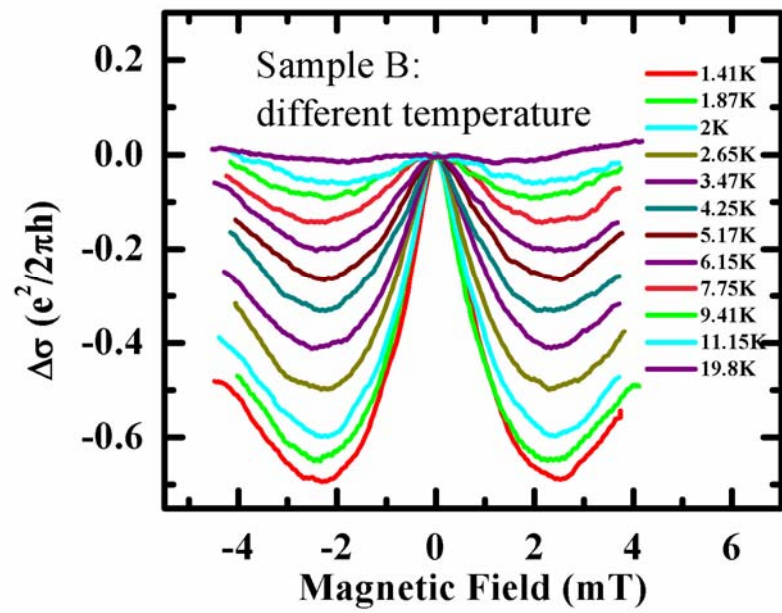


**Fig.6.4:** Experimental magnetoconductivity  $\Delta\sigma = \sigma(B) - \sigma(0)$  of sample B (a) at different temperatures and (b) at different bias dc currents at 0.28 K.

Hall bar by using equation  $P_e = I^2 R / (wLn)$ , where  $I$  is the device current,  $R$  the four terminal resistance of the Hall bar,  $n$  the two dimensional carrier density and  $w$  and  $L$  the width and length of the Hall bar structure. We plot the power dissipation vs. WAL amplitude and temperature vs. WAL amplitude in Fig. 6.5 for sample A at  $V_{gate} = 0$  V.

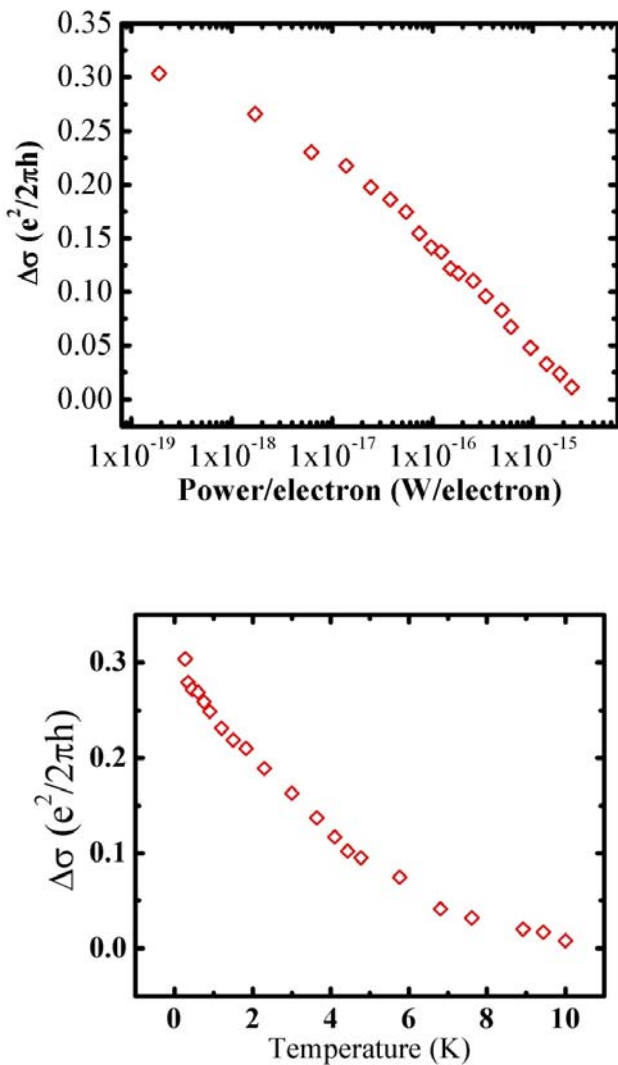


**Fig.6.5:** WAL amplitude can be used as a thermometer for electron temperature. For sample A at gate voltage 0 V: The upper diagram is the WAL amplitude vs. power dissipation per electron. The lower diagram is the WAL amplitude vs. electron temperature.

From this figure, the power dissipation vs. temperature can be extracted by using the WAL amplitude as the indication of temperatures. In this way, WAL measurement can be used as a thermometer at low temperature in this experiment.

## 6.5 Power dissipation in AlGaN/GaN Heterostructures

We plotted the power dissipated per electron vs.  $T_e$  for both sample A at gate voltages -4, 0, and 4 V and sample B in Fig 6.6.

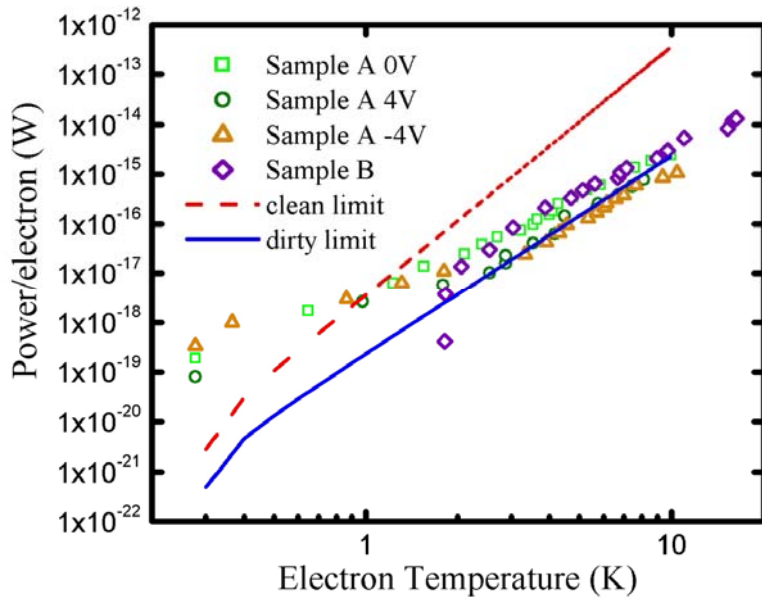


**Fig.6.6:** Power dissipated per electron versus electron temperature for Samples A and B. The solid line is the calculation for the dirty limit and the dash line is the calculation for the clean limit.

Plotted in this manner, the heating curves do not depend strongly on the carrier density or the mobility of 2DEG. We note that sample A was measured at a base

temperature of 0.28 K and sample B was measured at a base temperature of 1.5 K, thus the data obtained from sample A covered a wider temperature range.

In the low-temperature region, the samples are in the Bloch-Grüneisen (B-G) regime, where the average phonon wave vector,  $q$  ( $\sim k_B T / \hbar v_s$ ), is much smaller than Fermi wave vector,  $k_F$  ( $q \ll k_F$ ). In the B-G regime, the electron energy is not high enough to excite optical phonons; therefore the dominating power dissipation in the 2DEG system is through the emission of acoustic phonons via the piezoelectric and deformation potential coupling processes. In the B-G regime, the e-p interaction is expected to have various power-law dependences on temperature [100-103], [105-107]. For example, the phonon emission via piezoelectric coupling leads to  $T_e^5$  and  $T_e^3$  dependence for energy relaxation with and without static screening, and the phonon emission via deformation potential leads to  $T_e^7$  and  $T_e^5$  dependence with and without static screening[108].

## 6.6 Clean limit versus dirty limit

At low temperature, it is believed that the piezoelectric coupling is the dominating energy relaxation mechanism in the GaN system [100-103], which is the focus of this chapter. The electron screening effect of local potential must be included in the calculations of energy relaxation rates. At very low temperatures, when the wavelength of the emitted phonons becomes comparable to the mean free path of the electrons, the static screening is no longer suitable to describe the system. Instead, dynamic screening should be applied to calculate the piezoelectric coupling case, and as a result the energy relaxation scales as  $P_e \sim T_e^4$ . This regime,  $ql_e < 1$ , is known as the

hydrostatic regime, where  $q$  is the average phonon wave vector,  $v_s$  is the sound velocity and  $l_e$  is the elastic mean free path in the material [106]. This regime is also called the “dirty limit”, which is the case of relatively lower mobility systems and has been studied in GaAs 2DEGs [105-107] before.

The theory for electron energy relaxation in GaAs (zinc blende) 2DEG systems both in the dirty and the clean limit has been studied in Ref [107-108]. The characteristic function  $F_\lambda$  for the power dissipation through acoustic phonon[107] is equal to

$$F_\lambda = \sum_q \hbar \omega_\lambda(q) |M_\lambda(q)|^2 n_B(\hbar \omega_\lambda(q)/(k_B T)) G(q_{\parallel}, \omega_\lambda(q)), \quad (6.1)$$

where  $q$  is the phonon wave vector,  $q_{\parallel}$  the projection of  $q$  onto 2DEG plane,  $\omega_\lambda(q) = \hbar q v_\lambda$ ,  $n_B(x) = 1/(e^x - 1)$ ,  $v_\lambda$  is the phonon velocity,  $M_\lambda(q)$  is the electron-phonon matrix element and

$$G(q_{\parallel}, \omega) = \frac{2\omega(2\kappa\epsilon_0)^2}{e^2} \text{Re}\left(\frac{1}{\sigma_{xx}}\right), \quad (6.2)$$

where  $\sigma_{xx}$  is the component of 2DEG conductivity matrix,  $\kappa$  the semiconductor background dielectric constant,  $\epsilon_0$  the permittivity of free space. In clean limit,

$$\text{Re}\left(\frac{1}{\sigma_{xx}}\right) = \frac{1}{\sigma_{xx}}; \quad (6.3)$$

In dirty limit

$$\text{Re}\left(\frac{1}{\sigma_{xx}}\right) = \frac{q}{q_{TF}^2} \kappa \epsilon_0 v_F, \quad (6.4)$$

where  $q_{TF}$  is the Thomas-Fermi wave vector and  $v_F$  is the Fermi wave vector. Note the above equations are valid for both the deformation potential (DP) and the

piezoelectric interaction (PZ). The only difference between the DP case and the PZ case is a different  $M_\lambda(q)$  respectively.

In GaAs[108], for the DP case, the characteristic function is

$$\left|M^{DP}(\vec{q})\right|^2 = \frac{\Xi_d^2 q}{2\rho\nu_l}. \quad (6.5)$$

where  $\Xi_d$  is the DP constant. For the PZ, the longitudinal mode characteristic function is

$$\left|M_{LA}^{PZ}(\vec{q})\right|^2 = \frac{e^2 h_{14}^2}{2\rho\nu_l} \left( \frac{9q_\perp^2 q_{//}^4}{q^7} \right). \quad (6.6)$$

and the transverse mode characteristic function is

$$\left|M_{TA}^{PZ}(\vec{q})\right|^2 = \frac{e^2 h_{14}^2}{2\rho\nu_t} \left( \frac{8q_\perp^4 q_{//}^2 + q_{//}^6}{2q^7} \right). \quad (6.7)$$

where  $q_\perp$  is the perpendicular component of  $q$  to 2DEG plane and  $q_{//}$  is the parallel component.

However, for wurzite GaN 2DEG systems, the piezoelectric coupling is different from the zinc blende type. In wurzite crystals, the e-p matrix elements for longitudinal acoustic (LA) and transverse acoustic (TA) piezoelectric coupling are [109]

$$\left|M_{LA}^{PZ}(\vec{q})\right|^2 = \frac{\hbar e^2}{2\rho\nu_l q} \left( \frac{e_{33}q_\perp^3 + (e_{31} + 2e_{15})q_\perp q_{//}^2}{q^3 \epsilon} \right)^2 \quad (6.8)$$

and

$$\left|M_{TA}^{PZ}(\vec{q})\right|^2 = \frac{\hbar e^2}{2\rho\nu_t q} \left( \frac{-(e_{33} - e_{31} - e_{15})q_\perp^2 q_{//} - e_{15}q_{//}^3}{q^3 \epsilon} \right)^2, \quad (6.9)$$

respectively. In the above equations  $e_{33}$ ,  $e_{31}$ ,  $e_{15}$  are piezoelectric coefficients,  $q$  is the magnitude of the three-dimensional phonon wave vector,  $q_\perp$  and  $q_{//}$  are the components

of  $q$  perpendicular and parallel to the 2DEG plane, respectively,  $e$  is the electron charge,  $\rho$  is the mass density of GaN,  $\epsilon$  is the dielectric constant in GaN,  $v_l$  and  $v_t$  are LA and TA phonon sound velocities in GaN, respectively.

In the clean limit, we follow the procedures for GaAs reported by Ma *et al.* [108] and obtain the piezoelectric LA and TA e-p interaction characteristic function in GaN as

$$F_{LA}^C(T) = \frac{3\zeta(5)m^{*2}e^2}{32\pi\hbar^7k_F^3\rho v_l^4\epsilon^2q_s^2}(5e_{33}^2 + 6e_{33}(e_{31} + 2e_{15}) + 5(e_{31} + 2e_{15})^2)(k_B T)^5 \quad (6.10)$$

and

$$F_{TA}^C(T) = \frac{3\zeta(5)m^{*2}e^2}{32\pi\hbar^7k_F^3\rho v_l^4\epsilon^2q_s^2}(35e_{15}^2 + 10e_{15}(e_{33} - e_{31} - e_{15}) + 3(e_{33} - e_{31} - e_{15})^2)(k_B T)^5, \quad (6.11)$$

respectively, where  $\zeta(5)$  is the Riemann zeta function,  $m^*$  is the effective mass,  $k_F$  is Fermi wave vector and  $q_s = m^*e^2/(2\pi\hbar^2)$  is the screening wave vector.

In the dirty limit, we follow the procedure given by Chow *et al.* [107] and obtain the piezoelectric LA and TA e-p interaction characteristic function in GaN as

$$F_{LA}^D(T) = \frac{\pi^2}{15n\hbar^3\sigma_{xx}\rho v_l^3}\frac{2}{105}(15e_{33}^2 + 12e_{33}(e_{31} + 2e_{15}) + 8(e_{31} + 2e_{15})^2)(k_B T)^4 \quad (6.12)$$

and

$$F_{TA}^D(T) = \frac{\pi^2}{15n\hbar^3\sigma_{xx}\rho v_t^3}\frac{4}{105}(24e_{15}^2 + 8e_{15}(e_{33} - e_{31} - e_{15}) + 3(e_{33} - e_{31} - e_{15})^2)(k_B T)^4 \quad (6.13)$$

respectively, where  $\sigma_{xx}$  is the longitudinal conductivity and  $n$  is the carrier density.

The power relaxation rate is  $P_e = \sum_\lambda F_\lambda(T_e) - F_\lambda(T_l)$  with  $\lambda$  summed over all phonon modes. In piezoelectric coupling, only two phonon modes should be counted

[109]. We performed this calculation for all of our samples. When plotted in a logarithmic scale, the calculated  $P_e$  for our samples did not show obvious differences from each other. Therefore, for the purpose of clarity, we only show a representative calculation for our lowest mobility sample in the clean and dirty limit in Fig. 6.6. The following values were used in the calculations:  $n=3.41\times10^{12}\text{cm}^{-2}$ ,  $m^*=0.21m_e$ ,  $\rho=6150\text{ kg/m}^3$ ,  $\epsilon=10\epsilon_0$ ,  $v_l=6560\text{m/s}$ ,  $\nu_l=2680/\text{s}$ ,  $\sigma_{xx}=0.00468/\Omega$ ,  $e_{15}=-0.3\text{ C/m}^2$ ,  $e_{31}=-0.49\text{ C/m}^2$ ,  $e_{33}=0.73\text{ C/m}^2$ , [102,110]. It is important to emphasize that there are no fitting parameters in our calculations.

When comparing our results with the previous reports of energy relaxation by hot electrons [100-103], we find that our power dissipation rate per electron is one or two orders of magnitude below those results obtained by using SdH as a thermometer. When we compare our experimental data with theory, a better agreement with the dirty limit calculation was achieved; the power dissipation rate per electron scales as  $P_e\sim T_e^4$ . This dirty limit effect has also been observed in low mobility GaN 2DEG samples [100,103]. However, our electron mobilities are sufficiently high such that according to  $qI_e$  criteria, our samples should be in the *clean limit* where a  $P_e\sim T_e^5$  should be expected. This is contradictory to what we have observed.

In addition to energy relaxation by e-p coupling, other effects such as thermal boundary resistance can also play a significant role in determining the temperature of hot electrons. Based on noise measurements on GaN films grown on sapphire substrates, we have previously observed a large deviation between the measured and calculated electron temperatures from which we extracted a thermal boundary resistance for such an interface [111]. However, for the 2DEG samples, the total power

dissipation rate is small enough that we estimate at high bias conditions, when the electron temperature is above 10 K, the contribution due to the thermal boundary resistance is only about 0.01 K. Thus, the thermal boundary cannot explain the observed discrepancy between the measurement and theory.

## 6.7 Conclusion

In summary, we used WAL as a thermometer to measure the electron temperature,  $T_e$ , as a function of the bias current in wurtzite  $\text{Al}_{0.15}\text{Ga}_{0.85}\text{N}/\text{AlN}/\text{GaN}$  and  $\text{Al}_{0.83}\text{In}_{0.17}\text{N}/\text{AlN}/\text{GaN}$  heterostructures with polarization induced 2DEG in the Bloch-Gruneisen regime. We find that the power dissipated rate per electron,  $P_e$ , is proportional to  $T_e^4$  due to piezoelectric acoustic phonon emission by hot electrons. We calculated power dissipated per electron,  $P_e$ , as a function of  $T_e$  without using any adjustable parameters for both static and dynamic screening cases of piezoelectric electron-phonon coupling. In the temperature range of this experiment, the static screening mechanism is expected to be applicable; however, our data are in better agreement with the dynamic screening mechanism.

## CHAPTER 7

### OPERATION OF A SINGLE ELECTRON TRANSISTOR PLACED ON STACKED INTEGER QUANTUM HALL LAYERS AS A MAGNETOMETER

#### 7.1 AlGaAs/GaAs heterostructures and the quantum Hall effect

In our previous chapters, we focused mainly on GaN systems. In this chapter, we will discuss our work in the AlGaAs/GaAs heterostructure system. The main advantage of AlGaAs/GaAs heterostructures is that AlGaAs is almost lattice matched to the GaAs substrate. Thus, very high electron mobilities can be achieved in the AlGaAs/GaAs, system. This material system has been extensively used to study a variety of physical phenomena such as the integer quantum Hall effect (IQHE) and fractional quantum Hall effect (FQHE).

2D electron systems have been studied because of their unique states. The main physics of integer and fractional quantum Hall liquids are relatively well understood. When a perpendicular magnetic field is applied to the 2DEG and there are an integer numbers of electrons for each magnetic flux quanta (the ratio is called the filling fraction  $\nu$ ), the 2DEG will condense into an integer quantum Hall liquid (IQHL) at low temperatures, which can be viewed as an insulator since the Fermi level is not occupied [112-113]. Electron transport is mainly by edge states as there are no extended states at the bulk of the two-dimensional systems. [114] However, the role of bulk and edge currents has long been debated. There are various phenomena, such as scaling[115] and breakdown[116] of the integer quantum Hall effect, that cannot be described by the

edge state picture alone. It has been shown [117-120] that in certain situations the bulk states below the Fermi energy and the presence of bulk currents were also important and significant. Recent experiments performed by single electron transistors placed on IQHLs also reveal that, associated with the sweep of the magnetic field [119-120] or the gate voltage, the two-dimensional electron system can be placed in a non-equilibrium state where the chemical potential is not constant over the IQHL. Previous experiments from our group, reveal that at very low temperatures, the sample can stay in a non-equilibrium state over many hours [cite Farina's thesis]. During this time bulk currents proportional to the gradient of the chemical potential are expected to flow in the IQHL.

Motivated by these experiments [120-121], we calculated the bulk currents associated with a changing magnetic field in the integer quantum Hall regime. The total bulk current density is found to scale quadratically with the number of Landau levels below the Fermi energy. Most remarkably, we show when the number of Landau levels is much greater than the inverse fine structure constant  $1/\alpha = 137$ , these bulk currents can screen the additional magnetic field. Unfortunately, the integer quantum Hall effect has not been observed at very high filling fractions mainly due to disorder and non-uniformities in carrier density. However, we predict the screening of the additional magnetic fields can be achieved by stacking integer quantum Hall layers which is easy to realize by growing multiple quantum well structures.

## 7.2 Charge imbalance and long lived bulk currents

In an IQHL, the off-diagonal conductivity at a filling fraction  $\nu = n$  is quantized as  $\sigma_{xy} = ne^2/h$  whereas the diagonal conductivity  $\sigma_{xx} \approx 0$ . That means the bulk currents

flow perpendicular to the electric field on the IQHL plane. When the 2DEG is in an IQHL state with a perpendicular time varying magnetic field  $B_I(t)$  applied in addition to a static magnetic field  $B_0$ , the induced electrical field  $E_{ind}$  should follow

$$\frac{\partial \Phi_B(t)}{\partial t} = -\oint \vec{E}_{ind} \cdot d\vec{l}. \quad (7.1)$$

where  $\Phi_B$  is the magnetic flux. Then the response current in IQHL is given by  $|J_{ind}| = \sigma_{xy} |E_{ind}|$ , therefore

$$\oint \vec{E}_{ind} \cdot d\vec{l} = \int \vec{J}_{ind} \cdot dl \hat{n} = \frac{h}{ne^2} I_{ind}, \quad \Delta Q = \int I_{ind} \cdot dt = ne^2 \Delta \Phi_B / h, \quad (7.2)$$

where  $\Delta Q$  is the change in charge and  $\Delta \Phi_B$  is the change in magnetic flux. For simplicity, let us assume that the 2DEG is disk shaped located in the x-y plane with radius  $R$  and  $\Phi_B(t)$  is in the z direction (see Fig. 7.1). At low filling fraction  $n$ , the additional  $\Delta \Phi_B$  will penetrate uniformly through the IQHL and the induced charge  $\Delta Q$  will follow equation (7.2), which means that for every addition of magnetic flux there will be  $n$  electrons entering the IQHL.

To quantify the response of the IQHL to a changing magnetic field, we consider a simple case where the additional external magnetic field is swept from 0 to  $B_I$  as illustrated in Fig. 7.1. As we have shown above, Faraday's law of induction implies that associated with a changing magnetic field there must be motion of charges in and out of an IQHL. At low filling fractions, the additional external magnetic field will penetrate uniformly throughout the 2DEG and according to Eq. (7.2), there will be a uniform excess charge with a charge density of  $-neB_I/(h/e)$  throughout the 2DEG. At very low temperatures, the excess charge is expected to be nearly frozen, since  $\sigma_{xx} \approx 0$  and the

sample will be in a nonequilibrium state as the chemical potential of the 2DEG will no longer be uniform.

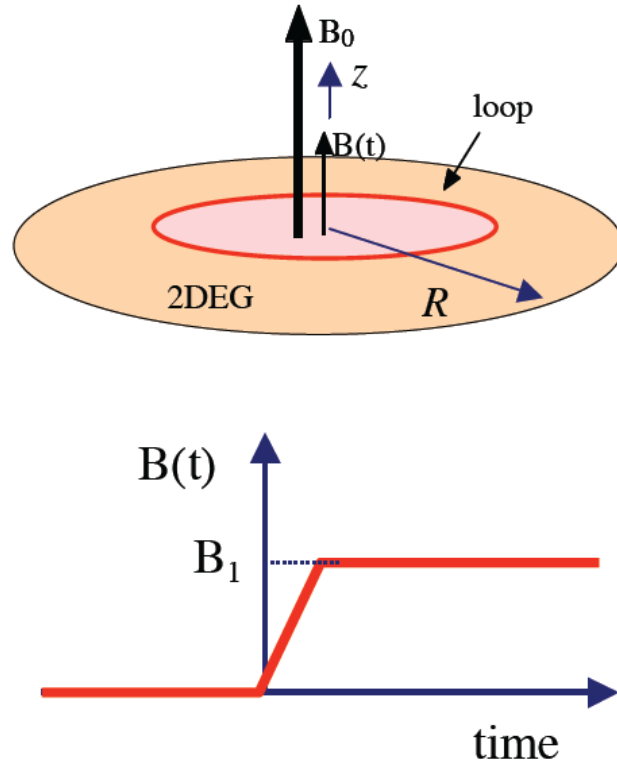


**Fig.7.1:** A schematic sketch of a 2DEG in a perpendicular magnetic field is shown above. The time dependence of the additional external magnetic field  $B(t)$  is illustrated below.

The induced electric field caused by  $\Delta Q$  follows Coulomb's law and the radial component  $E_r(r)$  is

$$E_r(r) = \frac{1}{4\pi\epsilon_0} \int_0^R \int_0^{2\pi} \frac{\sigma(r')r'(r - r'\cos\theta)d\theta dr'}{\left[(r - r'\cos\theta)^2 + (r'\sin\theta)^2\right]^{3/2}}, \quad (7.3)$$

where  $\epsilon_0$  is the permittivity,  $\sigma(r)$  is the excess charge density, and  $\theta$  and  $r'$  are the integration variables. For a uniform charge density  $\sigma(r) = \sigma$ , the radial electric field  $E_r(r)$  is proportional to  $r$  near the center of the 2DEG and has a logarithmic divergence at the edge of the 2DEG ( $r = R$ ). The logarithmic divergence is illustrated in Fig. 7.2, where

the radial electric field  $E_r(r)$  calculated at different distances just above the 2DEG is shown. To avoid the logarithmic divergence we will calculate the radial electric fields at height  $z=0.001R$ .

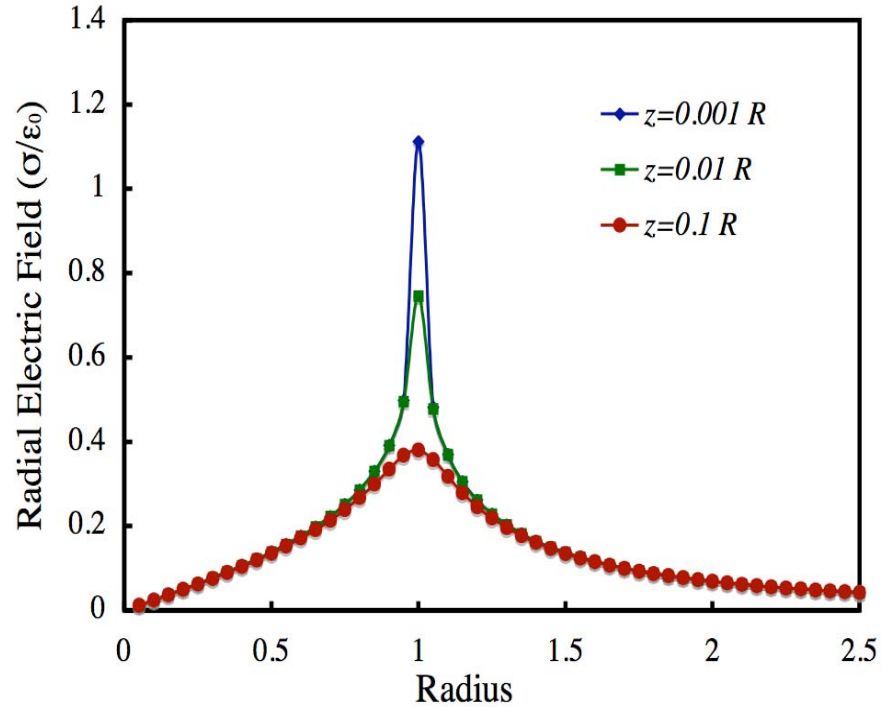


**Fig.7.2:** The radial electric field at different distance above a uniformly charged disk of radius  $R$  and charge density  $\sigma$ .

The associated persistent current  $j_\theta(r)$  caused by  $E_r(r)$  would flow perpendicular to  $E_r(r)$  as

$$j_\theta(r) = \sigma_{xy} E_r(r) = E_r(r) n e^2 / \hbar, \quad (7.4)$$

The axial component of the corresponding induced magnetic field  $B_z(r)$  is

$$B_z(r) = \frac{\mu_0}{4\pi} \int_0^{2\pi} \int_0^R \frac{j_\theta(r') r' (r - r' \cos \theta) d\theta dr'}{\left[ (r - r' \cos \theta)^2 + (r' \sin \theta)^2 \right]^{3/2}}. \quad (7.5)$$

Similar to the electric field there is a logarithmic divergence of the magnetic field at the edge of the 2DEG. The axial component of the magnetic field calculated at different distances just above the 2DEG is shown in Fig. 7.3.

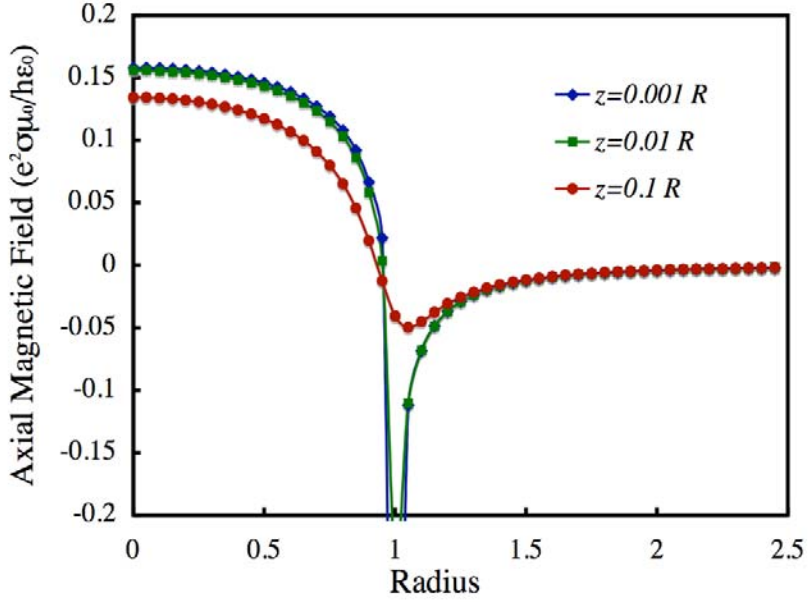


**Fig.7.3:** The axial magnetic field generated by the persistent bulk currents at different distance above a uniformly charged disk of radius  $R$  at a filling fraction  $v=1$ .

The calculation is done for a filling fraction of  $v=1$ . Near the center of the disk where the divergence is not significant the axial component of the magnetic field is

$$B_z(0) \approx 0.16(e^2 \sigma \mu_0 / h \epsilon_0), \quad (7.6)$$

Assuming a uniform charge density of  $\sigma = -eB_1/(h/e)$ , we get

$$B_z(0) \approx -0.16(e^2 / h)^2 (\mu_0 / \epsilon_0) B_1 = -0.64\alpha^2 B_1, \quad (7.7)$$

where  $\alpha = 1/137$  is the fine structure constant. This screening field  $B_z$  might look tiny compared to the original field  $B_1$ , but as  $v$  increases, the induced  $B_z$  will scale as  $v^2$  for a large  $v$ , and cannot be ignored in that case.

### 7.3 Screening of additional magnetic field at high filling fractions

At high filling fractions the additional magnetic field will not penetrate uniformly into the IQHL as some of the field will be screened by the persistent bulk currents. The excess charge density will no longer be uniform, but be given by

$$\sigma(r) = -ne^2(B_1 + B_z(r))/h. \quad (7.8)$$

According to (7.8), we can roughly estimate the relation between the induced charge and the magnetic field  $B_1$ . If we just assume that the induced charge and induced magnetic field both are uniform, they must obey

$$\sigma = -ne^2(B_1 + B_z(r))/h \sim -ne^2B_1/h + 0.64\alpha^2n^2\sigma. \quad (7.9)$$

Therefore we get

$$\sigma \sim \frac{n\sigma_0}{1 + 0.64\alpha^2n^2} \quad (7.10)$$

where  $\sigma_0 = -e^2B_1/h$  is a constant. From this equation we can see that the induced charge will reach its maximum value when the filling fraction  $n$  is close to  $1/\alpha=137$ . The total magnetic field  $B_t \sim \sigma h/(ne^2)$  will be close to zero when  $n$  is a large number, which also means that the IQHL can perform like an almost perfect diamagnet at large filling fraction  $v$ .

To calculate the induced charge more precisely for large  $v$ , since  $\sigma(r)$  will not be uniform in reality, we have to run the iteration from equations (7.2) to (7.9) to calculate the screening field. The self-consistent result is shown in Fig. 7.4.

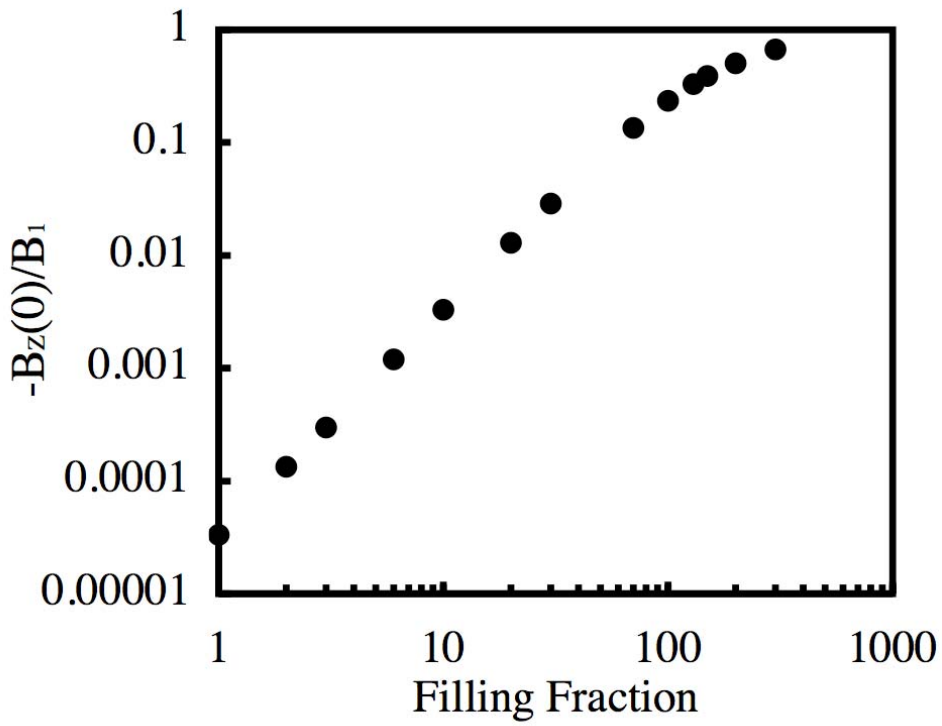


**Fig.7.4:** The ratio of the magnetic field generated by the bulk currents at the center of the disk  $B_z(0)$  and the additional external magnetic field  $B_1$  versus filling fraction.

At low filling fractions the magnetic field due to bulk currents is found to scale as  $B_z(0) = -0.64n^2\alpha^2B_1$ . On the other hand, at filling fractions when  $n \sim 1/\alpha$ , the magnetic field generated by the bulk currents is similar in magnitude to that of the additional external magnetic field. Finally, at very high filling fractions where  $n \gg 1/\alpha$ , the bulk currents are expected to fully screen the additional external magnetic field. Notice the above calculation can also be applied for the stacked layers of IQHL as long as the spacing between the layers is much smaller than the radius of the 2DEG. In this case the effective filling fraction number would be  $nm$  instead of  $n$ , where  $m$  is the numbers of stacks.

It is important to make a distinction between the diamagnetism of stacked layers of IQHLs and the perfect diamagnetism of superconducting systems. First, the integer quantum Hall effect is a high magnetic field phenomenon and the diamagnetism discussed in this chapter is only relevant to the additional external magnetic field. Second, at any finite temperature, the diagonal conductivity is close to but not zero. Thus, over long time scales the magnetic field will penetrate into the sample. And finally, there is not an effect analogous to the Meissner effect in stacked layers of IQHLs. When the stacked layer is cooled down with the additional external magnetic field the excess magnetic field will penetrate uniformly throughout the sample. The sample will be in equilibrium and there will be no excess charge density or bulk currents.

We note that the persistent excess charge in the IQHL associated with the additional external magnetic fields can also lead to an interesting device application: an electrometer, with a single electron transistor placed on top of stacked IQHL layers, can work as a magnetometer. Such a magnetometer can operate at very high magnetic fields where the superconducting quantum interference devices (SQUIDs) cannot operate.

#### 7.4 Stacked quantum hall layers and single electron transistor sample

In order to test this screening effect and achieve the predicted magnetometer, we decided to use a stacked quantum well sample with 25 identical layers. At low temperatures and certain magnetic fields, the 2DEG acts as an IQHL and a single electron transistor (SET) can be used to monitor the local chemical potential in the IQHLs associated with the changing magnetic field [119-124]. Owing to the high

charge sensitivity of the SET and the unique response of the 2DEG to the magnetic field, this hybrid device can also perform as a sensitive magnetometer operating in a large static magnetic field background.

The heterostructure was grown by Prof. Rachel Goldman's group in the Materials Science Department by MBE on a GaAs substrate with 25 identical stacked quantum well layers which have a carrier density  $4.32 \times 10^{11} \text{ cm}^{-2}$  per layer (see Fig.7.5).

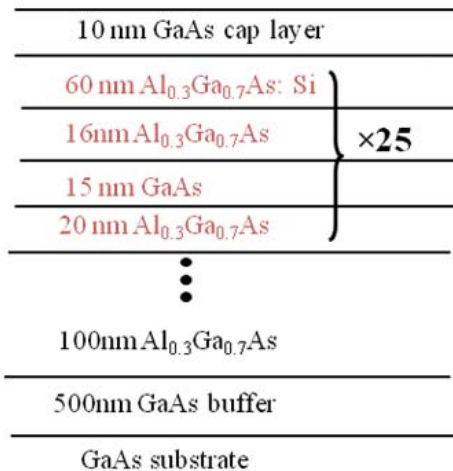


**Fig.7.5:** Multiple layers sample structure with 25 identical AlGaAs/GaAs layers.

Each layer contains 20 nm undoped Al<sub>0.3</sub>Ga<sub>0.7</sub>As, 15 nm GaAs, 16 nm Al<sub>0.3</sub>Ga<sub>0.7</sub>As and 60 nm Si-doped Al<sub>0.3</sub>Ga<sub>0.7</sub>As. A 10nm GaAs layer was grown on top to cap the whole heterostructures. Four ohmic contacts were made on the corners of a square sample to enable the Van der Pauw measurement for the 2DEG. We should point out that to make such a multiple-layers sample is not a trivial task and special care should be given to the growth conditions. The Ohmic contacts should also penetrate

deep into the sample layers to make the layer to layer contact resistance as low as possible.

The sample was characterized by magneto-transport measurements and the corresponding carrier density and mobility were extracted. In Fig. 7.6, we plotted the longitudinal and Hall resistance versus magnetic field for the multiple-layers 2DEG sample. Clear quantum Hall plateaus (marked by the grey shaded area) have been shown and the carrier density is extracted as  $4.32 \times 10^{11} / \text{cm}^2$  per layer.

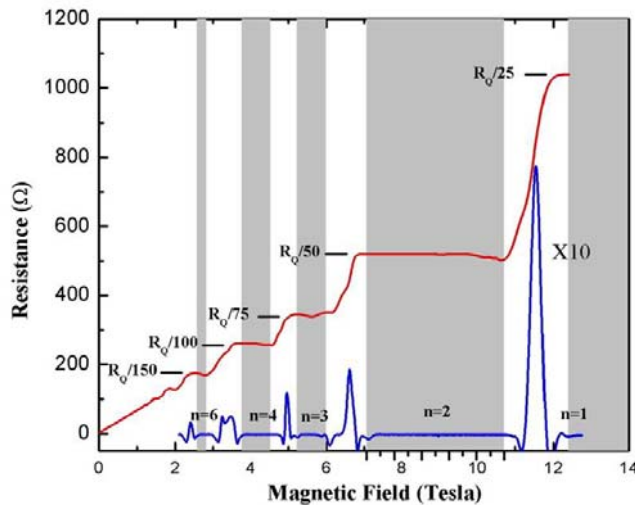


**Fig.7.6:** Longitudinal and Hall resistance versus magnetic field for multiple layers 2DEG sample. Clear quantum hall plateau (marked by the grey shaded area) has been shown and the carrier density is extracted as  $4.32 \times 10^{11} / \text{cm}^2$  per layer.

An aluminum SET was capacitively coupled to the 2DEG by the double shadow-evaporation technique. In Fig. 7.7(a), we plotted the steps for making double shadow evaporation of Al film.

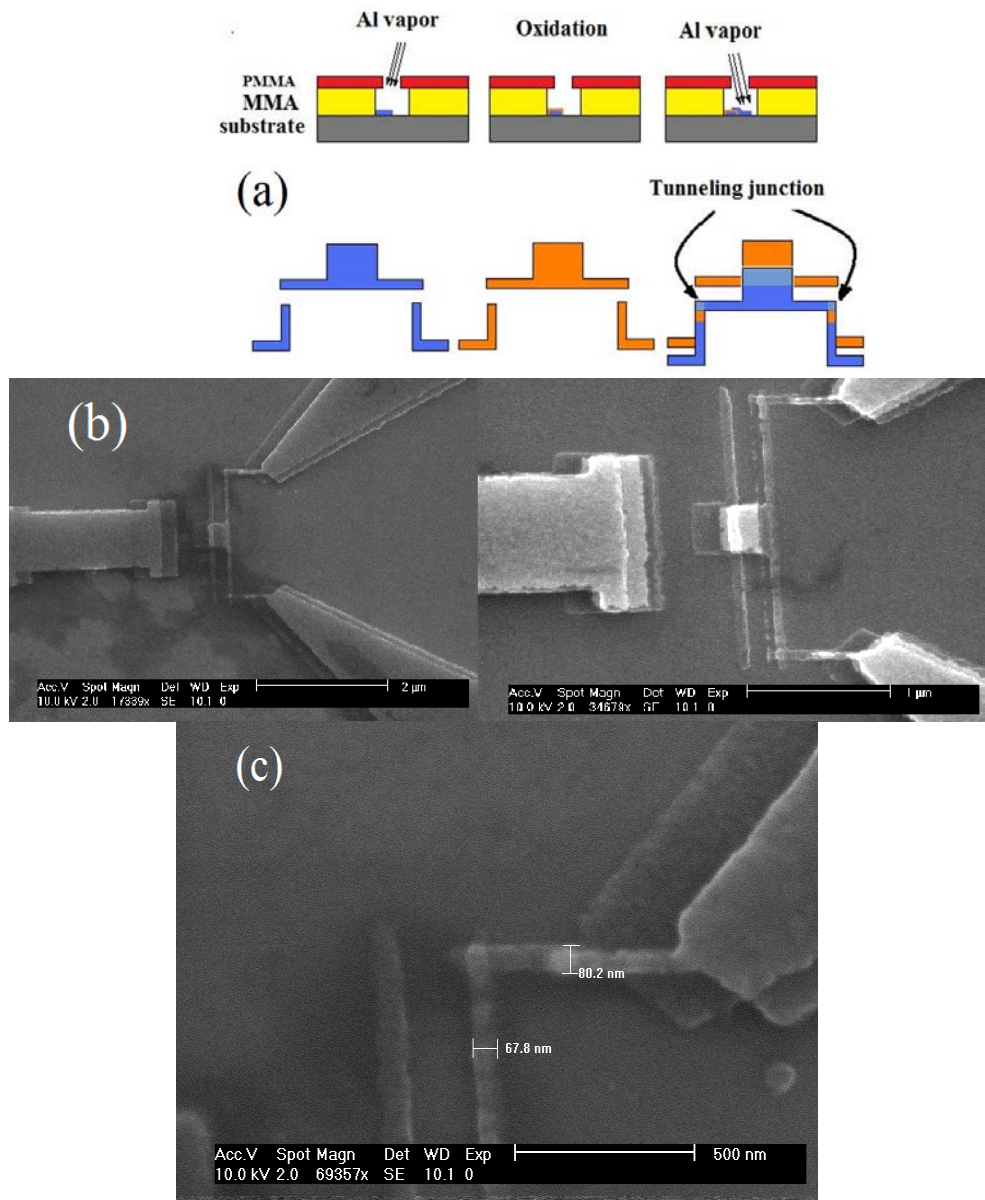


**Fig.7.7:** (a) The double shadow evaporation of Al film. Between the two evaporation, an oxidation step was performed to form the tunnel junctions. (b) The SEM image of the SET. (c) The SEM image of the tunnel junction.

First, a two layers e-beam resist was deposited on the surface of the sample. We used the e-beam lithography to draw the sample patterns. After development, the sample was put into a home-made bell-shaped vacuum chamber to do the Al evaporation. The first layer ( $\sim 40$  nm) of Al film was deposited at a predetermined

angle. After that, an oxidation step was performed to form a layer of insulating  $\text{Al}_2\text{O}_3$ . Finally, another Al layer was deposited at a different angle to form the SET tunnel junctions. In Fig. 7.7 (b) and (c), The SEM images of the SET were shown. An aluminum metal gate was deposited 400 nm away from the SET island to adjust the electric potential of the SET. All the measurements were performed in a dilution refrigerator at base temperature 20mK. We characterized the SET at different gate voltages by the corresponding DC current-voltage (I-V) measurements as shown in Fig. 7.8. Clear Coulomb-blockade behavior was derived and the nonlinear operation regime of the SET was observed as the gate voltage was changed from -25 mV to 25 mV.

Shown in the insert of Fig. 7.8(b) is a typical Coulomb-blockage oscillation (CBO) of the SET differential conductance ( $dI/dV$ ) versus the gate voltage measured by an AC lock-in technique at magnetic field 0.8 Tesla. At this magnetic field, the 2DEG is conductive liquid and the SET operates at normal condition (not superconductor), which is indicated by the low level of the noise and well-behaved CBOs. We should point out that the 2DEG can also be used as a gate for the SET, and similar CBOs were observed by scanning the 2DEG voltage. In our measurement, when the magnetic field increases, the 2DEG starts to change alternatively between the conductive state and the insulator IQHL starting from filling factor 8. As the 2DEG approaches IQHL, the 2DEG gradually loses its ability to screen local charge fluctuations and the differential conductance ( $dI/dV$ ) signal of SET becomes noisy. As well both the metal gate and the 2DEG gradually lose their ability to work as gates because the 2DEG around the SET becomes insulating. Owing to the extremely low conductivity of an IQHL, the charge redistribution took a long time to reach equilibrium. The equilibration time of hours has

been observed due to  $\sigma_{xx} \sim 0$ , which means that electrons respond to the electric field extremely slowly.

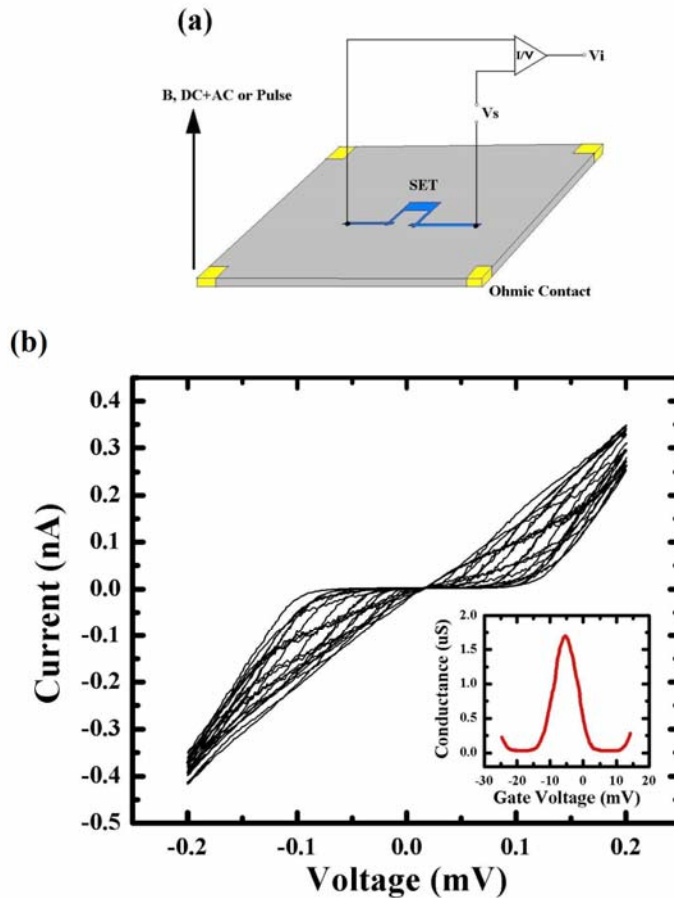


**Fig.7.8:** (a) Illustrative sketch of a SET coupled to a 2DEG sample. (b) Current versus voltage of the SET at different gate voltages at 0.8 Tesla. In the insert: differential conductance ( $dI/dV$ ) versus gate voltage with a Coulomb blockage oscillation shown.

When we increase the magnetic field, the 2DEG changes alternatively between the conductive state and the IQHL state. As the 2DEG approaches to IQHL,  $\sigma_{xx} \sim 0$  and  $\sigma_{xy} \sim nme^2/h$ . The linear relationship (Eq. 7.2) between  $\Delta Q$  and  $\Delta\Phi_B$  will enable us to detect small time-varying magnetic field by monitoring the change of the local potential

(charge density). To enhance this conversion ratio between  $\Delta Q$  and  $\Delta\Phi_B$ ,  $m=25$  layers of quantum wells structure was used. Fig. 7.9 (a) shows the charge induced by changing the magnetic field. In the IQHL, after the charges are driven in by the magnetic field, the local chemical potential is in nonequilibrium and will go back to the equilibrium state at a rate governed by  $\sigma_{xx}$ .

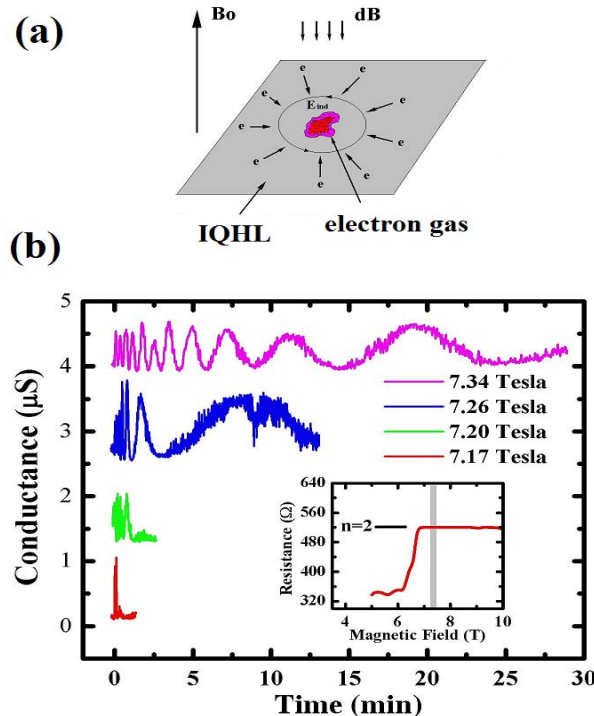


**Fig.7.9:** (a) A sketch of driven-in current induced by changing a small amount of magnetic field  $dB$ . (b) CBOs initiated by ramping up a 0.11 mT magnetic field at different quantum plateau positions from 7.17 to 7.34 Tesla, the range of which is indicated by grey shade in the insert.

The SET signal reflects the local chemical potential change (charge redistribution) and the CBO is observed in the conductance measurement. Notice it would take long time for the 2DEG to relax back to equilibrium. Fig. 7.7 (b) shows the

typical CBO as a 0.11 mT magnetic field applied at time 0 at different positions within the  $n=2$  quantum plateau. We name this type of measurements a DC-pulse measurement since a DC magnetic field pulse is applied. To reduce the noise, the superconductor magnet was set to persistent mode and an additional metal coil was used to vary the magnetic field. The mutual inductance between the metal coil and the superconductor magnet was calibrated correspondingly. CBOs from 2 to 12 oscillations were observed in a quantum plateau from 7.17 to 7.24 Tesla (see Fig. 7.9).

## 7.5 Charge/ magnetic field ratio measured by the DC pulse and AC techniques

By counting the number of oscillations, we can get a charge/magnetic-field ( $e/B$ ) conversion ratio because every CBO corresponds to an electron moving into or out of the SET capacitor. Strikingly in such a narrow range from 7.17 to 7.24 Tesla the equilibration time rises dramatically from a minute to 30 minutes. Deep into the quantum hall plateau, this relaxation time becomes immeasurably long due to  $\sigma_{xx} \sim 0$  in the IQHL; therefore the DC pulse measurement is no longer applicable deep into the quantum hall plateau.

To overcome this long relaxation time, we used a small AC magnetic field to modulate the charge distribution and the responding conductance of the SET was monitored at the modulation frequency (AC measurements).

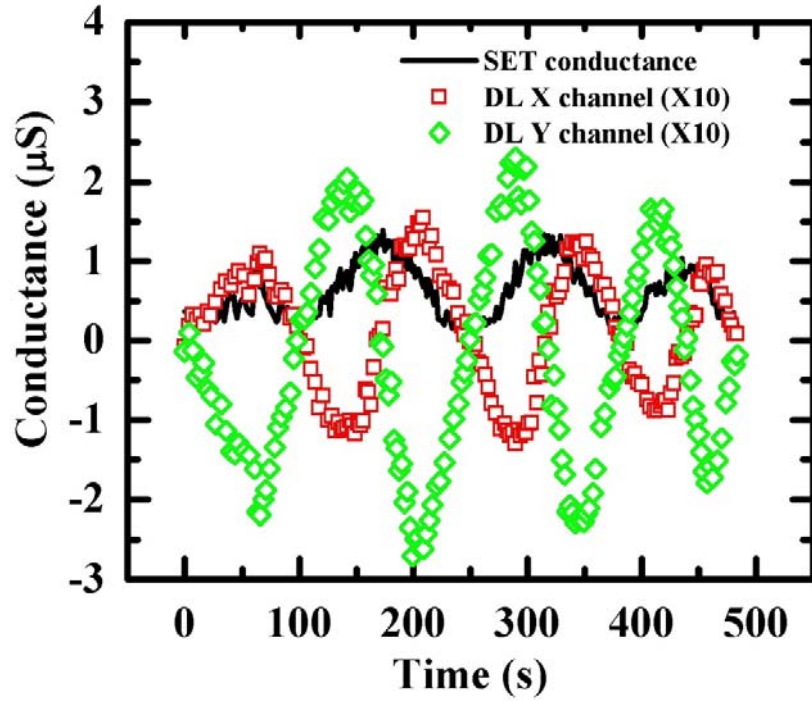


**Fig.7.10:** Differential conductance of the SET versus time with an AC magnetic field modulated at frequency 4.137 Hz with magnitude 170 nT. The black curve is SET's CBO curve. The square and diamond scatters are the responses (amplified by 10) in both X and Y channels of the second lock-in amplifier at  $f=4.137$  Hz responding to the 170 nT magnetic excitation.

In this AC technique, the first lock-in amplifier was used to monitor the conductance at a high frequency  $f_1$ . The output signal from the first lock-in amplifier was the input to the second lock-in amplifier that applied a small AC modulating magnetic field at a low modulation frequency  $f_2$ . The small AC magnetic field will induce an AC response of conductance of the SET at modulation frequency  $f_2$ . In our experiment, we used an AC magnetic field with rms value of 0.17  $\mu\text{T}$  with  $f_1=212.2$  Hz and  $f_2=4.137$  Hz. Fig. 7.10 shows the AC measurement at 2.668T within the filling factor=6 quantum plateau.

In Fig. 7.10, the black line is the SET conductance versus time measured by the first lock-in amplifier, and the square and diamond scatters represent the simultaneous AC signal in both X and Y channels of the second lock-in amplifier, where the signal has been magnified 10 times for clarity. The total responding conductance signal  $\Delta G$  is  $\sqrt{X^2 + Y^2}$  multiplied by a low-pass filter correction factor. The peak value of the AC signal was used to calculate the  $e/B$  conversion ratio of the SET. Usually one CBO corresponds to an effective charge moving in or out of the area monitored by the SET. To do so we must calculate the slope of CBOs' curve where the AC signal peak occurs and convert it to the conductance/charge by using  $G/e = dG/dt \times T$ , where  $dG/dt$  is the slope of CBOs' curve and  $T$  is the period of CBO. Then  $\frac{\Delta e}{\Delta B} = \frac{\Delta G}{\Delta B} \times \frac{e}{G}$  was used to calculate the  $e/B$  ratio of SET in the units of  $e/\mu\text{T}$ , where  $\Delta G$  is the response signal at peak value and  $\Delta B$  is the amplitude of the AC magnetic field. A small  $\Delta B$  of  $0.17 \mu\text{T}$  was carefully chosen to keep this measurement in the linear region. Sometimes the period  $T$  would drift as the charge distribution relaxed back to equilibrium, thereby introducing an additional error. To correct this, we found a strong correlation between the  $G/e$  value and the peak value of the SET conductance. We can calculate a corrected  $G/e$  value by using a simple statistical regression model with respect to the peak value of the SET conductance. The resulting  $e/B$  conversion ratio of the sample at different quantum plateau positions for both the DC and AC measurements are shown in Fig. 7.11 as a function of inverse magnetic field. The quantum hall plateau position is labeled out for clarity. We find that the AC measurements results are consistent with the DC measurements.

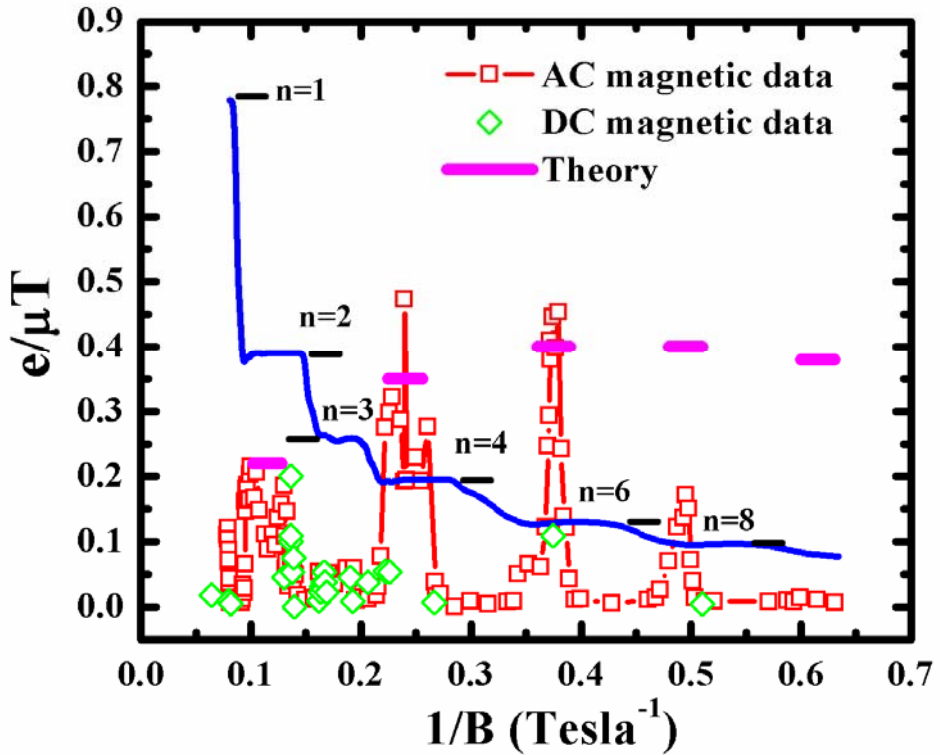


**Fig.7.11:** Charge/magnetic field conversion ratio versus inverse magnetic field. Deep into the quantum plateau, the DC measurement does not work due to long relaxation time, while the AC measurement can still get reasonable data. Also shown is the calculated data which agrees with our experiment up to the filling fraction 6.

## 7.6 The IQHL and SET composite device performs as a magnetometer

The advantage of the AC measurement is that it can cover the whole range of quantum plateaus while the DC measurement is not possible deep into the quantum hall plateaus due to the long relaxation times and noise. The result shows that the IQHL and SET composite device can perform as a magnetometer at filling factors  $n=1, 2, 3, 4, 6, 8$  and has a maximum  $e/B$  ratio at  $n=6$ . To verify the  $e/B$  ratio theoretically, we performed the calculations. By the method of image charges, the 2DEG area monitored

by the SET can be estimated effectively as a disk of  $\sim 2\text{-}4 \mu\text{m}$  in radius. According to equation 7.10, the maximum value of the  $e/B$  ratio occurs when the effective filling fraction  $=1/(0.8\alpha)=171$ . Then the maximum  $e/B$  is

$$(e/B)_{\max} = \sigma_{\max} \pi r^2 / eB \sim \frac{\sigma_0 \pi r^2}{0.8\alpha eB} = \frac{e \pi r^2}{0.8\alpha h} \quad (7.11)$$

where  $r$  is the radius. If we use  $r=2.5 \mu\text{m}$ , we will get the maximum  $e/B$  value as  $0.4 \text{ e}/\mu\text{T}$ , which agrees with our observation quantitatively (see Fig. 7.11). We also calculate the  $e/B$  ratio based on equation 7.10 and show the data in Fig. 7.11. Interestingly, according to the IQHL screening model (see equation 7.10),  $n=6$  ( $nm=150$ ) is the predicted filling fraction number (which is the closest number to the theoretical predicted filling fraction 171) in our experiment to get the maximum  $e/B$  ratio. Also according to the theory, we would expect the  $e/B$  ratio to (see equation 7.10) decrease monotonically after  $n=6$ , which is exactly what we observe in this experiment. Based on that, we conclude that this observation is direct evidence of the validity of our screening model of IQHL. On the other hand, we need to point out that the experimental value of the  $e/B$  ratio for filling fraction larger than 6 is much less than the calculated value (shown on Fig. 7.11), which might be due to the fact that at large filling fractions (low magnetic field) the IQHL has a relatively large  $\sigma_{xx}$  (not so insulating).

To estimate the sensitivity of the IQHL-SET device as a magnetometer, we performed a noise measurement for the SET at a position deep into the quantum plateau. In Fig. 7.12, we plot the noise level versus frequency at 7.09 Tesla (filling fraction  $n=2$ ).

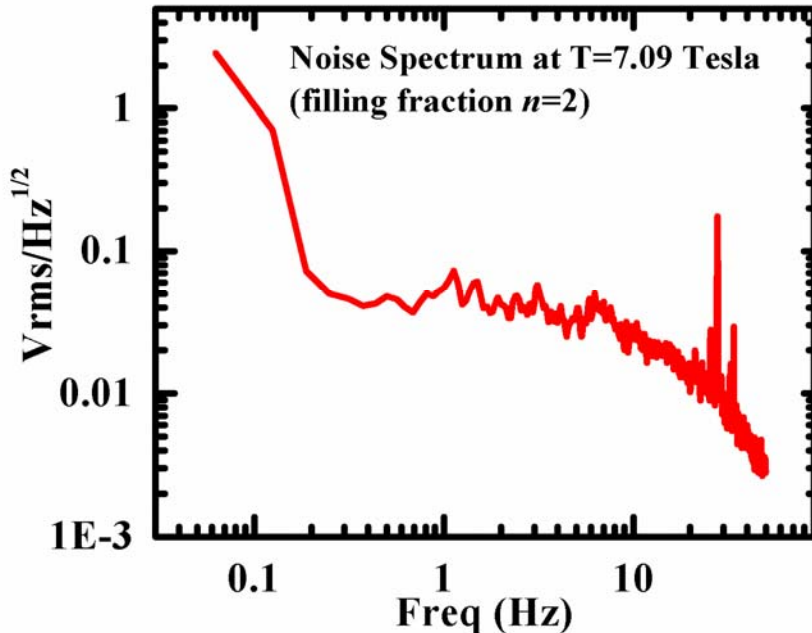


**Fig.7.12:** Noise level versus frequency at 7.09 Tesla (filling fraction  $n=2$ ). This data is taken by a spectrum analyzer with signal output from a lock-in amplifier which is measuring the differential conductance signal of the SET. The time constant of the lock-in amplifier is set to 10 ms.

This data is taken by a spectrum analyzer with signal output from a lock-in amplifier which is measuring the differential conductance signal of the SET. The time constant of the lock-in amplifier is set to 10 ms. Therefore the noise signal beyond frequency 100 Hz is actually cut off by the lock-in amplifier's low pass filter. In the noisy spectrum we observed the 1/f noise.

The typical noise spectrum shows a noise signal of  $0.04 \text{ Vrms}/\text{Hz}^{1/2}$  around 4 Hz, which corresponds to a value of  $0.067 \text{ e}/\text{Hz}^{1/2}$ . The best  $e/B$  ratio was achieved at filling factor  $n=6$  with a value of  $0.7 \text{ e}/\mu\text{T}$ . Therefore the maximum magnetometer sensitivity would be  $0.09 \pm 0.01 \mu\text{T}/\text{Hz}^{1/2}$ . Potentially this type of SET devices can be used as a

very sensitive magnetometer for detecting a small time-varying magnetic field in a high magnetic field environment. The combination of many 2DEG samples with different carrier densities (therefore different quantum plateau positions) will enable this device to cover a large range of DC magnetic fields.

## 7.7 Conclusion

In summary, we calculated the response of an IQHL to a small magnetic field and it was shown that when the effective filling fraction  $\nu > 1/\alpha = 137$ , the IQHL behaved like a perfect diamagnet. A SET placed on an IQHL with 25 identical quantum well structures can detect small time varying magnetic fields in a large constant magnetic field background, and the screening effect has been observed when the effective filling fraction  $\nu = 150$ . This device can also be used as a magnetometer. The equilibration times associated with small changes in magnetic field are found to be strongly dependent on the positions within quantum plateaus and become immeasurably long as we go deep into the quantum Hall plateaus. We characterized the SET magnetometer by DC and AC measurements. At  $T=20$  mK, the SET magnetometer worked at filling fractions up to  $n=8$  and was most sensitive at the filling fraction  $n=6$  with a maximum magnetometer sensitivity of  $0.09 \pm 0.01 \mu\text{T}/\text{Hz}^{1/2}$ .

# CHAPTER 8

## CHARGE MOTIONS DETECTED BY SINGLE ELECTRON TRANSISTORS IN QUANTUM HALL LIQUID

### **8.1 Topological quantum computation and quantum Hall liquids**

The promising computing ability of the quantum computer [125] has attracted intense research interest. A quantum computer relies on the interference and superposition of quantum states, which is usually referred to as quantum parallelism. In certain problems, such as factoring large numbers, the quantum computer has unique advantage over the traditional computer by using some special algorithms; therefore it can attack some computation tasks much faster than the traditional computer. More than that, some quantum information processes could also be used to simulate quantum many-body system and therefore achieve complicated simulations which are impossible to attack by traditional computation algorithms[126-127]. However, despite its great promise, it is extremely difficult to implement quantum computation in physical systems. The obstacle is clear: the unavailability of a perfect material system to create and manipulate quantum processes which are insensitive to local noise. Most proposed scenarios for quantum computing are based on microscopic systems such as cold atoms and quantum dots, which are vulnerable to local disturbances and suffer from a short coherence time which makes quantum computations impossible.

In this context, the emergence of topological quantum computation [128-129] was a particularly exciting as it potentially solves the problem of decoherence. The idea

of topological quantum computation utilizes the emergent properties of many-particle systems, more specifically the fractional quantum Hall liquid (FQHL), which are not vulnerable to local perturbations, to encode and manipulate quantum information. Lying at the heart of topological computation is a device called a quantum interferometer, which is an analog of the optical Fabry-Perot interferometer. In Fig. 8.1, we show the prototype diagram of a quantum interferometer, which is built on a FQHL sample with an antidot etched at the center. The current can travel either via path 1 or path 2 between the two leads. Those two tunneling paths can interfere with each other. When there are an even number of excitations (Laughlin's quasi-particles[5]) trapped in the antidot, there will be Aharonov-Bohm (AB) interference patterns (oscillations) observed in the magnetotransport measurement [130]. If an odd number of quasi-particles are trapped, there will be no interference patterns. However, even to implement this quantum interferometer turns out to be extremely difficult [131-132]. The obstacle comes from the precise control of the numbers of quasi-particles trapped in the antidot. In the FQHL, the two dimensional electron gases (2DEG) become basically an insulator; and it is hard to control the motion of quasi-particles by the electric field. Also, the motion of quasi-particles will suffer from the noisy environment. To overcome these problems, it is important to understand the dynamics of quasi-particles in the quantum Hall liquids (QHL).

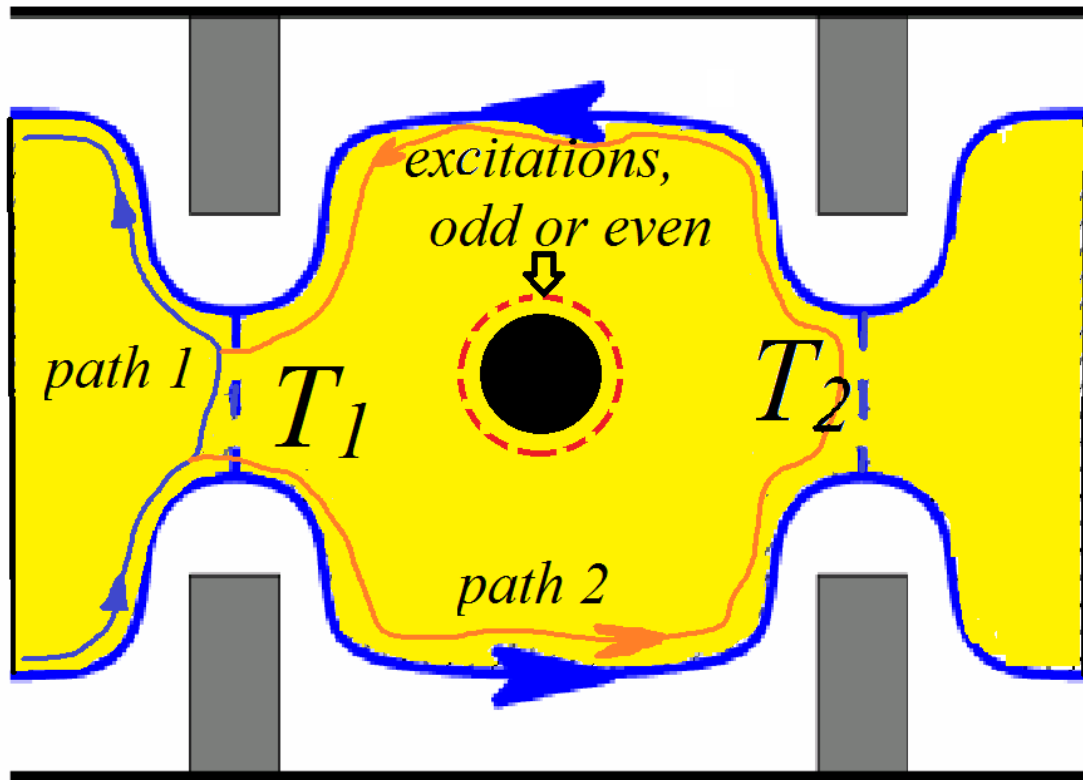


**Fig.8.1:** The quantum interferometer. The orange area is the fractional quantum Hall liquid. An antidot is etched at the center, which can trap excitations (quasi-particles).  $T_1$  and  $T_2$  are the transport matrixes. The current can travel by either path 1 or path 2 between the two leads. Those two tunneling paths can interfere with each other. When there are even number excitations (Laughlin's quasi-particles) trapped on the antidot, there will be Aharonov-Bohm(AB) interference pattern (oscillations) in the conductivity transport measurements as a function of magnetic field. If odd number quasi-particles are trapped, there will be no interference (AB oscillations).

## 8.2 The single electron transistors

In order to study the dynamics of excitations in the QHL, we need to observe the motion of charges in real time. As introduced in chapter 7, we used the single electron transistor (SET) to detect the charge movement in the QHL[102,119-120,123-124,133-134]. In chapter 7 we focused mainly on the response of multiple quantum

Hall layers to the magnetic field. In this chapter, we will focus on the quasiparticles' motion and the dynamics underneath.

The single electron transistors were fabricated by double shadow evaporation of Al as shown in chapter 7, Fig. 7.7. The requirements for the SET to work are very critical [135]. The first one is

$$\Delta E \cdot \Delta t = \frac{e^2}{2C} RC = \frac{e^2}{2} R > \frac{\hbar}{2}, \text{ therefore } R > \frac{\hbar}{e^2} = 25.9 \text{ k}\Omega, \quad (8.1)$$

where  $R$  and  $C$  are the tunnel junction's resistance and capacitance, respectively.  $R$  should be larger than 25.9 k $\Omega$ . From our experience, 100-400 k $\Omega$  would be ideal for tunnel junctions, which put a strict requirement for the thickness control of the oxidation process. The second requirement is

$$\frac{e^2}{2C} > kT \Rightarrow C < \frac{e^2}{2kT} \quad (8.2)$$

The capacitance should be as small as possible and the temperature should be as low as possible. To meet those conditions, we used electron beam lithography to write the SET pattern (~80 nm) and the sample was cooled down to 20 mK.

### 8.3 Charge motion detected by a single electron transistor in multiple QHL

The first sample used in this chapter is the same as that discussed in chapter 7. This sample is a multiple quantum well sample grown on a GaAs substrate with 25 identical stacked layers which has a carrier density  $4.32 \times 10^{11} \text{ cm}^{-2}$  per layer (see chapter 7). An aluminum SET was capacitively coupled to the 2DEG (see Fig. 7.7).

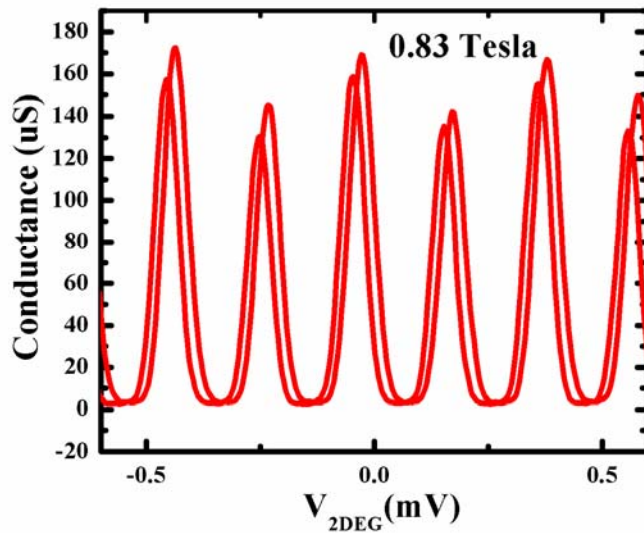
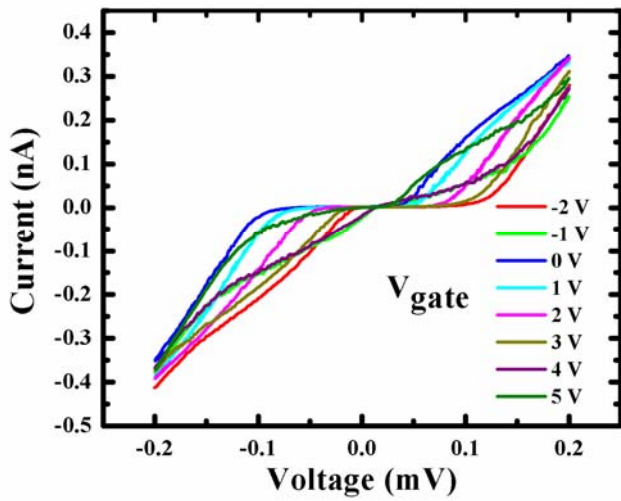


**Fig.8.2:** Upper: The SET current versus the SET voltage at different gate voltages. Lower: differential AC conductance measurements versus the 2DEG voltage. Interestingly in this diagram we found periodic double-peaked CBOs.

All the measurements were performed in a dilution refrigerator at a base temperature of 20mK. A metal gate was deposited which is used to change the local chemical potential around the SET. We characterized the SET at different gate voltages by current-voltage (I-V) measurements as shown in Fig. 8.2.

We also measured the differential conductance of the SET by using a lock-in amplifier. A small AC voltage (0.02 mV) was applied to the SET and the current signal was picked up by a current sensitive pre-amplifier. Clear Coulomb-blockade oscillation (CBO) behavior was observed (Fig 8.2). Each oscillation corresponds to one electron moving in or out of the area around the SET with a radius around  $\sim 2\text{-}4\mu\text{m}$  [121,136]. Both the metal gate and the 2DEG can be used as a gate to drive the CBOs. We should point out that the applied magnetic field is larger than 0.5 Tesla; otherwise the SET will be in superconductive state and the CBOs cannot be observed. Interestingly in this SET as we change the gate (or 2DEG) voltage, we observe periodic double-peak CBO patterns for reasons we do not understand.

At high magnetic fields, when the Fermi energy is in the middle of Landau levels, the 2DEG becomes a QHL. In the QHL regime, we cannot use the metal gate or 2DEG to change the local chemical potential near to the SET rapidly because the QHL is not conductive anymore, which means that the conductivity of the bulk,  $\sigma_{xx}$ , is very low when the Fermi energy is in the middle of Landau levels. Because the SET is capacitively coupled to the 2DEG, the response of the SET can be modeled by a RC circuit. The response time is characterized by the time constant  $R_Q C_S$ , where  $R_Q$  is the resistance of QHL and  $C_S$  the capacitance between the SET and 2DEG. Because the  $R_Q$  is large in a QHL, we would expect the SET to exhibit a long equilibration time [119,136-137] when we change the gate (or 2DEG) voltage.

As introduced in chapter 7, in the QHL regime the 2DEG becomes insulating and responds to electric field very slowly due to  $\sigma_{xx}\sim 0$ . The transverse conductivity matrix  $\sigma_{xy}$  is equal to  $ne^2/h$  at an effective filling fraction  $\nu=n$ , where  $e$  is the electron

charge and  $h$  is the Planck constant. That means for every added quantum flux into the QHL (see chapter 7), there will  $n$  electrons moving from the edge of the sample (Ohmic contacts) to the bulk. This process happens very quickly and cannot be detected by the SET. As those charges accumulate in the QHL bulk, the chemical potential is in non-equilibrium; therefore those extra charges in the bulk will move back to the sample edge (Ohmic contacts). This extra charge relaxation is a slow process driven by the extra electric field, and the time constant is governed by  $R_Q C_S$ . This slow process can be monitored by the SET.

To detect this process, we performed the experiment in a dilution refrigerator with a base temperature of 20 mK. The whole set-up is stored in a copper screen room to reduce the electro-magnetic interference. We monitored the SET's differential conductance by a low frequency lock-in amplifier and a current sensitive pre-amplifier. When the charge density or local chemical potential around the SET change, the resulting CBOs will be observed in the SET's conductance. In an intuitionnal picture, one CBO corresponds to a charge moving in or out of the SET area.

In this experiment, we first brought the 2DEG to the QHL state by applying a constant magnetic field using the superconducting magnet. Then we applied a magnetic pulse by using a second coil and observed the response of the QHL by monitoring the conductance of the SET. In this experiment, we always label the time of applying the magnetic pulse as the time 0. Some typical results are plotted in Fig. 8.3 - 8.6 for quantum plateau  $n=6, 4, 3$  and  $2$  respectively. In those figures, the upper diagram is the SET conductance versus time when an 11mT magnetic pulse applied at time 0 at  $v=n$  quantum plateau and the constant magnetic field is labeled to indicate the position in

the quantum plateaus. When an 11 mT magnetic pulse is applied at time 0, we see an immediate response in the SET's conductance, which is due to the extra charges brought immediately by the magnetic pulse. After the time 0, those extra charges start to relax back to the sample edge through the QHL bulk, which is a slow process. Therefore we observed the resulting conductance CBOs signals of the SET. Each CBO corresponds to a charge moving out of the SET area in this experiment. After the time 0, initially the SET's conductance signal oscillates in a relative fast pace because a lot of extra charges move out. After some time ( $\sim$ 100 seconds), those CBOs slow down due to the less extra charges left in the QHL bulk. Therefore in this experiment what we observed was the relaxation process of those extra charges brought by the 11 mT magnetic pulses into the QHL back to the sample edge. By counting the number of oscillations (peak or valley positions) in the SET's conductance signal, we can extract the number of charges moving out of the SET area. In the bottom diagrams of Fig 8.3-8.6, we plotted the number of oscillations obtained by counting the peak (or valley) positions versus the time. In the insert we label the magnetic field position (red line) inside the quantum plateau  $v=n$ . From these figures, we can see that the extra electrons start to move out immediately after the pulse is applied, and as the whole system moves towards its equilibrium (more than a few hundred seconds). We find the relaxation process slows down as the number of electrons left inside the QHL becomes less and less.

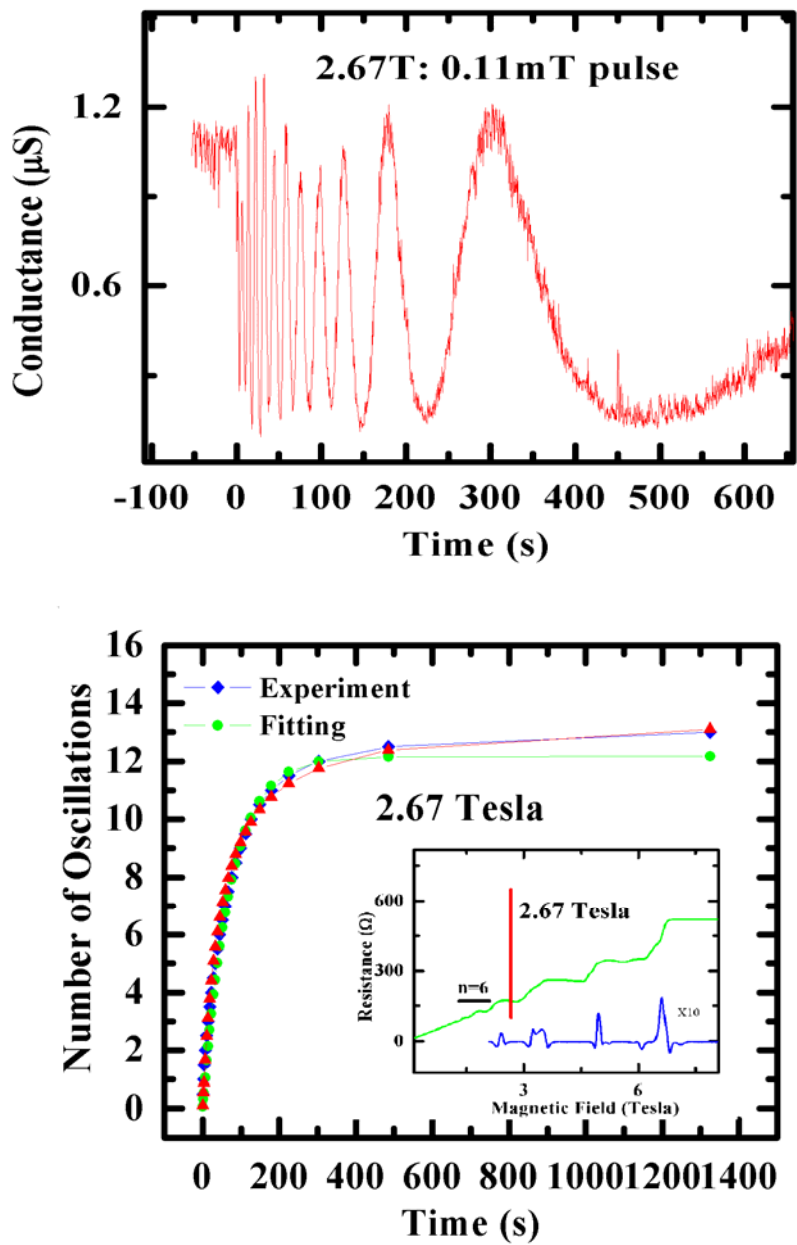


**Fig.8.3:** Upper: The SET conductance versus time when an 11mT magnetic pulse applied at time 0 at  $n=6$  quantum plateau (2.67 Tesla). Bottom: Number of oscillations in SET conductance obtained by counting the peak positions versus the time. In the insert we label the magnetic field position (red line) inside the quantum plateau  $n=6$ .

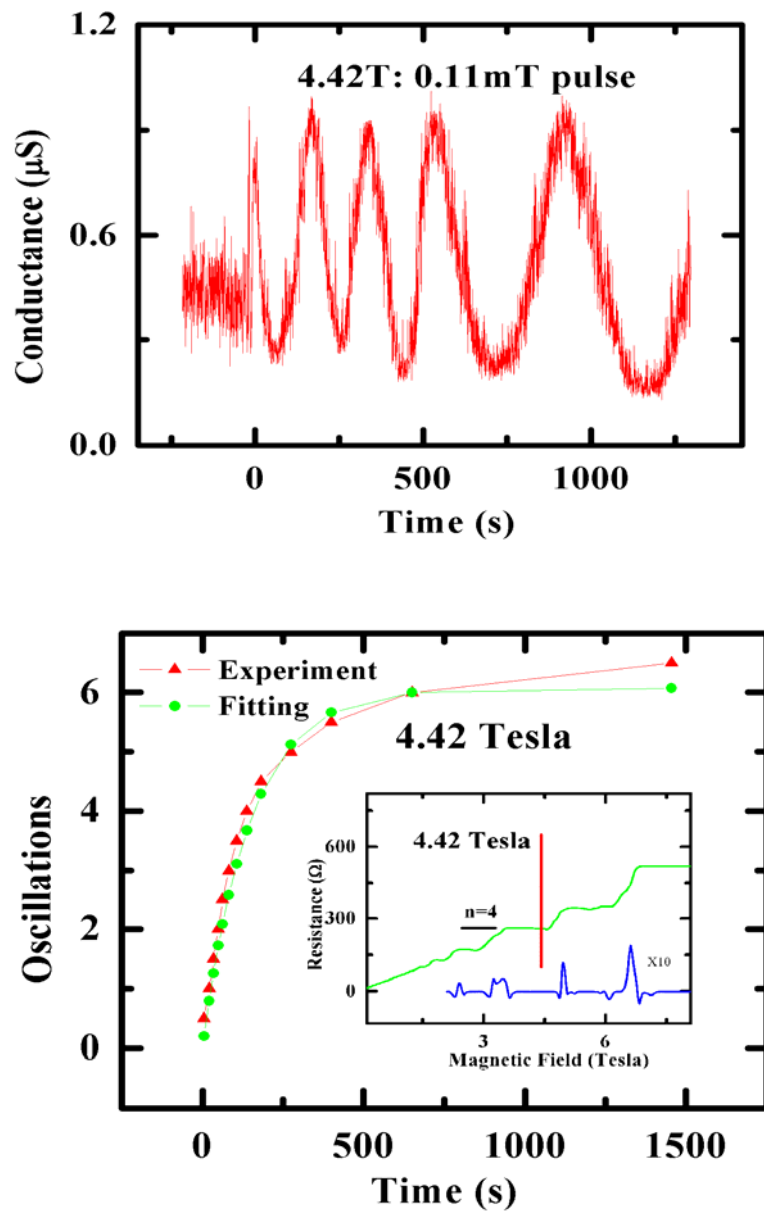


**Fig.8.4:** Upper: The SET conductance versus time when an 11mT magnetic pulse applied at time 0 at  $n=4$  quantum plateau (4.42 Tesla). Bottom: Number of oscillations in SET conductance obtained by counting the valley positions versus the time. In the insert we label the magnetic field position (red line) inside the quantum plateau  $n=4$ .

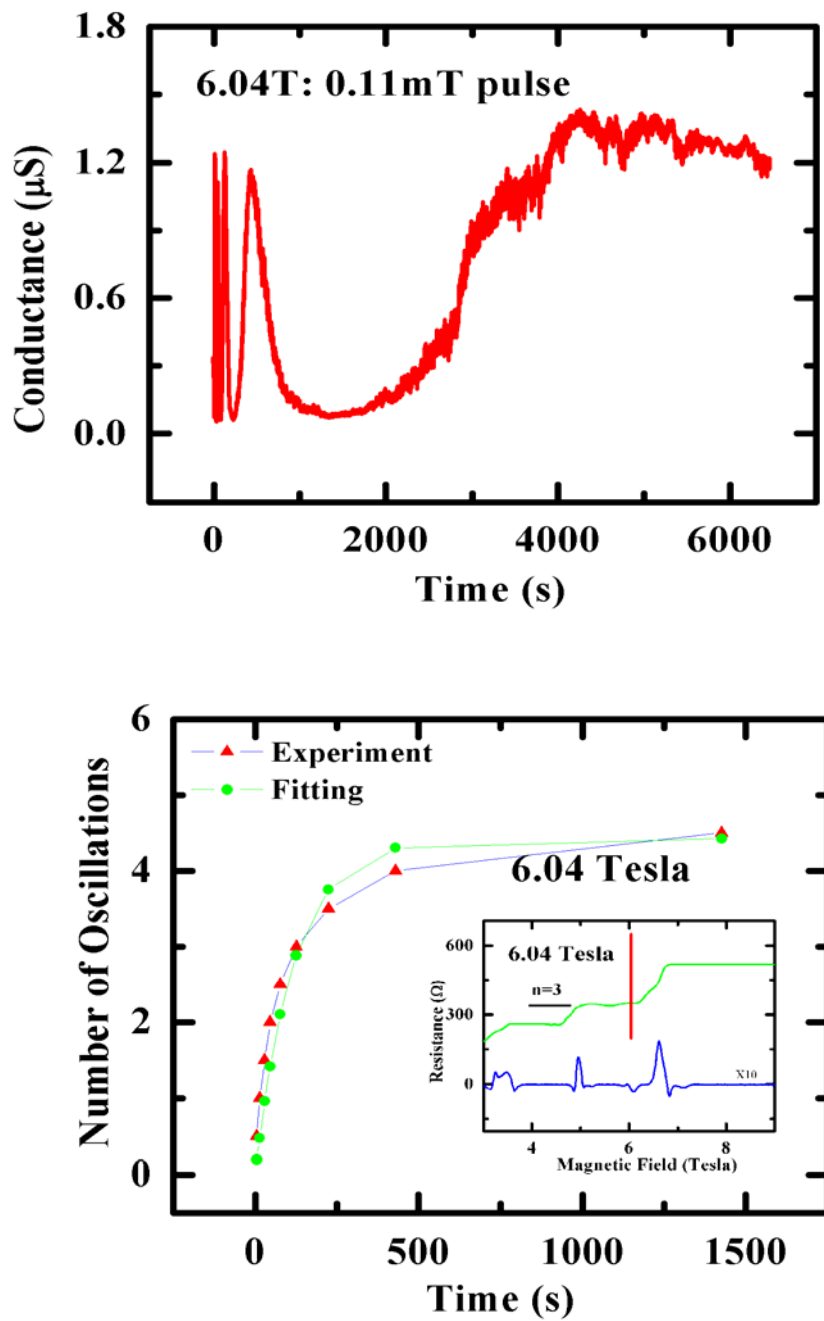


**Fig.8.5:** Upper: The SET conductance versus time when an 11mT magnetic pulse applied at time 0 at  $n=3$  quantum plateau (6.04 Tesla). Bottom: Number of oscillations in SET conductance obtained by counting the valley positions versus the time. In the insert we label the magnetic field position (red line) inside the quantum plateau  $n=3$ .

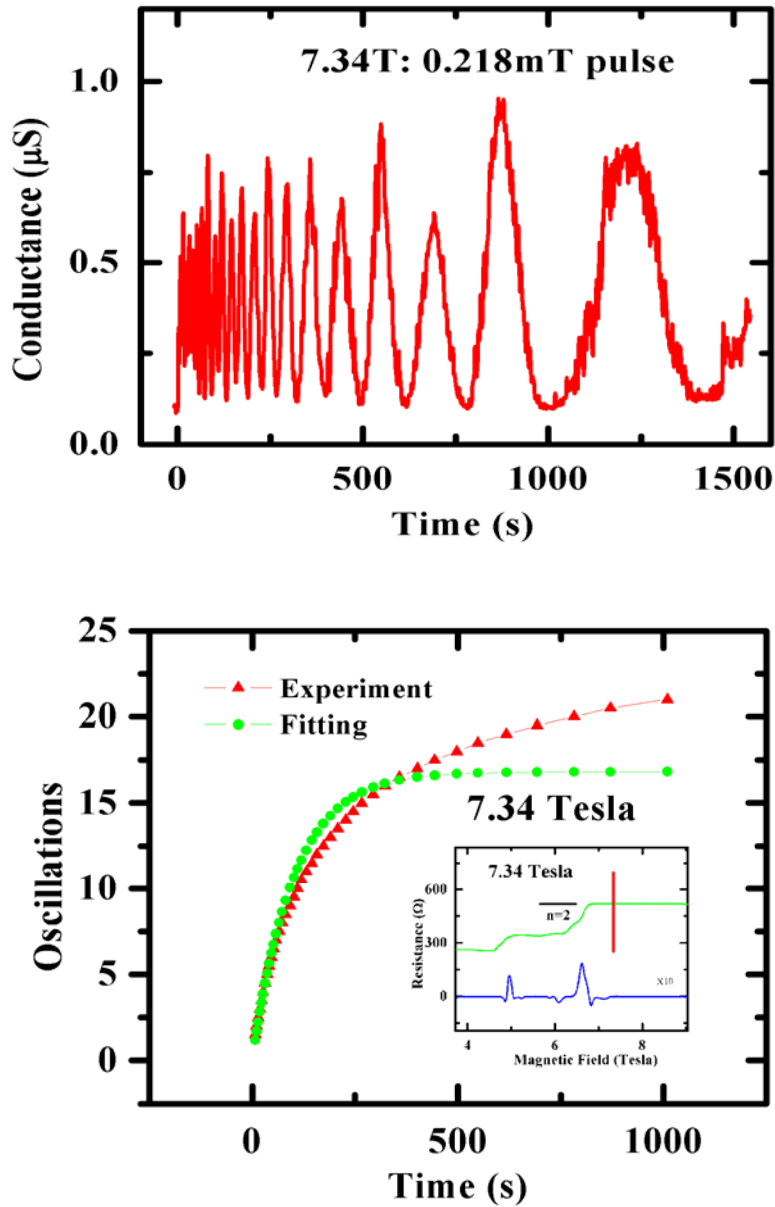


**Fig.8.6:** Upper: The SET conductance versus time when an 11mT magnetic pulse applied at time 0 at  $n=2$  quantum plateau (7.34 Tesla). Bottom: Number of oscillations in SET conductance obtained by counting the valley positions versus the time. In the insert we label the magnetic field position (red line) inside the quantum plateau  $n=2$ .

This relaxation process usually can be described by an exponential decay. In an insulator, the widely accepted model for conductivity is the variable-range hopping (VRH) theory [138]. The electrons transport via random hopping, and the resulting

conductivity would have temperature dependence. In the continuous charge density model, the extra electric field will be proportional to the extra charge in the QHL bulk, therefore we have

$$\frac{dQ}{dt} \sim E \sim Q \Rightarrow \frac{dQ}{dt} = -\alpha Q \quad (8.3)$$

where  $\alpha$  is the relaxation rate depending on VRH coefficients. Then the resulting oscillations in SET signal (moving charges) we observed should follow

$$Q(t) = Q_0(1 - e^{-\alpha t}) \quad (8.4)$$

where  $Q_0$  and  $\alpha$  are fitting parameters.

We used this exponential decay to fit our data. The exponential fitting agrees with the data in the time range from 0 to a few hundred seconds (see Fig 8.3-8.6). After a few hundred seconds, some small but obvious deviations from the exponential fitting were observed, which indicates that the relaxation time is not a constant through this process and becomes longer as time evolves. The reason for this phenomenon might be due to the non-uniformity of the charge distribution, non-linear I-V response of the insulator, the change of resistance in the QHL bulk in the relaxation process ( $RC$  time constant changes) or some other unknown dynamics due to the discrete nature of the charge motion.

## 8.4 Charge dynamics in normal and antidot QHL samples

In order to successfully build the quantum interferometer, we need to understand the charge dynamics around the antidot (see Fig. 8.1). The first challenge would come from how to load the quasi-particles on to the antidot. In the QHL, the charges are in the localized states, including those charges around the antidot area. The

response of those localized charges to the electric field is through variable range hopping [138-139], therefore the conductivity  $\sigma_{xx}$  of the QHL is extremely low. Even if the electric field can drive those charges, those charges must move from the sample edge (Ohmic contacts) to the bulk and this process could be very long. We can also load the charges using the magnetic field (see chapter 7).

Due to the relatively large  $\sigma_{xy}$ , the magnetic field could drive the charge into the QHL at a very fast rate, too fast to be detected by the SET. But the magnetic field loading will suffer a relaxation because this loading will bring extra charges from the sample edge and therefore put the QHL into a non-equilibrium state. After the magnetic field loading, those extra charges will relax back to equilibrium at a similar rate as electric field loading. If we apply the magnetic field first to load the extra charges into the QHL, and then immediately apply the electric field to hold those extra charges back to the equilibrium, in principle we can achieve a fast and stable loading in the antidot in equilibrium. This is a very important step to implement the quantum interferometer since we need a fast and stable quasi-particle loading to implement quantum interference and computation. In this chapter, we present an experiment showing the challenges and difficulties involved in successful quasi-particles loading.

First of all, we should point out there is a difference between the normal QHL sample and antidot samples (See Fig. 8.7).

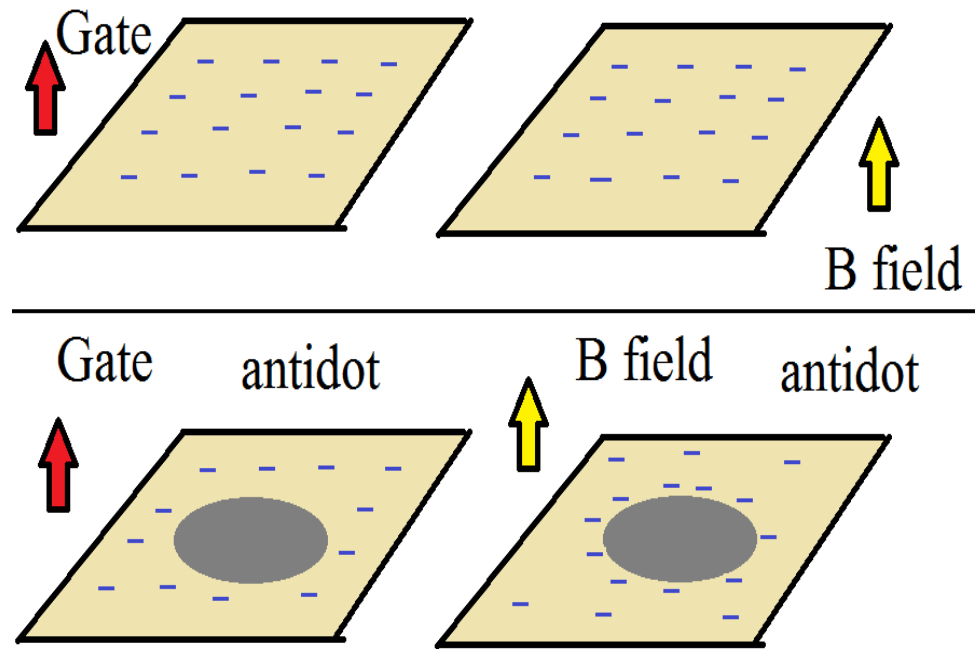


**Fig.8.7:** Loading of the quasi-particles to the normal QHL sample without antidot pattern and the antidot sample by the backgate and by the magnetic field, respectively. The antidot area is shown by the grey area in the diagram, and is expected to behave differently in the magnetic field loading. For the gate loading for both samples and the magnetic field normal sample loading experiment, the quasi-particles will accumulate in the QHL uniformly. While in the magnetic field loading to the antidot sample, because the quantum flux penetrate through the antidot area, the charges will accumulate around the antidot to form a higher charge density area, which will put the local chemical potential to a higher level than the bulk.

In the unpatterned normal sample, the gate and the magnetic field will load the charges into the QHL bulk uniformly as we expected since the electric field and the magnetic field will penetrate through the sample uniformly. In the antidot sample, the gate will load the charge uniformly as in normal sample case, and the antidot (etched away area) itself will not contain any charge. However, in the magnetic field loading, the quantum fluxes will penetrate through the antidot area; according to Laughlin's

description[112], each quantum flux will bring  $v=n$  ( $n$  is the filling fraction) charges into the QHL bulk. Since those extra charges cannot go inside the antidot, they must accumulate and condense around the antidot to form a higher charge density area than the QHL bulk. This phenomenon was expected to be observed in our experiment.

In order to test this, we fabricated four SETs on top of a FQHL sample with two normal SET and two antidots SET, respectively. We monitored the response of the SETs to the backgate voltage and the magnetic field pulse, and extracted the charge-to-magnetic field ( $e/B$ ) and the charge-to-gate voltage ( $e/V$ ) conversion ratios, respectively. We would expect to see different ratios of  $e/B:e/V$  for the antidot SETs and the normal SETs, respectively, and the antidot SET samples were expected to have a higher ratio for  $e/B:e/V$  than the normal SET samples.

In Fig. 8.8, we show the SEM images of the 4 SET samples. The SET patterns were defined by the e-beam lithography with alignment and then followed by double shadow evaporation technique on a FQHL sample (see the next section). SET A and B are antidot samples and SET C and D are control samples. The size of SET A is similar to the size of SET C (~950nm×750nm) and the size of SET B is similar to the size of SET D (~650nm×550nm).

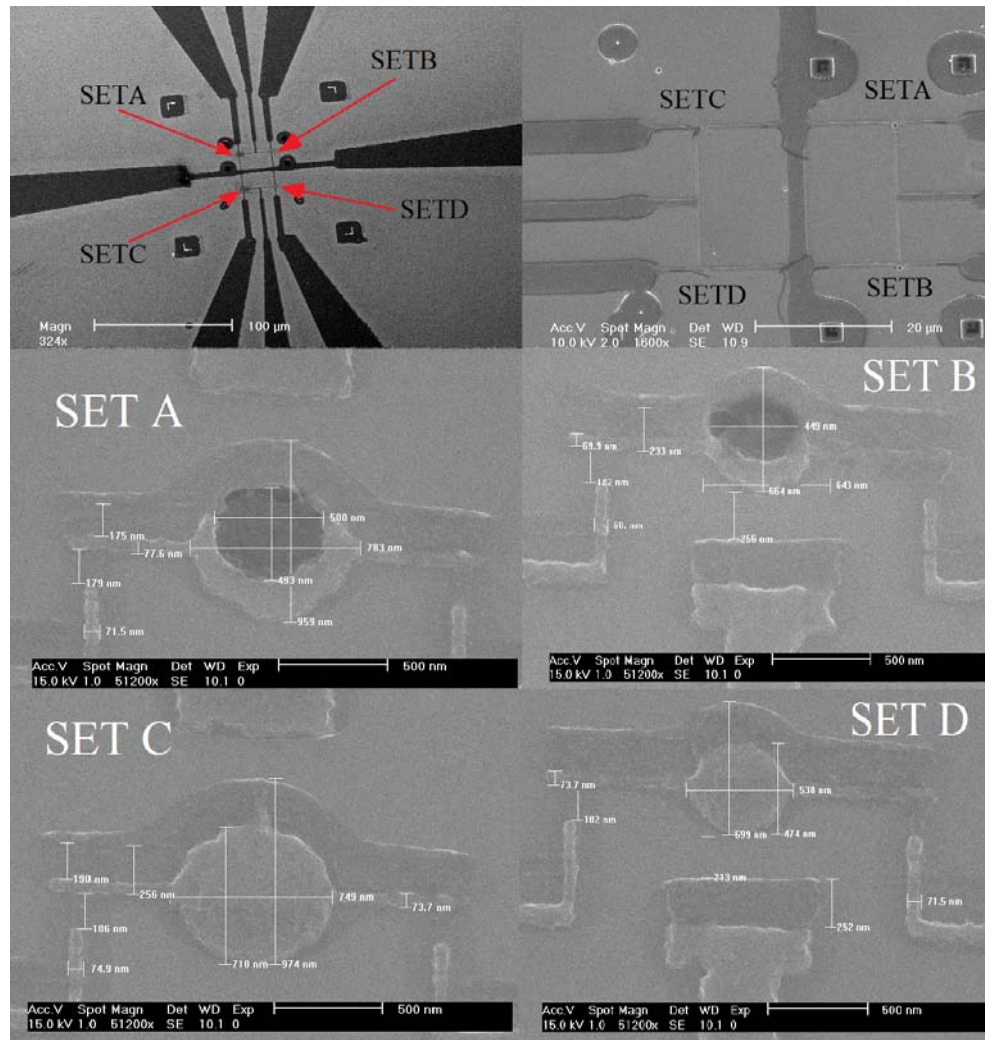


**Fig.8.8:** SEM images of four SET samples at different magnifications. SET A and B are antidot SET samples and SET C and D are normal SET samples.

## 8.5 Characterization of the FQHL sample and the SETs

The FQHL heterostructure was grown by Dr. Loren N. Pfeiffer at Lucent Technologies. This is a high quality GaAs/AlGaAs heterostructure sample with a single layer 2DEG 200 nm underneath the top surface. The carrier density is  $5.8 \times 10^{10} \text{ cm}^{-2}$  and mobility is 4,000,000  $\text{cm}^2/\text{V}\cdot\text{s}$  at liquid helium temperature. Van der Pauw

geometry was used to characterize the sample. When cooled down, one of the sample leads broke. Thus we only measured the Hall data, which was enough to extract the carrier density. We observed the quantum plateau  $n=1/3$ , 1, 2, 3, 4, and 6 in this sample as shown in Fig. 8.9.

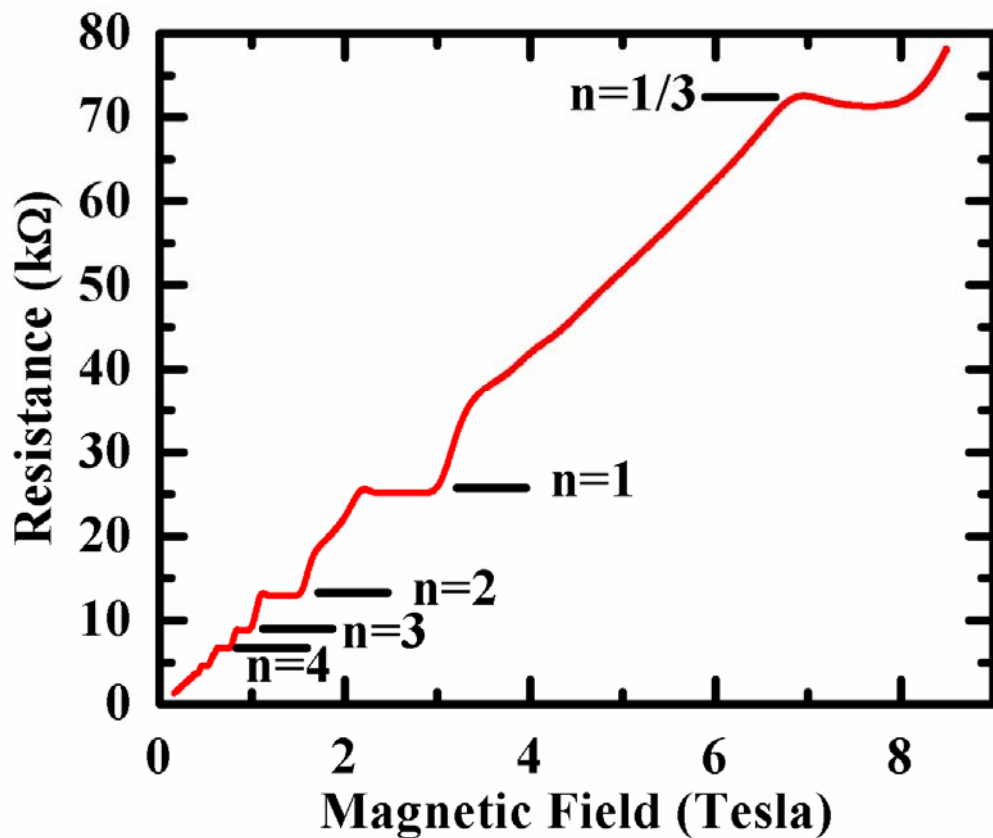


**Fig.8.9:** Hall measurement of the FQHL sample at base temperature 20 mK. We observed the quantum plateau  $n=1/3$ , 1, 2, 3, 4, and 6 in this sample and the carrier density of 2DEG can be extracted from this measurement.

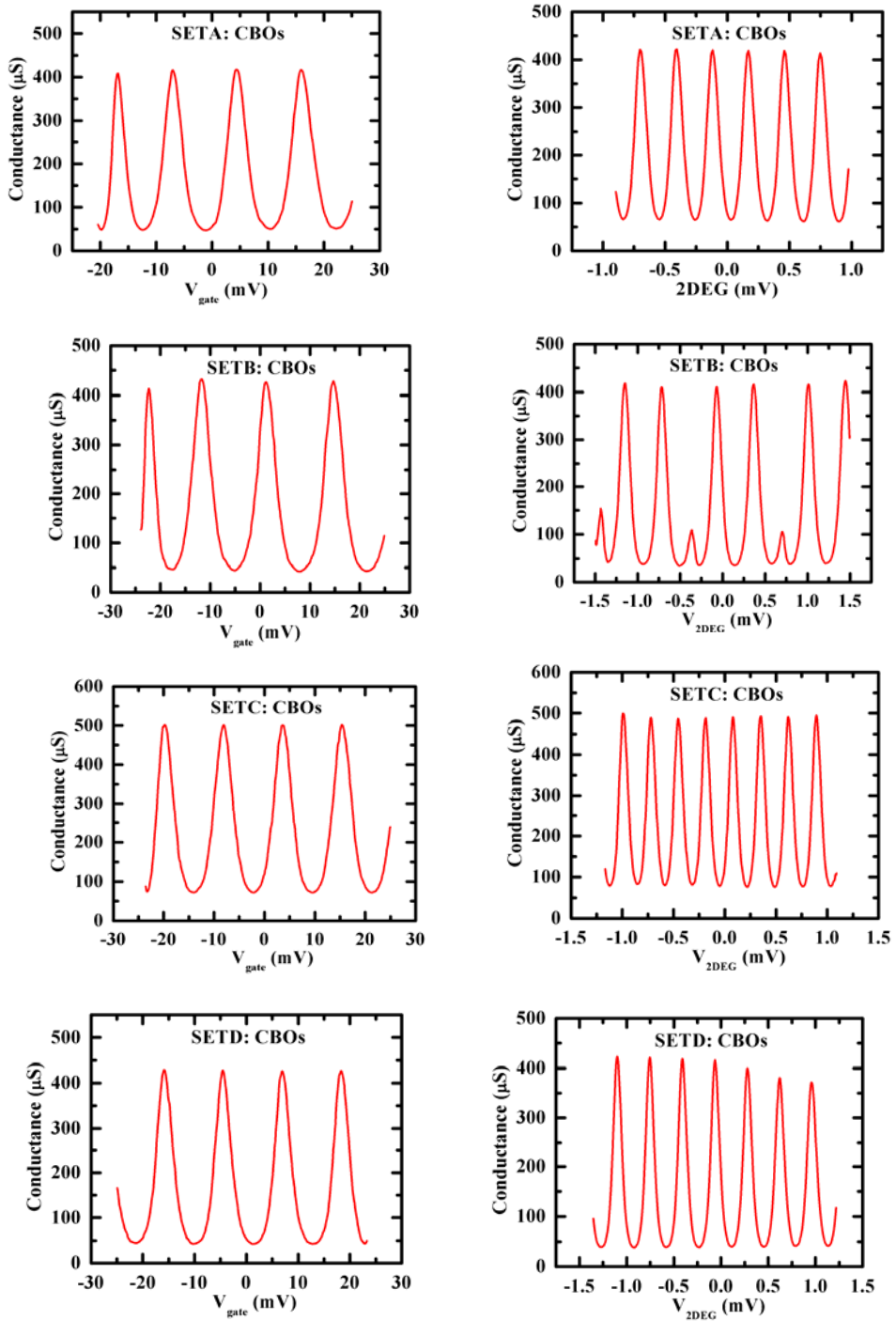


**Fig.8.10:** Characterization of SET A, B, C and D. The CBOs are shown by scanning the gate voltage or 2DEG voltage. The applied magnetic field is 0.5 Tesla.

To change the chemical potential in the SET, we fabricated a metal gate near the SET as well as a backgate put on the sample back. We used the AC differential conductance measurements to characterize the SETs (see section 8.3) and the CBOs are shown in Fig. 8.10. Those SETs are very similar to each other due to the same fabrication condition. The only exception comes from SET B, which shows a periodic 3 peaks CBOs by scanning the 2DEG voltage. Interestingly, if we use the metal gate scanning, it returns back to the normal periodic single peak CBOs, for reasons we do not understand.

In the QHL regime of the 2DEG, the signals from SET C and D were too noisy. This noise is not from the SETs, which had been measured to exhibit low noise in the metallic state of the 2DEGs. Most likely the noise comes from the offset charge motion in the doped layer of the AlGaAs bulk. We believe the offset charge fluctuations can be reduced by using heterostructures with a reduced level doping.

## 8.6 Responses of QHL to the backgate voltage

SET C and D are found to exhibit a higher level noise than SET A and B. A possible explanation is that SET A and B are antidot samples where the antidot area was etched away, therefore the impurities (doping centers) were significantly reduced. Even so, the signal from SET B in QHL was still too noisy to be meaningful. Therefore in this chapter we only focus on SET A. In Fig 8.11, we plotted the conductance of SET A versus time with a backgate voltage pulse 0.15 V applied at time 0 in different positions of quantum plateau  $n=1$ . As we discussed previously, each CBO observed in the SET's conductance corresponds to a charge moving in or out around the SET area.

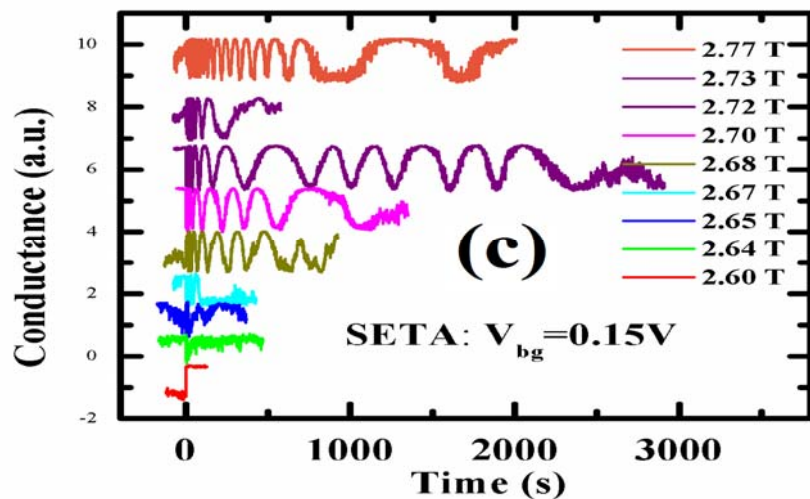
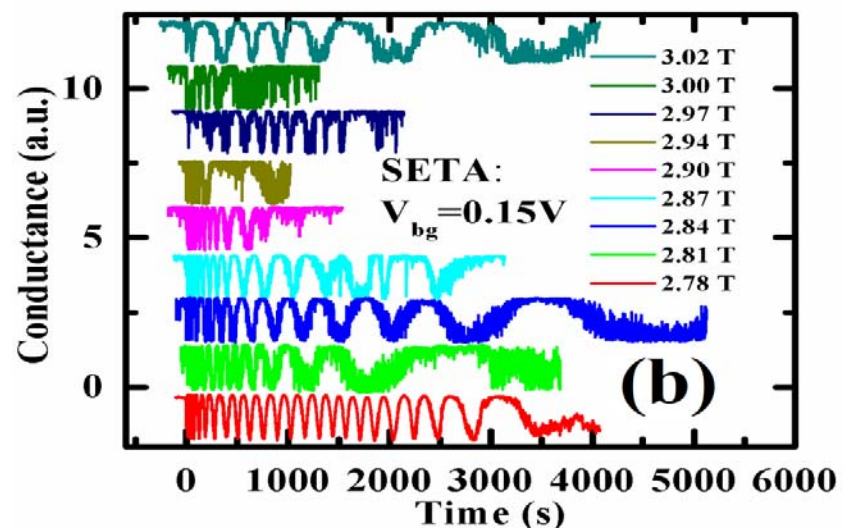
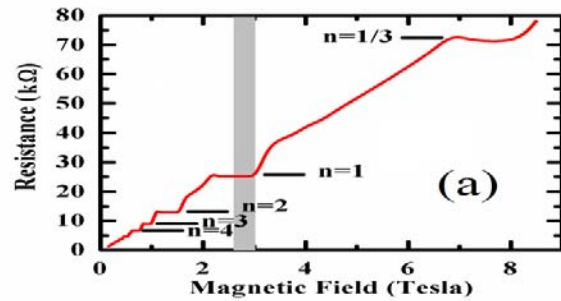


**Fig.8.11:** SET conductance to backgate voltage 0.15 V versus time in different positions of quantum plateau  $n=1$ , the range of which was labeled by grey shade in (a).

Therefore in this measurement what we observed is a charge equilibration process surrounding the SET area. As we change the backgate voltage, driven by the electric field, the 2DEG is not in equilibrium anymore and the charges will move from the sample edge into the 2DEG bulk. This process can be described by a RC circuit model. Due to the geometric shape of the SET island and the fact that in two dimensions the  $1/\sigma_{xx}$  is in the same unit as the resistance, we can roughly estimate the time constant of charge equilibration  $t_e$  given by the RC circuit model as[121]

$$t_e = C_{SET} / \sigma_{xx} \quad (8.5)$$

where  $C_{SET}$  is the effective capacitance of the SET.

From Fig. 8.11, in the magnetic field range from 2.6 Tesla to 3.02 Tesla, the SET's response changed dramatically. At 2.6 Tesla, when we apply a backgate voltage 0.15 V, the SET only shows a sudden response then just stabilizes there, which indicates that the 2DEG is still in conductive state with a large  $\sigma_{xx}$  and very small RC time constant. As we increase the magnetic field from 2.6 Tesla, the 2DEG moves deeper into the QHL regime. In a narrow range from 2.6 Tesla to 3.02 Tesla,  $\sigma_{xx}$  decreases and  $1/\sigma_{xx}$  increases dramatically, therefore we see a dramatic change of the equilibration time. From 2.6 Tesla, when we apply a backgate pulse 0.15 V at time 0, we start to see more and more CBOs and the equilibration time range becomes longer and longer from a few seconds to a few hundred seconds as a trend. This observation indicates that the QHL becomes more and more insulating starting from 2.6 Tesla.

However, when the magnetic field goes beyond 2.72 Tesla, the number of oscillations and the response time do not change monotonically anymore. To see it more clearly, we count the number of oscillations observed in the SET conductance in

every magnetic field and plot it as a function of time. In this manner, we can present the charge equilibration process more clearly. In this measurement, a positive voltage 0.15 V is applied to the backgate at time 0 when holding the 2DEG at 0 V by grounding the Ohmic contact, and the oscillations of SET conductance are recorded for a long time (a few hours). After the system equilibrates, we return the backgate voltage back to 0 V, which is equal to a negative voltage -0.15 V applied to the system and the corresponding oscillations in SET are recorded as well. As shown in Fig. 8.12, the number of oscillations observed in SET conductance seen over time is plotted in different positions of quantum plateau  $n=1$  for backgate voltage pulse 0.15V and -0.15V, respectively. We start to see large fluctuations in the number of oscillations and in the equilibration times in the middle of the quantum Hall plateau beyond 2.72 Tesla; also we should point out that those data are not well reproducible. The response of SET for the positive backgate voltage (0.15 V) is not identical for the negative gate voltage (-0.15 V).

We believe the large fluctuations are mostly due to the noise, for examples, the noise induced by the motion of offset charges. This measurement is important for measuring the noise level in the QHL. First, from this measurement, we can see that the noise level is different for different quantum plateau positions in QHL. For example, at 2.6 Tesla where the 2DEG is conductive, the noise is almost negligible comparing to the SET signal, while at 2.72 Tesla as 2DEG is insulating, the offset charge noise interfere with the signal and induce an equilibration process deviated largely from the exponential relaxation (see Fig.8.11 and Fig. 8.12). In other words, the less conductive is the 2DEG, the slower are the relaxation and the more vulnerable is the experiment

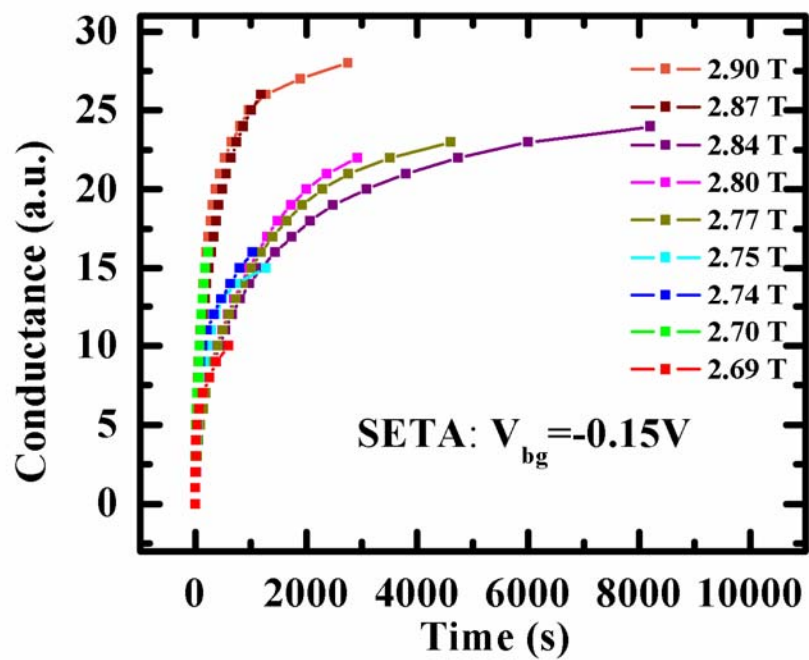
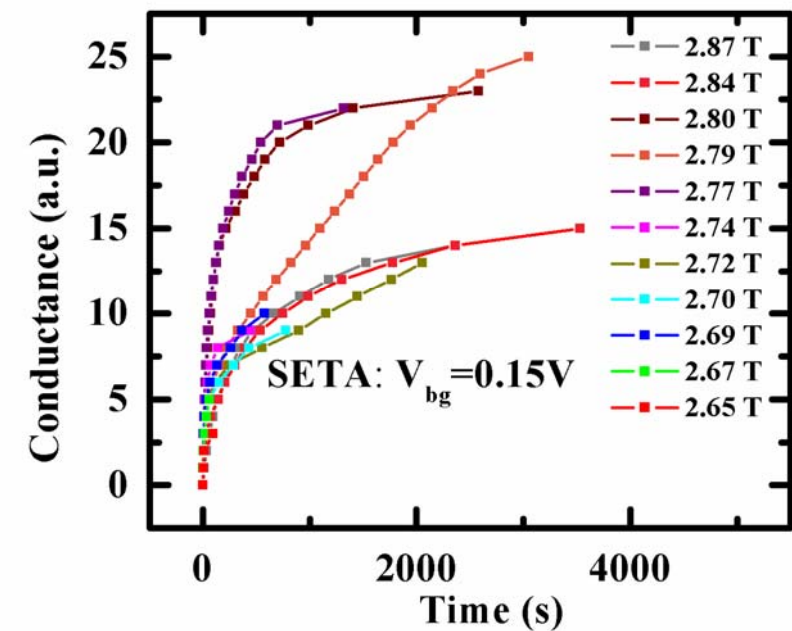


**Fig.8.12:** Number of oscillations in SET conductance seen over time in different positions of quantum plateau  $n=1$ , for backgate voltage pulse 0.15V and -0.15V.

to offset charge noise. Using this type of measurements, we can also extract the noise level at different magnetic fields by observing how much the signal deviates from the exponential decay.

Furthermore, the fact that the behavior of the QHL is different for the +0.15 V and -0.15 V backgate pulse might indicate that the equilibration time depends not only on the magnetic field but also on the backgate voltage. Finally, by using equations 8.5, this measurement can be used to extract the conductivity  $\sigma_{xx}$  of the QHL, which is usually too small to be measured by other methods. What we need to do is to fit the equilibration process by the exponential decay model (equation 8.4) and extract the equilibration time constant  $t_e$ . Once we get the  $t_e$ , the conductivity  $\sigma_{xx} \sim C_{SET}/t_e$ . In our measurement (see from Fig 8.11-8.12), we can conclude the  $\sigma_{xx}$  is much smaller when we go deeper into the quantum plateaus because the equilibration time constant is much longer.

## 8.7 Responses of QHL to the magnetic pulse and the backgate voltage together

For the application of the quantum interferometer, it is extremely important to precisely and stably control the number of the quasi-particles trapped in the antidot, otherwise the signal would be washed away by the quasi-particles movement. To achieve a stably and precise loading of quasi-particles into the antidot, in principle, we can apply a small magnetic pulse to load the quasi-particles into the antidot and use a backgate voltage to stabilize the system to equilibrium (see section 8.4). Therefore in this section we perform the following experiment to test the loading process. First, we used a stable constant magnetic field to bring the 2DEG into the QHL regime. We applied a

magnetic pulse to the sample while holding the 2DEG in 0 V by grounding the ohmic contacts, and at almost the same time applied a backgate voltage to stabilize the quasi-particles loading process. The responses of the QHL were recorded by the antidot SET conductance, as we did in the previous sections.

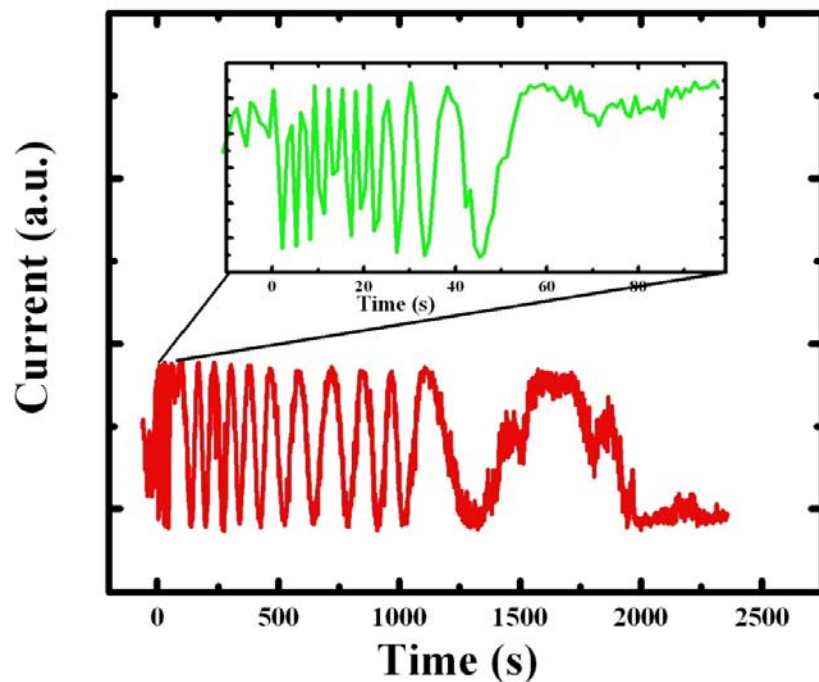


**Fig.8.13:** SET conductance monitored after a magnetic field pulse ramping from 2.702T to 2.710T and a backgate voltages 0V were applied at time 0. In the diagram we can see clearly there are two oscillations patterns. The first pattern occurs in the time range from 0-70 seconds (see insert) where we see 11 CBOs oscillates in a fast pace. After that, we observed a turning point at 70 seconds and in the time range from 70-2000 seconds, there is the second pattern which also shows 11 CBOs oscillating in a much slow pace. We believe the first pattern (0-70 seconds) corresponds to 11 charges moving in (11 CBOs) to the antidot area and the second pattern corresponds to those 11 charge moving (11 CBOs) out of the antidot area, and the turning point happens at 70 seconds.

In Fig.8.13, we showed a typical measurement for the SET conductance monitored after a magnetic field pulse ramping from 2.702T to 2.710T and a backgate voltage 0V were applied at time 0. In the diagram we can see clearly there are two oscillations patterns. The first pattern occurs in the time range from 0-70 seconds (see insert) where we see 11 CBOs oscillates in a relative fast pace. After that, we observed a turning point at 70 seconds; and in the time range from 70-2000 seconds, there is the second pattern which also shows 11 CBOs oscillating in a much slow pace. We believe that those CBOs observed from 0-70 seconds corresponds to 11 charges moving in (11 CBOs) to the antidot area and those CBOs observed from 70-2000 seconds corresponds to those 11 charge moving (11 CBOs) out of the antidot area, and the turning point happens at 70 seconds. This phenomena show that the charge loading into the antidot actually is more complicated than we anticipated, and this process can have two steps with charge moving in and then moving out motions like a breath.

We tried different magnetic field and backgate voltage pulses combinations and the results are shown in Fig. 8.14 and 8.15. Notice that in single layer 2DEG at quantum plateau  $n=1$ , we should apply relative large magnetic field pulse (a few mT) to load a few number of magnetic fluxes into the antidot area. This cannot be achieved by using the secondary magnetic coil due to its current limit. Therefore we have to use the superconductor magnet to apply a few mT magnetic field pulses, which happens in a slow pace as we need to involve the persistent switch heater of the superconducting magnet. Usually it takes the superconductor magnet up to 20 seconds to apply a stable 8 mT magnetic pulse. Therefore in this experiment we always apply the magnetic

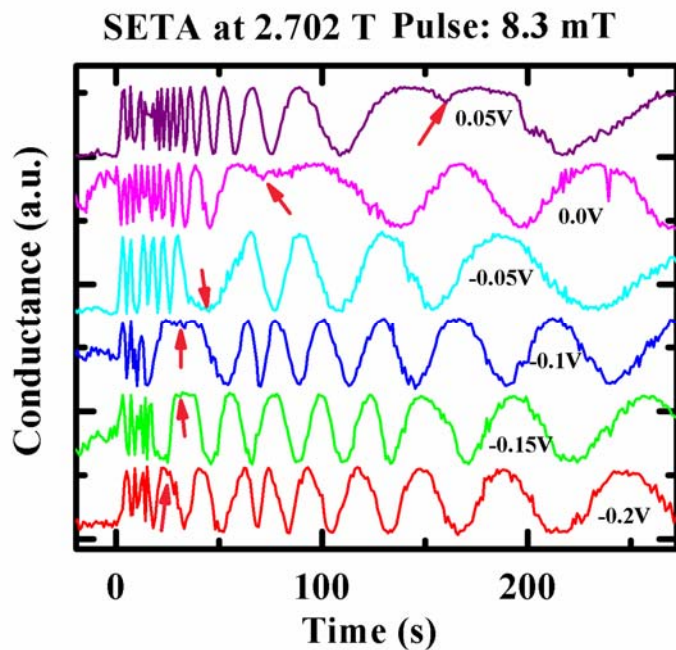
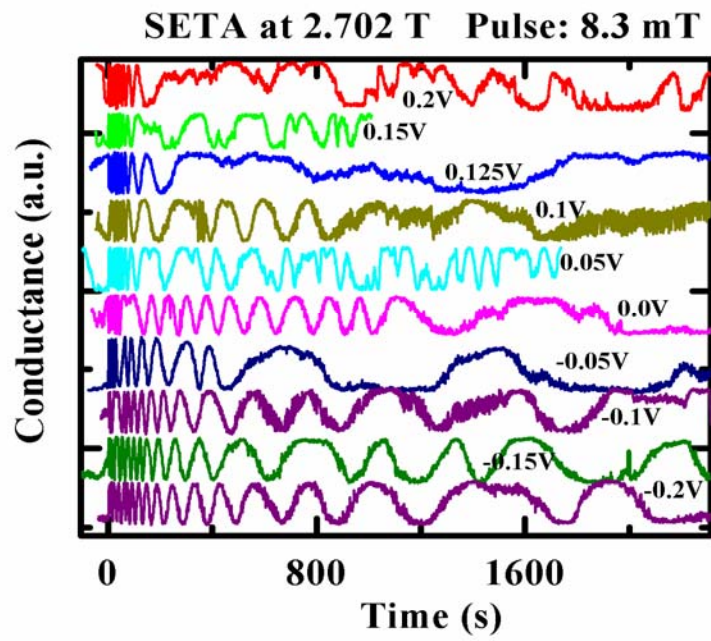


**Fig.8.14:** Responses of SET conductance to the magnetic field pulse ramping from 2.702T to 2.710T applied at time 0 and different backgate voltage pulses in quantum plateau  $n=1$ . The lower diagram shows the time range from 0 to 270 s, and obvious turning points were observed in the diagram (marked by red arrows).

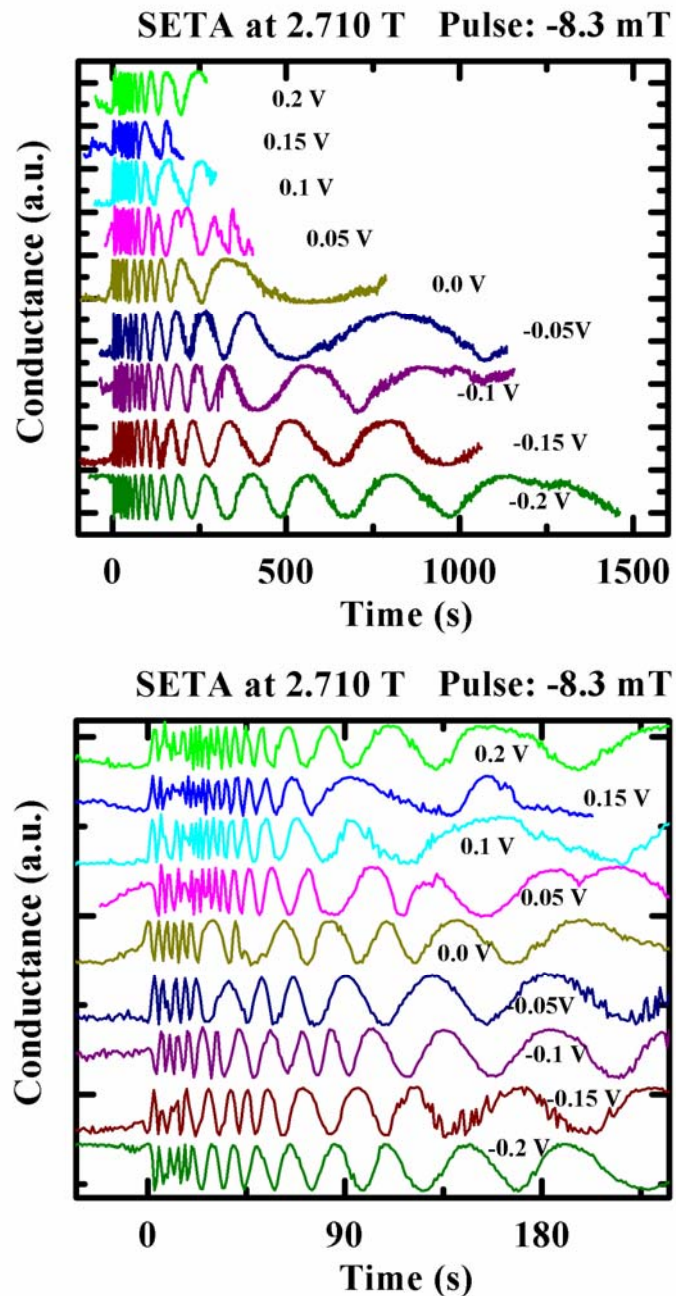


**Fig.8.15:** Reponses of SET conductance to magnetic field pulse ramping from 2.710T to 2.702T applied at time 0 and different backgate voltage pulses in quantum plateau  $n=1$ . The lower diagram shows the time range from 0 to 200 s, and no turning points were observed.

pulse at time 0 and apply the backgate voltage at the 10th second. Interestingly, as the 0 V backgate voltage case, in the responses of SET conductance to the magnetic field pulse ramping from 2.702T to 2.710T for other different backgate voltages in quantum plateau  $n=1$ , we also observed obvious turning points (marked by red arrows in Fig. 8.14) in the time range from 0 to 170 seconds,. Those turning points mean that the charges induced by the magnetic field would move in the antidot area during the time period 0~100 seconds. After that, the local chemical potential reaches the maximum nonequilibrium and the charges start to move out.

This observation contradicts with our initial physical picture. In our initial understanding, the charge loading is a fast process and almost instantaneously happens when we ramp the magnetic field, which is too fast to be detected by the SET. After the magnetic field ramping, the charges start to move out of the antidot area driven by the non-equilibrium chemical potential. This slow equilibration process could be detected by the SET's CBOs signal. However, our observation (the charges moving-in then moving-out motions) indicates that the charge loading is not as fast as we thought, which will take about 10-200 seconds for charge to move in, depending on the magnetic field pulse and the backgate voltage pulse, and only after the local chemical potential reaches the maximum non-equilibrium, the charges start to move out, but in a much slower pace.

On the other hand, when we ramped down the magnetic field from 2.710 to 2.702 Tesla, we did not observe the similar moving-out then moving-in process. In this experiment (see Fig. 8.15), we did not see those turning points as we saw in the magnetic field ramping up experiment, which indicates that in this experiment, the

charge unloading (moving-out process) happens too fast to be detected, finishing almost simultaneously at the same time of the magnetic field ramping, and what we observed in the measurements is only the charging moving-in motions driven by the non-equilibrium.

This is an obvious puzzle: why in the magnetic ramping-up case we observed the turning points in the SET conductance but not in the magnetic ramping-down case? To interpret the data, we have to consider the local environment around the antidot area. Due to the etched area's surface confinement, the carrier density around the SET antidot would be less than the 2DEG bulk; therefore when the 2DEG bulk becomes the QHL in certain magnetic field, the 2DEG around the antidot is still in conductive state. In Fig. 8.16, the charge profile around SET is shown. In that figure, the red color represents the QHL area and the blue color represents the normal conductive state. Initially the QHL is in equilibrium (see Fig. 8.16 (a)). Just after a magnetic pulse applied, the charges will be driven in and accumulate around the antidot area. This process is too fast to be detected. Because the carrier density must be continuous, inside the charge accumulated conductive area there must be an area with carrier density equal to the QHL (see Fig. 8.16 (b)), where a QHL barrier forms and acts as a transport barrier for the electron movement. After that, those accumulated electrons (with higher density) around the outside area of the antidot start to diffuse into the inner area through the QHL barrier in a relative fast pace. That is exactly the charge moving-in process (Fig. 8.16(c)) we observed in the experiment in the time range 0~100 seconds. After reaching the maximum non-equilibrium (the turning points) in the antidot area, the electrons start to move out in a much slower pace because those electrons have to go

through the QHL bulk, which has a larger RC equilibration time constant. This is exactly what we have observed in the experiment in the time range 100~2000 seconds.

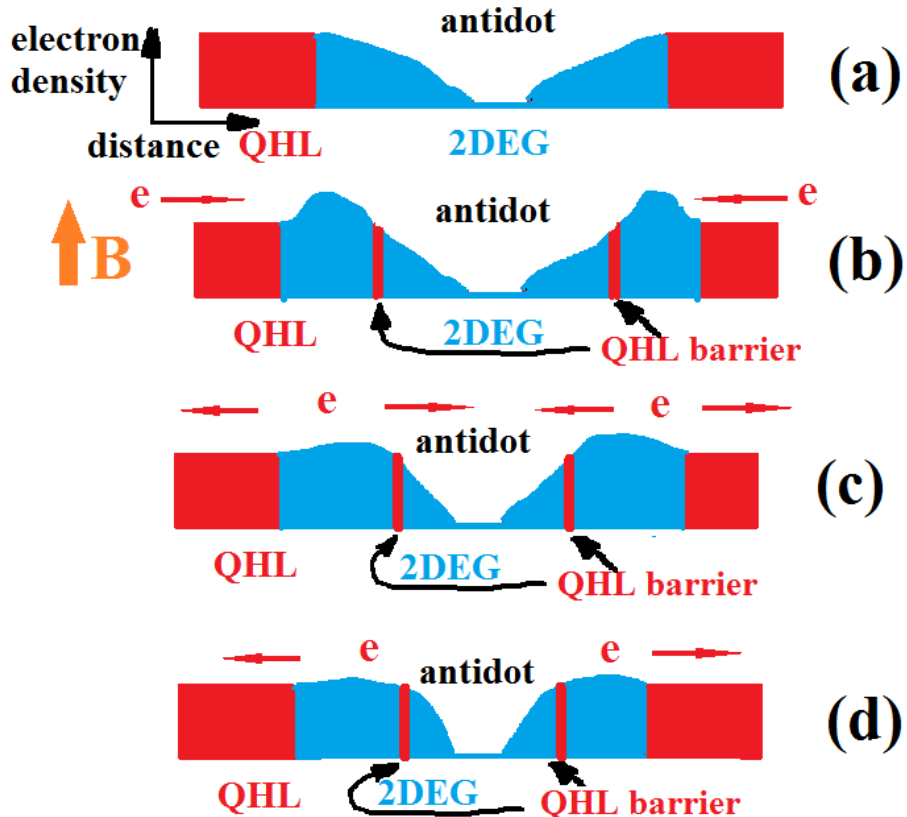


**Fig.8.16:** Cross section of the charge profile around the SET antidot. The red area represents the QHL insulator. The blue represents the normal conductive state. (a) The QHL is in equilibrium. Due to the surface confinement, the 2DEG density around the antidot is less than the QHL bulk; therefore the 2DEG there is still in conductive state. (b) Just after a magnetic pulse, the charge will be driven in and accumulate around antidot area. Because the carrier density must be continuous, inside the conductive area there must be an area with carrier density equal to QHL; therefore a QHL barrier forms inside the conductive area, which acts as a barrier for electron transport. (c) The electrons start to transport into the SET area through the QHL barrier in a slow rate. (d) After reaching the maximum non-equilibrium, the electrons start to transport out in a much slower rate.

Notice if this mechanism is correct, we will have an asymmetric behavior for magnetic field ramping-up and ramping-down. When the magnetic field ramps down,

the electron will be driven out of the antidot area (as quantum fluxes decrease) immediately and the QHL barrier will not be created. Just after the magnetic field ramping down, the electrons immediately start to transport back into the antidot area driven by the electron deficiency. This equilibration process is slow through the QHL bulk and no turning points will be observed. This is exactly what we have observed in this experiment. The data shown in Fig. 8.15 is the CBOs for the magnetic field ramping down from 2.710 Tesla to 2.702 Tesla and no obvious turning points observed.

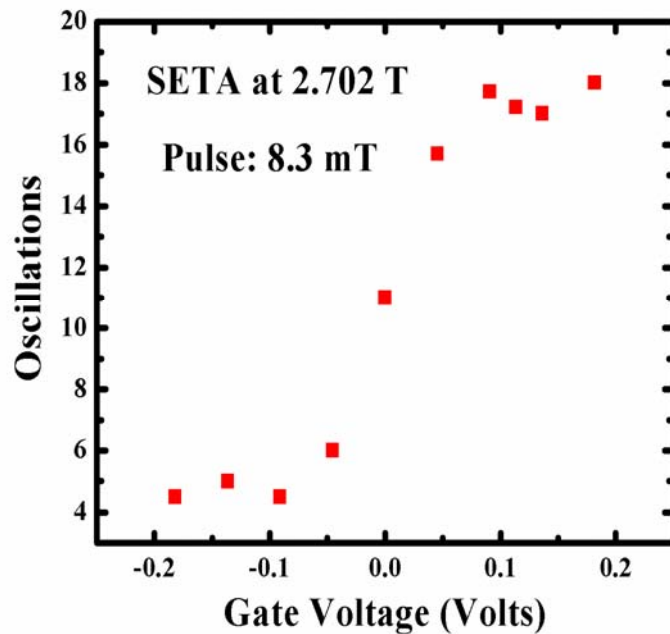


**Fig.8.17:** Oscillations observed in the SET conductance measurements before the turning point versus backgate voltages for SET A. As expected, the oscillations increase when we increase the backgate voltage. The oscillations saturate when the backgate voltage goes beyond certain range (-0.1 V to 0.1 V).

For the magnetic field and backgate voltage pulses combination loadings, we plot the CBOs observed in the SET conductance measurement before the turning points versus different backgate voltages in Fig. 8.17., where the magnetic field is ramped

from 2.702 to 2.710 Tesla. In Fig. 8.17, the oscillations increase as we increase the backgate voltage. This is expected because before the turning points the charges are in the moving-in movement, whose numbers are expected to increase with the increasing backgate voltages. The oscillations saturate when the backgate voltage goes beyond the range from -0.1 V to 0.1 V, which is also expected since the antidot area is small and cannot contain too much charges. Notice when backgate voltages is less than -0.1 V, the oscillations saturation ( $\sim$ 4 oscillations) before the turning points is due to the fact that the magnetic field is applied 10 seconds before the backgate voltage, and those oscillations ( $\sim$ 4 oscillations) are driven by this initial 10 seconds magnetic field ramping up. If we can apply the magnetic field and backgate voltage pulses at the same time, we would expect to see no oscillations before the turning points for backgate voltages less than -0.1 V. For backgate voltages larger than 0.1 V, the CBOs saturate and no obvious turning points observed (beyond 300 seconds the CBOs are mainly from noise). This suggests that beyond backgate voltage pulse 0.1 V, the loaded charges will stay in the antidot area for a long time without equilibration (no charge moving-out observed). The significance of this observation is that it means we could use the combination of 8 mT magnetic pulse and 0.1 V backgate voltage to stably fast load 11 electrons into the antidot without any significant charge relaxation motions. This stable fast loading is crucial for the application of the quantum interferometer in the future, and would be an important step toward quantum computation.

Furthermore, this experiment also indirectly confirms the prediction that the charges loading by magnetic field pulse will produce a higher carrier density area around the antidot than the carrier density in the bulk (see Fig. 8.7).

## **8.8 Conclusions and future directions**

In this chapter, we studied the charge motions in the QHL detected by single electron transistors. In the 25 layers multiple quantum wells sample, the charge equilibration process has been studied by applying magnetic pulses and the CBOs has been detected in the SET conductance measurements. The relaxation process was fitted by the exponential relaxation model and it was found that the data would deviate from the fitting model as time became longer and longer. The offset charge noise level can be extracted from the experiment and used as a figure of merit for the sample quality in terms of quantum information applications. It also gives us an error bar for this type of measurement, which could be served as an important parameter for tolerance design of the quantum interferometer. From this experiment, we believe a better 2DEG sample with less doping or doping far away from the 2DEG is crucial for the device application of quantum interferometer;

In a FQHL sample, antidot SETs were fabricated and the charge loading process was studied. An unusual process of charges moving in then moving out was observed in this sample, which we believe was owing to a QHL transport barrier formation in the SET area. Also the responses of the QHL to a simultaneously applied magnetic field and backgate voltage were studied. This experiment suggests that: (1) It is possible to load the quasi-particles into the antidot by using the magnetic field pulse, and this magnetic field loading process will create a higher charge density area around the antidot; (2) It is possible to load the quasi-particles into the antidot in the QHL by applying simultaneously the magnetic field and the backgate voltage without inducing

significant charge relaxation; and (3) The response of the QHL around SET is asymmetric to magnetic field ramping up and down.

These experiments are important for understanding the dynamics of charge motions in the QHL, therefore can be used as a guide for the fabrication and application of quantum interferometer.

For the future direction, we need to get samples with lower offset charge noise to perform this experiment again. Also we need to extend the study into other quantum plateaus, especially in those fractional quantum plateaus such as  $n=1/3$  and  $n=2/5$ . A second magnetic coil which can instantly apply a relatively large magnetic field ( $\sim 10$ - $100$  mT) is proved to be necessary for the success of those experiments. If we can achieve a stable and fast loading of quasi-particles, we can go further to fabricate a quantum interferometer and test those theoretical predictions associated with the unusual statistics of Laughlin quasi particles. In such a quantum interferometer device, we can also fabricate a SET antidot on the same 2DEG surface and use this SET antidot as a calibrator for charge loading and unloading process. Therefore in this manner, the charge loading can be precisely controlled.

Also as indicated by the relation between the equilibration time  $t_e$  and the conductivity  $\sigma_{xx}$ , we can use the SET measurement to study the conductivity in the QHL, which is usually hard to be measured by other methods. By combining other methods, such as Corbino geometry Hall bar measurements and RF-SET [139-144], the  $\sigma_{xx}$  range from  $10^{-17}$  S to  $10^{-3}$  S could be covered [121]. It would be important to discover if there are deviations from the variable range hopping picture in the deep QHL regime.

## CHAPTER 9

### SUMMARY AND SUGGESTIONS FOR FUTURE WORK

#### **9.1 Summary of present work**

In this dissertation, we have studied two dimensional electrons transport in GaN and GaAs heterostructure samples and the results were discussed.

In Chapter 2, we have investigated magnetotransport properties of four AlGaN/AlN/GaN gated Hall bar samples at different gate voltages, covering a broad range of carrier density from  $0.5 \times 10^{12} \text{ cm}^{-2}$  to  $1.0 \times 10^{13} \text{ cm}^{-2}$ . Well pronounced single frequency SdH oscillations have been observed at 1.6 K indicating high sample quality. We found that the mobility increases with increasing carrier density in the low carrier density regime, and decreases as a function of increasing carrier density in the high carrier density regime. The peak mobility occurs at carrier density close to  $5 \times 10^{12} \text{ cm}^{-2}$ . When the carrier density is low, the mobility is mostly limited by long-range Coulomb scattering processes, mainly arising from charged threading dislocations in our samples. As carrier density increases more, the mobility is limited by the alloy and interface roughness scattering in the high carrier density regime.

Based on our experiments performed on 2DEG samples, we have rather good understanding of electron transport and scattering process in the GaN heterostructure systems. The factors limiting the maximum electron mobility in GaN heterostructures are mostly from lattice mismatch of the substrate to the GaN layers and the threading dislocations induced henceforth.

In Chapter 3, we have continued our magnetotransport measurements on an  $\text{In}_{0.16}\text{Al}_{0.84}\text{N}/\text{AlN}/\text{GaN}$  gated Hall bar sample at different gate voltages, which covered a carrier density range up to  $2.32 \times 10^{13} \text{ cm}^{-2}$ . Well-pronounced two frequency Shubnikov-de Haas (SdH) oscillations have been observed at 0.28 K, which was attributed to the occupation of two subbands. Carrier densities and quantum lifetimes in those two subbands have been extracted from SdH oscillations. We also observed different rate of change of the electron density *vs.* gate bias,  $dn/dV_g$ , in two subbands, which is explained by the increase in energy level separation between the first and second subbands induced by increasing gate voltage. As shown in mobility versus carrier density data, the InAlN/AlN/GaN samples appear to have a better quality than the AlGaN/AlN/GaN samples, which is most likely due to the lattice matching, and they also have higher carrier densities due to stronger spontaneous polarization and larger bandgap offset.

In Chapter 4, based on the knowledge we learned from Chapter 2, we have continued to investigate the magnetotransport properties of AlGaN/GaN heterostructure samples grown by novel patterned growth techniques, aiming for reducing the charged thread dislocations and improving the sample quality. AlGaN/GaN control sample, SiN-GaN and ELO-GaN samples were studied and lower-bound mobilities of 40,700  $\text{cm}^2/\text{Vs}$  and 32,400  $\text{cm}^2/\text{Vs}$  were extracted for 2DEG samples grown on ELO-GaN and SiN-GaN templates, respectively. The improvement in the electron mobility in 2DEG structures grown on lateral overgrown templates is obvious. Both SiN-GaN and ELO-GaN templates with reduced threading dislocation densities helped to increase the low-temperature electron mobility in the overgrown 2DEG structures. The results show that

both *in situ* grown  $\text{SiN}_x$  and *ex situ* grown  $\text{SiO}_2$  masking layers effectively block the threading dislocations. The mobility enhancement factor was estimated to be around 2 or higher; however, we currently do not know the exact mobility values of these samples due to the unknown contact resistances to the parallel channel.

The 2DEG samples grown on conventional u-GaN templates demonstrated electron mobilities up to 20,000  $\text{cm}^2/\text{Vs}$ . The peak occurs around  $6 \times 10^{12} \text{ cm}^{-2}$  in the mobility curve for the reference samples and the mobility decreases for higher carrier densities due to alloy scattering caused by increased Al mole fraction and interface roughness scattering. The laterally overgrown GaN 2DEG samples show lower-bound mobility values higher than 40,000  $\text{cm}^2/\text{Vs}$ . And the trend shows that the mobility curve will increase toward lower carrier density regime and peaks in the low  $10^{12} \text{ cm}^{-2}$ 's due to the reduced charged-dislocation scattering in these samples. Also the model for contact resistance and parasitic channel was presented and its impact on 2DEG magnetotransport measurements was discussed.

In Chapter 5, we have studied spin-orbit coupling and electron phase coherence in wurtzite  $\text{Al}_x\text{Ga}_{1-x}\text{N}/\text{AlN}/\text{GaN}$  2DEG by weak antilocalization (WAL) measurements, with different Al concentrations ranging from  $x=0.1$  to 0.35 in samples. We changed the carrier density in 2DEG by using the persistent photoconductivity effect and gating. Densities up to  $10.6 \times 10^{12} \text{ cm}^{-2}$  have been explored in AlGaN/GaN 2DEGs. It was found that the electron spin splitting energy does not scale linearly with  $k_F$  at high carrier densities. We extracted the linear and cubic spin-orbit parameters,  $\alpha=5.01 \times 10^{-13} \text{ eV}\cdot\text{m}$  and  $\gamma=1.6 \times 10^{-31} \text{ eV}\cdot\text{m}^3$ , respectively, for this GaN 2DEG system. The linear spin-orbit coupling parameter is consistent with previous reports based on WAL

measurements and should be viewed as an effective coupling constant which is a sum of the Rashba parameter and the linear spin-orbit coupling parameter associated with the BIA of the crystal. The cubic parameter, however, has not been measured previously and arises purely from the BIA of the crystal. Meanwhile, we found that the SO parameters extracted from the SdH oscillations from literature did not agree with WAL measurements. Furthermore, we were not able to change the spin-orbit coupling significantly by the use of gating effect. This suggests employing the Rashba effect in spin-transistors would be particularly challenging in the GaN system.

We have also measured the phase coherence times for the AlGaN/GaN system. Similar to other 2D electron systems, phase coherence was strongly temperature dependent and was in agreement with theories based on electron-electron interactions.

We expanded the measurements to an even higher carrier density regime by using two InAlN/AlN/GaN 2DEG samples to investigate the spin-orbit coupling in InAlN/GaN systems. The carrier density reaches as high as  $21.5 \times 10^{12} \text{ cm}^{-2}$ . We find that the spin-orbit field is not a constant at high carrier densities and the electron spin splitting energies shows a deviation from linear behavior with  $k_F$ . Possible mechanisms have been proposed to explain the experimental data. Our observations in this experiment may evoke further experimental and theoretical research on the SO coupling in GaN system.

In Chapter 6, we found that the WAL feature was strongly temperature dependent at low temperatures and used WAL as a thermometer to measure the electron temperature,  $T_e$ , as a function of the bias current in wurtzite  $\text{Al}_{0.15}\text{Ga}_{0.85}\text{N}/\text{AlN}/\text{GaN}$  and  $\text{Al}_{0.83}\text{In}_{0.17}\text{N}/\text{AlN}/\text{GaN}$  heterostructures with polarization

induced 2DEG in the Bloch-Gruneisen regime. We found that the power dissipated rate per electron,  $P_e$ , was proportional to  $T_e^4$  due to piezoelectric acoustic phonon emission by hot electrons. We calculated power dissipated per electron,  $P_e$ , as a function of  $T_e$  without using any adjustable parameters for both static and dynamic screening cases of piezoelectric electron-phonon coupling. In the temperature range of this experiment, the static screening mechanism is expected to be applicable; however, our data are in better agreement with the dynamic screening mechanism.

In Chapter 7, we calculated the response of an integer Quantum Hall liquid (IQHL) to a small magnetic field and it was shown that when the effective filling fraction  $\nu > 1/\alpha = 137$ , the IQHL would behave like a perfect diamagnet. To test this theory, a SET placed on an IQHL with 25 identical quantum well structures was used to detect small time varying magnetic fields in a large constant magnetic field background, and the screening effect has been observed when the effective filling fraction  $\nu = 150$ . This device can also be used as a magnetometer. The equilibration times associated with small changes in magnetic field were found to be strongly dependent on the positions in quantum plateaus and became immeasurably long as we went deep into the quantum Hall plateaus. We characterized the SET magnetometer by DC and AC measurements. At  $T = 20$  mK, the SET magnetometer worked at filling fractions up to  $n = 8$  and was most sensitive at the filling fraction  $n = 6$  with a maximum magnetometer sensitivity as  $0.09 \pm 0.01$   $\mu\text{T}/\text{Hz}^{1/2}$ .

In Chapter 8, we have studied the charge motions in the quantum Hall liquid (QHL) detected by single electron transistors. In the 25 layers multiple quantum wells sample, the charge equilibration process has been studied by applying magnetic pulses

and the coulomb blockade oscillations (CBOs) has been detected in the SET conductance measurements. The relaxation process was fitted by the exponential relaxation model and it was found that the data would deviate from the fitting model as time became longer and longer. The offset charge noise level can be extracted from the experiment and used as a figure of merit for the sample quality in terms of quantum information applications. It also gives us an error bar for this type of measurement, which could be served as an important parameter for tolerance design of the quantum interferometer. From this experiment, we believe a better 2DEG sample with less doping or doping far away from the 2DEG is crucial for the device application of quantum interferometer;

In a fractional QHL (FQHL) sample, antidot SETs were fabricated and the charge loading process was studied. An unusual process of charges moving in then moving out was observed in this sample, which we believe was owing to a QHL transport barrier formation in the SET area. Also the responses of the QHL to a simultaneously applied magnetic field and backgate voltage were studied. This experiment suggests that: (1) It is possible to load the quasi-particles into the antidot by using the magnetic field pulse, and this magnetic field loading process will create a higher charge density area around the antidot; (2) It is possible to load the quasi-particles into the antidot in the QHL by applying simultaneously the magnetic field and the backgate voltage without inducing significant charge relaxation; and (3) The response of the QHL around SET is asymmetric to magnetic field ramping up and down.

These experiments are important for understanding the dynamics of charge motions in the QHL, therefore can be used as a guide for the fabrication and application of quantum interferometer.

## 9.2 Suggestions for future work

In GaN 2DEG system, as a historic trend, with advances in growth techniques there have been significant improvements in reducing the threading dislocations in GaN heterostructures. As a result of these improvements, the maximum mobilities in the GaN based heterostructures has kept increasing and are expected to continue to increase further in the future.

In GaN 2DEG system, InAlN/GaN is very interesting because the lattice matching between InAlN and GaN. In our present work, we have demonstrated its potential to have a higher mobility than AlGaN/GaN samples. In the near future, we hope to study higher quality InAlN/GaN samples and focus on the carrier density range from  $1 \times 10^{12} \text{ cm}^{-2}$  to  $10 \times 10^{12} \text{ cm}^{-2}$  so that we could compare the results from this system with that of AlGaN/GaN samples. In our measurements, we found that the gate current leakage was a problem beyond the gate voltage range from -1.6 V to 0.4 V. Therefore, a different gate fabrication recipe should be used to reduce the gate current leakage. If necessary, an insulating SiO<sub>2</sub> thin film between the gate and the InAlN/GaN 2DEG sample should be deposited before the gate fabrication to prevent the gate leakage.

GaN also shows great potential in terms of spintronics applications. In our present work, we studied the spin-orbit interaction in GaN 2DEG system by WAL

measurements, but there were still puzzles needed to be solved for the origin of spin-orbit interactions, which will have a deep impact in devices design like gate controlled spintronics device. In order to better understand the spin-orbit coupling parameters, a theory specially tailored for GaN heterostructures and more experimental work on GaN samples covering a broader carrier density range, for example from  $14.1 \times 10^{12} \text{ cm}^{-2}$  to  $19.9 \times 10^{12} \text{ cm}^{-2}$ , are needed.

We can also extend the magnetotransport and WAL measurements to other heterostructures based on wide bandgap materials, such as ZnO, ZnO is a promising II-VI semiconductor and predicted to be a potential candidate for spintronics devices. Similar to GaN, ZnO shows great potential to be a ferromagnetic semiconductor above room temperature when doped properly[145]. And the WAL measurements in ZnO for different doping of magnetic ions could help us to understand how spin dynamics changes at the transition from normal semiconductor to ferromagnetic semiconductor. Our collaborators in Prof. Morkoc's group are working on ZnO growth and will provide us samples for such measurements in the future.

In GaAs/AlGaAs 2DEG system, we have studied the charge dynamics in quantum Hall liquids (QHL) by using GaAs 2DEG and single electron transistor (SET) hybrid devices. It was suspected that the offset charge motion was the major source of noise in our measurements. Therefore, reducing the offset charge motions would be the priority in the near future. For the future work, we need to get samples with lower offset charge noise to perform this experiment again. In terms of sample growth, we need GaAs heterostructures with lower doping or doping far away from the 2DEG channel. Also in the future experiment, some tricks like cooling down with a negative

backgate voltage applied should be used to reduce the offset charges further. And if necessary, we can illuminate the samples to increase the carrier density in 2DEG channel by a LED.

When we obtain the right samples, we need to repeat the experiments presented in Chapter 8, at same time extend the measurements to other quantum Hall plateaus, especially to the fractional quantum plateaus such as  $n=1/3$  and  $n=2/5$ , which is predicted to be able to perform topological quantum computation. A second magnetic coil which can instantly apply a relatively large magnetic field ( $\sim 10\text{-}100$  mT) is proved to be necessary for the success of those experiments. Also it would be interesting to repeat the magnetic and backgate combination pulses for quasi-particle loading. In particular, in Chapter 8 we observed charge moving-in then out motions in quantum plateau  $n=1$ . We need to repeat this experiment in different samples in different quantum plateau positions to see if it is a universal phenomenon and test our proposed mechanism (see Chapter 8).

If we can achieve a stable and fast loading of quasi-particles, we can go further to fabricate a quantum interferometer and test those theoretical predictions associated with the unusual statistics of Laughlin quasi particles. In such a quantum interferometer device, we can also fabricate a SET antidot on the same 2DEG surface and use this SET antidot as a calibrator for charge loading and unloading process. In this manner, the charge loading can be precisely controlled and monitored.

Also as indicated by the relation between the equilibration time  $t_e$  and the conductivity  $\sigma_{xx}$ , we can use the SET measurement to study the conductivity in the QHL, which is usually hard to be measured by other methods. By combining other

methods, such as Corbino geometry, Hall bar measurements and RF-SET [139-144], the  $\sigma_{xx}$  range from  $10^{-17}$  S to  $10^{-3}$  S could be covered [121]. It would be important to discover, if there are deviations from the variable range hopping picture in the deep QHL regime.

Finally, the semiconductor 2DEG and SET hybrid devices gives us a very unique tool to study the charge dynamics in microscopic scale. Graphene is an emerging new 2DEG system and fantastic new physics has been discovered. In the future, we hope to fabricate graphene and SET hybrid devices and study the charge dynamics in graphene. The offset charge might not be a big challenge for graphene because usually in graphene we can easily use the gate to control the carrier density due to the unique band structure of graphene. The underlying physics is expected to different in graphene due to the unique property of Dirac fermions.

## APPENDIX A

### DILUTION REFRIGERATOR OPERATION

#### Preparation and Cooling to 77 K

- (1) Clean out the cold traps, pump with mechanical pump for **3 hr** (~1Torr on He3 panel gauge).
- (2) Load sample
- (3) Test leads and thermometers

Thermometer	Channel	RT value ( $\Omega$ )	77K value	4K value
1Kpot (SPEER)	0	496	575	958
Still (ROx)	1	1000	1030	1290
Plate (ROx)	2	1000	1030	1290
Mix (Lieden)	3	382		
Mix (Oxford)	4	72		
Mag bottom		333	436	7.26k
Mag top		1023	1406	32.8k

- (4) Attach radiation shield. Make sure nothing will touch the radiation shield.
- (5) Attach vacuum can using an indium seal,
- (6) Pump on IVC first with the mechanical pump, then with the turbo pump (**30 min?**)

- (7) Attach the leak detector and leave it on.
- (8) Spray the outside of the IVC to look for leaks.
- (9) Pump the 1K pot out with the mechanical pump and then fill with helium gas, 3-5 times. While doing this, make sure leak detector does not detect a leak.
- (10) Pump out the 1K pot, for 5 min, then close the valve on the dewar. At this point, you can either keep pumping on the IVC with the leak detector or close it up.
- (11) Lift up the dewar on the fridge and secure.
- (12) Attach the main pump line to the valve on top of the still at the dewar. Using first the mechanical pump and then the turbo pump, pump out the fridge (should be just helium gas, not the mixture) from both the still and condenser via the He4 panel. **(2hrs)**
- (13) When the pressure is very low in the fridge and does not rise quickly when pumping is stopped, close the still valve on the dewar and all the valves on the He3 panel. Connect the main bath line to the main bath port and cap the still valve.
- (14) Fill the cold traps with liquid nitrogen.
- (15) Perform a flow test, by passing mixture from the dump thru one cold trap into the condenser line. All other valves should be closed, including all valves to the still side.

Monitor the pressure rise at G2 over 10 minutes.

#### Typical Data

Time (min)	Pressure (mTorr)
0	0.001
1	0.005
2	0.011
3	0.018

4	0.025
5	0.032
6	0.039
7	0.044
8	0.051
9	0.056
10	0.061

If the leak detector is connected to the IVC still, you can check if any mixture leaks out of the fridge into the IVC during the flow test.

- (16) Close up all the valves on the He3 panel.
- (17) If the IVC has not been pumped on for a long time (about **2hr** to 10mTorr) pump on it again with the turbo pump. When you are done close the valve on the fridge.
- (18) Begin the process of transferring liquid nitrogen in through the fill line, use the screw-in insert. One full liquid nitrogen dewar is enough to fill the system. Process will take about **4-5 hrs.**
- (19) Attach the sealed He3 cylinder to the port on the He3 panel near valve 18. Now pump on the service line area of the He3 panel that will be used when He3 exchange gas is added (from the port to the IVC line) with the turbo pump (**1hr**)
- (20) Stop pumping, fill the pumped region with about 500mTorr of He3. Do this slowly, never open the two valves on the He3 at the same time.
- (21) Close the valve to the IVC line on the He4 panel. Open the IVC valve on the fridge. Then open the IVC line on the panel, the pressure should drop as the He3 is

sucked into the IVC. Close the IVC valve on the fridge. Close all valves.

(22) Now the system is ready to be cooled to liquid nitrogen temperature all valves can be shut and pumps turned off. System will take about **2 hrs** to get to liquid nitrogen temperature.

### **Cooling to 4.2 K**

(1) When the system is cold, transfer the nitrogen out by pressurizing with helium gas.

Seal up the vapor cooled leads NPT connection and the pressure release valve. **(2hr)**

(2) When liquid stops flowing, blow helium for a few more minutes. Then switch to blowing helium in from the transfer line (10 min). Watch magnet resistors for evidence of evaporative cooling, then warming, when you see this you can stop the helium flow.

(3) Now helium transfer can begin. Make sure the main bath port is connected to main bath line, and is not capped. Start helium transfer. It will take a long time before liquid begins to collect in the bottom of the dewar (45min). When liquid is finally filling, pump on the 1K pot and open the needle valve for a short time, just to make sure it is not clogged. Initial transfer to 75% takes 95 L and approximately **2 hrs**.

(4) Remove cap on vapor cooled leads and pressure relief.

(5) Wait for fridge to get to liquid helium temperature. If it does not seem to be cooling down, then you might want to add more exchange gas. If the IVC pressure is 0.01 Torr or less, it probably needs more.

(6) Pump out exchange gas in IVC with turbo pump for a long time (**3hrs**), you can start when the fridge is 6K.

(7) At this point, the system is ready to begin condensing and then circulating.

### **Flow test at 4.2 K**

(1) First pump out the fridge from both sides. By pass the safety. Open the path to the dump, 9, 16 and turn on the scroll pump and wait for it to settle down. Turn on the turbo pump. O with the scroll pump and turbo pump, the safety might need to be bypassed.

(2) Perform a flow test again. Turn the safety back on.

(3) Turn off the turbo pump

### **Condensing and Circulating the Mixture**

*Note: Throughout this section it is assumed that the cold traps will be kept filled and the liquid helium level will be kept high enough to keep the 1K pot filled (about 55%). Also, the load on the 1K pot changes during different parts of this procedure, so the needle valve may need to be adjusted.*

(1) Fill the 1K pot by opening about  $\frac{3}{4}$  turn, once it is full begin pumping and maintain a temperature of 1.5 K or less (resistance of 1500 is optimal). The pressure should be somewhere around -28" and 10 Torr on gauge P2, but the gauges are not that sensitive in this range. There will be some icing (not instantly) but it should not extend up to the flexible line.

- (2) Open up the dump and let the mixture pass through a cold trap and into the still via valve 4. The system will cool and the pressure will drop. When the pressure drops to around 50 Torr, it is time to start circulating a bit.
- (3) Start sending the mixture in through the condenser instead of the still. Close valve 4 and 6. Open 25. Close valve 9 and open 13.
- (4) Turn on the safety and the scroll pump. Start circulating by opening 1. Open 7 and then open 2 very slightly, so start getting the rest of the mixture out of the dump. Open 17.
- (5) The back pressure will start to increase. When the pressure nears 600 Torr, start to close 2 slightly until pressure is stable or decreasing.
- (6) The fridge can be left in this state, excess pressure will go into dump 2 via 13. The system will slowly cool down (overnight). If the pressure gets too high, the safety valve at 17 will open and you will need to recondense a lot of mixture again.
- (7) As the back pressure gets low you can open 2 more. When most of the mixture is out, you can also open the main valve over time (while monitoring the back pressure)
- (8) When the still pressure is low (less than 2 Torr), close the main valve and 2 and 7. Turn on the turbo pump. Slowly open the main valve, while monitoring the back pressure. When the valve can be fully opened with a safe back pressure, you can also pump the rest of the mixture out of the dump. This is a good time to switch cold traps.
- (9) When the mixture is all in and temperature falls below about 0.5 K, start heating the still to increase circulation, start gently to prevent the backpressure from getting too high. Still current should be 2.8-3.2 mA to achieve base temperature, this should result in a still pressure of 0.006-0.017 Torr and still temp of 3700-3450  $\Omega$ . Wait for

temperature to decrease to the base temperature. (multiple hours)

### **Normal Operation State**

#### **He3 panel**

- Both pumps are on.
- Main valve to still is open.
- Either cold trap 1 or 2 is open
- 25 to condenser is open.
- Safeties:
  - Safety switch light on pump power supply box is on.
  - 17, 14, 16, and 8 are all open.
- All other valves are closed.

#### **He4 panel**

- Mechanical pump is on and pumping on 1K pot.
- 1K pot valve on dewar is open.
- Needle valve is partially open.
- All IVC valves are closed.
- Main bath port on dewar is connected to main bath tubing and pressure relief is attached to main bath port on panel.

System uses about 1% He in 1.5 hrs in the range of 80%-55%. Cold traps can be filled

about once a day

### **Warming up**

- (1) Stop circulating and send everything to the dump.
- (2) Turn off the turbo pump (?)
- (3) Heat the still and mix with less than 10mV each. (*Do not heat the mix or still when the system is very warm! Do not leave it unattended with the heaters unless you are sure it will not be empty when you get back!*)
- (4) Close the main valve when the temperature reaches about 10 K and the pressure is low.
- (5) Before letting the cold traps warm up, pump them out in to the dump from both sides.
- (6) Pump out the region between valves 4 and 25.
- (7) When you are done, turn off the pump, note the pressure and close 14 and all other valves. Fridge can be left in this state.
- (8) Before lowering the dewar, add -2.2 in Hg of He to the fridge from the main bath line hooked up to the little valve on the still.

### **Cleaning cold traps**

*Do not let cold traps warm up unless you have pumped all the mixture out!*

- (1) First pump all of the mixture out with the He3 pumps. The pressure should go down

to ~60-100 mTorr.

(2) When the trap is emptied of mixture, close the valves leading to the He3 pumps. Then pump on them through the service line with the mechanical pump. Lift the cold traps out of the nitrogen and let them warm up. Cold traps are clean when they are warm and the pressure is ~1 Torr or less (2-3hrs).

### **Magnet Operation**

- (1) Remove the weights and put them in the far corner of the screen room.
- (2) Remove the cables and s-hooks.
- (3) Move any other ferromagnetic objects out of the screen room.
- (4) Connect the magnet cables and push the magnet leads on the dewar down.
- (5) Make sure that the persistence switch is connected to the dewar.
- (6) Make sure that the pressure relief valve for vapor cooling of the leads is opened.
- (7) Run the magnet power supply off of a noise suppressing power strip.

## APPENDIX B

### EVAPORATION PROCEDURE FOR TUNNEL JUNCTIONS

#### **Turning on the pumps:**

- (1) Check that the V1 & V2 are open.
- (2) Turn on the mechanical pump.
- (3) Turn on power.
- (4) Open the foreline valve (pressure on TC2 should go down).
- (5) Turn on the two water lines.
- (6) Turn on the heat exchange.
- (7) Turn on the diffusion pump; touch the bottom side of the pump, which should be at room temperature. Wait 1/2 hr. then feel side of evaporator - if it is warm then proceed.

#### **Loading the sample and pumping:**

*(Can be performed while waiting for the diffusion pump to warm up.)*

- (1) Open air release valve. (You can do this as long as Roughing Valve and vacuum value is close).
- (2) While waiting for bell Jar to open, clean the evaporator boats and Al with acetone then blow dry. Twist up the Al so that it can easily fit into the boat. Have more Al cleaned for the second evaporation than for the first evaporation.

(3) Open bell jar by lifting up. Put boat in between the knobs or screws. Put boat on opposite ends (Front boat is close to you - and Back is close to the wall.) Place the smallest amount of Al in the Front boat (1<sup>st</sup> evaporation) & other Al in the Back boat (2<sup>nd</sup> evaporation)

(4) Move the shutter so that it covers the 1<sup>st</sup> evaporation boat.

(5) When placing the sample in the chamber make sure the sample is lined up in the middle of the boats you will evaporate from (perpendicular) and parallel to the boats.

(6) Move the handle on front panel of the evaporator to the notch marked "F" for front boat.

(7) Close the bell jar.

(8a) If you will use oxidation for this evaporation then leave air release valve open and close V1. Open V2. Open the cylinder valve on the oxygen-argon mixture. (Do not turn on the Black Valve yet.) Close the Foreline Valve and open the roughing valve just a bit then push down on the bell jar until vacuum catches. Then open the roughing valve completely. If the pressure on the oxygen-argon line is -20 (or below zero). **Then close V2 valve (make sure V3 is closed) – open black valve on the oxygen tank – close black valve on tank – open V2 valve.** Then repeat process above in bold at least three times. At the end of the process on the 3<sup>rd</sup> time the V2 valve should be open & air release valve should also be open.

(8b) If you will not use oxidation then close the air release valve, once the pressure is on TC1 is below 0.2 Torr then Close the foreline valve.

(9) Open the roughing valve a little then push on the top of the bell jar until vacuum seals then open the roughing valve completely. Pump until the TC1 is 0.2 Torr.

- (10) Close roughing valve once TC1 reaches .2 Torr.
- (11) Open foreline valve.
- (12) Open the Main valve until you hear a ‘clunk’. Then open the valve slowly while monitoring the pressure on TC2. (Turn counter clockwise to open). When the pressure rises on TC2 stop momentarily and wait for the pressure to go close to 0.5 then open the valve more. Continue to do this until the main valve is completely open.
- (13) Turn on the ion gauge. Wait for 1hr. 45 min. until the pressure is in the  $10^{-7}$  Torr range.

Once the pressure has been reached.

- (14) Turn on the thickness monitor. It will do some testing; just press the Stop button to override this.
- (15) Check the Material Density 2.70; Tooling Factor 100.

### **Evaporation of Metal**

- (1) Turn the power supply (SCR)
- (2) Slowly turn the knob and monitor the Ampmeter (to the far right of the power supply) and the evaporation rate on the thickness monitor. Do turn the dial pass 2 Amps.
- (3) When the evaporation rate is steady (5-15 A°/s). Open the shutter (uncover the boat you will evaporate from) and press the Start button on the thickness monitor.
- (4) When the correct thickness is reached. Then cover the evaporation boat and press Stop on the thickness monitor. Turn the power supply dial to zero and turn off the SCR power supply.

- (5) Record the thickness.
  - (6) If you are not doing another evaporation then proceed to shut down process.
  - (7) If you are ready to oxidize then wait 2 minutes.
  - (8) Close main vacuum valve.
  - (9) Turn off the ion gauge.
- (10) Close V2 and check that V3 is closed.**
- (11) Open the black valve on the oxygen-argon tank.**
- (12) Close the black valve**
- (13) Open V2 and repeat the steps above in bold.**
- (14) Repeat steps 10 times. On 10 the V2 valve should be open and black valve should be closed.
  - (15) Close air release valve and Turn off cylinder valve on oxygen-argon mixture. Wait 3 minutes.
  - (14) Close the Foreline Valve.
  - (15) Open the roughing valve and wait till TC1 goes to .2 Torr.
  - (16) Close the roughing valve.
  - (17) Open the Foreline Valve.
  - (18) Open the main valve and monitor pressure on TC2.
  - (19) Wait till pressure pumps down again (15 minutes) evaporate the second metal following same steps and record the thickness.

### **Shut Down**

- (1) Wait 10 minute for cooldown.

- (2) Close the main valve.
- (3) Open V1 (V1 and V2 should be open). Turn off ion gauge
- (4) Open air release valve.
- (5) Turn off the diffusion pump.
- (6) Open the chamber and remove the samples.
- (7) Close chamber and close air release valve.
- (8) Close the foreline valve.
- (9) Open the roughing a little and push down on the Bell Jar until vacuum is sealed.  
Then open roughing valve completely. Wait until pressure on TC1 is .2.
- (10) Close roughing valve.
- (11) Open foreline valve.
- (12) Wait about 1/2 hr. for system to cool by feeling on the side of the evaporate panel  
(you want it to reach room temperature).
- (13) After 1/2 hr. turn off heat exchange and two water valves.
- (14) Close foreline valve.
- (15) Turn off mechanical pump and turn off power.

## APPENDIX C

### GaAs 2DEG HALL BAR FABRICATION

#### Procedure for photolithography fabrication in the cleanroom:

Making the masks by mask maker (My mask file is HB.DAT).

##### Definition of mesas using positive photoresist

- a) Cleave samples into square pieces (~2-4mm).
- b) Clean samples with Acetone, IPA, water, Blow dry with Nitrogen gas.
- c) Mount samples onto cover glass with photo resist (1813 or others) as a glue.  
Prebake for 1-2 min at 110°C by hot plate. (110 °C is for 1813. Other photo resist please see the manual for the crystallization temperature)
- d) Spin coating HMDS, 30s, 4000 rpm (using spinner)
- e) Spin coating 1813, 30s, 4000 rpm
- f) Prebake at 105°C, for 1min on hotplate
- g) Go to mask aligner, expose it for 6s (using MJB3 mask aligner)
- h) Develop with MF351:DI=1:5, for 1min
- i) Rinse in DI water for 3min
- j) Inspect: use filtered light (using microscope)
- k) Descum: 1min/80W/250mT/17% O<sub>2</sub> plasma
- l) Hard bake: 120°C for 15 min (using Oven)

- m) Mesa etch for 2.5min (GaAs: 1600Å/min) w/ H<sub>3</sub>PO<sub>4</sub>:H<sub>2</sub>O<sub>2</sub>:H<sub>2</sub>O (1:1:25)
- n) Strip resist: Ace/IPA/N<sub>2</sub> Dry
- o) Dektak Mesa

Definition of contact pads using negative photoresist:

- a) Mount samples onto cover glass with photoresist (1813). Prebake for 1-2 min at 110°C by hot plate.
- b) Spin coating HMDS, 30s, 4000 rpm
- c) Spin coating 5218, 30s, 4000 rpm (can use 5214 see step note on step \*.)
- d) Prebake on hotplate at 105°C for 1min
- e) Go to mask aligner, expose it for 6s
- \*) Bake on hotplate at 120°C for 2-4min (only for 5214)
- f) Flood expose for 1min
- g) Develop in MIF319 for 1min
- h) Rinse in DI water for 3min
- i) Inspect: use filtered light
- j) Descum PR for 1-2min at 80W, 250mTorr, 17% O<sub>2</sub>
- k) Oxide Remove with Ammonium Hydroxide (NH<sub>4</sub>OH:H<sub>2</sub>O, 1:15) for 15s
- l) No DI rinse, N2 dry, place into evaporator immediately
- m) Evaporate contacts (Ni/Ge/Au/Ti/Au=200/325/650/200/2000 Å)  
(Alternative contact recipe: Ni/Ge/Au=200/325/1500 Å), annealing for 30s at 450°C
- n) Liftoff with warm acetone, IPA for 1min, DI rinse for 1min

- o) Anneal contacts for 1-2min at 410-425°C at anneal station (might be different for different 2DEG samples, rising the temperature usually take 1-2 minutes).

*Definition of gates using negative photoresist:*

- a)-n) same as definition of contacts.
- o) Evaporate gate (Ti/Au=500/1500 Å) (using SJ20 evaporator)
- p) Lift off with warm acetone, followed by IPA for 1min, DI water rinse for 1min.

## **APPENDIX D**

### **NPGS AND PHILIPS XL30 EBEAM LITHOGRAPHY INSTRUCTRIONS**

#### **Prepare Sample**

- Place the sample onto the sample holder, clip down firmly
- Put small drops of Ni beads in IPA on two corners of the sample

#### **Prepare SEM**

- Log into SEM logbook.
- Connect the 9 pin and 37 pin connectors.
- Vent the SEM chamber.
- Load the sample mount into the chamber, adjust the height so that the Au standard is at approximately 10mm, connect the sample to picometer contact in the chamber, and hook up the picometer to the BNC on the SEM.
- Click “Pump” button.
- Wait for SEM to read “Vacuum OK”
- Check View → SE, Beam → 30kV, Spot → 1
- Click on “Beam” button

- Check to make sure Magnification is on “Videoprint”, that stage is not tilted and that scan angle (open Stage window) is set to zero.

## **Measure Current**

- Find the hole on Faraday cup, switch to Scan->Spot, place the +(spot) on the Faraday cup hole, measure currents for spot sizes that will be used in the write.
- Switch back to smallest spot size( $\sim 10 \mu\text{m}$ ) that will be written in.

Typical values (for 30kV)

Spot	current
1	23pA
2	45pA
3	
4	
5	
6	1300pA

## **Focus on Au standard**

- Find the gold standard, focus on it using the right mouse button, click Z↔ FWD and make sure that z is around 10+/-1 mm
- Using slow scan 2, zoom in and keep adjusting focus until the image cannot be improved by focusing alone (update z by clicking Z↔ FWD)

- Center aperture. Maximize “Beam” window, check “lens modulator”, adjust x and y knobs (besides the electron source cylinder) until the image does not move shake, then uncheck “lens modulator”, minimize “Beam” window.
- Adjust astigmatism with shift+right mouse button. Adjust the focus again. Zoom in. Repeat this step until image looks good at 100,000x magnification
- Click “Z↔ FWD” button.

### **Find the sample coordinates and focus values**

- Find an edge of the sample and line things up using the Rotation knob
- Find the nickel beads on the corner, **use “Z” knob to focus** (~30,000-70,000x’s mag)
- Click “Z↔ FWD” to update
- Fine tune the focus with the mouse, click “Z↔ FWD”, and write down the (x,y,z) value.
- Go to nickel beads on the other corner. Focus on this using the mouse.
- Click “Z ↔ FWD”. Record (xyz) values for this corner.
- Average the two z values, and using the mouse (update “Z↔FWD”) adjust the z value to the average of the two. For good focus, the difference between your estimated focal length and the actual focal length should be less than 60 um.

### **Prepare to write**

- Check the current for the smallest spot size again.
- Move the beam to somewhere on the edge or off the sample.

- Calculate how much the SEM will have to move to get to the middle of the sample
- Input parameters (beam currents, x,y move values for the first entity and the move only entity) in Runfile Editor (in Nabity).
- Save File
- Run “SCS” on the SEM computer and set Scan to “external XY”
- Check time required for the writing, (Command → Process Run File → Time Test Mode). To look at the results, click “lastRun.log”. This process will also reveal some errors in the files.
- Set Magnification to the first magnification that will be written in,
- Set “DAC” to 10,10 or 5,5 (in Nabity)

### **Write**

- Run file, click “Process Run file”
- Make sure that the system does not indicate an error and watch for the XY knobs to turn indicating Stage motion.
- If multiple current settings are used, when system pauses writing, change to the appropriate spot size on SEM , hit “space” bar to continue.
- At the end of the run, the Move only command should move the stage so the beam is away from the active region.
- When Nabity program returns from DOS mode, the write it finished.

### **Finish**

- Replace cables 37 and 9 pin cables.

## Troubleshooting

If you need to stop the program, Ctrl-Alt-Del usually works (the Nabit escape commands usually don't).

## Tips on choosing parameters for electron beam lithography pattern and run files

Field of View = 90000/magnification (determined by the SEM)

The smallest magnification possible is about 35, it depends on the working distance.

Magnification where coil gain changes:

Zooming in	Zooming out
345	310
1590	1410
43254	38254

These values are approximate, because they change slightly with working distance, they are determined by zooming in and out on the SEM and listening for a clicking noise, it is usually accompanied by a slight change in position of the SEM image. This is one of the reasons an overlap between pattern elements is recommended. For the best precision, you should avoid using magnifications where there may be a change in coil gain.

Approximated field of view	Center to center distance and line spacing	Spot Size	Magnification
----------------------------	--	-----------	---------------

40 – 45 um	120A	1	2000-1800
200 um	300-500	3 or 6	400
2.5 um	2000-4000	6	35-40

Actual values will depend on specific pattern

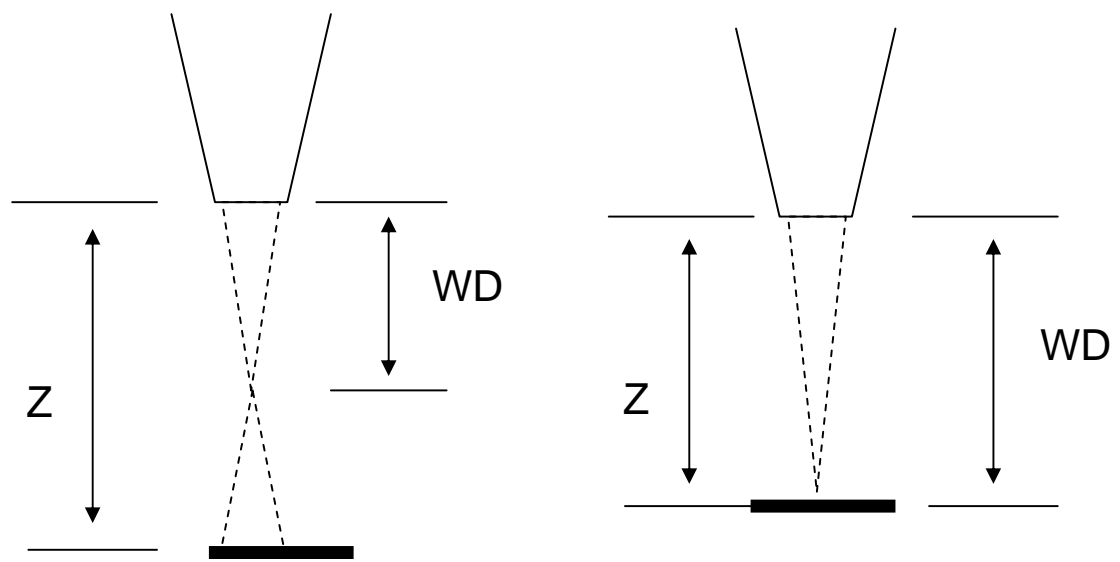
It is important to understand the difference between Z (actually distance between sample and electron gun) and FWD( focal working distance). It is easy to think of this in terms of a spot of light projected through an adjustable lens onto a screen. Adjusting the lens changes the point at which the light is focused (WD). Adjusting the position of the screen changes the distance between the lens and the screen (Z). In the SEM, Z is initially determined when you focus on a surface and then click Z↔ FWD. The SEM uses the known working distance to determine Z. If you do not do this initially, the Z value will be a meaningless number. Notice that if you focus on another surface on the stage, with a different height, the working distance will change but the SEM will still give a z that is the distance between the first surface and the gun, unless you update Z again.

In order to get a focused spot of light on the screen actual Z and WD must agree, you can either adjust the distance between the screen and lens (Z) or adjust the lens (FWD). When you are just looking at a sample, it does not really matter too much which technique you use (as long as you do not crash the sample into the gun!). However, in the electron beam lithography process it is very important.

When you initially focus on the gold standard, you are free to use the mouse (adjusting the working distance) to bring the sample into focus. When you are done, you click on Z↔ FWD to find out the distance between the Au standard and the gun. The Au standard is used for focusing on, but you really want to focus on the sample for the write. Unfortunately, there are two problems with this:

- 1.) The sample you want to write on and the Au standard are not usually at the same height.
- 2.) Changing the working distance of the lens with the mouse messes up the astigmatism that you spent so long perfecting.

For these reasons, to focus on the sample, the z knob is used to slowly bring the sample up to the correct height and into focus. This is like changing the position of the screen to bring the spot of light into focus. When you are done doing this, the z value will give a lower value, that is the distance between the gold standard and the lens. By clicking Z↔ FWD, you set the z value to the distance between the sample and the gun. Once you have done this, the focus might need some fine tuning, it is ok to do this with the mouse. Usually the fine tuning should be in the range of 0.1 mm or less.



Z and WD do not agree, image is out of focus

Z and WD agree, image is in focus

## APPENDIX E

### TIPS FOR SINGLE ELECTRON TRANSISTOR FABRICATION

- 1) In spin coating, the GaAs sample should be placed off the center of the substrate.
- 2) Spin coating MMA E-9 (or E-11), 4000 rpm, 45 seconds, pre-baking at convention oven 140 °C for 10-15 minutes. (thickness ~320nm) Then spin coating PMMA 950 A2, 4000 rpm, 45 seconds, pre-baking at convention oven 170 °C for 20 minutes. (thickness~50nm)

*Note: Always use convention oven, never do hot plate. I do not recommend to do the e-beam lithography immediately after the spin coating. Usually I will wait for a day for the MMA/PMMA double layer to be cured.*

- 3) In e-beam, in order to write fine features (~50 nm), we need to increase the numerical aperture. Therefore, instead of 10 mm working distance recommended for SEM user, I always push it to 7-8 mm working distance in SEM. But be cautious not to bump the SEM gun to the sample.
- 4) Etching recipe for GaAs: H<sub>3</sub>PO<sub>4</sub>:H<sub>2</sub>O<sub>2</sub>:H<sub>2</sub>O=1:8:40. Etching rate for GaAs ~15 nm/sec.
- 5) For the alignment marks, 15 seconds etching is good enough for the SEM scan. We do not need to coat Au to increase the image contrast in SEM and NPGS. But, some

adjustment in SEM software might be needed. I usually set contrast to ~40 and brightness to ~55. If you do not see the SEM image of the alignment marks, do not panic. Most likely the contrast and brightness are not set up right. If necessary, perform “slow scan” in SEM.

6) Always use the smallest aperture and smallest spot size for fine features. My measured smallest current is about 23 pA.

7) In alignment, always do the manual alignment (by adjusting the X and Y screws) until the last step. In the last step, you can do the manual alignment first to roughly align the marks, and then use the NPGS software to change the position of the alignment mark in the computer screen and the NPGS will do the correction for you.

For manual alignment, the precision could be within a few hundred nm.

8) The dosage for GaAs SET fine features: ( $740\text{-}810 \mu\text{C}/\text{cm}^2$ ). If the alignment mark is near to the SET, due to proximity effect, we need to lower the dosage ( $740 \mu\text{C}/\text{cm}^2$ ). Otherwise,  $800 \mu\text{C}/\text{cm}^2$  might be good. But it always depends on the materials and other features nearby.

9) The dosage for large features (contact pads, etc.) is  $350\text{-}400 \mu\text{C}/\text{cm}^2$ .

10) In developing, MIBK:IPA=1:3, rinse for 65 seconds, then rinse by IPA for 30 seconds.  $\text{N}_2$  dry.

11) Al evaporation:

Need to put the Al wire uniformly in the heating boat. I use leads 2 (first) and 4 (second) for evaporation. Usually pump down to  $2\text{-}4 \times 10^{-7}$  torr as the vacuum background.

*First evaporation:* evaporating rate 10-20Å/second, thickness in thickness monitor: 2000 Å. (real thickness in sample is around 500 Å). Then lower the holder (~10 turns), wait for one minutes and do the oxidation. 580 mtorr O<sub>2</sub>, 3 minutes.

*Second evaporation:* evaporating rate 10-20Å/second, thickness in thickness monitor: 2000-2500 Å. (real thickness in sample is around 500 Å)

12) There are sometimes problems in making good ohmic contacts with Al contact pads. (Al<sub>2</sub>O<sub>3</sub> will form at the surface). Therefore before wiring, we need coat the contacts pad with Au. In order to protect the SET, we need to cover the SET area by a tiny drop of photo resist. I always use 1813 for that purpose. Do not use PMMA or MMA for covering the SET area. From my experience, MMA/PMMA is too sticky and it might peel off the SET from the substrate during the liftoff. I cut a piece of Al foil into a triangular shape and use the triangle tip as a brush to drop the 1813 droplet into the small area around SET. In this process, you need to ground yourself.

13) Au evaporation: 100 nm thick Au is good enough. Be careful when you do the liftoff. I used the hot acetone in clean room to do the liftoff. After liftoff, it is OK to take a SEM picture of the SET devices. From experience, the SEM scan will not destroy the SET. But be very careful during the process.

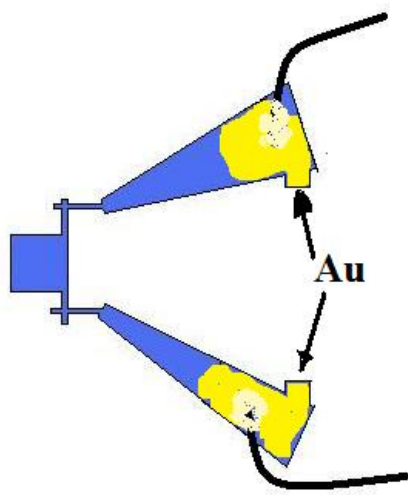


Fig. E1: Diagram showing the Au deposited on contact pads.

14) Never use the Indium solder to wire the sample. Always use the silver paste. Silver paste will cure in a day.



Fig. E2: Silver paste used in the lab.

15) Ground yourself when you are wiring, and be careful about the static charge.

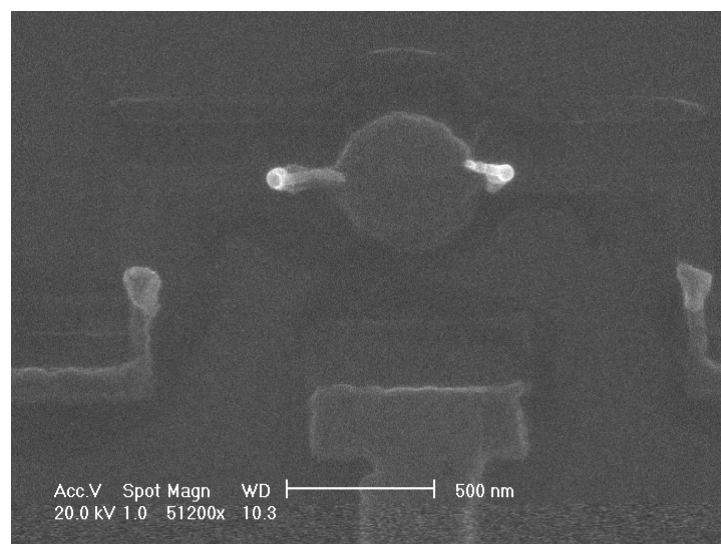


Fig. E3: SEM image of a burned SET due to static charge.

## BIBLIOGRAPHY

- [1] Gordon E. Moore, "Cramming more components onto integrated circuits," Electronics Magazine, 4 (1965).
- [2] Pallab Bhattacharya, "Semiconductor Optoelectronic Devices," (1997).
- [3] K. v Klitzing, G. Dorda, and M. Pepper, "New Method for High-Accuracy Determination of the Fine-Structure Constant Based on Quantized Hall Resistance," Phys. Rev. Lett. **45**, 494 (1980).
- [4] D. R. Yennie, "Integral quantum Hall effect for nonspecialists," Rev. of Mod. Phys. **59**, 781 (1987).
- [5] R. B. Laughlin, "Anomalous Quantum Hall Effect: An Incompressible Quantum Fluid with Fractionally Charged Excitations," Phys. Rev. Lett. **50**, 1395 (1983).
- [6] Horst L. Stormer, "Nobel Lecture: The fractional quantum Hall effect," Rev. of Mod. Phys. **71**, 875 (1999).
- [7] D. C. Tsui, H. L. Stormer, and A. C. Gossard, "Two-Dimensional Magnetotransport in the Extreme Quantum Limit," Phys. Rev. Lett. **48**, 1559 (1982).
- [8] B. I. Halperin, "Statistics of Quasiparticles and the Hierarchy of Fractional Quantized Hall States," Phys. Rev. Lett. **52**, 1583 (1984).
- [9] K. S. Novoselov, Z. Jiang, Y. Zhang, S. V. Morozov, H. L. Stormer, U. Zeitler, J. C. Maan, G. S. Boebinger, P. Kim, and A. K. Geim, "Room-Temperature Quantum Hall Effect in Graphene," Science **315**, 1379- (2007).
- [10] P.Y. Yu and M. Cardona, Fundamentals of semiconductors (1996).
- [11] R. A. Stradling and P. C. Klipstein, "Growth and characterization of semiconductors," (1990).
- [12] Gordon Baym and Christopher Pethick, "Landau Fermi-Liquid Theory," (1991).

- [13] John H. Davis, The physics of low-dimensional semiconductors: An introduction, Cambridge University Press (1998).
- [14] M. K. Sheinkman and A. Y. Shik, Soviet Physics Semiconductors-Ussr **10**, 128 (1976).
- [15] A. S. Dissanayake, J. Y. Lin, and H. X. Jiang, "Persistent photoconductivity in  $Zn_{0.04}Cd_{0.96}Te$  semiconductor thin films," Physical Review B **48**, 8145 (1993).
- [16] J. Y. Lin and H. X. Jiang, "Relaxation of stored charge carriers in a  $Zn_{0.3}Cd_{0.7}Se$  mixed crystal," Physical Review B **41**, 5178 (1990).
- [17] D. V. Lang and R. A. Logan, "Large-Lattice-Relaxation Model for Persistent Photoconductivity in Compound Semiconductors," Physical Review Letters **39**, 635 (1977).
- [18] D. V. Lang, R. A. Logan, and M. Jaros, "Trapping characteristics and a donor-complex (DX) model for the persistent-photoconductivity trapping center in Te-doped  $Al_xGa_{1-x}As$ ," Physical Review B **19**, 1015 (1979).
- [19] D. J. Chadi and K. J. Chang, "Energetics of DX-center formation in GaAs and  $Al_xGa_{1-x}As$  alloys," Physical Review B **39**, 10063 (1989).
- [20] D. J. Chadi and K. J. Chang, "Theory of the Atomic and Electronic Structure of DX Centers in GaAs and  $Al_xGa_{1-x}As$  Alloys," Physical Review Letters **61**, 873 (1988).
- [21] L. J. van der Pauw, "A method of measuring specific resistivity and Hall effect of discs of arbitrary shape," Philips Research Reports **13**, 1 (1958).
- [22] H. Morkoç, Handbook of Nitride Semiconductors and Devices, Wiley-VCH, **Vol 3** (2008).
- [23] S. N. Mohammad, A. Salvador, and H. Morkoç, "Emerging GaN-based devices," Proc. IEEE, 1420 (1996).
- [24] M. J. Manfra, L. N. Pfeiffer, K. W. West, H. L. Stormer, K. W. Baldwin, J. W. P. Hsu, D. V. Lang, and R. J. Molnar, "High-mobility AlGaN/GaN heterostructures grown by molecular-beam epitaxy on GaN templates prepared by hydride vapor phase epitaxy," Appl. Phy. Lett. **77**, 2888-2890 (2000).
- [25] L. McCarthy, I. Smorchkova, H. Xing, P. Fini, S. Keller, J. Speck, S. P. DenBaars, M. J. W. Rodwell, and U. K. Mishra, "Effect of threading dislocations on AlGaN/GaN heterojunction bipolar transistors," Appl. Phy. Lett. **78**, 2235 (2001).

- [26] I. P. Smorchkova, L. Chen, T. Mates, L. Shen, S. Heikman, B. Moran, S. Keller, S. P. DenBaars, J. S. Speck, and U. K. Mishra, "AlN/GaN and (Al,Ga)N/AlN/GaN two-dimensional electron gas structures grown by plasma-assisted molecular-beam epitaxy," *J. Appl. Phys.* **90**, 5196-5201 (2001).
- [27] M. J. Manfra, K. W. Baldwin, A. M. Sergent, K. W. West, R. J. Molnar, and J. Caissie, "Electron mobility exceeding 160 000 cm<sup>2</sup>/V s in AlGaN/GaN heterostructures grown by molecular-beam epitaxy," *Appl. Phys. Lett.* **85**, 5394-5396 (2004).
- [28] C. Skierbiszewski, K. Dybko, W. Knap, M. Siekacz, W. Krupczynski, G. Nowak, M. Bockowski, J. Lusakowski, Z. R. Wasilewski, D. Maude, T. Suski, and S. Porowski, "High mobility two-dimensional electron gas in AlGaN/GaN heterostructures grown on bulk GaN by plasma assisted molecular beam epitaxy," *Appl. Phys. Lett.* **86**, 102106 (2005).
- [29] E. F. Schubert, [www.lightemittingdiodes.org](http://www.lightemittingdiodes.org).
- [30] J.W. Chung, O.I. Saadat, J.M. Tirado, X. Gao, S.P. Guo, and T. Palacios, "Gate-Recessed InAlN/GaN HEMTs on SiC Substrate With Passivation," *IEEE Elec. Dev. Lett.* **30**, 904 (2009).
- [31] M. Gonschorek, J.-F. Carlin, E. Feltin, M. A. Py, N. Grandjean, V. Darakchieva, B. Monemar, M. Lorenz, and G. Ramm, "Two-dimensional electron gas density in Al<sub>1-x</sub>In<sub>x</sub>N/AlN/GaN heterostructures (0.03<x<0.23)," *J. Appl. Phys.* **103**, 7 (2008).
- [32] J. Kuzmík, "Power electronics on InAlN/(In)GaN: prospect for a record performance," *IEEE Elec. Dev. Lett.* **22**, 510 (2001).
- [33] J. H. Leach, M. Wu, X. Ni, X. Li, Ü. Özgür, and H. Morkoç, "Effect of lattice mismatch on gate lag in high quality InAlN/AlN/GaN HFET structures," *Phys. Stat. Solidi (a)* **207**, 211 (2010).
- [34] P. T. Coleridge, R. Stoner, and R. Fletcher, "Low-field transport coefficients in GaAs/Ga<sub>1-x</sub>Al<sub>x</sub>As heterostructures," *Phys. Rev. B* **39**, 1120 (1989).
- [35] L. Shen, S. Heikman, B. Moran, R. Coffie, N.-Q. Zhang, D. Buttari, I. P. Smorchkova, S. Keller, S. P. DenBaars, and U. K. Mishra, "AlGaN/AlN/GaN High-Power Microwave HEMT," *IEEE Electron Dev. Lett.* **22**, 457 (2001).
- [36] Isao Kidoguchi, Akihiko Ishibashi, Gaku Sugahara, and Yuzaburoh Ban, "Air-bridged lateral epitaxial overgrowth of GaN thin films," *Appl. Phy. Lett.* **76**, 3768-3770 (2000).

- [37] S. Schmult, M. J. Manfra, A. M. Sergent, A. Punnoose, H. T. Chou, D. Goldhaber-Gordon, and R. J. Molnar, "Quantum transport in high mobility AlGaN/GaN 2DEGs and nanostructures," *physica status solidi (b)* **243**, 1706-1712 (2006).
- [38] I. P. Smorchkova, C. R. Elsass, J. P. Ibbetson, R. Vetur, B. Heying, P. Fini, E. Haus, S. P. DenBaars, J. S. Speck, and U. K. Mishra, "Polarization-induced charge and electron mobility in AlGaN/GaN heterostructures grown by plasma-assisted molecular-beam epitaxy," *J. Appl. Phys.* **86**, 4520-4526 (1999).
- [39] L. Hsu and W. Walukiewicz, "Effect of polarization fields on transport properties in AlGaN/GaN heterostructures," *J. Appl. Phys.* **89**, 1783-1789 (2001).
- [40] M. J. Manfra, S. H. Simon, K. W. Baldwin, A. M. Sergent, K. W. West, R. J. Molnar, and J. Caissie, "Quantum and transport lifetimes in a tunable low-density AlGaN/GaN two-dimensional electron gas," *Appl. Phys. Lett.* **85**, 5278-5280 (2004).
- [41] L. Hsu and W. Walukiewicz, "Transport-to-quantum lifetime ratios in AlGaN/GaN heterostructures," *Appl. Phys. Lett.* **80**, 2508-2510 (2002).
- [42] D. Jena, I. Smorchkova, A.C. Gossard, and U.K. Mishra, "Electron Transport in III-V Nitride Two-Dimensional Electron Gases," *Phys. Stat. Soli. (b)* **228**, 617-619 (2001).
- [43] Z. W. Zheng, B. Shen, R. Zhang, Y. S. Gui, C. P. Jiang, Z. X. Ma, G. Z. Zheng, S. L. Guo, Y. Shi, P. Han, Y. D. Zheng, T. Someya, and Y. Arakawa, "Occupation of the double subbands by the two-dimensional electron gas in the triangular quantum well at  $\text{Al}_x\text{Ga}_{1-x}\text{N}/\text{GaN}$  heterostructures," *Phys. Rev. B* **62**, R7739 (2000).
- [44] Ikai Lo, J. K. Tsai, M. H. Gau, Y. L. Chen, Z. J. Chang, W. T. Wang, J. C. Chiang, K. R. Wang, Chun-Nan Chen, T. Aggerstam, and S. Lourdudoss, "Study of two-subband population in Fe-doped  $\text{Al}_x\text{Ga}_{1-x}\text{N}/\text{GaN}$  heterostructures by persistent photoconductivity effect," *Phys. Rev. B* **74**, 245325 (2006).
- [45] Z. W. Zheng, B. Shen, C. P. Jiang, Y. S. Gui, T. Someya, R. Zhang, Y. Shi, Y. D. Zheng, S. L. Guo, J. H. Chu, and Y. Arakawa, "Multisubband transport of the two-dimensional electron gas in  $\text{Al}_x\text{Ga}_{1-x}\text{N}/\text{GaN}$  heterostructures," *J. Appl. Phys.* **93**, 1651-1655 (2003).
- [46] J. H. Leach, C. Y. Zhu, M. Wu, X. Ni, X. Li, J. Xie, U. Ozgur, H. Morkoc, J. Liberis, E. Sermuksnis, A. Matulionis, H. Cheng, and C. Kurdak, "Degradation in InAlN/GaN-based heterostructure field effect transistors: Role of hot phonons," *Appl. Phys. Lett.* **95**, 223504 (2009).

- [47] J.H. Leach, X. Ni, X. Li, M. Wu, H. Morkoç, L. Zhou, D.A. Cullen, D.J. Smith, H. Cheng, Ç. Kurdak, J.R. Meyer, and I. Vurgaftman, "Bias dependent two-channel conduction in InAlN/AlN/GaN structures," *J. Appl. Phys.* **107**, 083706 (2010).
- [48] H. L. Stormer, A. C. Gossard, and W. Wiegmann, "Observation of inersubband scattering in a 2-dimensional electron system," *Solid State Comm.* **41**, 3 (1982).
- [49] M. Ahoujja, S. Elhamri, R. S. Newrock, D. B. Mast, W. C. Mitchel, Ikai Lo, and A. Fathimulla, "Multiple subband population in delta-doped AlAsSb/InGaAs heterostructures," *J. Appl. Phys.* **81**, 1609-1611 (1997).
- [50] H. van Houten, J. G. Williamson, M. E. I. Broekaart, C. T. Foxon, and J. J. Harris, "Magnetoresistance in a GaAs-Al<sub>x</sub>Ga<sub>1-x</sub>As heterostructure with double subband occupancy," *Phys. Rev. B* **37**, 2756 (1988).
- [51] R. Fletcher, E. Zaremba, M. D'Iorio, C. T. Foxon, and J. J. Harris, "Evidence of a mobility edge in the second subband of an Al<sub>0.33</sub>Ga<sub>0.67</sub>As-GaAs heterojunction," *Phys. Rev. B* **38**, 7866 (1988).
- [52] I. Vurgaftman and J. R. Meyer, "Band parameters for nitrogen-containing semiconductors," *J. Appl. Phys.* **94**, 3675 (2003).
- [53] S. Elhamri, R. S. Newrock, D. B. Mast, M. Ahoujja, W. C. Mitchel, J. M. Redwing, M. A. Tischler, and J. S. Flynn, "Al<sub>0.15</sub>Ga<sub>0.85</sub>N/GaN heterostructures: Effective mass and scattering times," *Phys. Rev. B* **57**, 1374 (1998).
- [54] J. P. Harrang, R. J. Higgins, R. K. Goodall, P. R. Jay, M. Laviron, and P. Delescluse, "Quantum and classical mobility determination of the dominant scattering mechanism in the two-dimensional electron gas of an AlGaAs/GaAs heterojunction," *Phys. Rev. B* **32**, 8126 (1985).
- [55] S. Schmult, M. J. Manfra, A. M. Sergent, A. Punnoose, H. T. Chou, D. Goldhaber-Gordon, and R. J. Molnar, "Quantum transport in high mobility AlGaN/GaN 2DEGs and nanostructures," *Phys. Stat. Soli. (b)* **243**, 1706-1712 (2006).
- [56] P. Gibart, "Metal organic vapour phase epitaxy of GaN and lateral overgrowth," *Rep. Prog. Phys.* (2004).
- [57] S. Sakai, T. Wang, Y. Morishima, and Y. Naoi, "A new method of reducing dislocation density in GaN layer grown on sapphire substrate by MOVPE," *Journal of Crystal Growth* **221**, 334-337 (2000).

- [58] A. Dadgar, M. Poschenrieder, A. Reiher, J. Blasing, J. Christen, A. Krtschil, T. Finger, T. Hempel, A. Diez, and A. Krost, "Reduction of stress at the initial stages of GaN growth on Si(111)," *Appl. Phy. Lett.* **82**, 28-30 (2003).
- [59] X. L. Fang, Y. Q. Wang, H. Meidia, and S. Mahajan, "Reduction of threading dislocations in GaN layers using in situ deposited silicon nitride masks on AlN and GaN nucleation layers," *Appl. Phy. Lett.* **84**, 484-486 (2004).
- [60] K. Pakua, R Bozýek, J.M. Baranowski, Jasinski J., and Z. Liliental-Weber, "Reduction of dislocation density in heteroepitaxial GaN: role of SiH<sub>4</sub> treatment," *J. Cryst. Growth* **267**, 1 (2004).
- [61] Ashutosh Sagar, R. M. Feenstra, C. K. Inoki, T. S. Kuan, Y. Fu, Y. T. Moon, F. Yun, and H. Morkoç, "Dislocation density reduction in GaN using porous SiN interlayers," *Phys. Stat. Soli. (a)* **202**, 722-726 (2005).
- [62] Y. Fu, F. Yun, Y. T. Moon, U. Ozgur, J. Q. Xie, X. F. Ni, N. Biyikli, H. Morkoc, Lin Zhou, David J. Smith, C. K. Inoki, and T. S. Kuan, "Dislocation reduction in GaN grown on porous TiN networks by metal-organic vapor-phase epitaxy," *J. Appl. Phys.* **99**, 033518 (2006).
- [63] Ok-Hyun Nam, Michael D. Bremser, Tsvetanka S. Zheleva, and Robert F. Davis, "Lateral epitaxy of low defect density GaN layers via organometallic vapor phase epitaxy," *Appl. Phy. Lett.* **71**, 2638-2640 (1997).
- [64] S. Haffouz, H. Lahreche, P. Vennegues, P. de Mierry, B. Beaumont, F. Omnes, and P. Gibart, "The effect of the Si/N treatment of a nitridated sapphire surface on the growth mode of GaN in low-pressure metalorganic vapor phase epitaxy," *Appl. Phy. Lett.* **73**, 1278-1280 (1998).
- [65] T. Akasaka, Y. Kobayashi, S. Ando, and N. Kobayashi, "GaN hexagonal microprisms with smooth vertical facets fabricated by selective metalorganic vapor phase epitaxy," *Appl. Phy. Lett.* **71**, 2196-2198 (1997).
- [66] B. Beaumont, V. Bousquet, P. Vennégùès, M. Vaille, A. Bouillé, P. Gibart, S. Dassonneville, A. Amokrane, and B. Sieber, "A Two-Step Method for Epitaxial Lateral Overgrowth of GaN," *Phys. Stat. Soli. (b)* **176**, 567-571 (1999).
- [67] N. Biyikli, X. Ni, Y. Fu, J. Xie, H. Morkoc, H. Cheng, C. Kurdak, I. Vurgaftman, and J. Meyer, "Magnetotransport properties of Al<sub>x</sub>Ga<sub>1-x</sub>N/AlN/GaN heterostructures grown on epitaxial lateral overgrown GaN templates," *J. Appl. Phys.* **101**, 113710 (2007).
- [68] N. Biyikli, U. Ozgur, X. Ni, Y. Fu, H. Morkoc, and C. Kurdak, "Illumination and annealing characteristics of two-dimensional electron gas systems in metal-

- organic vapor-phase epitaxy grown  $\text{Al}_x\text{Ga}_{1-x}\text{N}/\text{AlN}/\text{GaN}$  heterostructures," *J. Appl. Phys.* **100**, 103702 (2006).
- [69] R. Winkler, Spin-Orbit Coupling Effects in Two-Dimensional Electron and Hole Systems (2003).
- [70] Igor Zutic, Jaroslav Fabian, and S. Das Sarma, "Spintronics: Fundamentals and applications," *Rev. of Mod. Phys.* **76**, 323 (2004).
- [71] T. Dietl, H. Ohno, F. Matsukura, J. Cibert, and D. Ferrand, "Zener Model Description of Ferromagnetism in Zinc-Blende Magnetic Semiconductors," *Science* **287**, 1019-1022 (2000).
- [72] J. Y. Fu and M. W. Wu, "Spin-orbit coupling in bulk ZnO and GaN," *J. Appl. Phys.* **104**, 093712 (2008).
- [73] Supriyo Datta and Biswajit Das, "Electronic analog of the electro-optic modulator," *Appl. Phys. Lett.* **56**, 665-667 (1990).
- [74] E.I Rashba, *Fiz. Tverd. Tela (Leningrad)* **2**, 1224 (1960).
- [75] G. Dresselhaus, "Spin-Orbit Coupling Effects in Zinc Blende Structures," *Phys. Rev.* **100**, 580 (1955).
- [76] L. C. Lew Yan Voon, M. Willatzen, M. Cardona, and N. E. Christensen, "Terms linear in  $k$  in the band structure of wurtzite-type semiconductors," *Phys. Rev. B* **53**, 10703 (1996).
- [77] S. Schmult, M. J. Manfra, A. Punnoose, A. M. Sergent, K. W. Baldwin, and R. J. Molnar, "Large Bychkov-Rashba spin-orbit coupling in high-mobility GaN/  $\text{Al}_x\text{Ga}_{1-x}\text{N}$  heterostructures," *Phys. Rev. B* **74**, 033302 (2006).
- [78] C. Kurdak, N. Biyikli, U. Ozgur, H. Morkoc, and V. I. Litvinov, "Weak antilocalization and zero-field electron spin splitting in  $\text{Al}_x\text{Ga}_{1-x}\text{N}/\text{AlN}/\text{GaN}$  heterostructures with a polarization-induced two-dimensional electron gas," *Phys. Rev. B* **74**, 113308 (2006).
- [79] V. I. Litvinov, "Electron spin splitting in polarization-doped group-III nitrides," *Phys. Rev. B* **68**, 155314 (2003).
- [80] V. I. Litvinov, "Polarization-induced Rashba spin-orbit coupling in structurally symmetric III-nitride quantum wells," *Appl. Phys. Lett.* **89**, 222108 (2006).
- [81] Ikai Lo, W. T. Wang, M. H. Gau, S. F. Tsay, and J. C. Chiang, "Wurtzite structure effects on spin splitting in GaN/AlN quantum wells," *Phys. Rev. B* **72**, 245329 (2005).

- [82] N. Thilloesen, S. Cabanas, N. Kaluza, V. A. Guzenko, H. Hardtdegen, and Th Schapers, "Weak antilocalization in gate-controlled Al<sub>x</sub> Ga<sub>1-x</sub> N/GaN two-dimensional electron gases," Phys. Rev. B **73**, 241311 (2006).
- [83] S. V. Iordanskii, Y.B. Lyanda-Geller, and G. E. Pikus, "Weak localization in quantum wells with spin-orbit interaction," JETP Lett. **60**, 207 (1994).
- [84] P. D. Dresselhaus, C. M. A. Papavassiliou, R. G. Wheeler, and R. N. Sacks, "Observation of spin precession in GaAs inversion layers using antilocalization," Phys. Rev. Lett. **68**, 106 (1992).
- [85] B. N. Narozhny, G. Zala, aacute, bor, and I. L. Aleiner, "Interaction corrections at intermediate temperatures: Dephasing time," Phys. Rev. B **65**, 180202 (2002).
- [86] Wan-Tsang Wang, C. L. Wu, S. F. Tsay, M. H. Gau, Ikai Lo, H. F. Kao, D. J. Jang, Jih-Chen Chiang, Meng-En Lee, Yia-Chung Chang, Chun-Nan Chen, and H. C. Hsueh, "Dresselhaus effect in bulk wurtzite materials," App. Phy. Lett. **91**, 082110 (2007).
- [87] W. Desrat, D. K. Maude, Z. R. Wasilewski, R. Airey, and G. Hill, "Dresselhaus spin-orbit coupling in a symmetric (100) GaAs quantum well," Physical Review B **74**, 193317 (2006).
- [88] H. Cheng, Ç Kurdak, J. H. Leach, M. Wu, and H. Morkoc, "Two-subband conduction in a gated high density InAlN/AlN/GaN heterostructure," In Press (2010).
- [89] R. J. Elliott, "Theory of the Effect of Spin-Orbit Coupling on Magnetic Resonance in Some Semiconductors," Phys. Rev. B **96**, 266 (1954).
- [90] M.I. D'yakanov and V.I. Perel', Sov. Phys. JETP **33**, 1053 (1971).
- [91] H. Cheng, N. Biyikli, Ü Özgür, Ç Kurdak, H. Morkoç, and V. I. Litvinov, "Measurement of linear and cubic spin-orbit coupling parameters in AlGaN/AlN/GaN heterostructures with a polarization-induced two-dimensional electron gas," Physica E **40**, 1586-1589 (2008).
- [92] W. Z. Zhou, T. Lin, L. Y. Shang, L. Sun, K. H. Gao, Y. M. Zhou, G. Yu, N. Tang, K. Han, B. Shen, S. L. Guo, Y. S. Gui, and J. H. Chu, "Influence of the illumination on weak antilocalization in an Al<sub>x</sub>Ga<sub>1-x</sub>N/GaN heterostructure with strong spin-orbit coupling," Appl. Phys. Lett. **93**, 262104-262103 (2008).
- [93] J. E. Hansen, R. Taboryski, and P. E. Lindelof, "Weak localization in a GaAs heterostructure close to population of the second subband," Phys. Rev. B **47**, 16040 (1993).

- [94] W. Z. Zhou, T. Lin, L. Y. Shang, L. Sun, K. H. Gao, Y. M. Zhou, G. Yu, N. Tang, K. Han, B. Shen, S. L. Guo, Y. S. Gui, and J. H. Chu, "Weak antilocalization and beating pattern in high electron mobility  $\text{Al}_x\text{Ga}_{1-x}\text{N}/\text{GaN}$  two-dimensional electron gas with strong Rashba spin-orbit coupling," *J. Appl. Phys.* **104**, 053703 (2008).
- [95] Ikai Lo, J. K. Tsai, W. J. Yao, P. C. Ho, Li-Wei Tu, T. C. Chang, S. Elhamri, W. C. Mitchel, K. Y. Hsieh, J. H. Huang, H. L. Huang, and Wen-Chung Tsai, "Spin splitting in modulation-doped  $\text{Al}_x\text{Ga}_{1-x}\text{N}/\text{GaN}$  heterostructures," *Phys. Rev. B* **65**, 161306 (2002).
- [96] N. Tang, B. Shen, M. J. Wang, K. Han, Z. J. Yang, K. Xu, G. Y. Zhang, T. Lin, B. Zhu, W. Z. Zhou, and J. H. Chu, "Beating patterns in the oscillatory magnetoresistance originated from zero-field spin splitting in  $\text{Al}[\text{sub } x]\text{Ga}[\text{sub } 1 - x]\text{N}/\text{GaN}$  heterostructures," *Appl. Phys. Lett.* **88**, 172112 (2006).
- [97] Ning Tang, Bo Shen, Kui Han, Fang-Chao Lu, Fu-Jun Xu, Zhi-Xin Qin, and Guo-Yi Zhang, "Zero-field spin splitting in  $\text{Al}_x\text{Ga}_{1-x}\text{N}/\text{GaN}$  heterostructures with various Al compositions," *Appl. Phys. Lett.* **93**, 172113 (2008).
- [98] S. B. Lisesivdin, N. Balkan, O. Makarovskiy, A. Patane, A. Yildiz, M. D. Caliskan, M. Kasap, S. Ozcelik, and E. Ozbay, "Large zero-field spin splitting in AlGaN/AlN/GaN/AlN heterostructures," *J. Appl. Phys.* **105**, 093701 (2009).
- [99] M. Ramonas, A. Matulionis, J. Liberis, L. Eastman, X. Chen, and Y. J. Sun, "Hot-phonon effect on power dissipation in a biased  $\text{Al}_x\text{Ga}_{1-x}\text{N}/\text{AlN}/\text{GaN}$  channel," *Phys. Rev. B* **71** (2005).
- [100] C. E. Martinez, N. M. Stanton, A. J. Kent, M. L. Williams, I. Harrison, H. Tang, J. B. Webb, and J. A. Bardwell, "Energy relaxation by hot 2D electrons in AlGaN/GaN heterostructures: the influence of strong impurity and defect scattering," *Semiconductor Science and Technology* **21**, 1580-1583 (2006).
- [101] K. J. Lee, J. J. Harris, A. J. Kent, T. Wang, S. Sakai, D. K. Maude, and J. C. Portal, "Investigation of phonon emission processes in an AlGaN/GaN heterostructure at low temperatures," *Appl. Phys. Lett.* **78**, 2893-2895 (2001).
- [102] N. M. Stanton, A. J. Kent, S. A. Cavill, A. V. Akimov, K. J. Lee, J. J. Harris, T. Wang, and S. Sakai, "Energy relaxation by warm two-dimensional electrons in a GaN/AlGaN heterostructure," *Phys. Status Solidi B-Basic Res.* **228**, 607-611 (2001).
- [103] P. Hawker, A. J. Kent, T. S. Cheng, and C. T. Foxon, "Heat pulse studies of the energy relaxation rate of hot electrons in n-type GaN epilayers," *Physica B* **263**, 227-229 (1999).

- [104] J. Q. Xie, X. F. Ni, M. Wu, J. H. Leach, U. Ozgue, and H. Morkoc, "High electron mobility in nearly lattice-matched AlInN/AlN/GaN heterostructure field effect transistors," *Appl. Phys. Lett.* **91** (2007).
- [105] R. Fletcher, Y. Feng, C. T. Foxon, and J. J. Harris, "Electron-phonon interaction in a very low mobility GaAs/Ga<sub>1-x</sub>Al<sub>x</sub>As delta-doped gated quantum well," *Phys. Rev. B* **61**, 2028-2033 (2000).
- [106] E. Chow, H. P. Wei, S. M. Girvin, W. Jan, and J. E. Cunningham, "Effect of disorder on phonon emissions from a two-dimensional electron gas in GaAs/Al<sub>x</sub>Ga<sub>1-x</sub>As heterostructures," *Phys. Rev. B* **56**, R1676-R1679 (1997).
- [107] E. Chow, H. P. Wei, S. M. Girvin, and M. Shayegan, "Phonon emission from a 2D electron gas: Evidence of transition to the hydrodynamic regime," *Phys. Rev. Lett.* **77**, 1143 (1996).
- [108] Y. Ma, R. Fletcher, E. Zaremba, M. Diorio, C. T. Foxon, and J. J. Harris, "Energy-loss rate of 2-dimensional electrons at a GaAs/Al<sub>x</sub>Ga<sub>1-x</sub>As interface," *Phys. Rev. B* **43**, 9033-9044 (1991).
- [109] P. Tripathi and B. K. Ridley, "Dynamics of hot-electron scattering in GaN heterostructures," *Phys. Rev. B* **66**, 195301 (2002).
- [110] F. Bernardini, V. Fiorentini, and D. Vanderbilt, "Spontaneous polarization and piezoelectric constants of III-V nitrides," *Phys. Rev. B* **56**, 10024-10027 (1997).
- [111] T. A. Eckhouse, O. Suzer, C. Kurdak, F. Yun, and H. Morkoc, "Electric-field-induced heating and energy relaxation in GaN," *Appl. Phys. Lett.* **82**, 3035-3037 (2003).
- [112] R. B. Laughlin, "Quantized Hall conductivity in two dimensions," *Phys. Rev. B* **23**, 5632 (1981).
- [113] B. I. Halperin, "Quantized Hall conductance, current-carrying edge states, and the existence of extended states in a two-dimensional disordered potential," *Phys. Rev. B* **25**, 2185 (1982).
- [114] M. Buttiker, "Absence of backscattering in the quantum Hall effect in multiprobe conductors," *Phys. Rev. B* **38**, 9375 (1988).
- [115] H. P. Wei, D. C. Tsui, M. A. Paalanen, and A. M. M. Pruisken, "Experiments on Delocalization and Universality in the Integral Quantum Hall Effect," *Phys. Rev. Lett.* **61**, 1294 (1988).

- [116] K. V. Kavokin, M. E. Portnoi, A. J. Matthews, A. Usher, J. Gething, D. A. Ritchie, and M. Y. Simmons, "Induced currents, frozen charges and the quantum Hall effect breakdown," *Solid State Communications* **134**, 257 (2005).
- [117] E. Yahel, D. Orgad, A. Palevski, and H. Shtrikman, "Inductive Probing of the Integer Quantum Hall Effect," *Phys. Rev. Lett.* **76**, 2149 (1996).
- [118] E. Yahel, A. Tsukernik, A. Palevski, and H. Shtrikman, "Evidence for Bulk Current in Hall Bar Samples and Potential Screening in the Integer Quantum Hall Effect," *Phys. Rev. Lett.* **81**, 5201 (1998).
- [119] J. Huels, J. Weis, J. Smet, K. v Klitzing, and Z. R. Wasilewski, "Long time relaxation phenomena of a two-dimensional electron system within integer quantum Hall plateau regimes after magnetic field sweeps," *Phys. Rev. B* **69**, 085319 (2004).
- [120] L. A. Farina, X. Bai, Ç Kurdkar, S. Chakrabarti, P. Bhattacharya, and M. Shayegan, "Stability of charged impurities in a coupled single electron transistor and antidot system," *Physica E* **34**, 187 (2006).
- [121] Lee Adrienne Farina, "Studies of two-dimensional electron and superconducting vortex systems using hybrid devices," Thesis, University of Michigan (2005).
- [122] Jens Martin, Shahal Ilani, Basile Verdene, Jurgen Smet, Vladimir Umansky, Diana Mahalu, Dieter Schuh, Gerhard Abstreiter, and Amir Yacoby, "Localization of Fractionally Charged Quasi-Particles," *Science* **305**, 980 (2004).
- [123] Y. Y. Wei, J. Weis, K. v Klitzing, and K. Eberl, "Edge Strips in the Quantum Hall Regime Imaged by a Single-Electron Transistor," *Phys. Rev. Lett.* **81**, 1674 (1998).
- [124] Y. Y. Wei, J. Weis, K. v. Klitzing, and K. Eberl, "Single-electron transistor as an electrometer measuring chemical potential variations," *Appl. Phys. Lett.* **71**, 2514 (1997).
- [125] Issac L. Chuang and Michael A. Nielsen, "Quantum Computation and Quantum Information," (2000).
- [126] K. Kim, M.-S. Chang, R. Islam S. Korenblit, E. E. Edwards, J. K. Freericks, G.-D. Lin, L.-M. Duan, and C. Monroe, "Quantum Simulation of Frustrated Ising Spins with Trapped Ions," *Nature* **465**, 590 (2010).
- [127] P. W. Shor, "Scheme for reducing decoherence in quantum computer memory," *Phys. Rev. A* **52**, R2493-R2496 (1995).

- [128] Chetan Nayak, Steven H. Simon, Ady Stern, Michael Freedman, and Sankar Das Sarma, "Non-Abelian anyons and topological quantum computation," Rev. of Mod. Phys. **80**, 1083 (2008).
- [129] S. Das Sarma, M. Freedman, and C. Nayak, "Topologically protected qubits from a possible non-Abelian fractional quantum Hall state," Phys. Rev. Lett. **94**, 166802 (2005).
- [130] C. L. Kane, "Telegraph Noise and Fractional Statistics in the Quantum Hall Effect," Physical Review Letters **90**, 226802 (2003).
- [131] F. E. Camino, Wei Zhou, and V. J. Goldman, "Aharonov-Bohm Superperiod in a Laughlin Quasiparticle Interferometer," Physical Review Letters **95**, 246802 (2005).
- [132] V. J. Goldman, I. Karakurt, Jun Liu, and A. Zaslavsky, "Invariance of charge of Laughlin quasiparticles," Phys. Rev. B **64**, 085319 (2001).
- [133] S. Ilani, J. Martin, E. Teitelbaum, J. H. Smet, D. Mahalu, V. Umansky, and A. Yacoby, "The microscopic nature of localization in the quantum Hall effect," Physica E-Low-Dimensional Systems & Nanostructures **25**, 219-226 (2004).
- [134] S. Ilani, J. Martin, E. Teitelbaum, J. H. Smet, D. Mahalu, V. Umansky, and A. Yacoby, "The microscopic nature of localization in the quantum Hall effect," Nature **427**, 328-332 (2004).
- [135] M. A. Kastner, "The single-electron transistor," Rev. of Mod. Phys. **64**, 849 (1992).
- [136] A. M. Dabiran, R. T. Zeller, F. F. Fang, S. L. Wright, and P. J. Stiles, "Electrochemical potential oscillations of the two-dimensional electron-gas in GaAs/AlGaAs heterostructures in high magnetic-fields," Surf. Sci. **196**, 712 (1988).
- [137] V. M. Pudalov, S. G. Semenchinsky, and V. S. Edelman, "Hysteresis phenomena in charging of Si MOSFET in quantizing magnetic-field," Solid State Communications **51**, 713-717 (1984).
- [138] N. F. Mott, Philos. Mag. **19**, 835 (1969).
- [139] G. Ebert, K. Vonklitzing, C. Probst, E. Schuberth, K. Ploog, and G. Weimann, "Hopping conduction in the Landau-level tails in GaAs-Al<sub>x</sub>Ga<sub>1-x</sub>As heterostructures at low-temperatures," Solid State Communications **45**, 625-628 (1983).

- [140] M. Furlan, "Electronic transport and the localization length in the quantum Hall effect," *Physical Review B* **57**, 14818 (1998).
- [141] Y. Katayama, D. C. Tsui, and M. Shayegan, "Experimental study of  $\sigma_{xx}$  (T) for quasiparticle charge determination in the fractional quantum Hall effect," *Physical Review B* **49**, 7400 (1994).
- [142] R. K. Goodall, R. J. Higgins, and J. P. Harrang, "Capacitance measurements of a quantized two-dimensional electron gas in the regime of the quantum Hall effect," *Physical Review B* **31**, 6597 (1985).
- [143] K. Oto, S. Takaoka, and K. Murase, "Bulk conductivity at quantum Hall plateaux by magnetocapacitance measurement," *Physica B* **227**, 189-191 (1996).
- [144] R. J. Schoelkopf, P. Wahlgren, A. A. Kozhevnikov, P. Delsing, and D. E. Prober, "The radio-frequency single-electron transistor (RF-SET): A fast and ultrasensitive electrometer," *Science* **280**, 1238-1242 (1998).
- [145] J. Y. Fu and M. W. Wu, "Spin-orbit coupling in bulk ZnO and GaN," *J. Appl. Phys.* **104**, 093712-093717 (2008).